Hollow microneedle-based sampling and sensing of dermal interstitial fluid

by

Taher Abbasiasl

A Dissertation Submitted to the
Graduate School of Sciences and Engineering
in Partial Fulfillment of the Requirements for
the Degree of

Doctor of Philosophy

in

Biomedical Sciences and Engineering



KOÇ ÜNİVERSİTESİ

November, 2024

Hollow microneedle-based sampling and sensing of dermal interstitial fluid

Koç University

Graduate School of Sciences and Engineering

This is to certify that I have examined this copy of a doctoral dissertation by

Taher Abbasiasl

and have found that it is complete and satisfactory in all respects,
and that any and all revisions required by the final
examining committee have been made.

Committee Members:

Assist. Prof. Levent Beker (Advisor)

Prof. Dr. Erdem Alaca

Assist. Prof. Murat Kuşcu

Assoc. Prof. Ender Yıldırım

Assoc. Prof. Yegan Erdem

Date: 22.11.2024

This thesis is dedicated to my beloved family.

ABSTRACT

Hollow microneedle-based sampling and sensing of dermal interstitial fluid

Taher Abbasiasl

Doctor of Philosophy in Biomedical Sciences and Engineering

November, 2024

Microneedle-based biosensing platforms have emerged as a promising alternative for blood-based health monitoring devices. Microneedles (MNs) can access the dermal interstitial fluid (ISF) in a painless and blood-free manner, enabling the detection of a wide range of biomarkers. Although in-skin biomarker monitoring using functionalized solid MNs remains attractive due to the challenging task of ISF sampling, there is growing attention toward the integration of biosensors into ISF sampling platforms. ISF sampling can be followed by measuring the biomarker level using the integrated biosensors. Recently, microfluidic-based biosensing devices have been incorporated with hollow MNs (HMNs) to enable the detection of target biomarkers in the collected dermal ISF. In this thesis, we report the development of HMN-based platforms integrated with microfluidic ISF collection chambers to provide the necessary contact between the sampled ISF and biosensors. Chapter one establishes a concise overview of recent advancements in the manufacturing of various HMNs and their integration into diverse biosensing devices. In chapter two, we demonstrate the integration of laser-drilled HMNs with a touch-activated vacuum source to enable continuous sampling of ISF with subsequent electrochemical sensing of glucose and pH levels. The wearable vacuum system leverages the self-recovery feature of the utilized elastomer to create the necessary negative pressure for ISF sampling. The developed touch-activated system shows ISF extraction rate of approximately 17 $\mu L\ h^{-1}$ in vivo. We demonstrate the capacity of the developed platform in continuous health monitoring by measuring the glucose and pH levels in animal models. Chapter three presents our efforts in developing a hydrophilic 3D-printed HMN-based platform for measuring the pH and urea levels in the collected ISF using colorimetric techniques. Multichannel MNs are fabricated using high-precision projection micro stereolithography technology, followed by deposition of an oxide layer using plasma enhanced chemical vapor deposition (PECVD) to enhance the wettability of MNs for effective ISF collection. The oxide layer results in a significant decrease in water contact angle of the 3D-printed films from about 72° to 9°, rendering them superhydrophilic. The enhanced wettability of the surfaces leads to an improved liquid uptake capability of the MNs from agarose hydrogel and rat skin samples. We demonstrate the applicability of the developed approach by ex vivo colorimetric sensing of pH and urea. Overall, the devices developed offer promising advancements in technology and exhibit great promise for enhancing biomedical sensing and diagnostic applications.

ÖZETÇE

İçi boş mikroiğne bazlı dermal interstisyel sıvının örnekleme ve algılanması

Taher Abbasiasl

Biyomedikal Bilimler ve Mühendislik

Kasım, 2024

Mikroiğne tabanlı biyoalgılama platformları, kan bazlı sağlık izleme cihazlarına umut verici bir alternatif olarak ortaya çıkmaktadır. Mikroiğneler (MN'ler), dermal interstisyel sıvıya (ISF) ağrısız ve kansız bir şekilde erişim sağlayarak çok çeşitli biyobelirteçlerin tespit edilmesine olanak tanımaktadır. Fonksiyolandirilmiş katı MN'leri kullanarak cilt içi biyobelirteç izleme, ISF örneklemenin zorlukları nedeniyle cazipliğini korusa da biyosensörlerin ISF örnekleme platformlarına biyosensörlerin entegrasyonuna yönelik ilgi giderek artmaktadır. ISF örnekleme işlemini, entegre biyosensörler aracılığıyla biyobelirteç seviyelerinin ölçümü takip edebilmektedir. Son dönemde, mikroakışkan tabanlı biyoalgılama cihazları, toplanan dermal ISF'te hedef biyobelirteçlerin tespit edilmesini sağlamak amacıyla içi boş mikroiğnelerle (HMN'ler) birleştirilmiştir. Bu tezde, örneklenen ISF ile biyosensörler arasında gerekli teması sağlamak amacıyla mikroakışkan ISF toplama odalarıyla entegre edilmiş HMN tabanlı platformların geliştirilmesi sunulmaktadır. Birinci bölüm, çeşitli HMN'lerin üretiminde ve bu cihazların farklı biyoalgılama sistemlerine entegrasyonunda kaydedilen son gelişmelerin kısa bir özetini sunmaktadır. İkinci bölümde, lazerle delme yöntemiyle üretilmiş HMN'lerin, ISF'nin sürekli olarak toplanmasını ve ardından glukoz ve pH seviyelerinin elektrokimyasal olarak algılanmasını sağlayan dokunmatik bir vakum kaynağı ile entegrasyonu gösterilmektedir. Giyilebilir vakum sistemi, kullanılan elastomerin kendini yenileme özelliğinden yararlanarak ISF örnekleme için gerekli negatif basıncı oluşturmaktadır. Geliştirilen dokunmatik sistem, canlı hayvanlarda yaklaşık 17 µL/saat ISF ekstraksiyon oranı göstermektedir. Platformun, hayvan modellerinde glukoz ve pH seviyelerinin sürekli sağlık izlemesinde kullanılabilirliği gösterilmiştir. Üçüncü bölümde, kolorimetrik yöntemleri kullanılarak toplanan ISF'te pH ve üre seviyelerinin ölçümü için hidrofilik 3D baskılı HMN tabanlı bir platform geliştirme çalışmalarımız sunulmaktadır. Çok kanallı MN'ler, yüksek hassasiyetli projeksiyon mikro-stereolitografi teknolojisiyle üretilmiş ve ardından mikroiğnelerin ISF toplama etkinliğini artırmak için plazma destekli kimyasal buhar biriktirme (PECVD) yöntemiyle bir oksit tabakası kaplanmıştır. Oksit tabakası, 3D baskılı filmlerin su temas açısını yaklaşık 72°'den 9°'ye düşürerek onları süperhidrofilik hale getirmiştir. Yüzeylerin geliştirilmiş ıslanabilirliği, mikroiğnelerin agaroz hidrojel ve sıçan deri örneklerinden sıvı alma kapasitesini artırmıştır. Geliştirilen yaklaşımın uygulanabilirliği, pH ve üre renk değişim algılamasıyla ex vivo olarak gösterilmiştir. Genel olarak, geliştirilen cihazlar, teknolojide önemli ilerlemeler sunmakta ve biyomedikal algılama ve tanısal uygulamaları geliştirme konusunda büyük bir potansiyel sergilemektedir.

ACKNOWLEDGEMENTS

Completing this PhD thesis has been a transformative journey, one that would not have been possible without the support and guidance of many individuals. I am deeply grateful to everyone who has contributed to my academic and personal growth throughout this period.

I would like to express my heartfelt thanks to my supervisor, Prof. Beker, for his invaluable guidance, patience, and encouragement. I also extend my gratitude to the jury members, Prof. Alaca, Prof. Kuşcu, Prof. Yıldırım, and Prof. Erdem, for their insightful feedback and suggestions, which have greatly enriched this work. My appreciation also goes to Prof. Koydemir, Prof. Öztürk, Prof. İskender Yilgör, and Emel Yilgör for their constructive collaboration and support.

I am thankful to all the members of Bio-integrated Microdevices Lab (BMDL) for their camaraderie, support, and stimulating discussions that made my time in the lab enjoyable and productive. Special thanks to my friends, whose encouragement and company have been a source of strength throughout this journey.

Finally, I owe my deepest gratitude to my family. Their unwavering love, patience, and belief in me have been my greatest source of motivation. To my parents, siblings, and extended family, thank you for being my anchor through it all.

TABLE OF CONTENTS

ACKNOWLEDGEMENTS ..... **vi**

LIST OF FIGURES ..... **xi**

LIST OF TABLES ..... **xvi**

ABBREVIATIONS ..... **xvii**

Chapter One: Introduction **1**

1.1 Engineering Considerations and Technology Requirements 1

1.1.1 Skin structure 1

1.1.2 Interstitial fluid and biomarkers 2

1.1.3 Importance of ISF in continuous health monitoring 4

1.1.4 Microneedles in health monitoring 5

1.1.5 Microneedles for ISF extraction and continuous health monitoring 6

1.2 Materials and Methods for Microneedle Fabrication 7

1.2.1 Material 7

1.2.2 Structure 11

1.3 Strategies for Fabrication of HMNs 14

1.3.1 MEMS-based technologies 15

1.3.2 Laser micromachining 17

1.3.3 3D printing 18

1.3.4 CNC machining 19

1.3.5 Drawing lithography 19

1.3.6 Combining multiple fabrication strategies 19

1.4 Biosensing 21

1.4.1 Electrochemical sensing 22

1.4.2 Colorimetric sensing 24

Chapter Two: ISF Sampling and Sensing Through Integration of Laser-Drilled Microneedles and a Finger Actuated Vacuum System 26

2.1 Introduction 26

2.2 Materials and Methods 29

2.2.1 Chemicals and materials 29

2.2.2 Fabrication of HMNs 29

2.2.3 Fabrication of vacuum generation chamber and check valves 31

2.2.4 Fabrication of electrochemical sensor array 35

2.2.5 Preparation of glucose sensor 36

2.2.6 Preparation of pH sensor 36

2.2.7 Design of PCB 36

2.2.8 Assembly of vacuum-integrated ISF extraction and sensing system (VIES) 37

2.2.9 Characterization of vacuum generation system 38

2.2.10 Morphology characterization of MNs and HMNs 39

2.2.11 Mechanical characterization of MNs and HMNs 39

2.2.12 Skin penetration efficiency test 40

2.2.13 In vitro electrochemical detection of glucose and pH 40

2.2.14 Ex vivo ISF extraction and measurement of glucose and pH 41

2.2.15 In vivo ISF extraction and measurement of glucose and pH 42

2.2.16 Statistical analysis 43

2.3 Results and Discussion 44

2.3.1 System design and working principle of wearable vacuum-integrated ISF extraction and sensing system (VIES) 44

2.3.2 HMN patch fabrication and characterization 47

2.3.3 Performance and characterization of vacuum generation system 51

2.3.4 Performance and characterization of electrochemical sensing system .. 59

2.3.5 Ex vivo evaluation of VIES system in ISF extraction and electrochemical sensing 68

2.3.6 Integration of VIES and in vivo studies 74

2.4 Conclusions 83

Chapter Three: 3D-Printed Multichannel Microneedle Platform for Extraction and Colorimetric Sensing of ISF 84

3.1 Introduction 84

3.2 Materials and Methods 86

3.2.1 Materials and chemicals 86

3.2.2 Design of MN arrays and 3D printing 87

3.2.3 Mechanical characterization of 3D-printed MN arrays 90

3.2.4 Morphological characterization of MNs 91

3.2.5 Hydrophilic coating and characterization 94

3.2.6 Integration of microfluidic module 95

3.2.7 In vitro ISF extraction experiments 95

3.2.8 ISF collection from rat skin ex vivo 96

3.2.9 Forming the colorimetric assay 102

3.2.10 Color development and biomarker detection of the colorimetric assay 102

3.2.11 Cell culture and cell viability assay 103

3.2.12 Statistical analysis 104

3.3 Results and Discussion 104
3.3.1 Design and fabrication of the MN patches 104
3.3.2 Liquid uptake into microchannels by capillary flow 105
3.3.3 Mechanical performance of the 3D-printed MNs 108
3.3.4 Surface modification and biocompatibility of the MNs 109
3.3.5 Liquid uptake capability of the MNs 112
3.3.6 In vitro and ex vivo parametric study on liquid uptake 115
3.3.7 Quantitative colorimetric analysis and detection of biomarkers 119
3.4 Conclusions 122
Chapter Four: Conclusion and Future Outlook 124
4.1 Summary and Conclusions 124
4.2 Future Directions 125
BIBLIOGRAPHY 127
List of Publications 150

LIST OF FIGURES

Figure 1.1. Schematic of the overall structure of the skin layers. 2

Figure 1.2. Schematic illustration of ISF flow. 3

Figure 1.3. MNs fabricated using different materials. 10

Figure 1.4. Morphology and design parameters of MNs. 14

Figure 1.5. Different strategies to manufacture HMNs. 20

Figure 1.6. Integration of biofluid collection systems with electrochemical sensors. 24

Figure 2.1. Fabrication process flow of the HMN patch. 30

Figure 2.2. Designs and dimensions of the 3D-printed molds and HMNs used for the experiments. 31

Figure 2.3. Designs and dimensions of the vacuum generation device used in the in vitro and in vivo experiments, along with the 3D-printed molds which were used to fabricate the device. 33

Figure 2.4. Photographic images of the fabrication process of the vacuum generation device. 34

Figure 2.5. Fabrication process of screen-printed electrodes. 35

Figure 2.6. Integration process of the HMN patch, microfluidic layers, and vacuum generation system. 38

Figure 2.7. Experimental setup for characterization of the vacuum generation system. . 39

Figure 2.8. Ex vivo characterization experimental setup. 42

Figure 2.9. Illustration of the HMN-based wearable device for on-demand extraction of ISF and electrochemical sensing. 45

Figure 2.10. Different steps of vacuum generation in the VIES device. 46

Figure 2.11. Characterization of MN and HMN patches. 48

Figure 2.12. Mechanical characterization of the PC-based MNs before and after laser drilling..... 49

Figure 2.13. Confocal microscopy images of MN insertion in skin. The three images show confocal results of three different MNs from the HMN patch. 49

Figure 2.14. H&E-stained sections of rat skin showing HMNs penetration sites and the surrounding tissue. 50

Figure 2.15. Working principle of the vacuum generation system. 52

Figure 2.16. Illustration of different steps of vacuum generation in CH #1 in three successive cycles. 53

Figure 2.17. Comparison of the pressure profiles inside CH #1 and CH #2 with and without CV #2. 55

Figure 2.18. Characterization of chambers with different dimensions. 56

Figure 2.19. Capability of vacuum generation system to create negative pressure in different time frames..... 57

Figure 2.20. Investigating the effect of embedding a solid layer in bottom side of vacuum generation chamber. 57

Figure 2.21. Pressure profile in the vacuum chamber under oscillatory motions. 58

Figure 2.22. Experimental characterization of the glucose sensor at low concentrations. 60

Figure 2.23. Experimental characterization of the glucose sensor at high concentrations. 61

Figure 2.24. Characterization experiments to test the reproducibility and stability of the glucose sensor. 62

Figure 2.25. In vitro characterization of the pH sensor. 64

Figure 2.26. Potentiometric responses of the pH sensor against abrupt changes and stability study. 65

Figure 2.27. Selectivity performance of the electrochemical against different interferents. 65

Figure 2.28. In vitro characterization of the pH sensor using the developed electronic board. 66

Figure 2.29. Interference investigation of simultaneous data recording using the developed system. 67

Figure 2.30. Ex vivo characterization of the VIES system. 69

Figure 2.31. Pressure profile of the vacuum generation chamber during ex vivo ISF extraction experiment. 69

Figure 2.32. Characterization of vacuum drop inside the VIES device used for ex vivo and in vivo experiments. 71

Figure 2.33. Measuring the required force to generate different vacuum levels in the VIES system used for ex vivo and in vivo experiments. 72

Figure 2.34. ISF extraction from skin samples to investigate the effect of different parameters. 72

Figure 2.35. Ex vivo characterization of the electrochemical sensors. 74

Figure 2.36. Images of skin recovery after peeling off the HMN patch. 76

Figure 2.37. H&E-stained sections of rat skin 5 days after HMN patch removal. 76

Figure 2.38. In vivo ISF collection and sensing performance of the HMN-based VIES system. 77

Figure 2.39. ISF extraction in vivo to investigate the effect of different parameters. 77

Figure 2.40. In vivo glucose and pH measurement using the VIES system. 81

Figure 2.41. Continuous long-term in vivo investigation of the performance of pH sensor. 82

Figure 3.1. Design and dimensions of the 3D-printed HMN patches. 88

Figure 3.2. Sliced images generated by VoxelDance software, which was used as UV masks during printing process. 89

Figure 3.3. SEM top view images of 3D-printed MNs. 89

Figure 3.4. Image analysis of SEM images to determine the size of printed microchannels in the needles. 90

Figure 3.5. Mechanical behavior of the MN arrays under compression administered by vertical force. 92

Figure 3.6. Mechanical behavior of the MN arrays under shear load. 93

Figure 3.7. Assessment of the required force during MN administration to skin. 94

Figure 3.8. Experimental setup used for in vitro extraction experiments. 97

Figure 3.9. Demonstration of liquid uptake through microchannels. 98

Figure 3.10. Liquid uptake by the 3D-printed MNs from blue-dyed aISF. 99

Figure 3.11. Liquid uptake by the 3D-printed MNs from agarose gel containing aISF. 100

Figure 3.12. Sequential images of liquid uptake into the microfluidic chamber integrated to the MNs. 101

Figure 3.13. Experimental setup used for ex vivo ISF extraction experiments. 102

Figure 3.14. Illustration of 3D-printed MNs for extraction and colorimetric sensing of dermal ISF. 107

Figure 3.15. Capillary rise and the resulting meniscus inside a tube with wetting angle less than 90°. 108

Figure 3.16. Mechanical characterization of the MN patches. 110

Figure 3.17. Surface modification of 3D-printed MNs to enhance the wettability. 111

Figure 3.18. Water contact angle of the treated SiO_2-coated samples over time. 111

Figure 3.19. In vitro cell cytotoxicity test of the 3D-printed MNs. 112

Figure 3.20. In vitro characterization of the liquid extraction capability of the MNs. .. 114

Figure 3.21. Liquid uptake by the half bare/half SiO_2-coated MN patch. 115

Figure 3.22. Effect of different parameters on the extraction capacity of the MNs. 118

Figure 3.23. Ex vivo ISF extraction from rat skin samples. 119

Figure 3.24. Colorimetric detection of urea and pH. 122

LIST OF TABLES

Table 2.1. Dimensions of different chambers used for the characterization of vacuum generation chamber. 56

Table 2.2. Summary table of some recent studies on ISF extraction and sensing. 79

Table 3.1. Design of different MN patches used in this study. 87

ABBREVIATIONS

AA	Ascorbic Acid
ADC	Analog to Digital Converter
AFE	Analog Frond-End
aISF	Artificial Interstitial Fluid
BLE	Bluetooth Low Energy
CGM	Continuous Glucose Monitoring
CH	Chamber
CHP	Capillary Hydrostatic Pressure
CNC	Computer Numerical Control
COP	Capillary Osmotic Pressure
CV	Cyclic Voltammetry
CV	Control Valve
CVD	Chemical Vapor Deposition
DI	Deionized
FDA	Food and Drug Administration
FFC	Flexible Flat Cable
FPCB	Flexible Printed Circuit Board
HMN	Hollow Microneedle
IPA	Isopropyl Alcohol
ISF	Interstitial Fluid
ISF OP	Interstitial Fluid Osmotic Pressure
MN	Microneedle
OCP	Open Circuit Potential
OCT	Optical Coherence Tomography
PANI	Polyaniline
PB	Prussian Blue
PBS	Phosphate-Buffered Saline
PC	Polycarbonate
PCB	Printed Circuit Board

PDMS	Polydimethylsiloxane
PECVD	Plasma Enhanced Chemical Vapor Deposition
PEEK	Polyether Ether Ketone
PEG	Polyethylene glycol (PEG)
PET	Polyethylene Terephthalate
PGMA	Poly (glycidyl methacrylate)
PI	Polyimide
PLA	Polylactic Acid
PμSL	Projection Micro Stereolithography
RI	Reverse Iontophoresis
RSD	Relative Standard Deviation
SD	Standard Deviation
SEM	Scanning Electron Microscopy
SoC	System on a Chip
TIA	Transimpedance Amplifier
UV	Ultraviolet
VIES	Vacuum-Integrated ISF Extraction and Sensing System
WCA	Water Contact Angle

1 Chapter One: Introduction

1.1 Engineering Considerations and Technology Requirements

1.1.1 Skin structure

As the largest and most accessible organ of the body, the skin protects the internal organs and tissues, regulates body temperature and pressure, controls body dehydration, and acts as a shield against pathogens [1]. Most importantly, the skin serves as a large reservoir of interstitial fluid (ISF), a biofluid with a biomarker composition similar to that of blood, and possesses sensory functions in response to external stimuli such as pain, temperature, and pressure [2]. Therefore, transdermal sensing has attracted great attention in developing minimally invasive health monitoring devices [3]. The skin essentially comprises three primary layers: the epidermis, dermis, and hypodermis (**Figure 1.1**).

The epidermis is the outermost layer of the skin with an approximate thickness of 100 μm in common sites to access ISF, such as the abdomen and arms, has the lowest ISF content among the three skin layers (15–35% by mass) [4], and consists of two main regions: stratum corneum and stratum Malpighii (viable epidermis). As the outermost layer of the epidermis, stratum corneum has a thickness of 8-20 μm, and despite having a cell depth of about 10–15, plays the key role in preventing loss of moisture from the body and acts as the primary barrier against the permeation of potential harmful microorganisms. Stratum corneum has a wall-like structure with 10–30 brick layers of dead corneocytes [5], [6]. The viable layer with a thickness of 50–100 μm lies below the stratum corneum, which comprises randomly oriented living cells such as keratinocytes and basal cells. The viable layer is crucial in renewing the stratum corneum layer by continuous division and keratinization of keratinocytes.

Below the viable epidermis is the dermis layer with a thickness of about 2–5 mm, with the main composition of collagen fibrils, elastic connective tissues, fibroblasts, mast cells involved in immune and inflammatory response, and melanocytes. The volume of the dermis layer contains at least 70% water, with 40% being ISF and 30% bound water [4]. The dermis comprises two main layers: the highly vascularized papillary dermis with an approximate

thickness of 15 µm, which provides the necessary nutrients for the epidermis layer, and the gel-like reticular dermis, which is mainly composed of fibroblasts and immune cells and holds the structure of the tissue against mechanical disruptions [2]. Due to the special structure of the dermis layer, it offers a minimal barrier against the permeation of most drugs. The dermis layer contains nerve endings, blood vessels, sweat glands, and lymph nodes. The high ISF content and proximity to capillaries have rendered the dermis layer the most desirable skin layer to access ISF.

The innermost layer of the skin is the hypodermis (also known as the subcutaneous tissue or adipose layer). It is composed of a layer of fat cells with interconnecting collagen and elastin fibers. Owing to its high content of fat and connective tissues, its primary function is to serve as a heat insulator and a shield against disruptive shocks [7], [8]. Similar to the epidermis layer, the hypodermis is also low inn ISF content, rendering it a less suitable candidate to access ISF compared to the dermis layer.

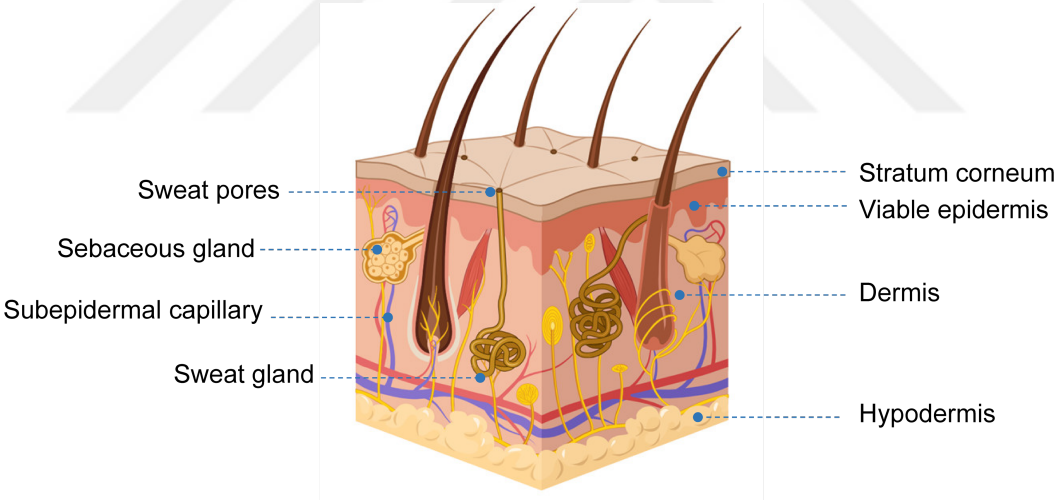


Figure 1.1. Schematic of the overall structure of the skin layers. Created with BioRender.com

1.1.2 Interstitial fluid and biomarkers

Body fluids can be classified into two main categories: extracellular fluid, which is the fluid that surrounds all the cells in the body, and intracellular fluid, which is the fluid content of the cells in the body. As an extracellular fluid, ISF has a volume of three times that of blood in the range of 9–13.5 L [3], [9]. The ISF content around the cells within the tissues provides the necessary nutrients and assists the cells with waste secretion and molecular

communication. ISF is formed as plasma diffuses back and forth through the blood vessels and creates an equilibrated medium with the cells and tissue environment. The hydrostatic pressure generated by the blood vessels and the osmotic pressure of ISF form a pressure difference that is the driving force for fluid flow from plasma to ISF [9], [10]. The osmotic pressure in human capillaries is approximately 28 mmHg, which helps retain the fluid in the capillaries. The capillary hydrostatic pressure, which is the pressure that forces the fluid out of the capillaries, is estimated to be about 20 mmHg, relative to the atmospheric pressure. The interstitial fluid hydrostatic and osmotic pressures are about 8 and -1 to -3 mmHg, respectively (**Figure 1.2a**). The remaining proteins in the capillaries create an osmotic pressure, which leads to water flow back into the capillaries. Any excess water in the interstitial space is drained by the lymphatic vessels. As depicted in **Figure 1.2b**, the fluid moves towards the interstitial compartment (interstitium), followed by flowing towards lymphatic vasculature. The interstitium mainly comprises a network of collagen, elastin, and glycosaminoglycans. The ISF within this network transports nutrients, metabolites, and electrolytes to tissues, muscle cells, bone cells, and organs [9], [10].

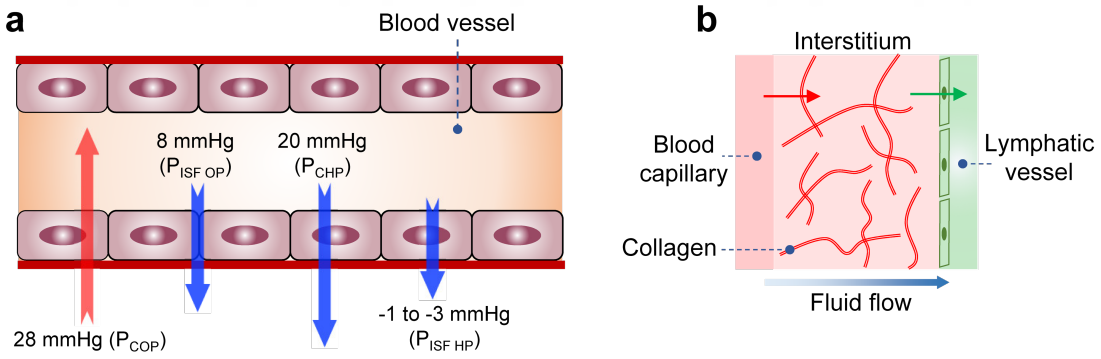


Figure 1.2. Schematic illustration of ISF flow. **(a)** Hydrostatic and osmotic pressures in capillaries and the surrounding interstitium. **(b)** Fluid flow between blood capillaries and lymphatic system.

The dermal ISF, which is the ISF content of the dermis layer, is believed to have an equivalent biomarker composition to that of blood and a negative pressure of -1 to -4 mmHg [3], [11], [12]. Since dermal ISF is located close to the skin surface, it allows for easier access to biomarkers, minimizing pain or blood clotting. It is believed that almost every biomarker present in blood can also be found in ISF, including over 92% of RNA species and nearly 90% of circulating proteins. Several studies have reported that 99% of the blood proteins can

also be found in ISF. ISF is separated from plasma by an endothelium of capillaries (**Figure 1.2b**). Although large proteins and red blood cells cannot diffuse through this endothelium barrier, analytes and small molecules, such as sodium, chloride, glucose, and uric acid freely equilibrate between plasma and ISF, thus rendering the composition of ISF and plasma similar except for large proteins. Additionally, ISF contains metabolites produced by the cell processes, such as sugars, salts, amino acids, coenzymes, hormones, and waste products of cells [13]–[15]. Despite the apparent easy access to ISF throughout the skin, ISF can be challenging to access because the amount of accessible dermal ISF is very small. Assuming 40% of the dermis is ISF content, only 120 $\mu L/cm^2$ is accessible in the thickest regions of the dermis. However, the greater constraint against ISF access is the natural rate at which ISF is refreshed in the dermis. The high hydraulic resistance in the dermis hinders the fluid flow in this layer. It takes almost 30 hours for fluid flow to fully refresh the ISF content in the dermis [16].

1.1.3 Importance of ISF in continuous health monitoring

ISF, which contains key biomolecules associated with metabolism and the immune system, correlates with the glucose level in the blood and is emerging as a promising alternative to current gold-standard blood-based devices. ISF presents several advantages over blood. It does not clot because of the impartial availability of coagulation factors. Additionally, it can be sampled in a non-invasive way and is widely available through the skin. Moreover, owing to having lower concentrations of blood-based proteins such as albumin and globulins, ISF provides simpler samples for biological analysis [17], [18]. ISF has great potential in the development of health monitoring devices, as it shares a similar biomarker composition to plasma and contains some unique biomarkers that can only be found in ISF or have elevated concentrations compared to plasma [19].

Over the past decades, many studies have been done, resulting in significant progress in the area of ISF-based continuous glucose monitoring (CGM). Several commercial CGM devices such as Abbott, Dexcom, and Eversense have been developed to continuously measure the blood glucose level directly from ISF. For most practical continuous biomarker measuring applications, the sensors need to have the ability to rapidly track any decrease or increase in the analyte level without any need for mixing, washing, and post-processing.

Therefore, many works have dedicated their studies to the development of sensors that can directly measure different analytes from ISF. To this day, CGM devices are the only systems that are used for clinical applications, and they have a needle positioned in the dermis for high ISF accessibility. Because of the successes in the area of glucose monitoring using ISF, there has been extensive research and development to explore the new analytes that can be monitored using ISF for different diagnostics and continuous monitoring applications [20]–[22]. Although there are several studies on the development of multianalyte sensing (sodium, potassium, pH, etc.) using ISF, there is a need for further research to find a reliable relationship between concentrations of different analytes in ISF and blood during continuous monitoring.

1.1.4 Microneedles in health monitoring

In recent years, microneedle-based systems have attracted great attention as a promising tool to directly access ISF for real-time analysis of various biomarkers and other applications such as drug delivery and skincare [18], [23]–[25]. Compared to hypodermic needles, the sharp microscopic structures of microneedles (MNs) could reach the dermis by avoiding the nerves and vascular structures placed in the lower layers of the dermis, thereby considerably minimizing the associated risks of pain and infection [3].

So far, MNs have been mainly used in cosmetics, therapeutics, and diagnostics, among which the cosmetic industry has been benefited from MNs the most. Currently, MN-based therapeutics are at the stage of clinical trials, and most research is focused on the development of drug delivery for influenza vaccination or for the treatment of cancer, diabetes, neuropathic pain, obesity, and hair regrowth. Recently, MNs have gained great attention in integration into point-of-care testing (POCT) systems [25]. Because of accessing the ISF with minimal or no pain and eliminating the contamination and inaccuracies concerned with sweat, saliva, and tear-based sensors, MN-based diagnostics hold great potential as an ideal platform for POCT purposes. Currently, there are two modes for MN-based diagnostics using ISF: 1) ISF extraction followed by analysis of the extracted ISF using benchtop equipment. 2) Integration of the sensing system into the MNs and analysis of the target analytes at the site of care. As mentioned before, wearables have recently been getting great attention because of their applicability in continuous health monitoring. Because of their great potential in being

integrated into wearable systems, MNs appear to be a promising tool for different healthcare purposes in the future.

Similar to the success of CGM devices in continuous health monitoring, MN-based sensors can present the next milestone in the advancement of wearable devices. The first system which used MN in their method was introduced in 2000 [26]. In this approach, a silicon MN was integrated with a microcuvette and used to analyze the glucose level of the 200 μL collected blood sample. Following that work, many studies used the same principle to extract ISF rather than blood. One notable example is the study of Mukerjee et al., where they used a hollow silicon MN to extract ISF from the skin and analyze the glucose content using the integrated colorimetric sensor on the backside of the MN patch [27]. Since then, many studies have integrated MNs into wearable devices for continuous measurement of different analytes, from glucose and lactate to multiple ions. Most studies have assembled the sensing components to the tip of the needles (similar to the conventional CGM devices), or they have functionalized the needles so that they can measure the biomarker concentration directly in the dermis without extracting ISF [28]–[30]. However, there are some issues regarding these devices that have yet to be addressed. Some notable problems are unreliable penetration of all the MNs into the skin, biofouling, and sensor instability and degradation [31]–[33]. Therefore, several studies have focused on using MNs for ISF extraction and then using the extracted ISF for biomarker analysis.

1.1.5 Microneedles for ISF extraction and continuous health monitoring

As mentioned before, because of the problems associated with devices that measure the biomarker concentration directly in the dermis, several studies have been working on the development of MN-based continuous monitoring devices that use extracted ISF for biomarker measurements. Cheng et al. developed a wearable device that uses MNs to pierce the skin, followed by using reverse iontophoresis to extract ISF [34]. Although the created channels by the needles increased the rate of ISF extraction, the needles needed to be pierced every few minutes to re-open the healed skin channels. In another study, Zhu et al. developed a paper-integrated hydrogel MN to measure the concentration of glucose, lactate, alcohol, and pH at the same time using colorimetric techniques [35]. However, their device could only measure the concentration of biomarkers once. Other hydrogel-based MNs have also been

developed to measure the target biomarkers in the extracted ISF, but their devices were not applicable for long-term continuous health monitoring because of the saturation of the hydrogels [36]–[39]. There are also studies that have used porous MNs to passively extract ISF [40]–[42]. However, their developed devices might not be suitable for applications where a higher volume of ISF is required, which can only be achieved if a minimum vacuum pressure is applied. As a result of these problems, it is highly desirable to develop fully wearable MN-based devices that can generate the required negative pressure on the device for ISF uptake and then use the extracted ISF for continuous biomarker monitoring.

1.2 Materials and Methods for Microneedle Fabrication

MNs comprise micron-sized needle arrays with a length ranging from 50 μm to 2 mm and a tip diameter of 1–100 μm [25]. The main advantage of MNs is that they secure access to biofluids in an easy-to-use and pain-free way. MNs can perforate the stratum corneum, and depending on the length of MNs, they can access the ISF content in the epidermis or dermis layer. Different materials, such as metals, silicon, glass, and polymers, are used to fabricate MNs in various structures, including solid, hollow, and porous [43]. Owing to their short length, MNs avoid potential damage to pain-related nerve endings and blood capillaries, rendering them an appealing minimally invasive transdermal health monitoring technique. Compared to the hypodermic needles used in commercial continuous glucose monitoring devices (e.g., Abbott Freestyle Libre and Dexcom CGMs), which have their needles (5–11 mm long) positioned in the skin, MN platforms considerably reduce pain and inflammatory responses at the administration site. MNs can gain access to dermal ISF in a minimally invasive and blood-free manner, and a slight force could be sufficient for them to puncture the skin. These advantages have made MNs attractive tools for integration into wearable platforms ranging from drug delivery applications to biosensing and wound healing [44]–[46].

1.2.1 Material

Different materials, including glass, silicon, ceramic, polymers (e.g., polycarbonate and polymethylmethacrylate (PMMA)) and metals (e.g., stainless steel and nickel), have been reported for manufacturing hollow, porous, solid, or swellable MNs (**Figure 1.3**) [28], [47]–

[51]. The type of material used to fabricate MNs strongly affects their mechanical strength, biocompatibility, and biodegradability. For successful skin penetration without fracture, MNs need to possess a high Young's modulus and yield strength. Additionally, the biocompatibility of MNs guarantees minimal inflammatory responses within the skin. Furthermore, the type of material is essential in determining the optimum fabrication process to minimize the required time and expenses. Depending on their application, each material offers several advantages compared to others. For instance, due to the extremely sharp needles in silicon MNs (tip radii of a few micrometers) [50], [52], they can provide skin penetration with shorter needle lengths compared to other materials. Dervisevic et al. utilized MNs with a tip radius and length of 1 and 250 μm, respectively, to access ISF and measure the glucose and pH levels in live animals [52], [53]. In addition, microfluidic chips with very small dimensions can be integrated into the MN patch, enabling the fabrication of miniaturized biofluid sampling and sensing devices. Mukerjee et al. developed a silicon hollow MN (HMN) patch with microfluidic reservoir on the backside of MNs for ISF collection and measuring the glucose level (**Figure 1.3b**) [27]. The inherent hydrophilicity of silicon and glass compared to polymers renders them favorable for biofluid collection. The micro/nanofabrication processes involved in the preparation of MNs ensure fine control over MNs' size, shape, tip size, and geometry [54]–[56]. However, silicon and glass MNs face multiple challenges, such as expensive fabrication procedures and low mechanical strength. Moreover, the thickness of the employed silicon wafer in the fabrication process determines the maximum achievable MN height [18].

A wide range of polymeric materials can be used to fabricate porous and swellable MNs, which can be employed in different drug delivery and wound healing applications (**Figure 1.3d,e** and **g-i**). In the literature, polymer MNs have been fabricated using various fabrication techniques, including micromolding, micromilling, 3D printing, drawing lithography, and casting [28], [47], [57]–[62]. Owing to their easy fabrication, biocompatibility, and low cost, polymeric MNs have been used for numerous applications, especially for drug delivery [44], [63]–[66]. However, the number of reports on the use of polymeric MNs for biofluid extraction and integration of microfluidics remains limited. This is mainly due to the hydrophobic nature of polymers, necessitating the integration of external stimuli to provide the required driving force for fluid collection. Some studies have tried to circumvent this by enhancing the wettability of MNs through plasma treatment or deposition of an oxide layer

[50], [67], [68]. While dissolving and swellable MNs provide sustainable release of the target drug through continuous swelling and degradation of the drug-loaded MNs, porous MNs allow the permeation of drugs into the skin through their pores [42], [69], [70]. Although polymeric MNs exhibit relatively weaker mechanical stability compared to metals, careful selection of MN material and their design according to their application can ensure the successful penetration of MN tips into the skin without breakage or buckling. For instance, although the mechanical strength of hydrogel MNs against skin penetration decreases upon swelling, the mechanical compatibility between the flexible MNs and the skin lowers the risk of needle breakage. Nevertheless, considering the weaker mechanical stability of hydrogel MNs compared to other materials, choosing the optimal design and geometry is essential to ensure successful skin penetration without damage [69].

Metal MNs (**Figure 1.3f**) have shown superior mechanical stability compared to polymeric and silicon MNs. Because of their high Young's modulus and yield strength, metal MNs can easily pierce through the skin without any fracture, rendering them favorable for developing health monitoring and point-of-care testing devices. Conventional CGMs employ hypodermic stainless steel needles to detect glucose levels in ISF [18], [25]. Several studies have deployed the excellent mechanical strength of metal MNs for biofluid sampling [32], [71]–[73] and continuous health monitoring devices [34], [74].

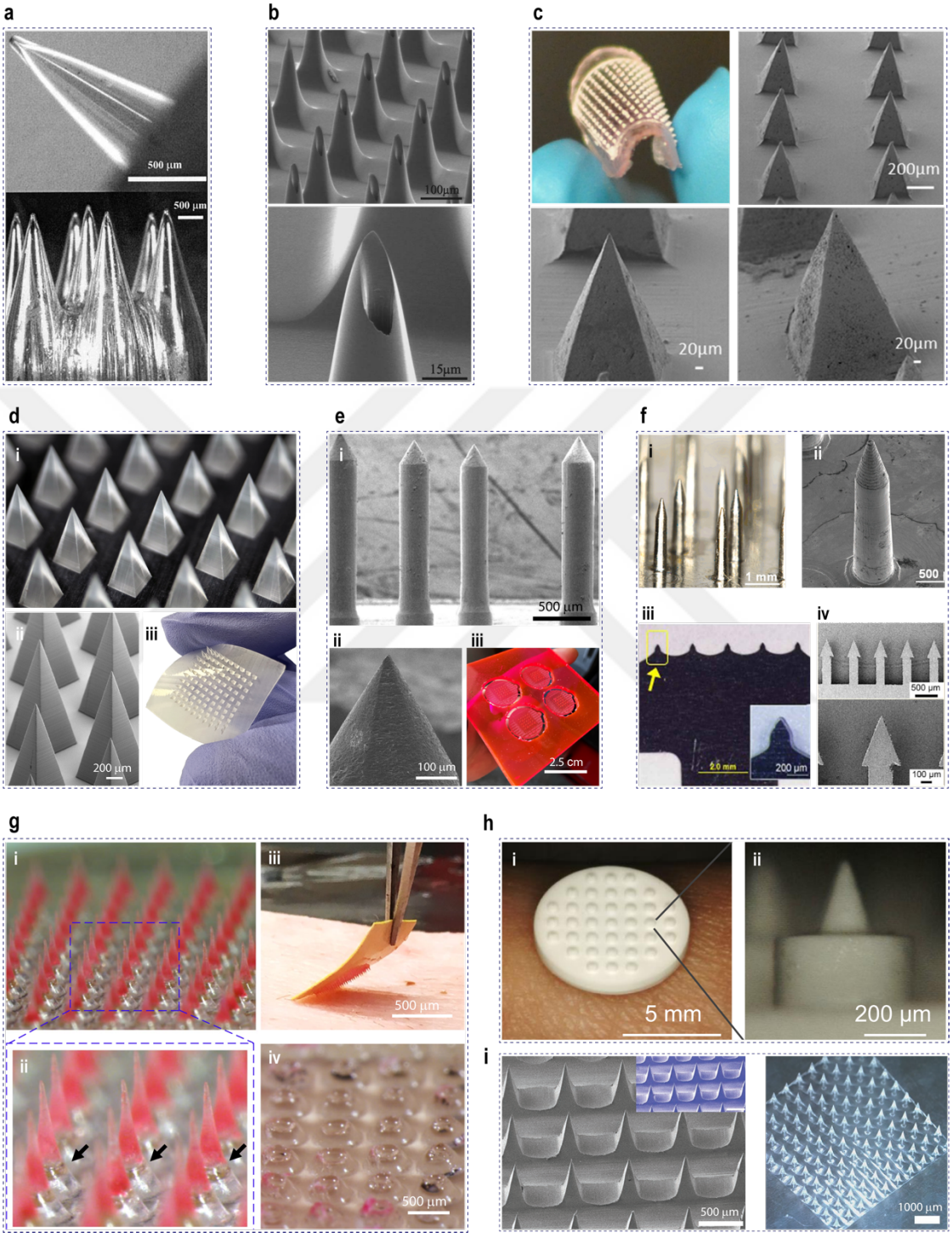


Figure 1.3. MNs fabricated using different materials. **(a)** Images of hollow single glass MNs fabricated for ISF extraction [49]. **(b)** SEM images of hollow silicon MNs fabricated using MEMS technologies for ISF extraction [27]. **(c)** Bioceramic MNs on a flexible substrate fabricated via micromolding for drug delivery [51]. **(d)** Polycarbonate MNs prepared using hot embossing [47]. **(e)** PMMA MNs manufactured using CNC micromachining employed for in situ electrochemical sensing of glucose, lactate, and alcohol. SEM images showing side

view of (i) a single MN and (ii) multiple MNs, (iii) A batch of four micromachined MN patches [28]. **(f)** Stainless steel MN. (i) Microscopic image and (ii) SEM image of a micromachined cylindrical MN patch used for ISF extraction and electrochemical sensing of glucose, Flat MNs manufactured using laser-cutting utilized for (iii) ISF extraction and (iv) electrochemical sensing of glucose and reactive oxygen species [32], [34], [75]. **(g)** Biodegradable PLA MNs fabricated using micromolding for controlled delivery of levonorgestrel. (i) Representative microscopy images of the MN patch before administration, (ii) magnified images, (iii) Photograph of the MN patch applied to a porcine skin ex vivo, (iv) Microscopy image of the MN patch upon after administration to porcine skin ex vivo [59]. **(h)** Polymer-based porous MNs used for drug delivery. (i) Photograph and (ii) representative SEM image [42]. **(i)** SEM and optical image of a swellable MN patch utilized for ISF extraction and subsequent sensing of glucose [76].

1.2.2 Structure

Different applications require various shapes and dimensions of MNs to meet the specific demands such as continuous biomarker monitoring or biofluid collection. The structural features of MNs should be carefully tailored according to intended applications. Therefore, several MN morphologies, such as solid, hollow, and porous, have been developed. Additionally, it is also essential to carefully select the dimensions and design of MNs to ensure an optimized fabrication process, sufficient mechanical strength, and dimensions appropriate for the intended application (**Figure 1.4a,b**).

Solid MNs can be manufactured using a broad selection of materials ranging from stainless steel [32], [34], [48] to PMMA [28], polycarbonate [47], [77], [78], epoxy [79], optical adhesives [80], poly(vinyl alcohol) [81], silk fibroin [82], silicon [50], and photocurable resins (**Figure 1.4d–g**) [62], [83]. The primary function of solid MNs is to create pores on the skin surface by piercing through the stratum corneum, thereby opening pathways for fluid exchange (drug delivery or ISF extraction) or enabling in situ biomarker detection. Due to their easy fabrication process, favorable robustness, and wide choice of materials, solid MNs have been implemented for the development of several in situ health monitoring devices. The high mechanical stability of solid MNs facilitates skin penetration, ensuring proper accommodation of functionalized MN tips in the dermis in contact with the ISF content. Furthermore, solid MNs can be incorporated into ISF collection techniques such as reverse iontophoresis [34], [84] and suction [32], [85] as minimally invasive tools to create skin pores. Due to the lack of liquid routes within the needle while the solid MNs are in the skin, this type

of MN has not been incorporated into microfluidic integrated ISF collection systems. The most notable application of solid MNs is their extensive usage in continuous biomarker monitoring and drug delivery. Numerous studies have functionalized solid MN tips using enzymatic and non-enzymatic materials to detect the concentration of different biomarkers, such as glucose [28], [34], [52], [75], [82], [86], alcohol [28], [87], cholesterol [35], [76], [88], lactate [28], [89], [90], drugs [33], [91], Na^+ [74], [92], [93], K^+ [74], [93], Ca^{2+} [74], [93], H^+ [93], and ketone [94] in ISF using electrochemical sensing. In addition, solid MNs have shown great potential in integration into multiplexed biomarker monitoring devices. Tehrani et al. developed an MN-based platform for continuous detection of two metabolites (glucose and alcohol or glucose and lactate) in human subjects [28]. The solid MNs were fabricated using micromachining techniques from PMMA, followed by functionalization of the MNs using different enzymes specific to each biomarker for amperometric sensing. Several other studies have reported the development of solid MN-based multi-analyte sensing devices [74], [93], [95]. Moreover, there have been reports on the usage of coated solid MNs for biosensing via the surface-enhanced Raman spectroscopy (SERS) technique [80], [96]. Besides biosensing applications, solid MNs can be coated with drug-loaded substances for drug delivery [97], [98] or antibodies to capture specific biomarkers [99], [100]. Solid MNs can be easily fabricated in different shapes, including conical [92], pyramidal [90], [93], cylindrical [28], [34], [94], and planar (**Figure 1.4c** and **h–k**) [74], [75]. In addition, many studies have tried to leverage the versatility of 3D printing and lithography techniques in the production of different structures to develop complex bio-inspired MNs to enhance their mechanical strength and adhesive properties [57], [101], [102].

Porous MNs enable fluid transport into the skin or liquid uptake from the skin through the enhanced capillary action resulted from their porous structure. A wide array of materials such as polymers (e.g., poly lactic acid [103], [104], methacrylate-based resin [105], poly(lactic-co-glycolic acid [106], and poly-glycidyl methacrylate [42]) have been used to manufacture porous MNs. Polymeric porous MNs are mainly fabricated using micromolding technique, where porogens can be incorporated into MNs' structure. The porous structure enhances the performance of biosensors by providing a larger surface area for immobilization and sensing [41], [107]. Li et al. integrated porous MNs with an iontophoretic system to develop a closed-loop system capable of measuring the glucose level and insulin injection [41]. They fabricated

the MNs using a mixture of poly (glycidyl methacrylate) (PGMA) and polyethylene glycol (PEG) as porogen in 2-methoxyethanol. The mesoporous structure of their MNs facilitated the ISF extraction, glucose sensing, and drug delivery processes, whereas the mechanical stability of the MNs could be compromised. Several other studies have leveraged the interconnected structures and improved capillary action of porous MNs to develop ISF-based biomarker detection and drug delivery devices [108]–[110]. When integrated with iontophoretic systems, porous MNs penetrate through the skin and provide an effective way for ISF extraction or drug delivery. Porous MNs are mainly advantageous for ISF extraction by obviating the need for micromachining processes, which is required for HMNs, providing an alternative approach to HMNs in integration into microfluidic systems [67], [111].

Among all types of MNs, HMNs have been extensively integrated into microfluidic systems. HMNs contain microfluidic channels within their structure, enabling the transport of liquid (biofluid or drug) either through capillary action or with the aid of external forces, such as vacuum systems or injection pumps. HMNs with microfluidic channels have been mostly utilized for three purposes: housing electrochemical sensors, ISF extraction, and drug delivery. Abbott Freestyle Libre and Dexcom CGMs contain electrochemical sensors within the cavity of their hypodermic needle. Upon skin penetration, these sensors come in contact with the ISF content within the skin, enabling the measurement of blood glucose levels. Recently, there have been several reports on the employment of HMNs in the electrochemical sensing of different biomarkers in ISF [112]–[115]. In addition, in another approach, HMNs have been filled with conductive pastes such as carbon paste to establish the required electron carriers for electrochemical sensing [116], [117]. Over the last few years, ISF collection has gained increasing attention, highlighting the importance of HMNs as a minimally invasive method to access ISF. Some studies have reported the integration of microfluidic platforms into HMNs to enable electrochemical [47], [54]–[56], [118], [119], colorimetric [120]–[122], or SERS sensing [123], [124] of ISF biomarkers. Additionally, some studies have leveraged the capacity of HMNs to achieve increased liquid flow rates through their microfluidic channels, enhancing their potential for drug delivery applications [125]–[127]. However, some issues associated with HMNs, such as compromised mechanical strength, clogging by the skin, or improper penetration of the microchannel part of the needle into the skin are yet to be fully addressed. Moreover, although several new techniques, such as 3D printing and

micromachining, have facilitated the fabrication process of complex HMNs, the preparation process of these needles remains more complicated and expensive than solid MNs [128], [129].

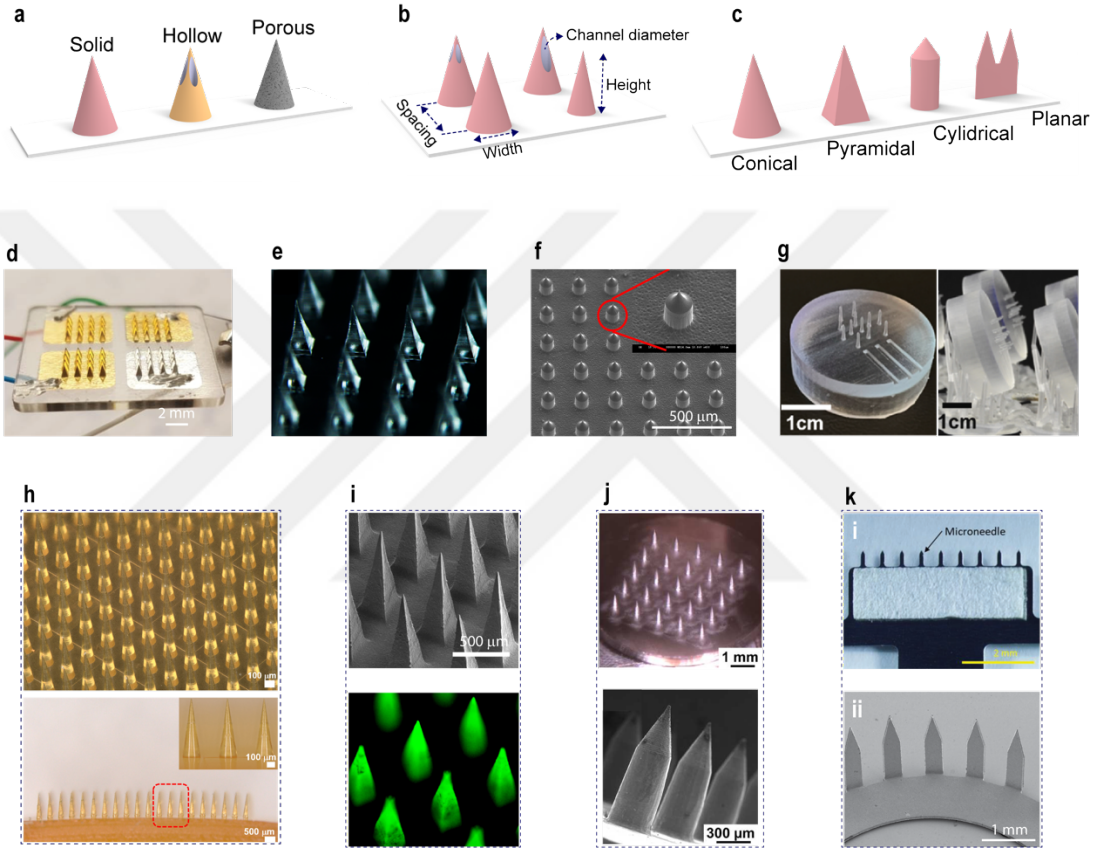


Figure 1.4. Morphology and design parameters of MNs. **(a)** Different types of MNs. **(b)** Design and dimensions of MN structures. **(c)** Various shapes of MNs. **(d)** Solid polycarbonate MNs [77]. **(e)** Solid MNs fabricated using optical adhesives [130]. **(f)** Solid silicon MNs [131]. **(g)** Solid 3D-printed MNs [132]. **(h)** Conical [85], **(i)** pyramidal [133], **(j)** cylindrical [40], and **(k)** planar solid MNs [71], [134].

1.3 Strategies for Fabrication of HMNs

The fabrication process of MNs is crucial in optimizing their mechanical strength, biocompatibility, biodegradability, and production costs depending on a wide range of applications. The conventional and modern MN fabrication strategies can be classified into three categories: formative, subtractive, and additive manufacturing methods (**Figure 1.5a**)[128]. In the formative method, the MNs are formed to the desired shape using a master

mold, while the weight remains unchanged. Micromolding, hot embossing, casting, and lithography are among the most popular formative MN manufacturing methods [128], [135]. Subtractive manufacturing involves the formation of MNs through layer-by-layer removal of bulk material through processes such as computer numerical control (CNC) machining, laser micromachining, and etching, thus leading to a lower weight compared to the original material. Additive techniques (3D printing) enable high-precision manufacturing of complex MN structures by sequential addition of material layers [136]. Over the recent years, many fabrication processes based on these three strategies have been developed to enable the manufacturing of sturdy, biocompatible, complex, and cheap HMNs.

1.3.1 MEMS-based technologies

The technological advancements in the fabrication of microelectromechanical systems (MEMS) have enabled the manufacturing of MEMS-based HMNs with narrow tip diameters. There are already commercial silicon-based HMNs used for drug injection. NanoPass technologies' MicronJet is a single-use and sterile device consisting of an array of four pyramidal silicon HMNs (600 μm long) attached to a plastic adaptor, which can be connected to injection syringes (**Figure 1.5b(i)**). The fabrication process involves several techniques, such as deep-reactive ion etching (DRIE), wet etching, and thin film deposition [137]. Ascilion has recently developed a silicon HMN-based device for sampling dermal ISF using DRIE etching, followed by anodic bonding of glass (**Figure 1.5b(ii)**). The device comprises three main components: a single-use and sterile silicon chip, a vacuum source, and a monitoring system. The silicon chip includes several MNs (less than 500 μm long) with a microchannel within each needle on one side of the chip and microfluidic channels on the other side. With the aid of capillary action and mild vacuum pressure, the extracted ISF through MN channels can be routed through the microchannels and collected inside a microfluidic reservoir for analysis. Similar to MicronJet, the silicon chips were realized by utilizing MEMS-based processes. Several studies have implemented similar technologies to fabricate silicon HMNs. Li et al. employed a combination of DRIE and wet etching to develop a silicon HMN chip with a needle height of 200–300 μm, base diameter of 100 μm, and through microchannels of 30 μm diameter [50]. To achieve sharp needle tips (diameters less than 5 μm) and mitigate the clogging issue, the boreholes were shifted 30 μm from the center.

In another study, a novel approach was developed to fabricate silicon HMNs to obviate the need for a wet etching process, thus avoiding further complications and being subject to hazardous chemicals [138]. There have been multiple reports on the fabrication of silicon HMNs for drug and vaccine delivery purposes [139]–[148]. Griss et al. fabricated complex silicon HMNs with four openings at the shaft rather than the tip. Such design enables increased flow rates during drug injection and lowers the clogging risk.

Owing to their high Young's modulus and sharp needle tips, silicon HMNs have shown great promise in integration into health monitoring devices. Arkal Medical Inc. developed a silicon HMN-based device with 200 needles of 300 μm length to access dermal ISF for continuous monitoring of glucose levels [56]. Unlike Ascilion, the boreholes in this device were in the center of each needle, leading to an increased risk of clogging. In another recent study, silicon HMNs were fabricated through two silicon bulk etchings, followed by integration into microfluidic glass reservoirs to enable drug delivery and ISF collection using capillary action on a wearable platform [149]. Other studies have deployed a similar approach to construct and optimize biomarker monitoring devices using silicon HMNs [27], [54], [55].

Some reports have fabricated polymeric or metallic HMNs using MEMS-based fabrication processes (**Figure 1.5c**)[23], [150]. In a study, a HMN-based wearable device was fabricated using polymerized SU-8 for blood-free colorimetric detection of malaria infection [68]. The conical HMNs (length: 750 μm, base diameter of 375 μm, and bore diameter of 80 μm) were prepared by UV exposure of SU-8 through a photomask, which was prepared using a laser-cutting machine. Because of the inherent hydrophobicity of polymeric MNs, the HMNs were UV/ozone-treated to increase the hydrophilicity of the surface, enhancing the liquid uptake by the improved capillary action. Davis et al. implemented a modified LIGA process that included a combination of laser micromachining, plasma-enhanced chemical vapor deposition (PECVD), and electroplating for manufacturing conical metallic (nickel) HMNs [151], [152]. The electroplating of nickel on the laser-drilled polymeric substrate rendered the HMNs with a wall thickness, length, and a tip diameter of 10, 250, and 50 μm, respectively. The presence of boreholes at the needle tips increases the risk of tissue clogging, while the thin walls of the HMNs render them prone to fracture. Given the different hole diameters at the tip and base of the needles, this fabrication method could also be advantageous in the development of wedge-shaped wettability-patterned HMNs to promote biofluid collection processes [153], [154].

Moon et al. used the LIGA process to fabricate PMMA-based HMNs with different designs. The out-of-plane structure, high-aspect-ratio shanks, sharp tapered tips, side openings for needle channels, and excellent mechanical stability of the fabricated MNs rendered them a promising candidate for drug delivery applications. In another study, Kim et al. used a modified SU-based UV-LIGA process to fabricate conical metallic HMNs of 200 and 400 μm length with integrated microfluidic chamber to enable sample collection on the backside of MNs [155], [156].

1.3.2 Laser micromachining

Laser micromachining is a typical subtractive MN manufacturing technology that uses a laser beam to melt or vaporize the material to create the desired structures. Excimer (UV) or infrared (IR) laser machining can be used to prepare polymeric molds from materials like polyimide or polyethylene terephthalate for electroplating-based fabrication of metallic HMNs [150], [151], [157]. The fabricated positive or negative molds by laser ablation can later be used for electrodeposition of metals such as nickel to create HMNs with a wall thickness of 5–50 μm [150]. CO_2 lasers have been employed to prepare polydimethylsiloxane or acrylic negative molds, which can later be used for fabricating solid and HMNs [158], [159].

HMNs can also be fabricated using direct laser micromachining of the bulk material (**Figure 1.5d**). Parrilla et al. utilized a laser micromachining technique (nanosecond-pulse, diode-pumped, solid-state laser operating at a wavelength of 355 nm) to fabricate an array of pyramidal HMNs with a height, width and, hole diameter of 1000, 750, and 100 μm, respectively, from polyether ether ketone (PEEK) sheets [160], [161]. Due to the hydrophobic nature of the fabricated polymeric HMNs, they were integrated with a vacuum system to provide the necessary driving force for ISF extraction. In another study, a femtosecond laser was used to fabricate conical HMNs from stainless steel, which were later used for in vivo transdermal delivery of insulin [162]. Recently, UV lasers have been employed to drill through microchannels on solid polycarbonate MNs for the development of a wearable vacuum-integrated ISF sampling and sensing device [47].

1.3.3 3D printing

Upon its development in 1986 through the stereolithography (SLA) process, 3D printing has been extensively used as an additive manufacturing method for fabricating a wide variety of complex three-dimensional structures [163]. The process involves successive and layer-by-layer deposition of materials to form the final 3D structure with high precision and design versatility [62]. Recently, 3D printing has attracted great attention in the fabrication of HMNs because it enables the single-step fabrication of intricate structures (**Figure 1.5e**) [23]. Several 3D printing methods, such as SLA, fused deposition modeling (FDM), selective laser sintering (SLS), and digital light processing (DLP) have been used for the fabrication of MNs. Over the last five years, two-photon polymerization (2PP) and projection micro stereolithography (PμSL) have been extensively used for the development of solid and HMNs [120], [122], [125], [127][164]–[173].

Since the fabrication of the first MNs using 2PP from Ormocer® (an organic-inorganic composite material) [174], it has been widely implemented for direct manufacturing of MNs or fabrication of MNs via replication molding [175]–[180]. 2PP allows the reproducible fabrication of MNs with complex structures in a reliable manner (**Figure 1.5f**). Faraji Rad et al. used the 2PP technique to fabricate MNs with open microchannels [167]. They also successfully used the 3D-printed MNs to manufacture thermoplastic replicas through soft embossing. Most of the studies have used Nanoscribe GmbH to fabricate their MNs. However, there are other commercially available devices using the 2PP method, such as Workshop of Photonics® [176]. Although 2PP offers easy and single-step fabrication of extremely complex MNs, the process is highly expensive and time-consuming, limiting its main application to prototyping and scientific applications rather than being used for industrial applications.

In recent years, PμSL has also been widely utilized for fabricating solid and HMNs (**Figure 1.5g**). High-resolution PμSL was first developed in 2005 and has since been employed for various applications with resolutions ranging from 0.6 to 30 μm [181]. Similar to 2PP, PμSL enables the fabrication of complex solid and HMNs, which can be used for drug delivery and biofluid extraction applications [57], [120], [124], [125]. Several studies have used PμSL-fabricated HMNs to access dermal ISF and use the extracted ISF for electrochemical or colorimetric analysis of different biomarkers [120]–[122], [124], [170], [172]. The capacity

of PμSL in fabricating complex structures in an easy manner enables the integration of fluid chambers into the MNs for biofluid extraction or drug delivery purposes, obviating the need for integration of extra microfluidic modules [127].

1.3.4 CNC machining

CNC micromachining is a subtractive fabrication method that uses a 3D model designed on a CAD software to create the desired structure. Similar to the 3D printing technique, CNC micromachining offers excellent reproducibility, high production speed, and sharp needles, thus being extensively used for the preparation of male molds in the fabrication of silicon female molds for micromolding. However, this technique has some drawbacks, such as the high cost of equipment and the need for highly specialized technicians. Although some reports have used HMNs fabricated by this technique for electrochemical sensing of ISF biomarkers (**Figure 1.5h**) [112], [116], recently, with the advancement in other fabrication methods, CNC micromachining has been mainly employed for fabricating solid MNs rather than HMNs.

1.3.5 Drawing lithography

Drawing lithography is an additive technique that enables direct fabrication of HMNs from thermoplastic and viscous materials without the need for any 3D design or mask [58]. Drawing pillars come in contact with a molten polymer that is coated onto a planar substrate, followed by separation, allowing the molten material to extend and create the MN-type structures (**Figure 1.5i**). Drawing lithography is particularly beneficial for fabricating ultra-high HMNs [61]. Although drawing lithography enables low cost and fast fabrication of high MNs, the limited choice of materials is the primary shortcoming associated with this method.

1.3.6 Combining multiple fabrication strategies

With the advancements in MN manufacturing process and the growing demand for HMNs in biomedical applications, many studies have implemented a combination of different fabrication methods to optimize the performance and versatility of HMNs. There is a tendency to combine micromolding with other fabrication techniques, thereby lowering the manufacturing cost by using female molds to produce several MNs. Polymeric MNs

fabricated using micromolding or hot embossing methods can later be drilled using high-precision lasers [47]. Although the female molds for micromolding are mainly prepared using solid MNs, recently, some studies have integrated 3D-printed techniques and micromolding to fabricate different morphologies of HMNs onto flexible substrates (**Figure 1.5j**) [182].

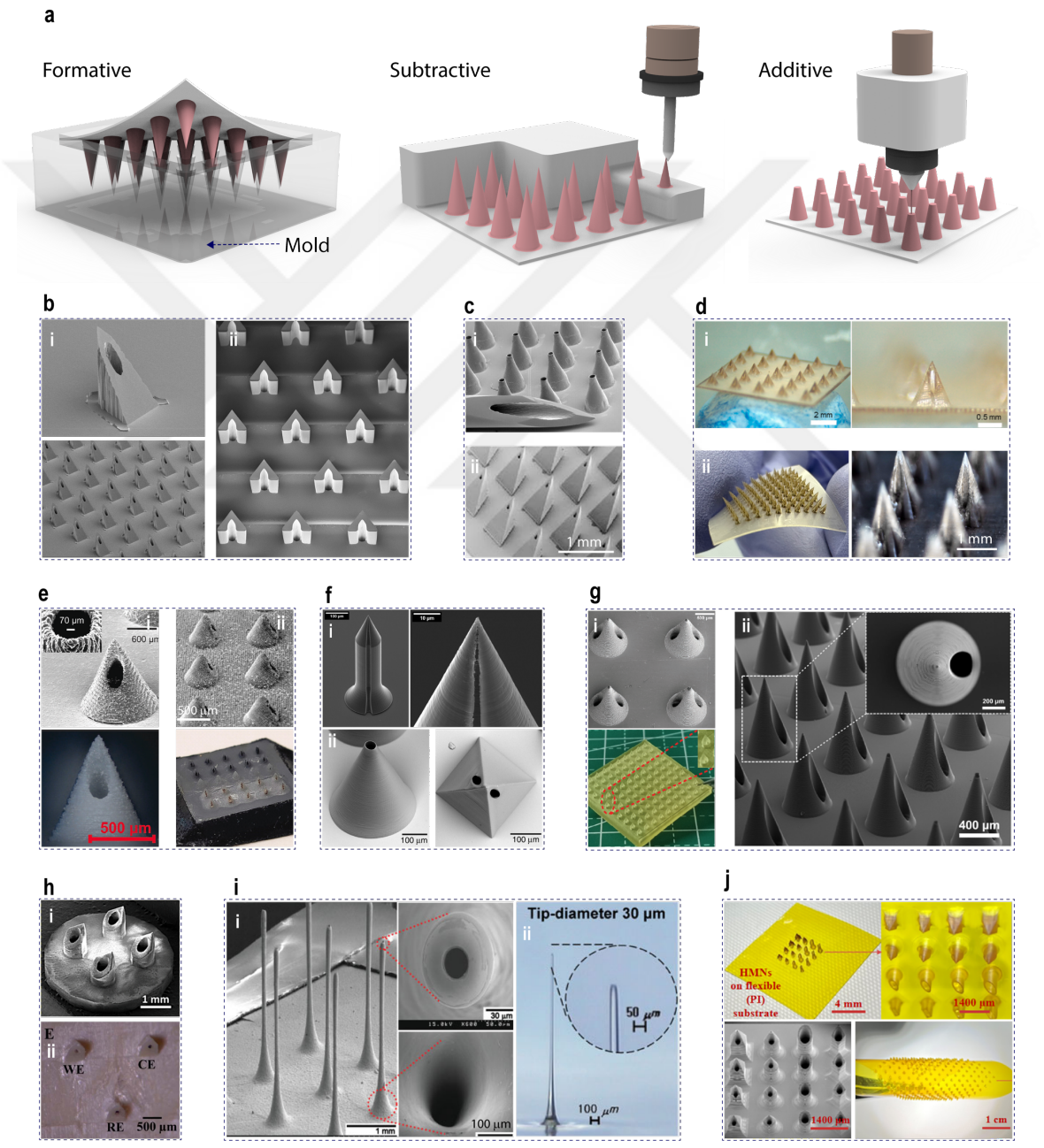


Figure 1.5. Different strategies to manufacture HMNs. **(a)** Classification of MN fabrication techniques. **(b)** Silicon HMNs fabricated using MEMS technologies. (i) NanoPass technologies' MicronJet drug injection device with 600-µm long MNs, (ii) Ascilion's hollow

silicon patch with 500-µm long MNs with liquid uptake capability [137][183]. **(c)** Metal (i) and polymeric (ii) HMNs fabricated using MEMS techniques [151], [184]. **(d)** PEEK (i) and PC (ii) MN patches fabricated using laser-drilling [47], [161]. **(e)** 3D-printed hollow polymeric MNs used for (i) plant health and (ii) pH monitoring [185], [186]. **(f)** HMNs fabricated using 2PP method. (i) Integration of side-channels to enable drug injection or biofluid extraction, (ii) 3D-printed pyramidal and conical HMNs fabricated using a femtosecond laser [164], [173]. **(g)** PµSL-fabricated HMNs. (i) Double-channel 3D-printed MN for ISF collection, (ii) HMNs used for ISF glucose sensing [120], [171]. **(h)** CNC micromachined HMNs utilized for electrochemical sensing of (i) alcohol and (ii) ketone, glucose, and lactate [112], [116]. **(i)** Manufacturing ultra-high HMNs using drawing lithography [58], [187]. **(j)** Integration of micromolding and high-precision 3D printing to realize HMNs on a flexible substrate [182].

1.4 Biosensing

Although there have been numerous reports on the development of sweat-based wearable devices due to the non-invasiveness of these devices [31], [188], [189], ISF-based health monitoring devices have drawn increasing attention over the last decade [17], [45]. This is mainly due to the similar composition of ISF and blood and easy access to dermal ISF in our body. MNs can reach the dermal ISF in a minimally invasive manner, enabling the collection of ISF biomarkers for ex situ analysis or in situ real-time detection of different biomarkers. Technological advancements in medicine and flexible electronics have brought about several innovations, enabling the detection of complex physiological signals. Several studies have developed biosensing devices by using functionalized solid MNs [28], [34], [52], [75], [86], [89]. However, as mentioned before, there are shortcomings to this approach, such as biofouling, unreliable penetration of MNs, and sensor degradation.

Alternatively, HMNs have been integrated with microfluidic collection chambers to provide the necessary contact between the sampled biofluid and biosensors. Several studies have integrated polymeric, metal, and silicon HMNs into their wearable devices to enable electrochemical or optical sensing of different biomarkers. The main obstacle against ISF sampling devices is the low sampling rate of dermal ISF, despite apparent easy access throughout our entire body [3], [18]. Therefore, HMNs, especially polymeric MNs, have been integrated with external vacuum pumps to provide the necessary driving force to draw dermal ISF into the microfluidic collection chambers through the microchannels in the MNs [47], [120], [121], [161], [170], [190]. Different sensing techniques, such as electrochemical,

colorimetric, and SERS sensing, have been incorporated into HMN-based health monitoring devices.

1.4.1 Electrochemical sensing

Electrochemical sensors are deposited with chemical compounds to initiate the chemical reactions upon contact between the sensor surface and the target biomarkers. Based on the received signal (current, potential, or impedance), electrochemical sensors can be categorized as amperometric, potentiometric, and voltammetric sensors [31], [191].

In amperometric biosensing, the current resulting from the electrochemical reaction of the electroactive materials coated on the working electrode is measured at a constant potential. There is usually a linear relationship between the detected signal and the concentration of the target biomarker [192]. Amperometric sensors may comprise two or three electrodes. The working electrode is typically fabricated from platinum (Pt), gold (Au), or carbon. A reference electrode, typically Ag/AgCl, provides a stable potential to measure and control the potential applied to the working electrode. There is sometimes a third electrode (counter or auxiliary electrode) to form a three-electrode system. Typically, working electrodes are immobilized with enzyme-based solutions, and the enzyme-catalyzed redox reactions of the target signal at a fixed voltage result in a detectable current (**Figure 1.6a**). The majority of HMN-based wearable devices have focused on glucose sensing. Jina et al. developed a continuous glucose monitoring device, incorporating silicon HMNs with the capacity to detect the ISF glucose level for 72 hours using amperometric sensing [56]. In another study, a highly stable electrochemical sensor was integrated with HMNs to enable measuring the glucose level in the extracted ISF (**Figure 1.6b**). A syringe was used to provide the required negative pressure for ISF sampling [161]. There have been other reports on the integration of silicon [54], [55], polymeric [47], [170], [172], [193], [194], or metal [190] HMNs into glucose sensing devices. Recently, HMNs have also been integrated with amperometric sensors for electrochemical sensing of other biomarkers than glucose, such as H_2O_2 and lactate. In a recent study, a 3D-printed HMN patch was integrated with a microfluidic ISF collection chamber for dual detection of β-hydroxybutyrate and glucose to help the development of ketogenic diets for treating chronic diseases (**Figure 1.6c**) [172]. They utilized vertical graphene for fabricating

their working electrode, leading to the excellent sensitivity of 234 μA mM^{-1} and limit of detection of 1.21 mM.

Potentiometric sensors measure the potential against a reference electrode based on the Nernst equation. The change in potential has a logarithmic correlation with concentration. Ion-selective membranes, which are semi-permeable membranes with the ability to selectively react with the target ions, can facilitate the potentiometric response of these sensors (**Figure 1.6d**). As ions traverse the ion-selective sensor, they can generate a potential difference, which is then transduced to the electrode. Although several potentiometric solid MN-based devices have been developed for measuring urea [168], pH [29], [53], [93], Na^+ [40], [74], [93] K^+ [40], [74], [93], Ca^{2+} [74], [93], potentiometric sensors have been scarcely integrated with ISF extraction devices (**Figure 1.6e**). Miller et al. integrated 3D-printed HMN with a PMMA-based microfluidic chip to enable ISF extraction and subsequent detection of potassium (K^+) (**Figure 1.6f**) [119]. In another study, a 3D-printed HMN patch was integrated into a potentiometric pH sensor the detect the pH level in ISF [185]. There have also been reports on the integration of dual pH and glucose sensors into HMNs [47], [193].

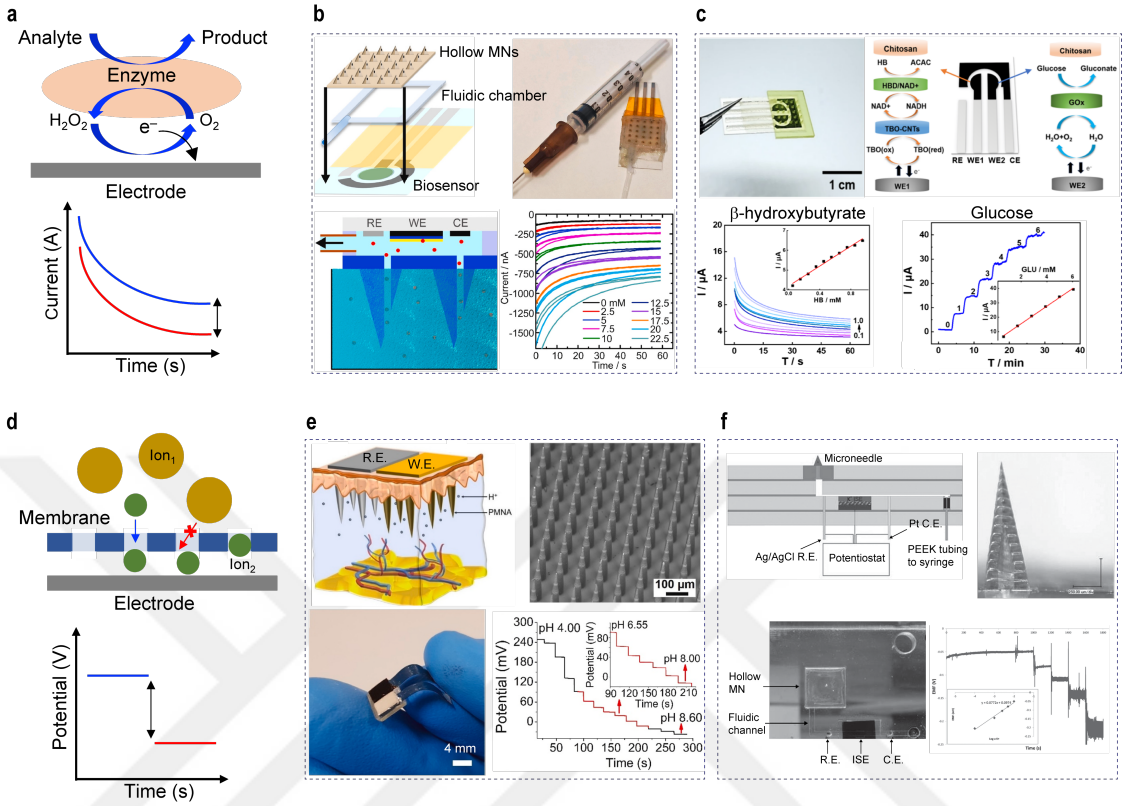


Figure 1.6. Integration of biofluid collection systems with electrochemical sensors. **(a)** Schematic representation of amperometric enzyme-based electrochemical sensors. **(b)** A three-electrode electrochemical glucose sensor integrated with laser-machined HMNs and the detected current signals against different glucose concentrations [161]. **(c)** A dual amperometric sensor integrated with 3D-printed HMNs for simultaneous detection of β-hydroxybutyrate and glucose [172]. **(d)** Working principle of ion-selective membrane-based potentiometric sensors. **(e)** Potentiometric MN-based sensor with functionalized polymeric solid MNs for inn situ pH sensing [53]. **(f)** Integration of a 2PP-fabricated HMN into a microfluidic chip to measure the potassium concentration in the sampled fluid [119].

1.4.2 Colorimetric sensing

The working principle of colorimetric sensors is based on the visual color change, which is usually detectable by the naked eye, or cameras and smartphones can be used to capture images for subsequent analysis of the RGB values. Owing to their easy fabrication process and cost-effectiveness, colorimetric sensors have been implemented for qualitative and quantitative analysis of a wide variety of biomarkers [195], [196]. Redox-responsive chromogenic materials can change their color upon oxidation or reduction reactions. For effective colorimetric sensing, it is essential for the fluid to make contact with colorimetric assays. Therefore, solid MNs cannot solely be integrated into these systems. Consequently,

most MN-based colorimetric sensing devices have incorporated swellable MNs into their designs. Swellable (hydrogel-forming) MNs have either encapsulated the colorimetric assays [197]–[199], or cellulose-based substrates with embedded colorimetric assays have been integrated into the backside of MNs [35], [200], [201]. Meanwhile, HMNs can route the sampled biofluid into a microfluidic collection chamber, where the fluid can react with the colorimetric assays of the embedded cellulose-based substrates. Several studies have integrated 3D-printed or metal MNs to enable colorimetric detection of glucose,[120]–[122], [202] pH [120], [122], and cholesterol [202] in the collected biofluid samples.

2 Chapter Two: ISF Sampling and Sensing Through Integration of Laser-Drilled Microneedles and a Finger Actuated Vacuum System

Materials from this chapter appear in "Abbasiasl, T.; Mirlou, F.; Mirzajani, H.; Bathaei, M. J.; Istif, E.; Shomalizadeh, N.; Cebecioğlu, R. E.; Özkahraman, E. E.; Yener, U. C.; Beker, L. A Wearable Touch-Activated Device Integrated with Hollow Microneedles for Continuous Sampling and Sensing of Dermal Interstitial Fluid. Adv. Mater. 2024, 36 (2), 2304704. https://doi.org/10.1002/ADMA.202304704".

2.1 Introduction

The ever-increasing rate of technological advances has brought about numerous benefits to personalized diagnostics and physiological health monitoring. In this regard, wearable healthcare monitoring devices have witnessed extensive progress over the past decade [17], [18], [203]. Recent efforts have focused on the development of non-invasive and minimally-invasive wearable devices for monitoring of dynamically altering health-related biomarkers in peripheral biofluids such as sweat, saliva, tear, and interstitial fluid (ISF) [28], [204], [205]. ISF, in particular, contains important metabolic and immunological biomolecules, and exhibits a close correlation with blood, thereby turning into a promising alternative to replace the current gold standard blood-based diagnostics [3], [52], [79], [92], [206]. ISF offers several advantages over blood including being widely accessible through the skin, availability of non-invasive or minimally-invasive sampling methods, and impartial presence of coagulation factors, thus making it favorable for continuous biomarker monitoring [3], [32], [76]. Several studies have demonstrated the similarities in composition between ISF, blood serum, and plasma [28], [32], [34], [41], especially for species with low molecular weight such as glucose, urea, lactate, H^+ (pH level), Na^+, K^+, etc., because of the rapid paracellular diffusion through the capillary walls compared to the turnover rate of ISF [17]. Despite its seemingly high accessibility and having a volume of three times that of blood, ISF sampling can still be a challenging task [3], [18].

Although several techniques have been developed for ISF extraction, such as microdialysis, suction blister, wick method, reverse iontophoresis (RI), sonophoresis, thermal ablation, and MN arrays, these methods could require skilled professionals or specialized equipment, and might cause skin disruption and local trauma [18], [24]. Among these strategies, only RI and MNs have shown compatibility for continuous health monitoring [28], [40], [41], [207]. In RI, a mild current is applied to the skin to induce an electroosmotic flow. Although the first FDA-approved RI-based wearable device was used in 2000 (GlucoWatch, Cygnus Inc., CA), the resulting skin discomforts by the applied current led to its retraction from the market. Additionally, there are still important limitations regarding RI-based ISF extraction such as mixing with sweat, considerable delay, and ISF dilution, which are yet to be properly addressed.

In recent years, MNs have emerged to be promising alternatives for ISF extraction and continuous biomarker monitoring. Owing to their micron-sized needles, MNs offer several advantages over the commercially available needle-based devices with indwelling sensors (e.g., Abbott Freestyle Libre and Dexcom). MNs can access the ISF in a blood-free, less bulky, and minimally invasive manner, and a small pressure can be adequate for penetration into the skin. More importantly, MNs have exhibited great potential in the accommodation of multiple sensors on a single MN array facilitating multiplexed biomarker sensing in a miniaturized device [22], [28], [40], [93]. Despite the difficulties regarding ISF sampling essentially due to the negative pressure, low volume per skin area, and filtration of large molecules [3], there is still extensive research on MN-based ISF collection [24], [76], [161], [208]–[210]. This is mainly because of the unmet issues in the development of MN-based in situ monitoring devices. Some notable problems are associated with the reliable penetration of all the MNs into the skin, biofouling, and sensor stability and degradation [31]–[33]. Therefore, in parallel to MN-based in situ monitoring, several studies have focused on ISF extraction and analysis using MNs.

HMNs made of glass [49], silicon [27], [50], and metal [48] are among the most common methods for ISF extraction, where ISF is collected either by passive diffusion or under negative pressure. In a continuous monitoring device developed by ArKal Medical Inc., a HMN array with 200 silicon HMNs of 300 μm length was used to access the epidermal ISF for continuous monitoring of glucose levels. They successfully measured the glucose levels

in diabetic patients over a 72-hour period [56]. Although these methods have facilitated ISF collection, some limitations are yet to be addressed. For instance, silicon or glass MNs might break off in the skin during ISF collection because of their brittle nature [211]. Hydrogel MNs have also been utilized to extract ISF by their swelling ability without the need for additional devices such as vacuum pumps. However, most hydrogel-based MNs are unable to extract enough amount of ISF, and they require expensive equipment and trained personnel for off-body biomarker quantification [48], [76], [209].

The majority of previous efforts in ISF collection have been limited by extraction of small volumes, mostly less than the required volume for diagnostic tests and other biomedical applications (generally at least multiple microliters). Additionally, during conventional vacuum assisted ISF extraction, the subjects might experience discomfort because of waiting for a long period, while being connected to external devices in a clinical environment limiting their mobility and potential monitoring applications outside the hospital environment. Given the issues mentioned regarding the commercial devices, conventional ISF extraction techniques, hydrogel-based MNs, and HMNs with external pumps, developing a wearable device for ISF extraction based on HMNs with an integrated vacuum and sensing system would be highly desirable.

Herein, for the first time to our knowledge, we report an HMN-based vacuum-integrated platform for continuous sampling and electrochemical sensing of ISF. The developed device can efficiently collect meaningful volumes of ISF by simple one-touch activation without any need for external components. The vacuum system is fabricated using polydimethylsiloxane (PDMS), and benefits from the self-recovery feature of this polymer to convert the finger force into a vacuum pressure. It is demonstrated that the vacuum system can achieve and maintain a comparable vacuum pressure with that of external equipment. The implementation of specially designed passive valves enables continuous and fine adjustment of the vacuum pressure. The HMN patch is made of polycarbonate (PC), which is a biocompatible polymer [212], followed by laser-assisted drilling of the needles to create the microchannels for ISF withdrawal. In vitro and ex vivo experiments demonstrate the attractive performance of the hybrid electrochemical sensor with excellent sensitivity, stability, and sufficient selectivity for glucose and pH analysis. Additionally, in vivo evaluation of the ISF collection highlights the potential of the proposed device in the extraction of high volumes of ISF in a simple

manner. We present the first in vivo demonstration of a vacuum-integrated HMN-based device for simultaneous ISF sampling and electrochemical analysis of glucose and pH levels. This platform offers great promise for future ISF-based point-of-care technologies and disposable biomedical devices.

2.2 Materials and Methods

2.2.1 Chemicals and materials

Glucose oxidase (GOx), high molecular weight chitosan, gold nanoparticles (AuNPs), potassium hexacyanoferrate ($K_3Fe(CN)_6$), iron (III) chloride ($FeCl_3$), calcium chloride ($CaCl_2$), lithium chloride (LiCl), potassium chloride (KCl), sodium chloride (NaCl), ascorbic acid ($C_6H_8O_6$), hydrochloric acid (HCl), acetic acid, and ammonium chloride (NH_4Cl) were purchased from Sigma-Aldrich (MO, USA). AuNPs were 10 nm in diameter and stabilized in citrate buffer solution. D(+)-Glucose and urea crystalline pure were obtained from neoFroxx, (Hesse, Germany). PDMS (Sylgard 184 Silicone Elastomer) was purchased from Dow Corning (MI, USA). The conductive silver and carbon pastes and all-polyimide double sided copper clad laminate were obtained from Dupont (DE, USA). Phosphate-buffered saline (PBS; 1×, pH 7.2; Gibco) was purchased from Thermo Fisher Scientific (MA, USA). Polycarbonate granules were purchased from Goodfellow (UK). Aniline was purchased from Alfa Aesar (MA, USA). The double-sided tape (9495 LE 300 LSE) and biomedical skin-adhesive (1524) were obtained from 3M (MN, USA). Transparent polyethylene terephthalate (PET) films were purchased from MG Chemicals (Burlington, Canada).

2.2.2 Fabrication of HMNs

PC-based MN patch was prepared via conventional hot embossing techniques and using a PDMS female mold. A master male mold was prepared by a microArch® S230 3D printer (BMF Material Technology Inc., Shenzhen, China) using HTL yellow resin, and then used for fabrication of the female mold. PDMS and its curing agent were mixed by 10:1 ratio and stirred well using a PDMS mixer. To remove any existing bubbles, the uncured mixture was placed under vacuum for 30 minutes. Then, the mixture was casted onto the MNs master mold and cured at 100 °C for 2 hours, which formed a female mold with inverted MNs. After

separating the PDMS mold, PC granules were placed onto the inverted MNs. The granules were heated up to 300 °C for 20 minutes, and then a weight was used to spread the PC granules inside the mold and fill the inverted MNs. After 15 minutes, the weight was removed followed by cooling down the mold to ensure complete solidification of the MN patch. After peeling off the MN patch, A UV-based laser-cutting machine (Protolaser U4; LPKF, Germany) was used for high precision drilling of through-microchannels in the needles. The optimized parameters of the laser beam for successful drilling of the needles were frequency of 45 kHz, pulse energy of 130 µJ, power of 5.85 W, and speed of 300 mm s^{-1}. The process was repeated 150 times with a delay of 100 ms between repetitions. The whole process of drilling takes about 20 seconds. Schematic representation of the fabrication process can be found in **Figure 2.1**. The HMN patches were designed in square patterns with array sizes of 3×3, 5×5, 7×7, and 9×9, and the total number of needles on each patch was 9, 25, 49, and 81, respectively (**Figure 2.2**).

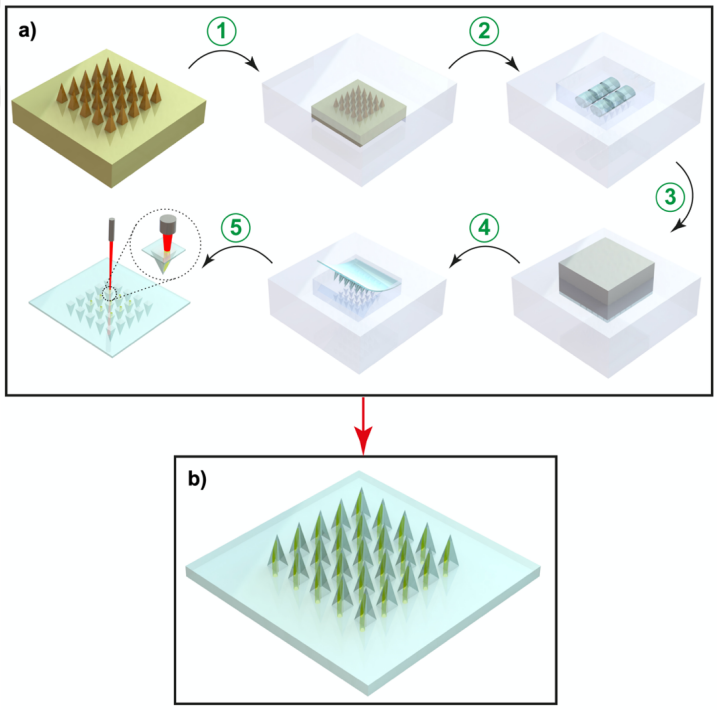


Figure 2.1. Fabrication process flow of the HMN patch. **(a)** A 3D-printed master male mold was used to prepare PDMS-based female mold, followed by fabrication of the PC-based MN patch through hot embossing technique. Then, a UV-based laser machine was employed to drill through the MNs to make the microchannels for ISF extraction. **(b)** Final form of the HMN patch.

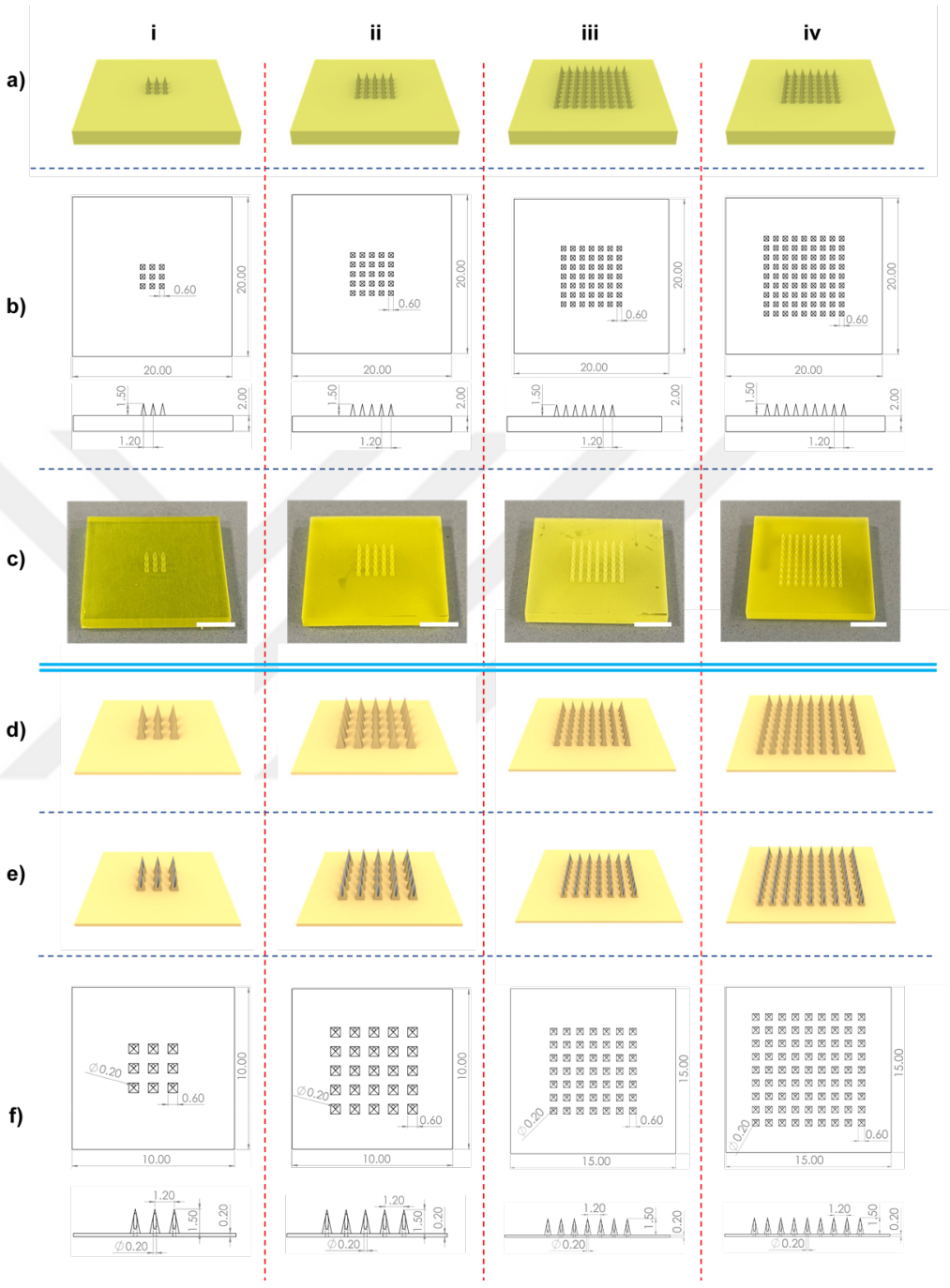


Figure 2.2. Designs and dimensions of the 3D-printed molds and HMNs used for the experiments. **(a)** Schematics and **(b)** 2D drawings and dimensions of the 3D-printed male molds. **(c)** Images of the 3D-printed male molds by MicroArch® S230 after Parylene-C deposition (scale bars are 5 mm). Schematics of the **(d)** MN and **(e)** HMN patches. **(f)** 2D drawings and dimensions of the HMN patches. Column (i): 3×3 array, column (ii): 5×5 array, column (iii): 7×7 array, and column (iv): 9×9 array. All the dimensions are in mm.

2.2.3 Fabrication of vacuum generation chamber and check valves

The vacuum generation chamber was fabricated using conventional molding techniques. Two master molds were prepared by 3D printing, followed by deposition of a 1 µm Parylene-C layer using SCS Labcoter Parylene Deposition System (IN, USA) to assist in peeling off PDMS from the molds. The PDMS mixture (10:1) was poured onto the master molds and cured at 100 °C for 2 hours. The resulting PDMS layers were assembled together using the techniques reported in the literature [213]. A biopsy punch was used to open holes with a diameter of 1 mm in the top layer of the vacuum generation chamber and the layer in between the vacuum generation chamber and the liquid extraction chamber. Next, 100 thick flaps of pre-cured PDMS were bonded to the outlets of the vacuum generation chamber to form the check valves. Detailed designs and drawings of the vacuum generation system that was deployed for in vitro and in vivo experiments, and the 3D-printed molds which were used to fabricate the top and bottom layers of the vacuum system are provided in **Figure 2.3**. Additionally, **Figure 2.4** provides detailed photographic images of the different parts of the vacuum generation system.

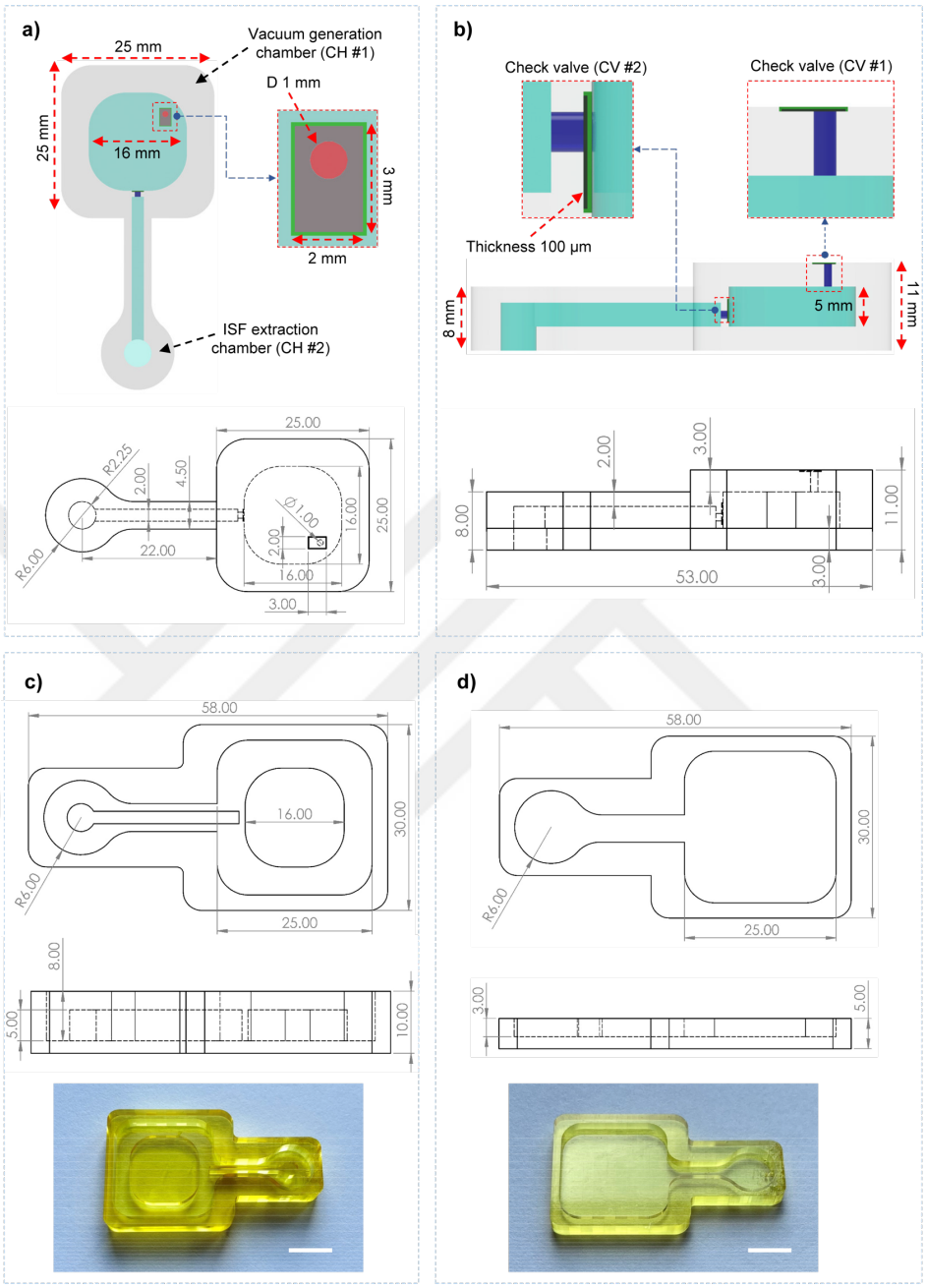


Figure 2.3. Designs and dimensions of the vacuum generation device used in the in vitro and in vivo experiments, along with the 3D-printed molds which were used to fabricate the device. **(a)** Top and **(b)** cross-sectional views of the vacuum generation system, with insets exhibiting the close-up views of the passive valves. The drawings in the bottom provide detailed information about the dimensions of the device. Drawings of male molds used for fabrication of the **(c)** top and **(d)** bottom layers of the vacuum generation system. The bottom pictures show the 3D-printed male molds by MicroArch® S230. All the dimensions are in mm. Scale bars are 1 cm.

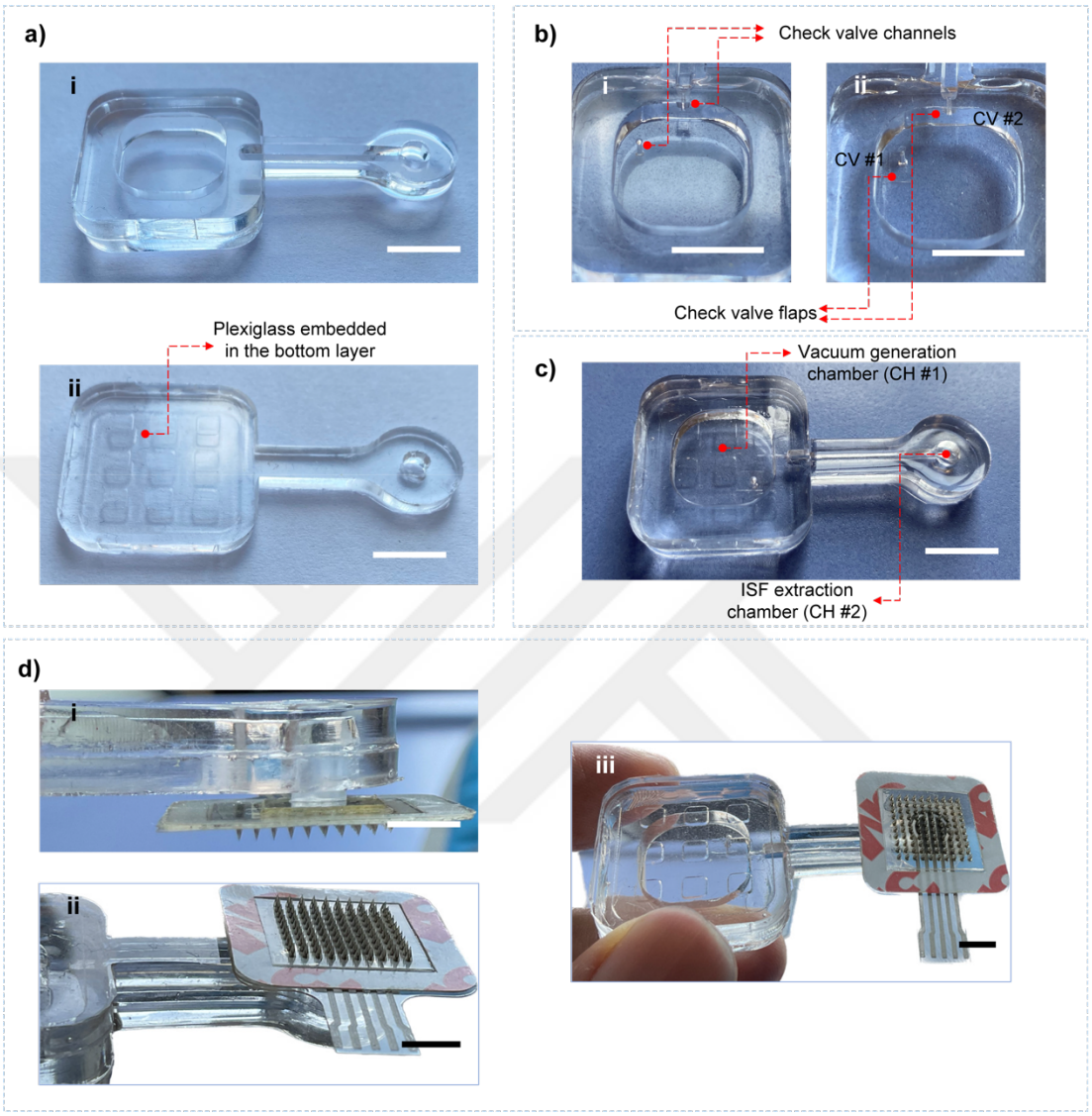


Figure 2.4. Photographic images of the fabrication process of the vacuum generation device. **(a)** Top (i) and bottom (ii) layers of the vacuum generation system. **(b)** Adding check valves to the top layer. (i) The channels of check valves were opened using a biopsy punch with a diameter of 1 mm. (ii) PDMS sheets of 100 µm thickness were used as the flaps of check valves. **(c)** Bonding the top and bottom layers of the vacuum generation device to each other to form the final device. **(d)** Attachment of the microfluidic module and HMNs to the vacuum generation device. (i) Cross-sectional and (ii) bottom views of the HMNs attached to ISF extraction chamber. (iii) Image of the fully integrated device (without the electronic board), ready for ISF sampling. (Scale bars; a, b, and c: 1 cm, d: 5 mm).

2.2.4 Fabrication of electrochemical sensor array

Electrochemical sensors were fabricated on a PET substrate through screen-printing techniques, consisting of two carbon electrodes as working electrodes (one for glucose and one for pH), one counter electrode made of carbon, and two Ag/AgCl electrodes as reference electrodes. The patterns of stencils for screen-printing were created by AutoCAD® (Autodesk, USA) and transferred onto the PET films using a laser machine. After screen-printing, a 500 nm Parylene-C insulation layer was deposited. The schematic representation of the fabrication process can be found in **Figure 2.5**. The Ag/AgCl electrodes were obtained by dropping the 0.1 M $FeCl_3$ solution on top of the Ag surface for 1 min.

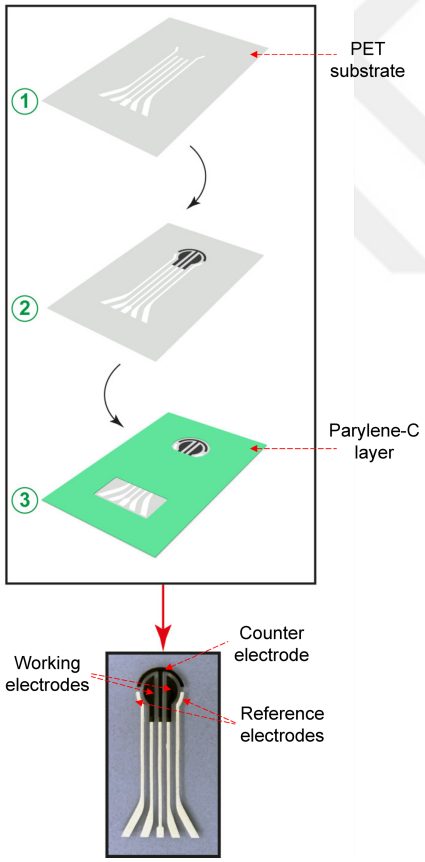


Figure 2.5. Fabrication process of screen-printed electrodes. Screen-printing a silver layer on a PET substrate using the first mask to create the connections and reference electrodes. 2) Using the second mask for carbon screen-printing to create the working electrodes and a counter electrode. 3) Deposition of Parylene-C as the insulation layer. The fabricated electrode can be seen in the bottom picture.

2.2.5 Preparation of glucose sensor

To prepare the glucose sensor, first, the electrode was cleaned by sonication for 10 min in isopropyl alcohol (IPA), followed by rinsing in DI water. Then, a Prussian blue (PB) mediator layer was electrochemically deposited on the working electrode by cyclic voltammetry from -0.2 to 0.2 V (versus Ag/AgCl electrode) for 2 cycles at a scan rate of 20 mV/s in a solution containing 100 mM potassium chloride, 2.5 mM iron (III) chloride, 2.5 mM potassium hexacyanoferrate, and 100 mM hydrochloric acid. After washing and drying the electrode, a 2 µL mixture solution containing GOx (50 mg mL^{-1} in PBS), chitosan in acetic acid (1% chitosan in 2% acetic acid), and AuNPs was drop-casted onto the glucose working electrode and was allowed to dry overnight at 4 °C with no light.

2.2.6 Preparation of pH sensor

For the pH sensor, the polyaniline (PANI) was electropolymerized on the carbon working electrode in a solution containing 0.1 M aniline and 1 M HCl using CV from −0.2 to 1 V for 15 cycles (versus Ag/AgCl electrode) at a scan rate of 50 mV s^{-1}. In the end, the PANI-coated electrode was washed and dried with an N_2 gun.

2.2.7 Design of PCB

The flexible printed circuit board (FPCB) was designed by Altium Designer software (Altium, Australia). The flexible thin copper/PI/copper substrate (Pyralux AP9131R, DuPont) was patterned by an ultraviolet (UV) 355 nm laser machine (ProtoLaser U4, LPKF, Germany). All the passive and active components were mounted on the FPCB using soldering paste and JBC NASE-2C precision soldering station. An ultra-low power Bluetooth Low Energy (BLE) system on a chip (SoC) (nRF52832, Nordic Semiconductor) was programmed and used as the main processor of the FPCB. To acquire the signals from amperometric glucose sensor, an analog front-end (AFE) potentiostat chip (LMP91000, Texas Instruments) was utilized and programmed through I^2C-controlled signals from the main processor. The AFE maintained a voltage difference of near-zero between the working and reference electrodes and converted the incoming current signals from the glucose sensor to voltage values using its internal transimpedance amplifier (TIA). For the potentiometric pH sensor, a voltage-divider was

designed to obtain the analog voltage values from the pH sensor and AFE's output for glucose sensor, and convert them to digital domain using the built-in 12-bit analog to digital converter (ADC) unit of the microcontroller. Furthermore, to monitor the pressure inside the device, a pressure sensor (BMP280, Bosch) was integrated to the system and transferred the data using I^2C protocol.

The electronic board layout was carefully designed to prevent any unwanted noises and signals from other sensors and digital components. The analog paths were kept separated from digitals with proper grounding and shielding to minimize the interference of the signals [28]. Additionally, amplifiers and appropriate filtering techniques were deployed to assist acquiring smooth signals during experiments. Also, the flexible flat cable (FFC) connector on the board established a robust and secure connection between the flexible sensor and the board, thereby ensuring high quality signal acquisition. Finally, a Parylene layer ensured reliable data recording of the physically isolated working electrodes (**Figure 2.5**) [214].

2.2.8 Assembly of vacuum-integrated ISF extraction and sensing system (VIES)

The PET layer containing the screen-printed electrodes was adhered to a double-sided tape (170 μm thick) as the microfluidic layer with an ISF collection chamber formed using the laser-cutting machine. Next, the HMN patch was assembled to the bottom of the chamber, rendering a microfluidic module capable of extracting and sensing ISF. In addition to the sensing chamber, another ISF microfluidic chamber, which was made of double-sided tape, was integrated into the microfluidic module. This chamber acts as a reservoir for ISF to prevent ISF accumulation in the sensing chamber, and enables liquid refreshing in the sensing chamber. For the in vivo and ex vivo experiments in this study, we designed an ISF chamber with volume of about 200 μL, which would have enough space for the collected ISF for one day with extraction rate of 8.33 μL h^{-1}. The dimensions of the ISF reservoir can be easily adjusted based on the required ISF collection rate and monitoring span. The pet layers which connect the HMN patch, ISF sensing chamber, and ISF reservoir to each other, have 50-μm-diameter holes to enable air and liquid flow between the layers. The small size of these holes ensures that ISF fills the chamber entirely before flowing towards the next chamber. Then, the vacuum generation system was attached to the PET layer to establish a channel for air exhaust out of the microfluidic module to create negative pressure for ISF extraction. A connector was

used to enable attachment of the PDMS-made vacuum system to the microfluidic module. The integration process is illustrated in **Figure 2.6**.

Finally, the PCB board can be integrated into the system using the FFC connector. The PCB board is covered with an encapsulation layer and can easily be coupled with the HMN patch.

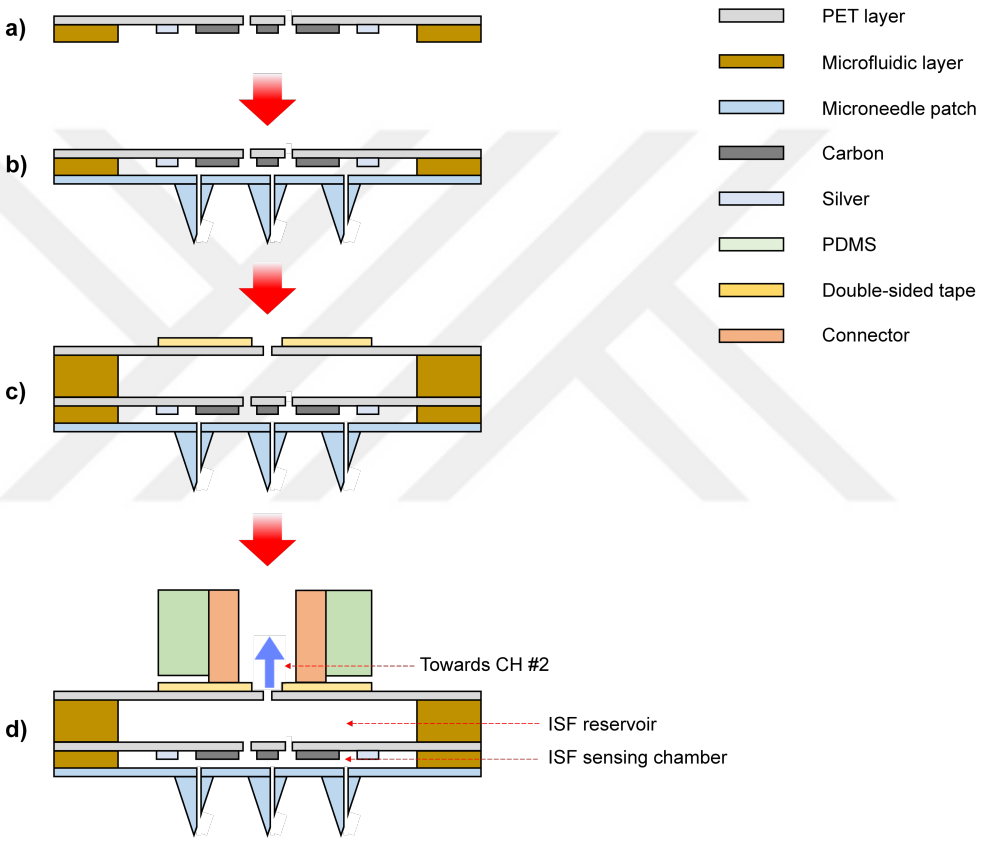


Figure 2.6. Integration process of the HMN patch, microfluidic layers, and vacuum generation system. **(a)** Attachment of the PET layer with screen-printed electrodes to the microfluidic sensing chamber. **(b)** Integration of the HMN patch to the bottom of the microfluidic chamber. **(c)** Attachment of a second chamber as an ISF reservoir. **(d)** Integration of the whole microfluidic module into the vacuum generation system.

2.2.9 Characterization of vacuum generation system

To examine the capability of the proposed method in vacuum generation, the pressure inside the vacuum and ISF extraction chambers were monitored using two pressure sensors (BMP 280), which were located inside the chambers. The pressure sensors were connected to Arduino boards by wire connectors to be able to record the pressure data by a computer. The

required electronic board for the pressure sensors was designed using Altium Designer, and the design was structured using a laser ablation machine (LPKF, Protolaser U4). The experimental setup is shown in **Figure 2.7**.

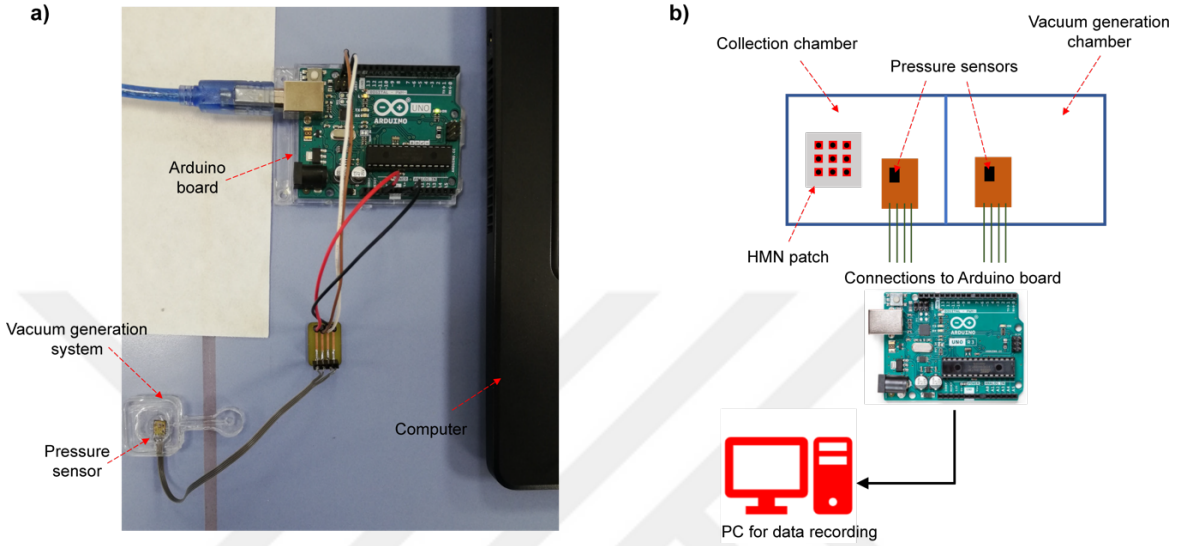


Figure 2.7. Experimental setup for characterization of the vacuum generation system. **(a)** Image of the test setup. **(b)** Schematic illustration of the experimental setup.

2.2.10 Morphology characterization of MNs and HMNs

The MN and HMN patches were characterized using scanning electron microscopy (SEM, Zeiss, Ultra Plus, Germany) and a 2D/3D motorized microscope (MRCL700 3D imager pro, Microqubic AG, Switzerland). The punctured skin by the HMN patch was also observed under SEM. Furthermore, SEM imaging was used to examine the robustness of the tip of MNs before and after laser drilling against deformation during insertion, compression, and shear load tests.

2.2.11 Mechanical characterization of MNs and HMNs

The mechanical properties of MN and HMN patches (compression, shear, and insertion tests) were examined with a force-displacement test station consisting of a MARK-10 force gauge and a Z-axis stage. The skin insertion test performed by mimicking the press and release action on skin. The skin sample was fixed on the Z-axis stage and the MN or HMN patches (5×5 needle array) were placed with the tips facing towards the skin sample, while the vertical force was applied on the patches at a rate of 5 µm s^{-1}. The loading force and displacement were recorded accordingly until a predefined maximum force of 0.4 N/needle was achieved.

For the compression test, the patches were placed on the Z-axis stage with needles facing upward, while the vertical force was applied on the tip of needles. For shear load test, the patched were fixed vertically on a stage and the force was applied on a single MN. For the compression and shear load tests, the maximum force per needle was 0.4 and 2 N, respectively. The conditions and needle array size were the same for all the mechanical characterization experiments.

2.2.12 Skin penetration efficiency test

Rat skin after administration of the MN patches was imaged by a digital camera to assess the skin penetration efficiency. 15 minutes after administration of the patches, the punctured skin was stained with 0.4% trypan blue solution. Excess trypan blue solution was wiped away and the skin sample was visualized by the digital camera and the perforated pores were considered as successful penetration. In a separate experiment, histologic analysis was performed to confirm the penetration of HMNs. The tissues were post-fixed for 24 hours in 4% paraformaldehyde and kept frozen in OCT gel before sectioning by cryostat device. The slides containing the tissue sections (10 μm thickness) were stained with Hematoxylin and Eosin solutions and visualized using an optical microscope (Zeiss, Germany).

We also used a laser confocal scanning microscope (Olympus, LEXT OLS5000) to view the holes made by MNs in the skin.

2.2.13 In vitro electrochemical detection of glucose and pH

All electrochemical experiments were performed on the CHI660E electrochemical workstation (Shanghai Chenghua Instrument Co. Ltd., Shanghai, China), unless indicated otherwise. The sensing performance of the glucose sensor was examined for a 0.02–15 mM concentration range in 0.1× PBS and artificial ISF as buffer solutions. The artificial ISF was prepared by following the procedure reported in the literature [215]. The sensitivity, stability, reproducibility, and selectivity of the electrodes were evaluated in chronoamperometric mode. The electrode was immersed in buffer solution, where the glucose concentration was increased in a stepwise manner by addition of glucose to the buffer solutions, while the solutions were under continuous stirring. For the selectivity test, interferent were added to the solution

successively. The selectivity of glucose sensor was tested using common electroactive interferents (NaCl, KCl, NH_4Cl, $CaCl_2$, glycine, urea, and ascorbic acid (AA)) within their physiological ranges. For the pH sensor, different interferents with physiologically relevant concentrations (LiCl, $CaCl_2$, KCl, NH_4Cl, and NaCl) were added to the artificial ISF solution with a pH of 7 to examine the selectivity of the pH sensor towards H+. The sensitivity is defined as the slope of the calibration curve. The long-term stability of the glucose sensor was investigated by storing the sensor at 4 °C and measuring their amperometric response every day for 7 days. The reproducibility of the electrodes was evaluated by recording the amperometric response of 7 electrodes at glucose concentrations of 100 µM and 5 mM.

The analytical performance of the pH sensor was examined measuring the open circuit potential (OCP) between the PANI-coated electrode and reference electrode. The electrochemical evaluation of the pH sensor was performed by drop-casting 100 µL of artificial ISF solution with different pH values on the electrode array. During the potentiometric measurements, the pH of standard solutions was adjusted by adding 0.1 M NaOH and 0.1 M HCl. The pH of the prepared solutions was compared with the values measured with a commercial pH meter (Mettler Toledo, Greifensee, Switzerland). The selectivity study was performed by successive addition of different interferents into the buffer solution. The stability of pH sensor was assessed by recording the OCP value over 1 hour, and in another experiment, the OCP value of the electrode was recorded over 7 days every day.

2.2.14 Ex vivo ISF extraction and measurement of glucose and pH

Rat skin was excised from the animals immediately after euthanasia and kept frozen at -80 °C until use. Square samples with an area of 4 cm^2 were used for ISF extraction. Before ISF collection, the samples were warmed up to room temperature and dried with a paper towel. Then, the skin samples were placed on the test setup and HMN patches were inserted into the skin. For each experiment, a single HMN array was integrated into the vacuum generation system. During the parametric studies, to investigate the effect of array size on ISF collection, HMN patches with array sizes of 3×3, 5×5, 7×7, and 9×9 were attached to the device, separately. To examine the effect of vacuum pressure and duration on the amount of collected ISF, HMN patches with array size of 5×5 were used. The vacuum generation chamber was attached to the skin and actuated using the finger to create the negative pressure for ISF

collection (55–80 kPa, absolute). During the experiments, the pressure inside the vacuum generation chamber was monitored using the pressure sensor. To determine the amount of collected ISF, the HMN patches were weighted before and after each experiment using a high precision scale. Schematic illustration of the test setup is shown in **Figure 2.8a**.

A similar experimental setup and liquid extraction method to ISF collection tests was used for ex vivo glucose and pH measurements. For glucose, skin samples were soaked in artificial ISF solutions with glucose concentrations ranging from 5 to 11 mM for 24 hours at 4 °C to an equilibrated state. For pH sensing, the samples were soaked in artificial ISF solutions with pH values of 6.94, 7.52, and 9.23. Schematic demonstration of glucose and pH sensing is shown in **Figure 2.8b**.

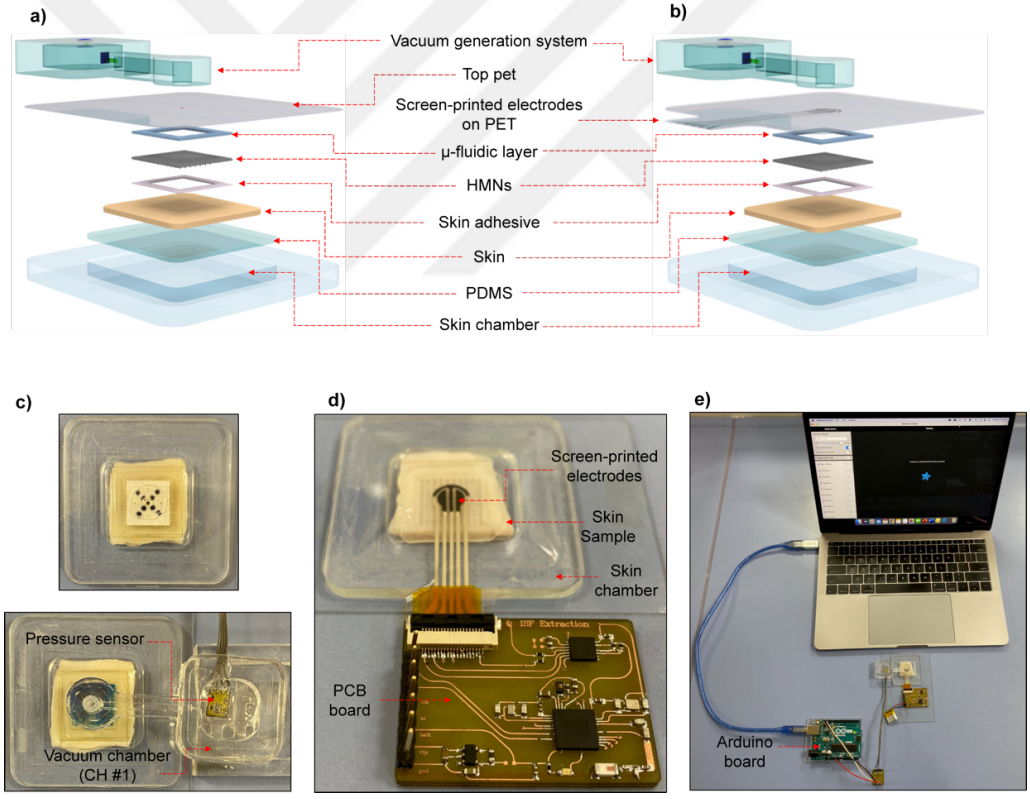


Figure 2.8. Ex vivo characterization experimental setup. Exploded view of the VIES system during **(a)** ISF extraction and **(b)** electrochemical sensing experiments. **(c)** Photos showing a placed skin sample in the skin chamber with dyed filter paper on top of it for visualization (top), and extracted ISF during ex vivo experiments using the VIES system (bottom). **(d)** Demonstration of the integration of PCB and screen-printed electrodes on top of the skin sample for glucose and pH readout. **(e)** Complete test setup for glucose and pH sensing.

2.2.15 In vivo ISF extraction and measurement of glucose and pH

Wistar rats (Female, 6–8 weeks, 150–200 g) were used in compliance with the guidelines and usage specifications of Koç University Animal Research Facility of Centre for Translational Medicine (2022.HADYEK.023). The rats were anesthetized and the dorsal hair was shaved off, and subsequently the skin was cleaned by distilled water and ethanol to assist proper adhesion of the patches. For the extraction experiments, previously-weighed HMN patches were applied to the bare skin, followed by attachment of the vacuum system. Similar to ex vivo experiments, for each in vivo experiment, only a single HMN array was attached to the vacuum generation system. The corresponding array sizes of HMN patches were the same as the ex vivo experiments. After ISF sampling, the HMN patches were immediately weighed again to calculate the amount of collected ISF. For glucose sensing experiments, after application of the VIES system, the amperometric signal was recorded using the developed FPCB board. The rats were intraperitoneally injected 1 M glucose solution (10%, in PBS) and insulin solutions to increase and decrease the glucose levels, respectively. Meanwhile, the tail vein blood was collected to measure the blood glucose level using a commercial blood glucometer (AccuChek; Roche Diagnostics, NJ, USA). For pH sensing experiments, the pH levels of ISF in rats were changed by intraperitoneal injection of two saline solutions with pH values of 6.5 ($saline_1$) and 8.2 ($saline_2$). Dynamic changing in ISF pH levels were monitored using the recorded potentiometric signal. To validate the response of the VIES system in pH sensing experiments, a commercial micro pH meter (Thermo Fisher Scientific, Orion 9826BN, micro pH electrode) was utilized to measure the pH value of ISF by placing the tip of the probe under the skin through a subcutaneous incision, which was made on dorsal side of the rat.

2.2.16 Statistical analysis

Statistical analysis was performed using Graphpad Prism 9.0. Statistical significance was assessed using t-tests. All experiments contain three replicates. All data are expressed as mean ± SD (standard deviation). P values of less than 0.05 ($P < 0.05$) indicated that the results were considered to be statistically significant. *$P < 0.05$, **$P < 0.01$.

2.3 Results and Discussion

2.3.1 System design and working principle of wearable vacuum-integrated ISF extraction and sensing system (VIES)

The VIES system was designed as a four-component system comprising: (a) vacuum generation and liquid extraction chambers, (b) a 3D flexible microfluidic module with integrated screen-printed electrodes for ISF sampling and sensing, (c) a laser-drilled HMN patch, and (d) a self-developed printed circuit board (PCB) for signal acquisition and data transmission via a Bluetooth module. **Figure 2.9a** illustrates the wearable VIES device, which is mounted on the human arm for ISF sampling and in-situ ISF analysis. Close-up illustrations of the three main parts of the VIES system are shown in **Figure 2.9b**. The measurement data can be acquired via wireless transmission of the electrochemical sensing signals to an electronic device (**Figure 2.9c**). As shown in **Figure 2.9d**, the microfluidic module is formed by vertical assembly of a double-sided tape, a transparent PET film with screen-printed electrodes, HMN patch, and skin adhesives. The double-sided tape contains a chamber for ISF sampling that was fabricated by laser-cutting. The 3D flexible microfluidic module was achieved by following an extensible integration approach that allows for the assembly of microfluidic layer, skin adhesives, and sensing electrodes within a compact footprint (**Figure 2.9e**).

To construct the vacuum generation system, a PDMS-based actuator was fabricated to leverage the elastic self-recovery feature of this polymer to create a negative pressure for ISF extraction. Owing to the mechanical resistance of the skin and negative hydrostatic pressure and low amount of ISF in the skin (120 µL of ISF per cm^2) [3], [18], [216], it is quite challenging to extract meaningful volumes of ISF. Practically, most ISF collection mechanisms extract volumes in the order of 1–10 µL, which is a significant limitation compared to blood-sampling techniques. Suction blisters that entail using vacuum pressure for continuous ISF extraction allow for ISF collection of up to 5 µL min^{-1} cm^{-1} at -200 mmHg [3]. However, due to the imposed damages to tissues by this method and the inconsistency of ISF composition obtained by this approach, there is a tendency to create micropores using MNs, followed by the application of vacuum pressure [32].

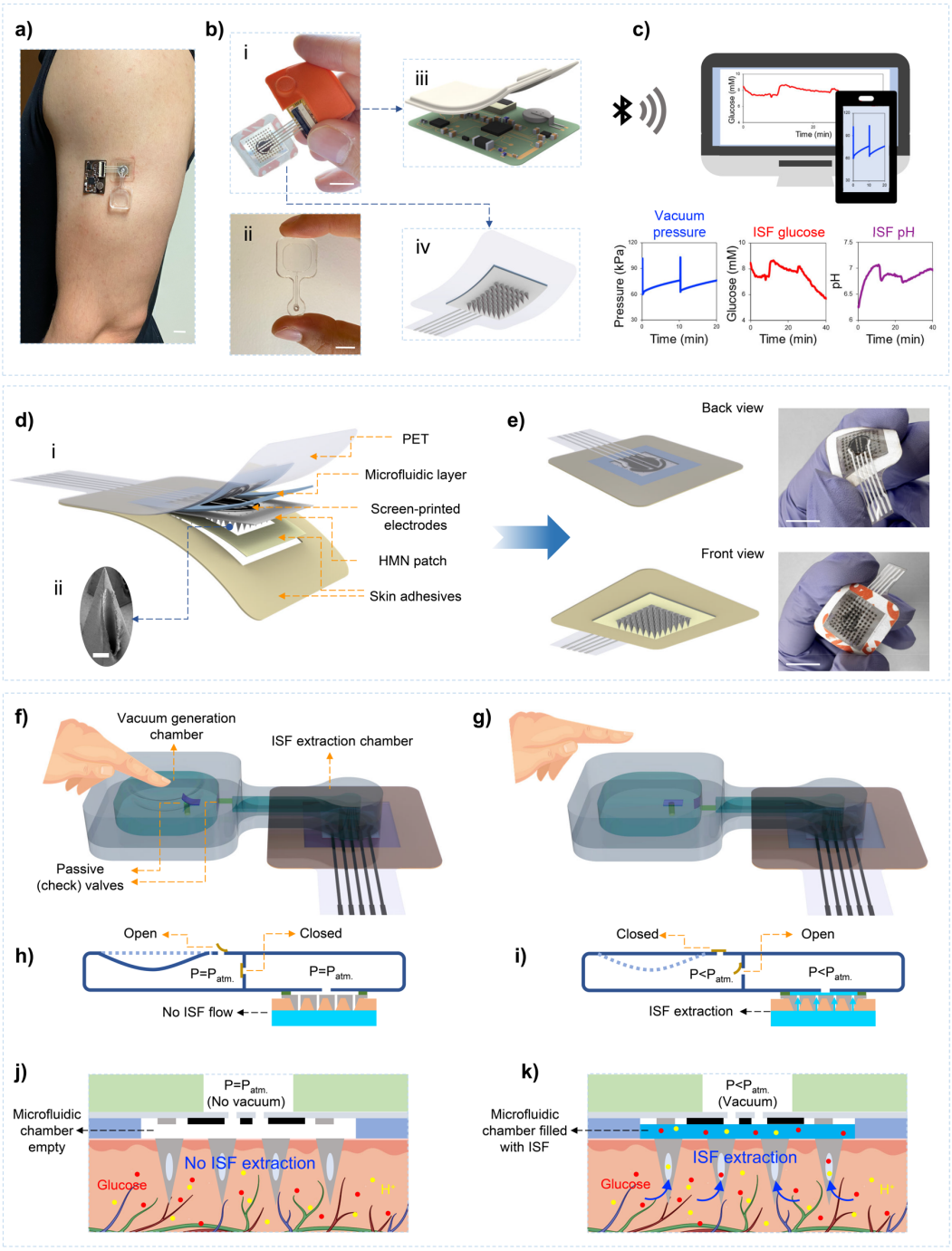


Figure 2.9. Illustration of the HMN-based wearable device for on-demand extraction of ISF and electrochemical sensing. **(a)** Photographic image of the developed device mounted on the human arm. **(b)** Close-up images of different parts of the VIES system. (i) Integration of HMN patch and flexible electronic board. (ii) Image of PDMS-based vacuum generation device. Schematics of (iii) electronic board with encapsulation layer and (iv) HMN patch. **(c)** Continuous monitoring of vacuum pressure and ISF glucose and pH levels. **(d)** Schematic of HMN patch integrated with the microfluidic module. (i) The layer-by-layer layout of the HMN patch. (ii) SEM image of a single HMN fabricated by laser-drilling (scale bar: 200 µm). **(e)**

Back and front view of the HMN patch integrated with the microfluidic module. Schematics of the vacuum generation system **(f)** upon applying and **(g)** after removing the compressive force. Formation of the check valves **(h)** upon applying and **(i)** after removing the compressive force. Detailed illustration of performance of the HMN-based VIES system, **j)** when there is no vacuum and **(k)** after vacuum generation. (Scale bars for a, b, and e are 1 cm).

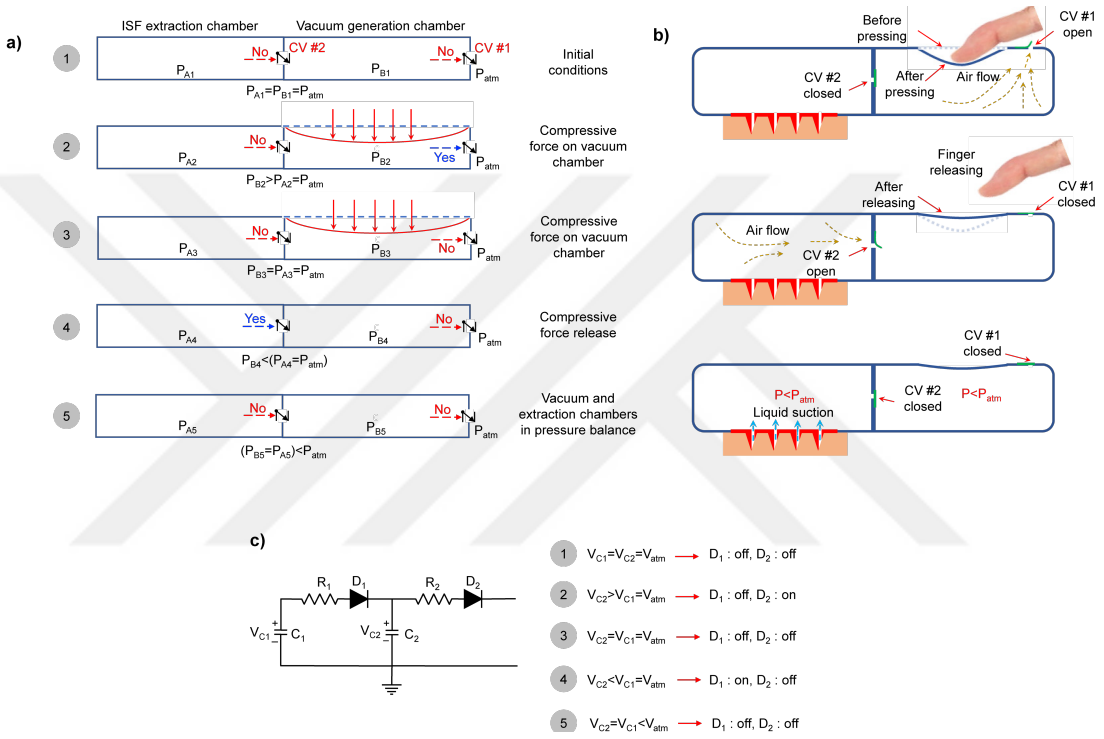


Figure 2.10. Different steps of vacuum generation in the VIES device. **(a)** Schematic illustration and **(b)** air flow directions after each step during vacuum generation. **(c)** Electrical circuit analogy of the vacuum generation system.

Here, we developed a finger-actuated PDMS-based system to generate the necessary negative pressure for ISF collection through the laser-drilled microchannels on the HMN patch. As demonstrated in **Figure 2.9f**, the vacuum generation system consists of three main parts: 1) vacuum generation chamber, 2) liquid extraction chamber, and 3) passive (check) valves. The outlet passive valve (CV #1) is activated by finger-pressing the chamber, while the valve between the two chambers (CV #2) remains closed (**Figure 2.10**). With compressive force removed, the elastic force of the vacuum generation chamber results in the self-recovery of this chamber. This produces a negative pressure in the chamber that opens CV #2 and closes CV #1 because of the established pressure gradient (**Figure 2.9g** and **Figure 2.10**). When

liquid extraction and vacuum generation chambers reach a balanced pressure, both passive valves are closed because of the lower pressure of chambers compared to the atmospheric pressure. The produced negative pressure facilitates ISF extraction through the HMNs into the microfluidic chamber (**Figure 2.9h,i**). Different steps of vacuum generation in the VIES are summarized as an electrical circuit analogy in **Figure 2.10c**. The implementation of CV #2 enables successive pressing of the vacuum generation chamber without reducing the vacuum pressure in the liquid extraction chamber. This is one of the major superiorities of the proposed design compared to the available finger-actuated devices for biofluid sampling [202], which allows continuous adjustment of vacuum pressure inside the device. **Figure 2.9j,k** provides schematic illustrations of ISF extraction using the VIES system.

2.3.2 HMN patch fabrication and characterization

The HMN patches were prepared using conventional hot embossing techniques, followed by laser-drilling the needles to establish the through microchannels for ISF transport from the skin to the microfluidic chamber (**Figure 2.1**). The MN patch consists of an array of pyramidal MNs, where the height, edge width, and space between pyramid centers are 1.5 mm, 0.6 mm, and 1.2 mm, respectively (**Figure 2.11a**). The fabricated PC-based MN patch exhibited excellent flexibility against minimum forces (**Figure 2.11b(i)**), suggesting its adaptable shape depending on the place and form of the skin. **Figure 2.11b(ii, iii)** gives a detailed morphological characterization of the MN patches, which were observed using optical and scanning electron microscopy, respectively. **Figure 2.11c** shows a schematic illustration of the PC-based MNs laser drilling with a hole diameter of 0.2 mm. To minimize the risk of blockage due to tissue clogging, the HMNs were designed with side openings, where the openings face perpendicular to the insertion direction, rather than openings on the tip of needles [27], [50], [113], [140], [217]. **Figure 2.11d** provides optical, microscopic, and SEM images of the HMN patch.

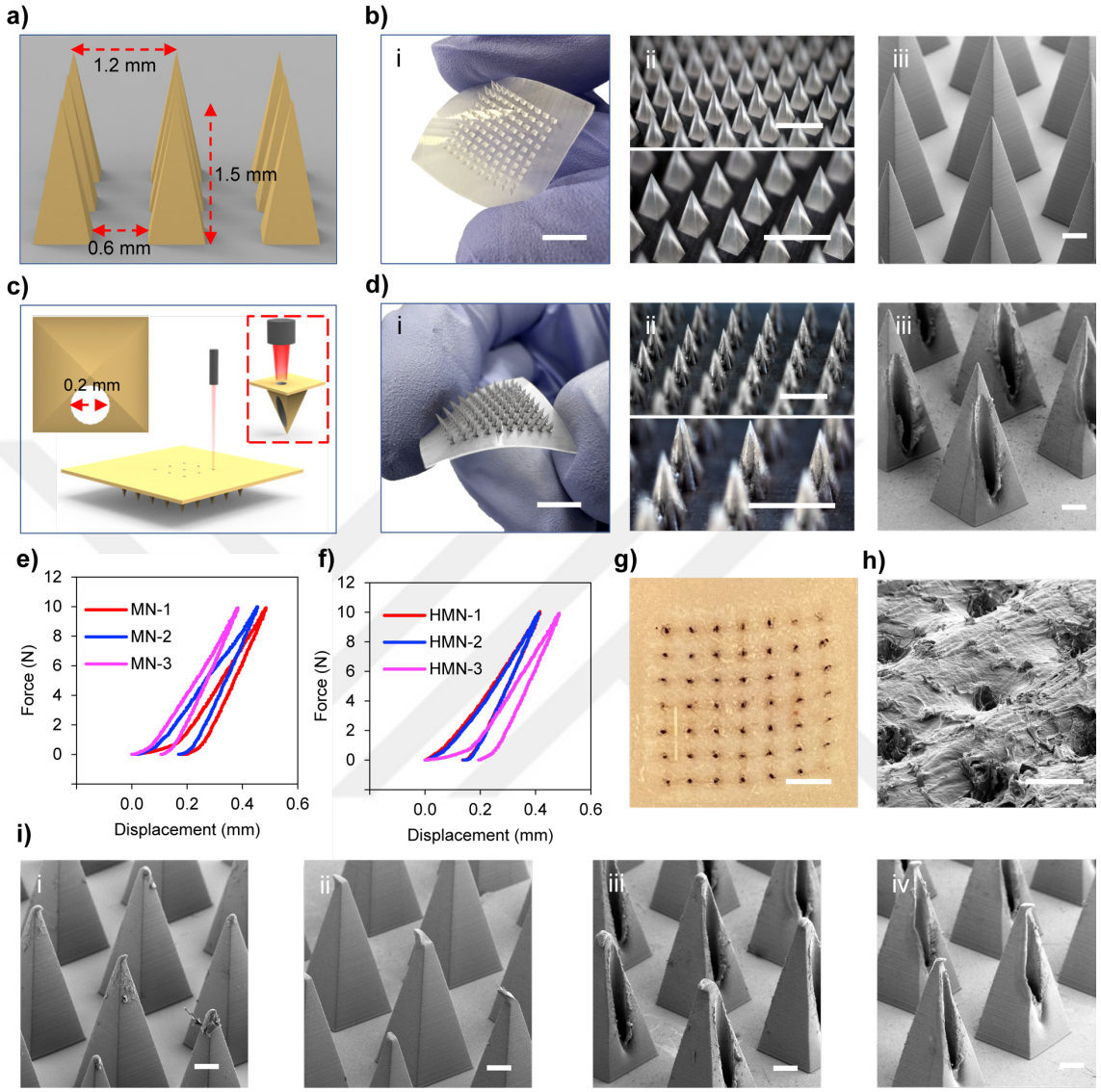


Figure 2.11. Characterization of MN and HMN patches. **(a)** Illustration of the MN patch with the corresponding dimensions. **(b)** PC-based MN patch fabricated by hot embossing technique. (i) Optical, (ii) microscopic, and (iii) SEM images of the MNs (scale bars: (i): 5 mm, (ii): 2 mm, and (iii): 200 µm). **(c)** Schematic illustration of laser drilling of the MNs. **(d)** PC HMN patch realized by laser-drilling. (i) Optical, (ii) microscopic, and (iii) SEM images of the HMNs (scale bars: (i): 5 mm, (ii): 2 mm, and (iii): 200 µm). Force-displacement curves of the **(e)** MNs and **(f)** HMNs in the mechanical compression test. **(g)** Trypan blue staining image (scale bar: 2 mm) and **(h)** SEM image (scale bar: 500 µm) of punctured skin by the HMN array. **(i)** SEM images of MNs after (i) multiple insertions and (ii) compression test. SEM images of HMNs after (iii) multiple insertions and (iv) compression test (scale bar: 200 µm).

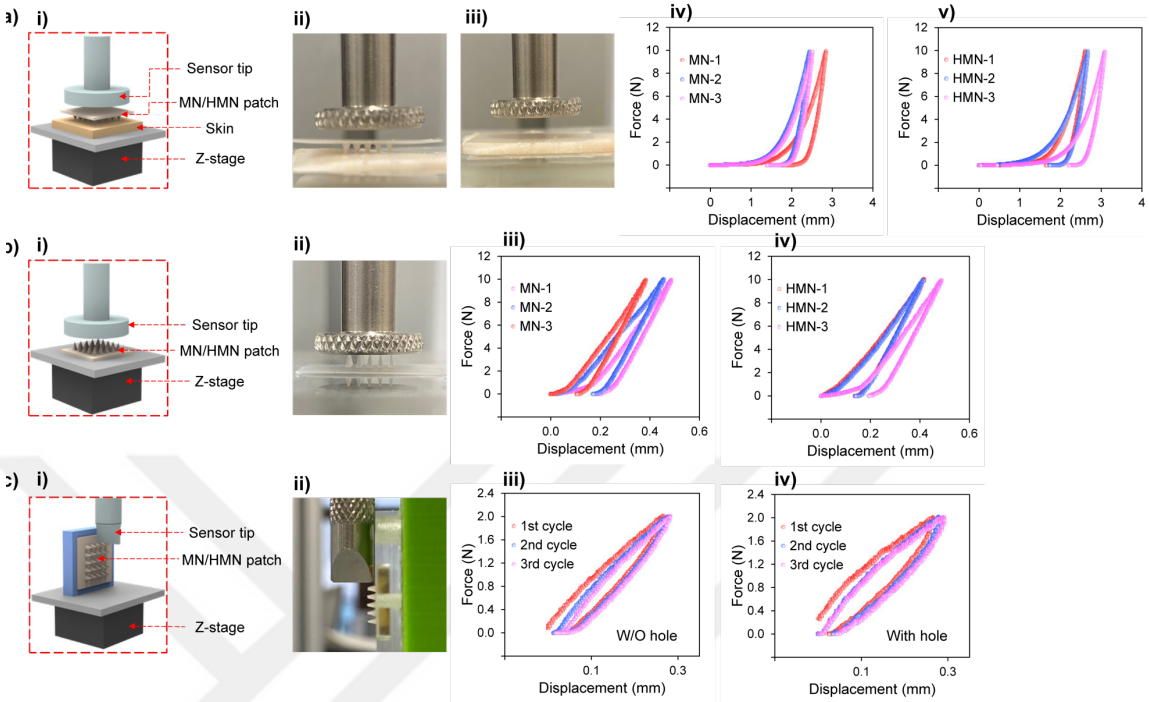


Figure 2.12. Mechanical characterization of the PC-based MNs before and after laser drilling. **(a)** Assessment of the required force during MN application. (i) Schematic illustration of the sensor application to the skin. Optical images of the MN array (ii) before and (iii) after insertion into the skin. Load-displacement profiles of (iv) MNs and v) HMNs with longitudinal compressing (n=3). **(b)** Mechanical compression test. (i) Schematic illustration of the setup. (ii) Optical image of the MN array with force sensor in contact with the tip of needles. Load-displacement profiles of the (iii) MNs and (iv) HMNs in the compression test with longitudinal compressing (n=3). **(c)** Mechanical shear force test. (i) Schematic illustration of the setup. (ii) Optical image of force application on a single MN from a MN array. Force displacement curve of the (iii) MNs and (iv) HMNs in the shear test. The force was applied for three cycles on the same MN.

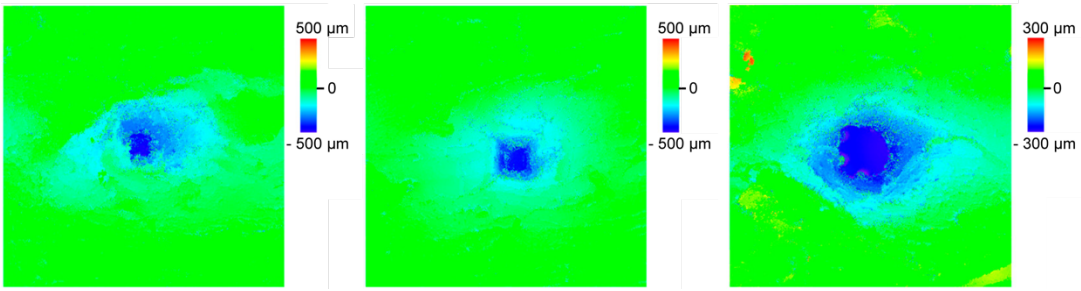


Figure 2.13. Confocal microscopy images of MN insertion in skin. The three images show confocal results of three different MNs from the HMN patch.

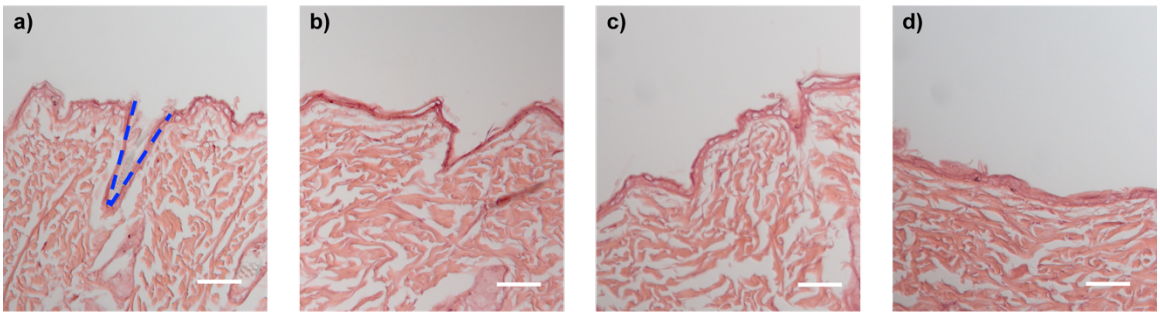


Figure 2.14. H&E-stained sections of rat skin showing HMNs penetration sites and the surrounding tissue. **(a)** Upon HMNs removal. **(b)** 5 mins after HMNs removal. **(c)** 15 mins after HMNs removal. **(d)** Control sample with no HMNs administration (scale bar: 100 µm).

To investigate the mechanical strength of the MNs, a customized force-displacement test setup was utilized, following previously reported protocols (**Figure 2.12**) [28], [33], [218]. The plots of force against displacement were obtained under compression load and shear load, and also for insertion into a skin sample. MN patches with 5×5 array were used for this purpose, and the maximum force was 10 N (0.4 N per needle), which is larger than the required force for skin insertion [208], [219]. The compression study (**Figure 2.11e** and **Figure 2.12b**) confirms the mechanical stability of the MN patch, as no fracture (smooth curve with no sharp drop of force in the graph) was observed. The resulting vertical displacement of the end of the needle tips was approximately 0.15 mm (about 10% of the needle height, n=3), thereby bringing about small effect to penetration performance of the MN patch. The insertion study (**Figure 2.12a**) indicated that less than 2 N (0.08 N per needle, n=3) was required to achieve a displacement of 1.5 mm (corresponding to the length of the MNs). A net displacement of 0.05 mm (n=3) was observed at the end of the insertion test, indicating the successful and complete insertion of the MN patch. It should be noted that because of the elastic nature of the skin, the penetration depth of needles into the skin would be lower than 1.5 mm (will be discussed later). In the shear load test, by decreasing the force to 2 N per needle, similar to the compression load, a smooth curve was obtained, and a minor displacement was observed that indicates the preservation of the structural integrity of the MN patch (**Figure 2.12c**).

Moreover, the mechanical characteristics of the HMN patch were investigated. Accordingly, similar characterization experiments to the MN patch were performed for HMN patches (**Figure 2.11f** and **Figure 2.12**). The results revealed that the HMN patches showed similar mechanical behavior to that of MN patches during compression, shear, and insertion

tests. Such mechanical robustness demonstrates the high mechanical stability of the HMNs against disruptive shear and compression forces relevant to the dermal application [59], [125]. Additionally, the penetration abilities of the patches were examined using SEM imaging and trypan blue staining. The HMN patch was pressed into the skin using thumb force and held in the skin for approximately 10 min. After removal of the HMN patch, the skin was immediately stained with 0.4% trypan blue solution for better visualization, followed by capturing the optical image of the skin sample. The patterns of HMN array could be observed clearly on the skin sample (**Figure 2.11g**). The histology studies and confocal microscopy results revealed that the efficient penetration depth of HMNs was about 400 μm (**Figure 2.13** and **Figure 2.14**), indicating successful penetration of HMNs to the dermis. SEM image of the skin sample after HMN patch application also revealed successful penetration of the needles into the skin (**Figure 2.11h**). SEM images of the MN and HMN patches were captured after five insertions into the skin samples, and after the compression test. As shown in **Figure 2.11i**, the structural integrity of both MN and HMN patches remained intact after dermal application and compressive force.

2.3.3 Performance and characterization of vacuum generation system

A sufficient pressure difference between the dermis and the VIES system can extract ISF from dermis into and through microchannels towards the microfluidic chamber. This can be accomplished by suction to generate a vacuum pressure on the skin. The performance of the vacuum generation system in lowering the pressure inside the ISF extraction chamber was investigated using the experimental setup shown in **Figure 2.7**. Due to the considerable effect of vacuum pressure on the amount of ISF extraction, it is of great significance to be able to monitor the pressure inside the chambers to ensure the optimal performance of the device.

Here, we placed pressure sensors inside each chamber (vacuum generation chamber (CH #1) and ISF extraction chamber (CH #2)) to be able to monitor the pressure profiles during characterization experiments. As shown in **Figure 2.15a**, applying a compressive force to CH #1 activates CV #1 because of the increased pressure inside CH #1. CV #1 remains open until achieving a pressure balance between CH #1 and outside pressure. After removal of the compressive force (**Figure 2.15b**), the elastic self-recovery of PDMS-based CH #1 results in a pressure drop inside this chamber that activates CV #2 to balance the pressure between the

two chambers. Upon achieving a negative gauge pressure inside both chambers, both CV #1 and CV #2 become closed (**Figure 2.15c**), and the vacuum pressure inside CH #2 acts as a driving force to assist ISF extraction from skin. A more detailed exhibition of different steps of the vacuum generation system is shown in **Figure 2.10**.

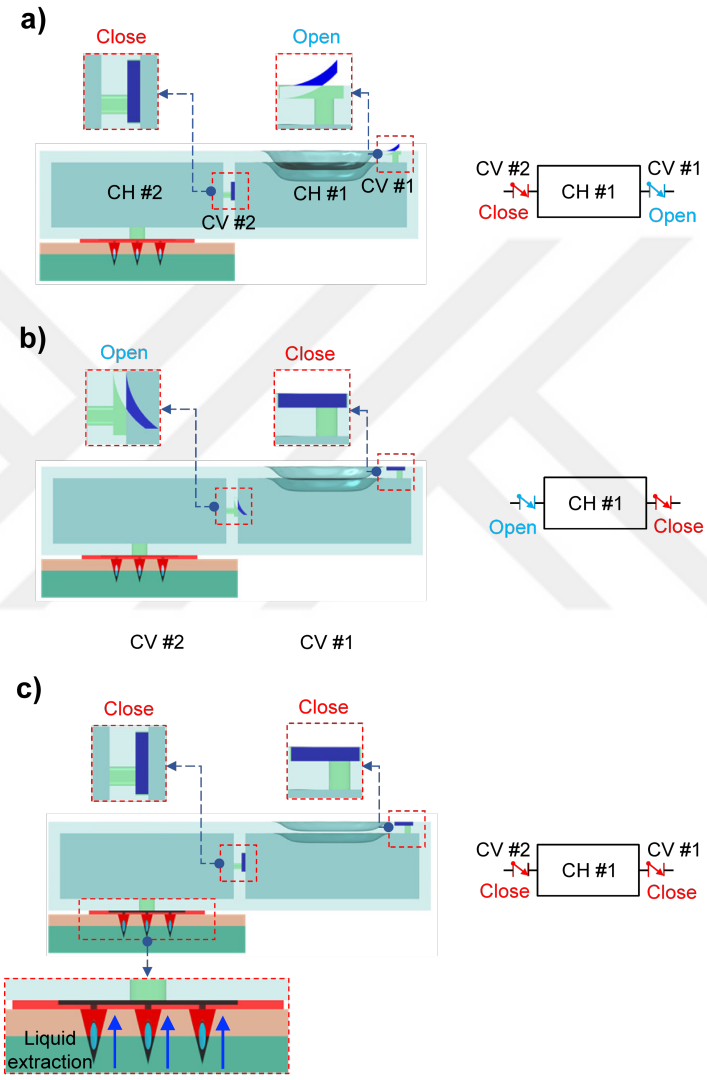


Figure 2.15. Working principle of the vacuum generation system. **(a)** pressing the vacuum generation chamber (CH #1) to open CV #1 and exhaust the air. **(b)** elastic self-recovery of PDMS-made CH #1 after releasing the compressive force, leading to air transport from CH #2 to CH #1 because of the pressure difference. **(c)** liquid extraction through HMNs into the microfluidic chamber. (Insets: close-ups of CVs #1 and #2 when they are closed or open, and liquid flow through the attached HMNs to CH #2 towards the sensing chamber.

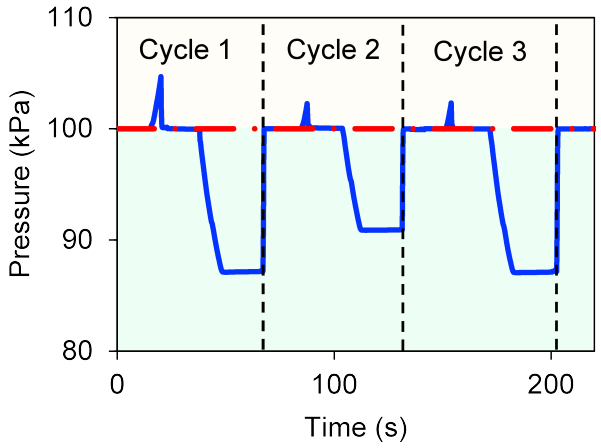


Figure 2.16. Illustration of different steps of vacuum generation in CH #1 in three successive cycles.

Figure 2.16 illustrates the pressure profile inside CH #1 during three cycles of finger press and release. As can be seen, first, the pressure inside the chamber rises because of the compressive force, which leads to the lowered volume of the chamber. The elastic nature of the check valve flaps results in a delay (from a few milliseconds to a few seconds depending on the applied force) between applying compressive force and opening of the check valve (CV #1), thereby causing a pressure buildup inside the vacuum generation chamber (CH #1). Following activation of CV #1, the pressure inside CH #1 drops to atmospheric pressure. Then, the pressure decreases upon the removal of the compressive force. After releasing the finger, the volume of the chamber begins to increase because of the elastic self-recovery of PDMS, resulting in a pressure drop in the chamber (vacuum generation). In the first cycle in **Figure 2.16**, the pressure increases from 100 kPa (assuming the initial pressure is 100 kPa) to an average pressure of 104.74 kPa as a result of pressure buildup during the initiation of pressing. Then, the pressure drops to about 101.02 kPa following CV #1 activation. The slight change compared to the initial pressure could be because of the error of the pressure sensor, or because the pressure difference is not large enough to keep the check valve open and balance the pressure completely. Upon removal of the compressive force, the pressure starts to decrease until it reaches 87.12 kPa. The same cycle was performed three times to demonstrate the repeatability of the process. A lower compressive force was applied during the second cycle to show that a lower vacuum can be easily obtained by only controlling the magnitude of the applied force.

Figure 2.17 shows the capability of VIES system in lowering the pressure in a stepwise manner for better adjustment of the pressure as well as achieving high vacuum pressures. Immediate administration of high vacuum pressures (-34 to -50 kPa gauge) can lead to bleeding onto the skin surface [32]. To avoid this, we designed our system in a way that the vacuum pressure can be continuously monitored and adjusted accordingly. As shown in **Figure 2.17c**, the pressure inside CH #1 was lowered from 100 to about 60 kPa (-40 kPa vacuum pressure) by successive pressing and releasing the chamber, which is a satisfactory vacuum pressure for ISF extraction [32], [48]. An important superiority of the proposed design over the similar methods available in the literature, is the addition of CV #2 between the two chambers. This enables adjustment of the pressure inside the device without affecting the vacuum pressure inside the ISF extraction chamber (**Figure 2.17d**). Because of the low amount of ISF in the skin [3], it is essential to maintain the minimum required vacuum pressure inside the device for maximal liquid extraction. Moreover, without using CV #2 (**Figure 2.17b**), the pressure inside CH #2 could rise to even above the atmospheric pressure during multiple pressing that might lead to the retraction of extracted ISF into the skin.

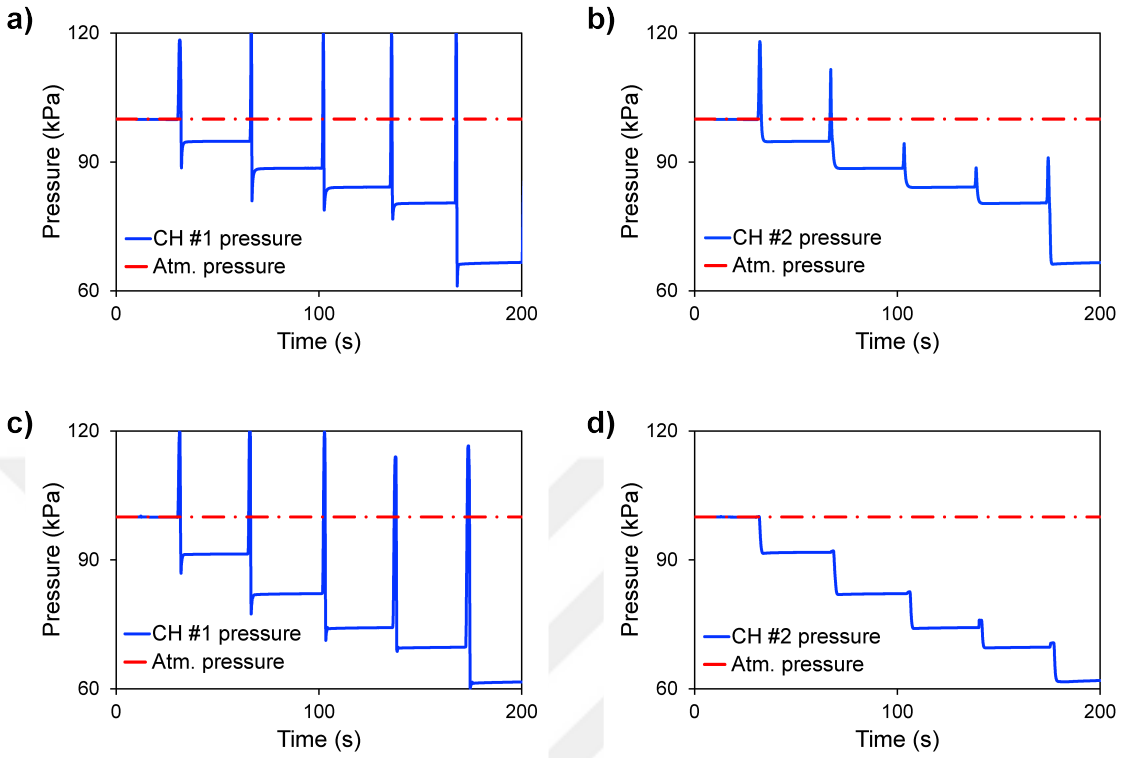


Figure 2.17. Comparison of the pressure profiles inside CH #1 and CH #2 with and without CV #2. Pressure profiles inside **(a)** CH #1 and **(b)** CH #2, when there is no CV #2 between the two chambers. Pressure profiles inside **(c)** CH #1 and (**d)** CH #2, after addition of CV #2.

To examine the effect of chamber dimensions and the pressing extent on the degree of created vacuum pressure, five separate chambers with different volumes were fabricated (**Table 2.1**). A customized experimental test section was prepared and each chamber was tested using this setup (**Figure 2.18a,b**). The results showed that by changing the dimensions of the chamber and increasing the pressing extent, the pressure inside the chamber can drop to as low as about 47.13 ± 1.16 kPa (~ -53 kPa vacuum pressure). Furthermore, according to the results, vacuum chamber with a lower volume could improve the generated vacuum pressure. This is because pressing a chamber with a smaller volume exhaust a higher portion of the inside air, leading to further pressure drop. For instance, 6 mm pressing of the chamber with volume of 7962.5 mm^3 caused the pressure of chamber to drop to 90.01 ± 0.11 kPa, while this value was 74.1 ± 2.2 kPa for the chamber with volume of 4062.5 mm^3. Moreover, an increase in chamber height led to an enhanced vacuum generation (**Figure 2.18b**).

Table 2.1. Dimensions of different chambers used for the characterization of vacuum generation chamber.

Label	Dimensions (Length × width × height, mm)	Volume (mm^3)
CH #1_1	25 × 25 × 6.5	4062.5
CH #1_2	25 × 25 × 8.5	5312.5
CH #1_3	30 × 30 × 6.5	5850
CH #1_4	30 × 30 × 8.5	7650
CH #1_5	35 × 35 × 6.5	7962.5

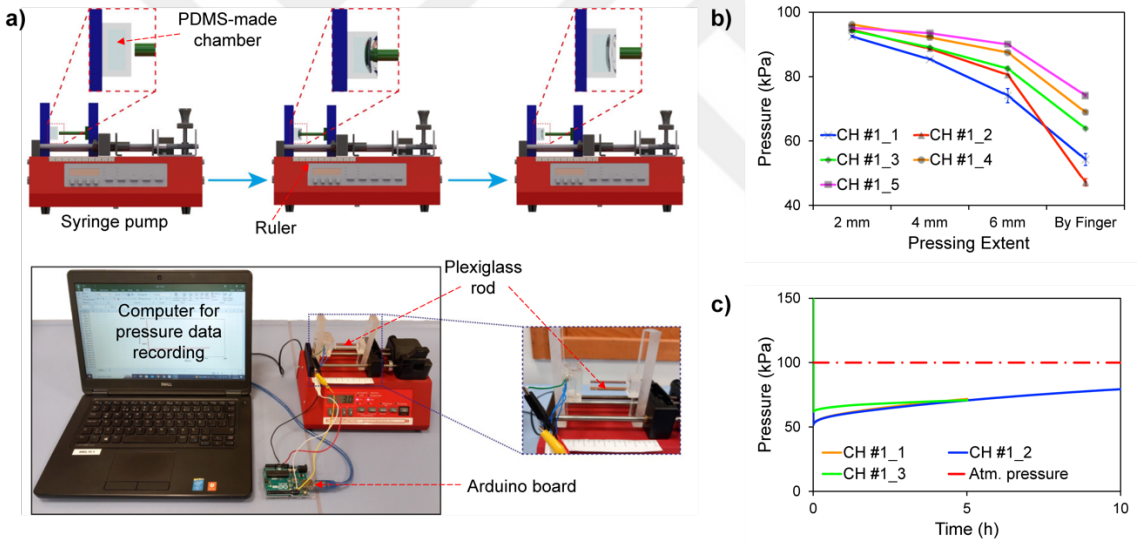


Figure 2.18. Characterization of chambers with different dimensions. **(a)** Experimental setup. The chambers were attached to a stage, which was fixed on a syringe pump. A plexiglass rod was cut in a small piece to play the role of finger for pressing the chamber. The rod was fixed onto the stage, which is normally dedicated for pressing the syringe. A ruler was attached to the syringe pump to control the forward/backward movement of the plexiglass rod. After turning on the syringe pump, the rod could move towards the chamber, causing pressings of 2 , 4 , and 6 mm. **(b)** The created negative pressure inside CH #1 corresponding to different pressing extents. 5 different chambers with various dimensions were used for this experiment (**Table 2.1**). **(c)** Vacuum pressure drop inside the vacuum generation chambers over a long period.

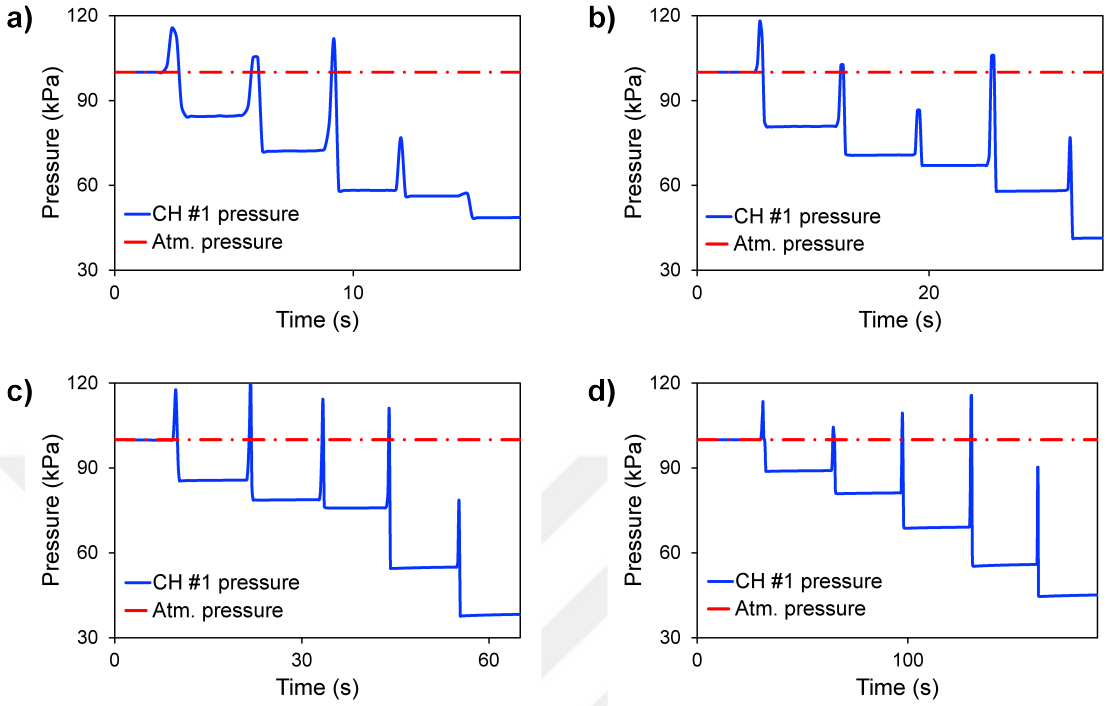


Figure 2.19. Capability of vacuum generation system to create negative pressure in different time frames. Applying multiple successive compressive forces using thumb every **(a)** 2, **(b)** 5, **(c)** 10, and **(d)** 30 seconds.

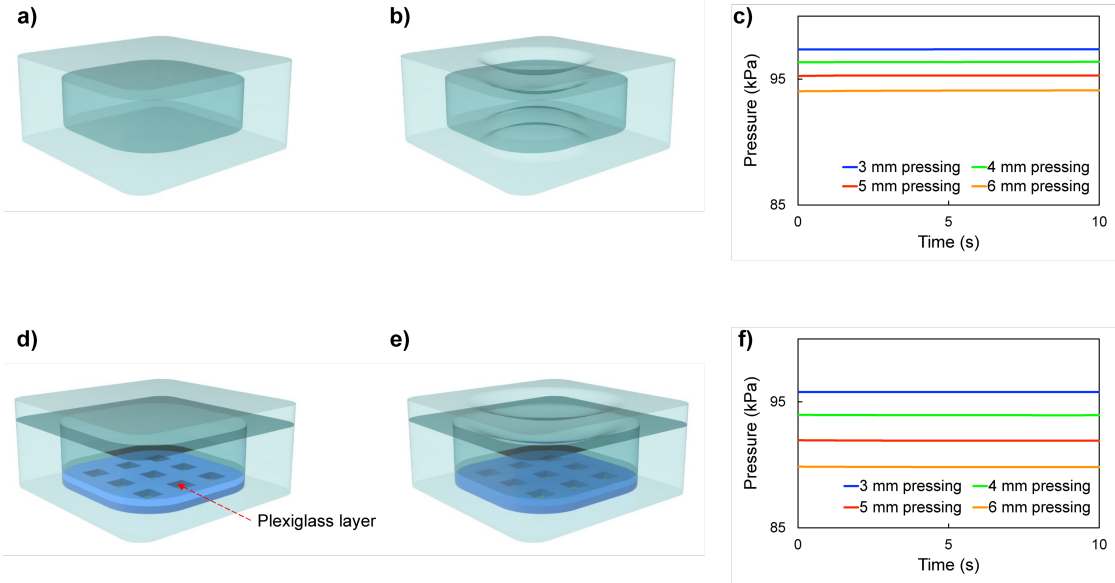


Figure 2.20. Investigating the effect of embedding a solid layer in bottom side of vacuum generation chamber. Schematics of vacuum generation chamber when there is no plexiglass embedded in the bottom layer, **(a)** before and **(b)** after application of compressive force. **(c)** Generated vacuum inside the chamber corresponding to different pressing extents. Vacuum generation chamber when a plexiglass embedded in the bottom layer, **(d)** before and **(e)** after

application of compressive force. As can be seen in e, only the top layer is remained bent. **(f)** Generated vacuum inside the chamber corresponding to different pressing extents.

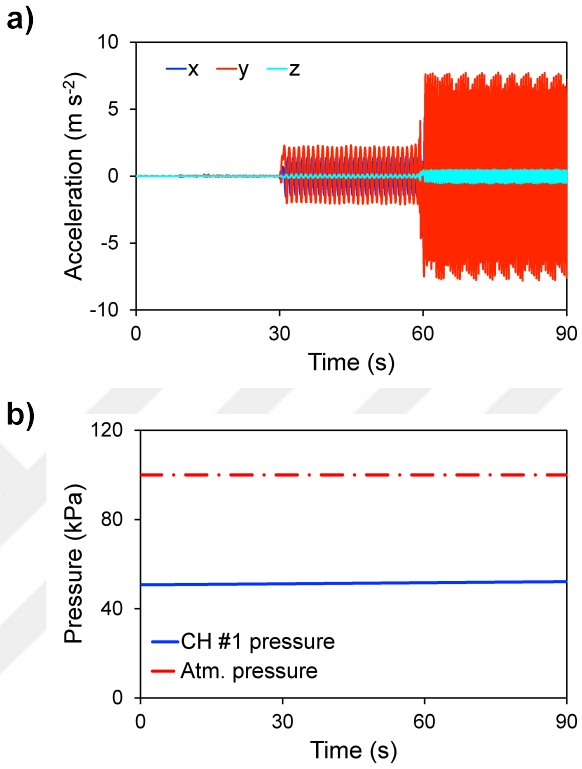


Figure 2.21. Pressure profile in the vacuum chamber under oscillatory motions. **(a)** Vibrational acceleration profiles. **(b)** Corresponding pressure readout in the vacuum generation chamber.

Figure 2.18c shows the pressure drop inside CH #1 over long periods for chambers of different volumes. For the chamber with volume of 4062.5 mm^3 and for initial vacuum pressure of ~48 kPa, the vacuum dropped about 20 ± 1.2 kPa after 5 hours. The results in **Figure 2.18c** suggest that the vacuum generation device is capable of generating and maintaining the required vacuum pressure for ISF extraction and continuous monitoring of different biomarkers in ISF. In addition, the VIES device could accomplish the vacuum pressure at different pressing speeds of 2, 5, 10, 30 seconds (**Figure 2.19**), indicating its flexibility to adjust the vacuum according to different needs.

In our design, different from the devices in the literature for similar applications [202], in which both top and bottom of the vacuum chambers are flexible, a plexiglass plate is embedded into the bottom layer of vacuum generation chamber, preventing the bottom layer

to remain flexed during self-recovery step, leading to an enhanced vacuum generation (**Figure 2.20**). Last, the performance of vacuum generation chamber was tested under oscillatory motions (created by a vortex mixer) to evaluate the stability of VIES system against motion artifacts (**Figure 2.21**). The pressure readout, shown in **Figure 2.21b** indicates no fluctuation over a 90-second period.

2.3.4 Performance and characterization of electrochemical sensing system

The HMN patch was integrated with a microfluidic module for ISF collection and in situ sensing of ISF to circumvent any post-processing processes for the analysis of different biomarkers in ISF, which is common in hydrogel-based MNs [76], [220]–[222]. To augment the efficiency of low-volume ISF extraction and enhance the temporal resolution of electrochemical sensing, a thin microfluidic module was carefully designed and attached to the back of the HMN patch to collect the extracted ISF into a chamber, and provide the necessary contact with the electrochemical sensors. Initially, we performed pH and glucose detection and analysis in vitro using potentiometric and amperometric measurements, respectively, with benchtop equipment (CHI660E). Briefly, the glucose sensor was realized by depositing a mediator layer of Prussian blue (PB) on the working electrode, followed by modification of the electrode with an enzymatic layer. The working electrode of the pH sensor is coated with an electropolymerized polyaniline (PANI) layer, which acts as the hydrogen ion-selective film for pH sensing.

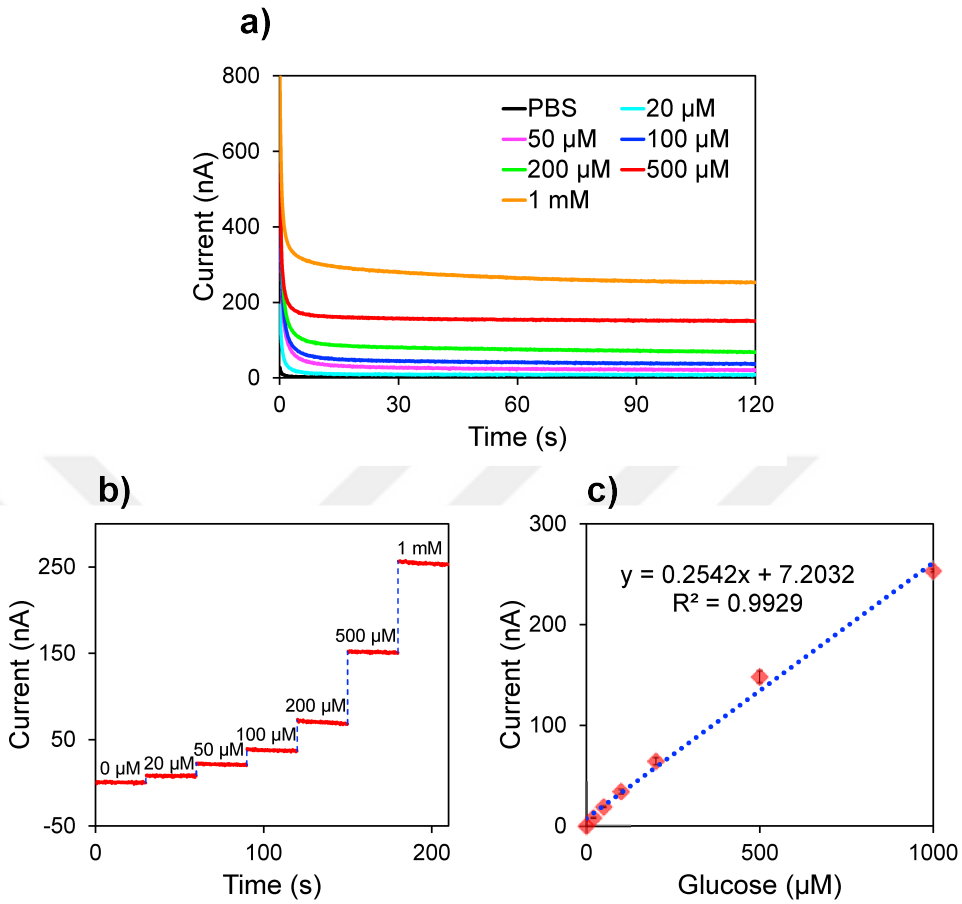


Figure 2.22. Experimental characterization of the glucose sensor at low concentrations. **(a)** Chronoamperometry response of the glucose sensor to increasing concentrations of glucose in artificial ISF from 20 to 1000 µM. **(b)** I-t curve of the glucose sensor with stepwise addition of glucose into artificial ISF. **(c)** The corresponding calibration curve (n=3). Data were expressed as the mean ± SD.

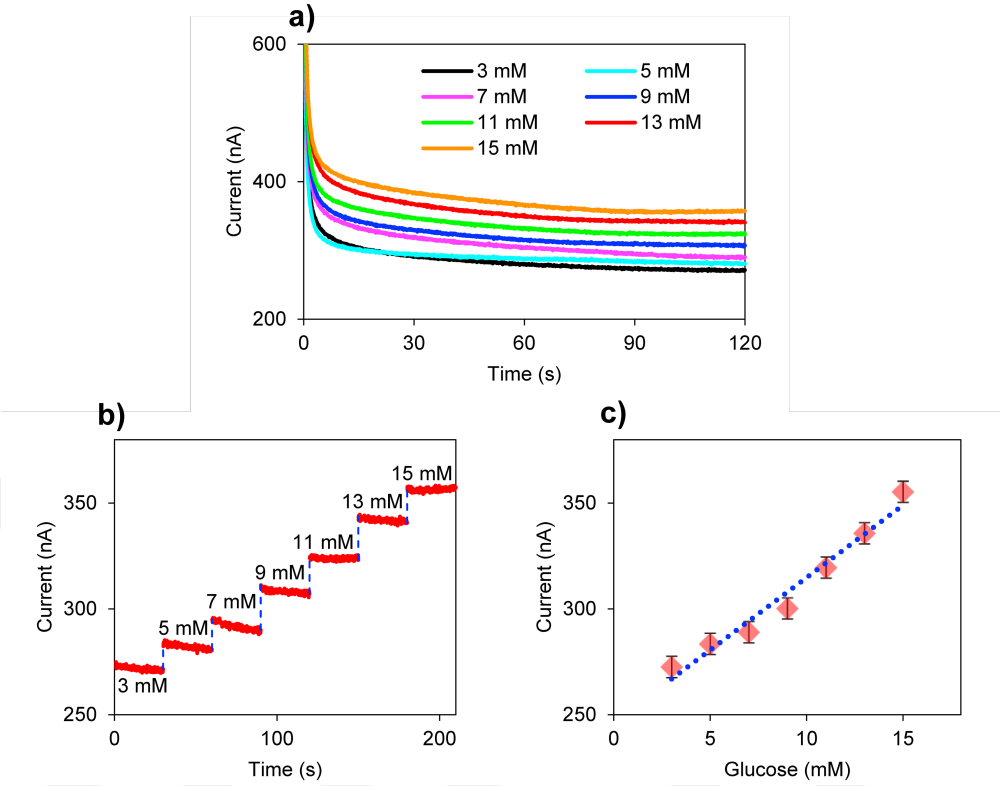


Figure 2.23. Experimental characterization of the glucose sensor at high concentrations. **(a)** Chronoamperometry response of the glucose sensor to increasing concentrations of glucose in artificial ISF from 3 to 15 in 2 mM increments. **(b)** I-t curve of the glucose sensor with stepwise addition of glucose into artificial ISF. **(c)** The Corresponding calibration curve (n=3). Data were expressed as the mean ± SD.

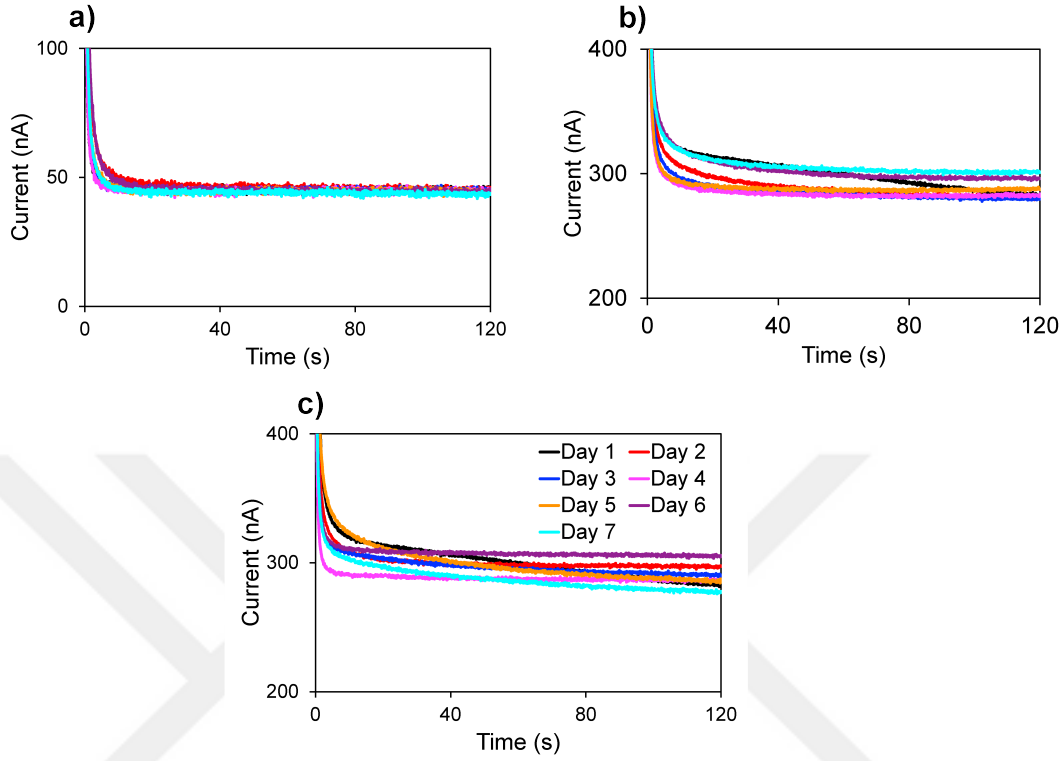


Figure 2.24. Characterization experiments to test the reproducibility and stability of the glucose sensor. Reproducibility of the glucose sensor at concentration of **(a)** 100 µM and **(b)** 5 mM (n=7). **(c)** Long term stability of the glucose sensor over 7 days for glucose concentration of 5 mM.

The response of the as-fabricated glucose electrode was examined with glucose solutions of different concentrations using the amperometric I-t method. To assess the sensitivity of the glucose sensor, first, the performance of the sensor was calibrated to the glucose concentration range between 20 µM and 1 mM. The measured current, which showed the representative amperometric response of the electrode to the different concentrations of glucose, increased with the addition of glucose (**Figure 2.22**). The sensitivity and limit of detection (LOD=3.3σ/S, where σ is the standard deviation of sensor response, and S is the slope of the calibration curve) of the electrode at low glucose concentrations (20–1000 µM) were 0.254 µA mM^{-1} and 5.6 µM, respectively. Subsequently, the sensor response was examined for glucose concertation ranging from 3 to 15 mM, relevant to the physiological glucose concentrations in ISF. As shown in **Figure 2.23a,b**, the measured sensor response increased with the addition of glucose, showing a linear trend with a correlation coefficient of 0.98, which could be further used to obtain the calibration curve (**Figure 2.23c**). The corresponding

sensitivity and LOD were calculated as 7.1 nA mM^{-1} and 0.2 mM, respectively. The results suggest that the glucose sensor could fulfill the requirements for glucose monitoring in a detection range that can cover normal glucose levels in human blood (around 4.4 to 6.6 mM) [223], which is practically the same as ISF glucose level. Reproducibility and stability experiments were also conducted to explore the detection consistency and storage stability of the glucose sensors. As depicted in **Figure 2.24a,b**, the relative standard deviation (RSD) of the measured current at glucose concentrations of 100 µM and 5 mM were 1.22% and 2.57%, respectively, indicating the reliable detection consistency of the sensors. Additionally, as shown in **Figure 2.24c**, a negligible deviation (RSD of 2.9%) was evidenced in the functionality of the sensors over a storage time of seven days, reflecting the robust enzyme immobilization.

For the pH sensor, the sensitivity, reproducibility, and stability tests were also performed. The sensitivity of the pH sensor was investigated by measuring the potential change at different pH levels. Since the VIES device will be used for pH monitoring of ISF, the measurements were carried out in an artificial ISF solution, which was prepared according to the procedures provided in the literature [215]. **Figure 2.25a** shows the potentiometric plot obtained by CHI660E electrochemical workstation for pH values in the range of 7.17 to 8.19, which was relevant to the physiological pH levels of ISF [224], [225]. The pH sensor exhibited a linear response of 50.38 mV pH^{-1} with a correlation coefficient and maximum RSD value of 0.98 and 9.07%, respectively, in three complete cycles of pH between 7.17–8.19 (**Figure 2.25b**). Because of the importance of the reversibility in potentiometric sensors, the cyclic response of the pH sensor was also examined for a broader range of pH values between 6.94–9.23. The results revealed good reversibility behavior with an average RSD value of 7.54% (**Figure 2.25c**). Besides, the sensors were exposed to various pH levels of between 6.94–9.23 in a staircase manner to explore the effect of abrupt pH change on the sensor performance. As shown in **Figure 2.26a,b**, the large pH variations had an effect on the continuous sensor response with a minimal deviation of 8.04%, and the pH of ISF can be reliably monitored using the sensor.

Moreover, the long-term stability of the pH sensor was investigated in artificial ISF solution by performing two experiments: daily recording of potential for seven days as the

storage time and continuous OCP readout for 1 hour (**Figure 2.26c,d**). The results indicated sufficient long-term stability (RSD of 0.9%) of the pH sensor.

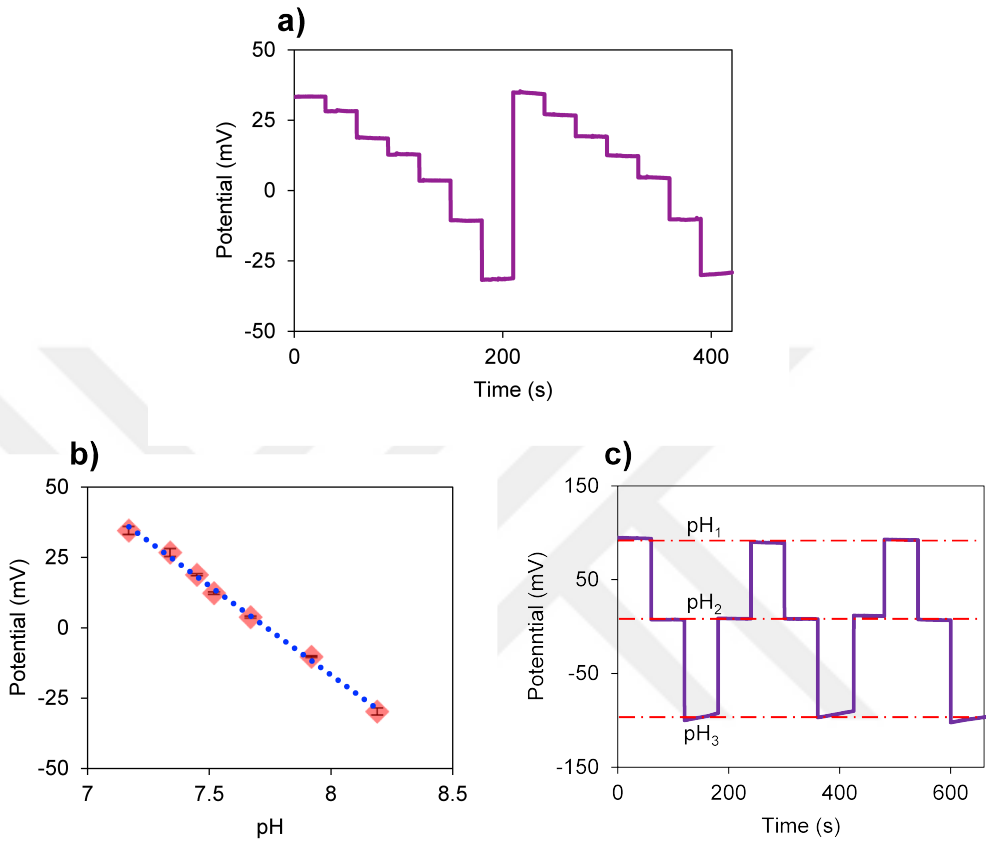


Figure 2.25. In vitro characterization of the pH sensor. **(a)** The open circuit response (OCP) measured for the pH sensor at pH levels in the range of 7.17–8.19 in artificial ISF. **(b)** The corresponding calibration curve (n=3). **(c)** OCP response of the pH sensor in the reversibility test at pH levels of pH_1=6.94, pH_2=7.52, and pH_3=9.23 in artificial ISF. Data were expressed as the mean ± SD.

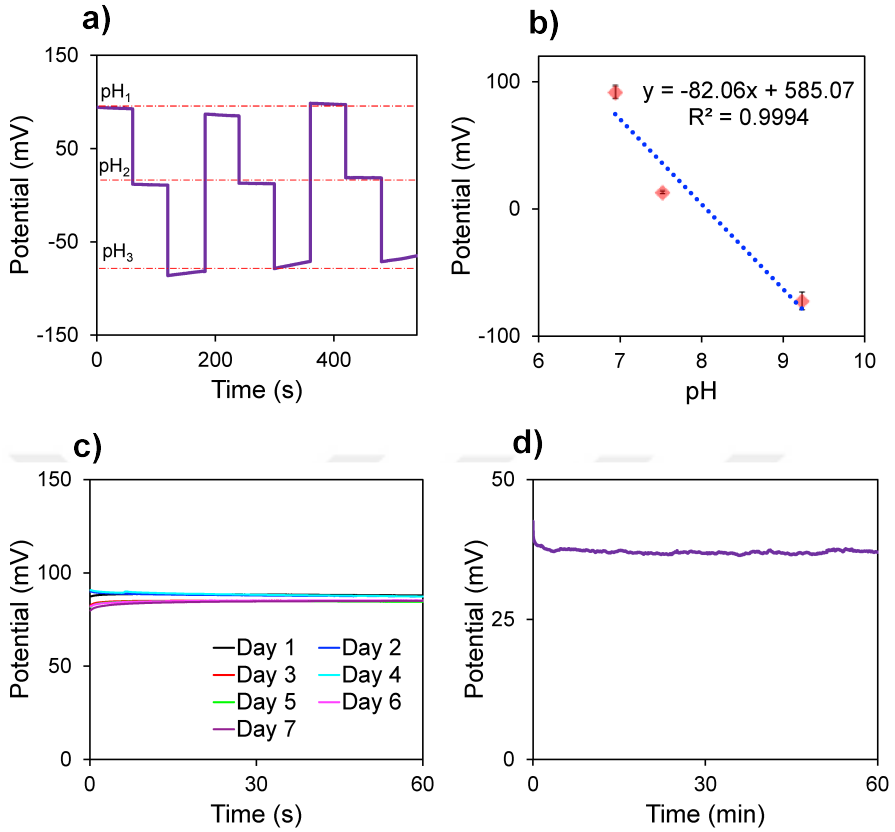


Figure 2.26. Potentiometric responses of the pH sensor against abrupt changes and stability study. **(a)** The open circuit response (OCP) measured for the pH sensor at pH levels of pH_1=6.94, pH_2=7.52, and pH_3=9.23 in artificial ISF. **(b)** The corresponding calibration curve (n=3). Long term stability of the pH sensor for **(c)** 7 days and **(d)** 1 hour.

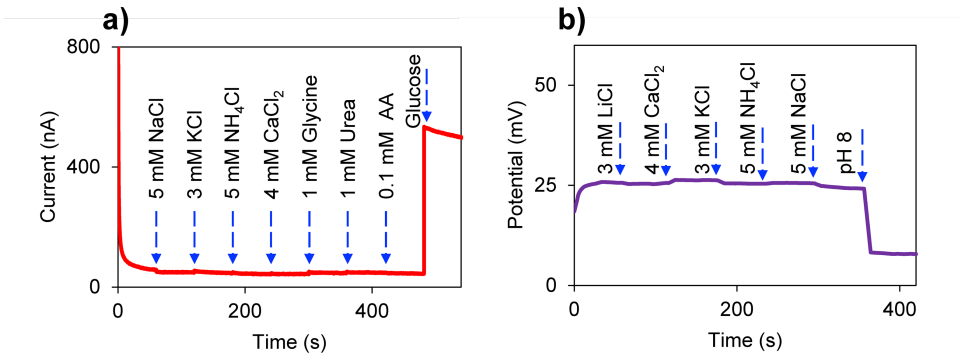


Figure 2.27. Selectivity performance of the electrochemical against different interferents. **(a)** Responsive current of the glucose sensor in the presence of various interferents. **(b)** Selectivity study of the pH sensor performed in artificial ISF in the presence of possible interferents.

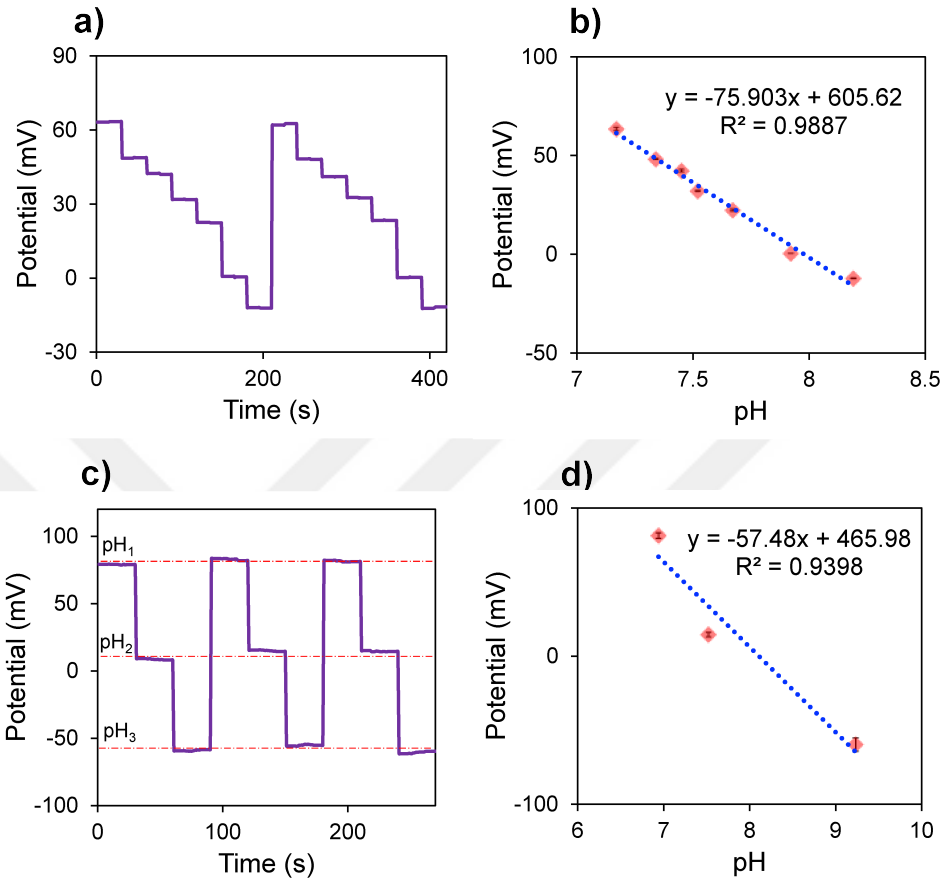


Figure 2.28. In vitro characterization of the pH sensor using the developed electronic board. **(a)** The OCP response measured by the electronic board for the pH sensor at pH levels in the range of 7.17–8.19 in artificial ISF. **(b)** The corresponding calibration curve (n=3). **(c)** The OCP measured by the electronic board for the pH sensor at pH levels of pH_1=6.94, pH_2=7.52, and pH_3=9.23 in artificial ISF. **(d)** The corresponding calibration curve (n=3). Data were expressed as the mean ± SD.

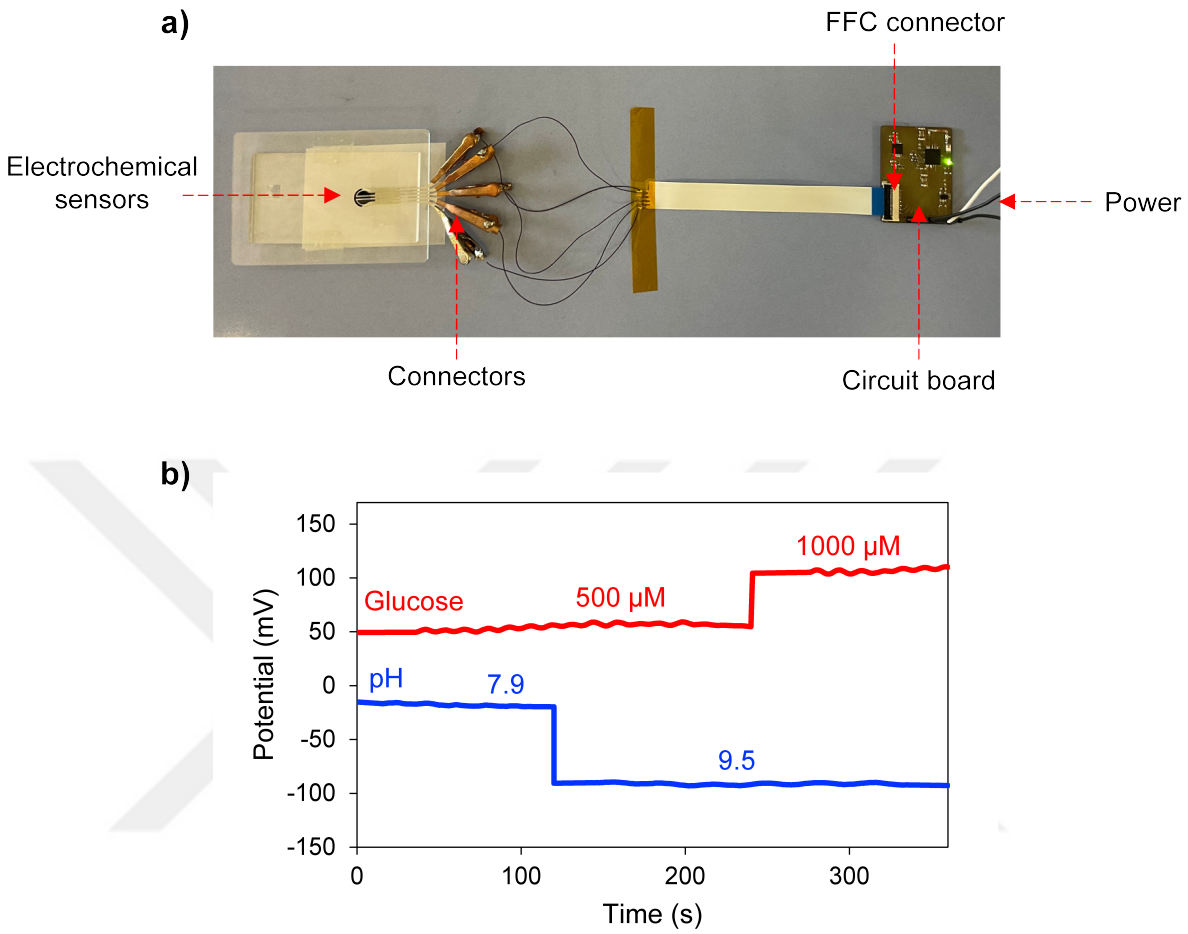


Figure 2.29. Interference investigation of simultaneous data recording using the developed system. **(a)** Experimental setup for simultaneous reading of glucose and pH levels. **(b)** System-level interference examination of the sensor array.

Because of the presence of different ions and interferents in ISF, the selectivity of sensors is critical. As evidenced by the results presented in **Figure 2.27a**, the target interferents caused a negligible effect on the response of the glucose sensor, which demonstrates the high anti-interference capability of the sensor. The selectivity studies of the pH sensor (**Figure 2.27b**) revealed that the maximum interference signal caused by the addition of interferents corresponds to only about 0.045 in pH change, which is considerably smaller than the sensor response to pH values in the range of 7–8. This suggests the selective response of the sensor to pH variations, making it feasible for continuous pH monitoring in ISF. Finally, the performance of pH electrodes was tested using the developed electronic board to obtain the required calibration curve and compare the results with benchtop measurements (**Figure 2.28**). Moreover, the amperometry AFE circuit was electrically separated from the

potentiometry circuit, resulting in the elimination of the current interference from the amperometry to the potentiometry channel (**Figure 2.29**). Overall, the in vitro characterization results revealed the satisfactory detection properties of the hybrid electrodes for both glucose and pH sensing.

2.3.5 Ex vivo evaluation of VIES system in ISF extraction and electrochemical sensing

Before conducting the in vivo experiments, the characterization of the VIES system in ISF extraction and sensing was extended by using ex vivo skin models that mimic the envisioned scenarios of ISF collection and biosensing. **Figure 2.30a** presents a schematic illustration of the experimental setup used for ex vivo tests. To evaluate the ISF extraction capability of the VIES system, the HMN patch was pressed against fresh skin samples (**Figure 2.8a,c**), and a filter paper stained with blue dye was placed in the microfluidic chamber to facilitate visualization, while the pressure inside vacuum generation system was monitored using the dedicated pressure sensors (**Figure 2.31**).

As demonstrated in **Figure 2.30b**, in the first 10 min almost no liquid has entered the microfluidic chamber. After about 17 minutes, the ISF started to flow through the microchannels in the needles towards the chamber. The delay in the ISF flow through the microchannels stems from the hydrophobic nature of PC-based MNs [226]. This issue can be partly resolved by plasma treatment, which leads to a reduction in contact angle. However, the main problem with this method is the hydrophobic recovery of the polymer over time, rendering this approach ineffective for continuous monitoring devices and devices with storage time before use [154]. Also, using hydrophilic material like glass, silicon, and metal might cause problems such as breakage and vacuum leakage [212]. Under vacuum conditions, and because of the absence of ISF negative pressure during ex vivo experiments, the ISF can easily flow through the HMNs after overcoming the hydrodynamic resistance originated from the hydrophobicity of channels. As shown in **Figure 2.30b(iii–v)**, the microfluidic chamber was almost filled within ~4 minutes after the extraction inception.

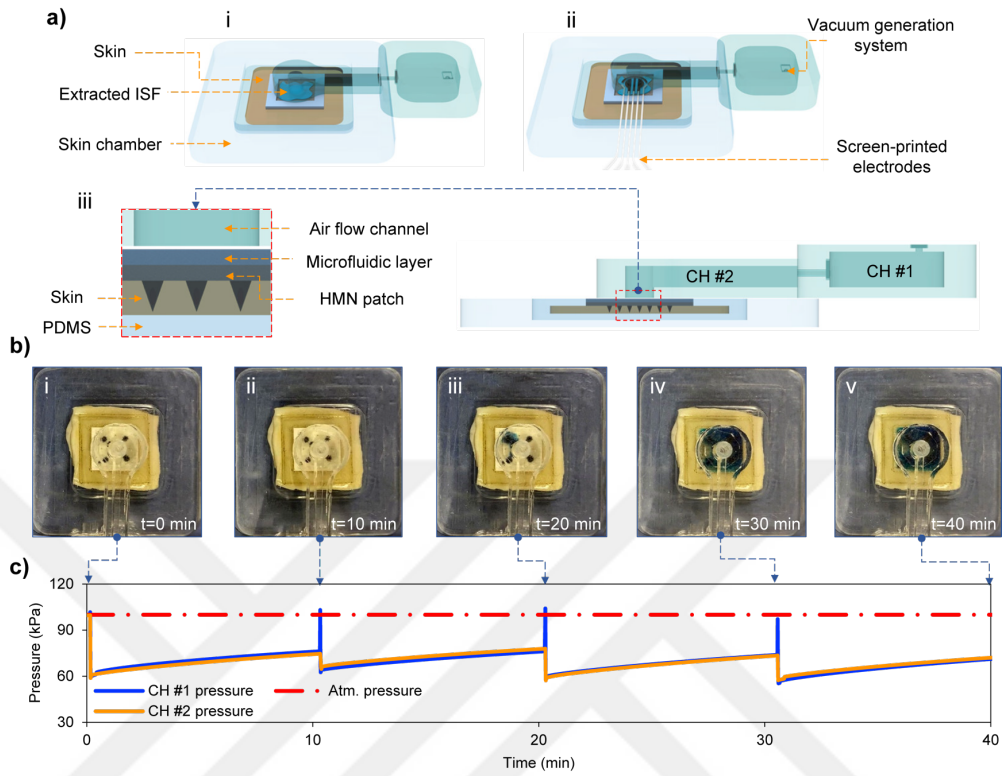


Figure 2.30. Ex vivo characterization of the VIES system. **(a)** Schematic illustration of the experimental setup for ex vivo evaluation of (i) ISF extraction and (ii) glucose and pH sensing, and (iii) cross-sectional view of the VIES system. **(b)** Photographic images demonstrating ISF sampling during ex vivo experiments using a blue dye. The VIES system was attached to fresh skin samples. **(c)** The corresponding pressure profiles inside the VIES system over time.

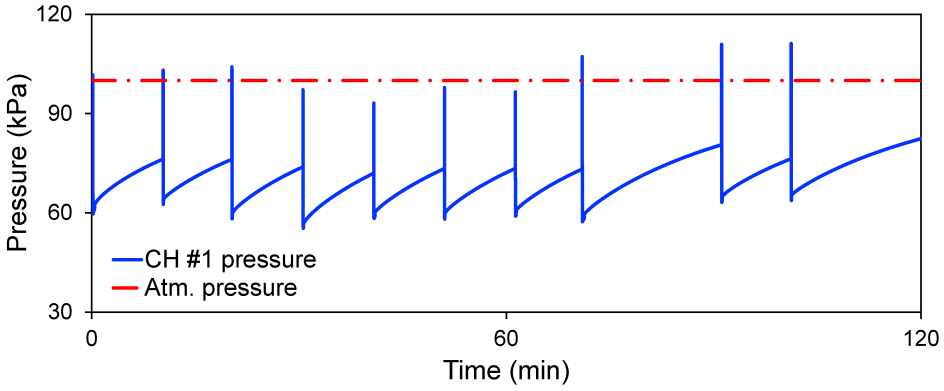


Figure 2.31. Pressure profile of the vacuum generation chamber during ex vivo ISF extraction experiment.

The pressure profiles inside CH #1 and CH #2 can be found in **Figure 2.30c**. The vacuum generation chamber was pressed every 10 min to demonstrate the capability of the VIES system in recovering the desired vacuum pressure during ISF extraction. The device also showed acceptable performance in maintaining the generated vacuum over long periods (**Figure 2.32**). According to **Figure 2.32a,b**, for CH #1, the average starting absolute pressure (n=3) after pressing was 54 ± 1.67 kPa, while this value was 54.221 ± 1.69 kPa for CH #2. After 1 hour, the absolute pressure inside CH #1 and CH #2 reached 72.14 ± 0.48 kPa and 72.12 ± 0.49 kPa (no significant difference, P=0.41), respectively, showing vacuum drop of 18.13 ± 1.25 and 17.9 ± 1.24 kPa for CH #1 and CH #2, respectively. The results suggest that similar initial vacuum pressure and vacuum drop over long periods can be expected inside the device. Moreover, as shown in **Figure 2.32c,d**, after 4 hours, the average pressure inside both CH #1 and CH #2 did not show any significant difference (P=0.42) (87.11 ± 0.37 kPa and 87.1 ±0.38 kPa, respectively) and have not reached 90 kPa yet. Although the ISF collection rate at this vacuum pressure would be much lower, it might meet the ISF turnover rate in the dermis over long periods. Therefore, the utilized device for ex vivo and in vivo experiments, could successfully extract and sense ISF for hours with just one push of a finger.

We further characterized the required force to achieve different vacuum levels inside the VIES device (**Figure 2.33**). **Figure 2.33b** gives the pressure drop (vacuum generation) in CH #1 for different compressive forces. The pressure dropped from 100 kPa (assuming the initial pressure was 100 kPa) to about 96.74, 93.59, 91.05, 89.24, and 86.75 kPa, for applied compressive forces of 2, 4, 6, 8, and 10 N, respectively. These results suggest that by a compressive force as low as 6 N, a 9 kPa vacuum can be generated in the device. Since it is already demonstrated that the device is capable of vacuum generation by successive pressing (**Figure 2.17** and **Figure 2.19**), there is no need to apply a force as large as 20 N to achieve the required vacuum pressure, and the desired vacuum pressure could be achieved by successive application of small forces. Moreover, the results presented in **Figure 2.33c** revealed that the fabricated devices showed similar force-displacement behavior under different forces.

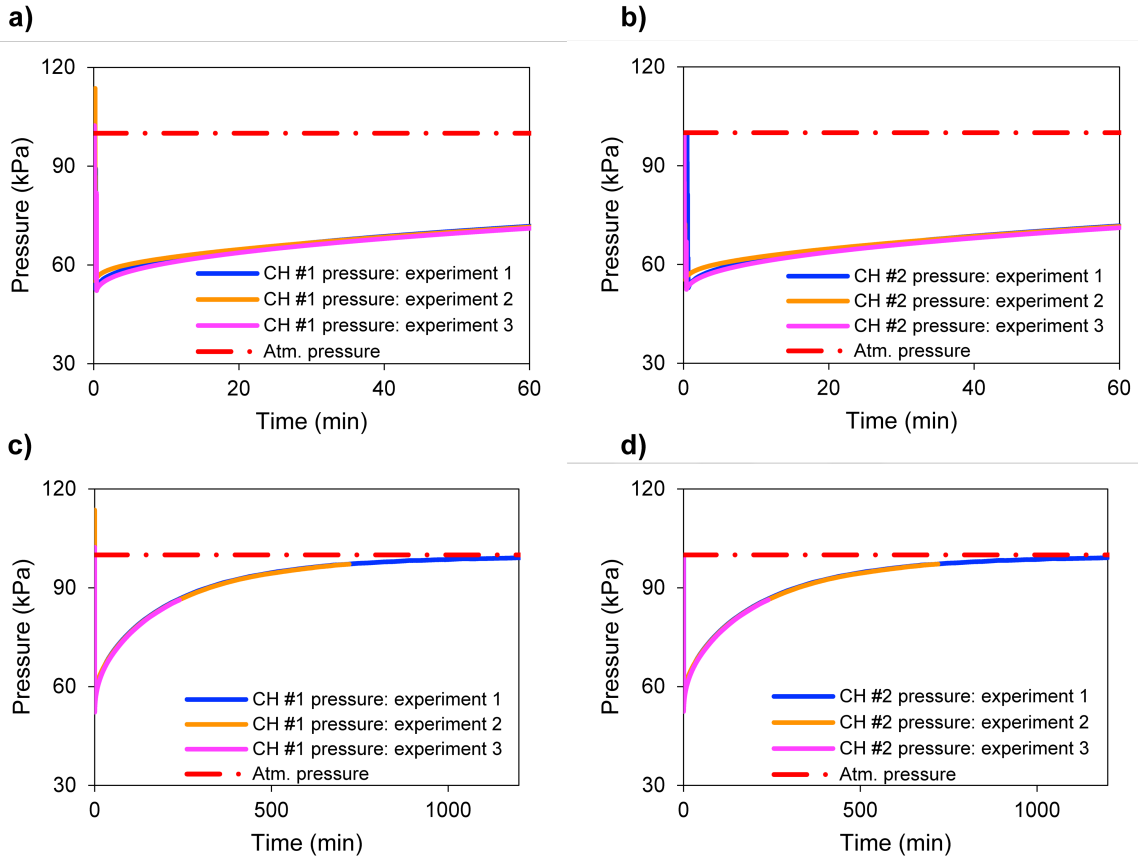


Figure 2.32. Characterization of vacuum drop inside the VIES device used for ex vivo and in vivo experiments. Pressure profiles of vacuum generation chamber (CH #1) and ISF extraction chamber (CH #2) were recorded simultaneously. Three replicates of the same experiment were performed to demonstrate the reproducibility of the same vacuum pressure by the device and similar vacuum drops over time. Pressure profiles inside **(a)** CH #1 and **(b)** CH #2 over 1 hour. Pressure profiles inside **(c)** CH #1 and **(d)** CH #2 over 4–20 hours.

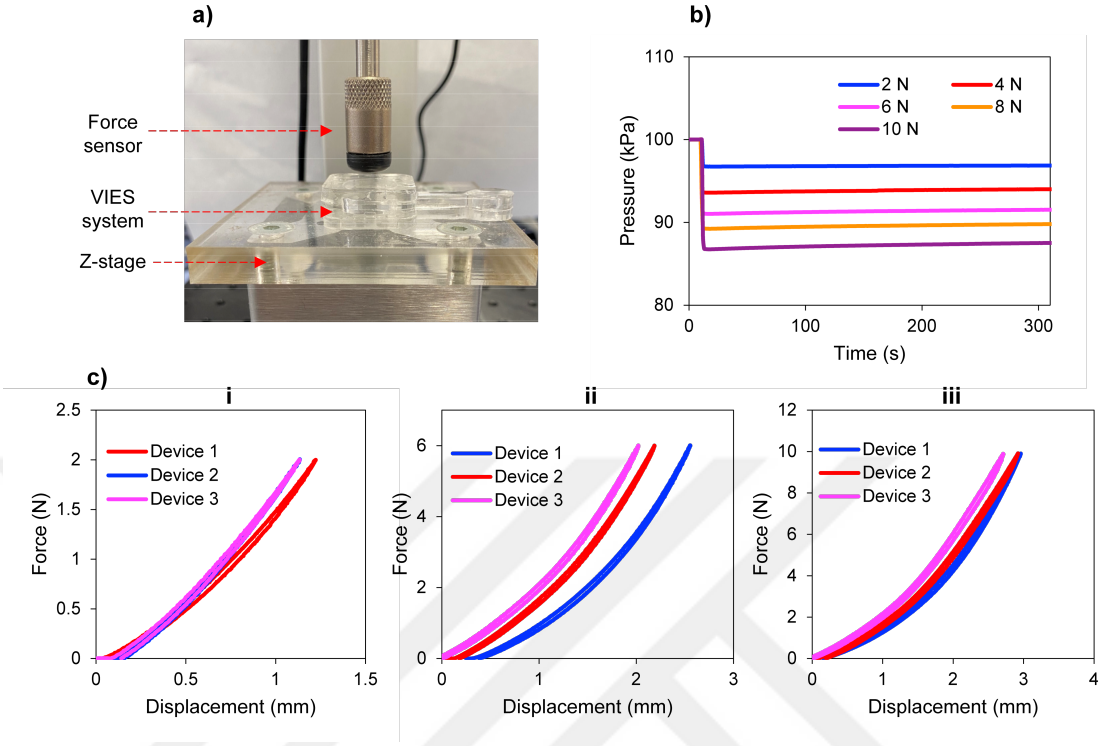


Figure 2.33. Measuring the required force to generate different vacuum levels in the VIES system used for ex vivo and in vivo experiments. **(a)** Image of the experimental setup used for the measurement of applied compressive force. **(b)** Pressure decrease in the device corresponding to different compressive forces. **(c)** Force-displacement curves for three VIES systems of the same dimensions. Compressive forces of (i) 2 N, (ii) 6 N, and (iii) 10 N.

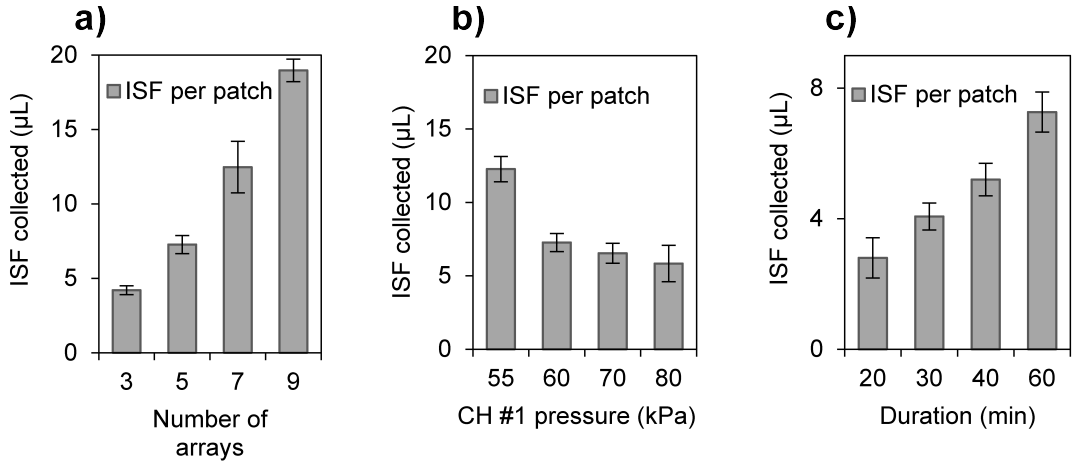


Figure 2.34. ISF extraction from skin samples to investigate the effect of different parameters. Effect of **(a)** array size, **(b)** chamber pressure, and **(c)** duration on the amount of collected ISF. HMN patches of 5×5 were selected to examine the effect of vacuum pressure and extraction duration. Data were expressed as the mean ± SD.

Although some studies have tried to characterize ISF extraction using different MNs [48], [134], [208], [220], [227], to the best of our knowledge, a parametric study on ISF collection using vacuum-integrated HMNs is yet to be performed. Here, the influence of needle array size, vacuum pressure, and sampling duration on the amount of ISF extraction was studied. To investigate the effect of needle array size on ISF collection, four HMN patches with array sizes of 3×3, 5×5, 7×7, and 9×9 were pressed on the skin samples with the same size, while the average pressure inside CH #1 was approximately 60 kPa (-40 kPa vacuum pressure), and the ISF extraction was performed for 1 hour. The varying number of HMN arrays from 3×3 to 9×9 increased the volume of collected ISF in rough proportion to the number of HMNs (correlation coefficient of 0.964). Increasing the vacuum pressure from -20 kPa to -45 kPa caused a significant increase ($P < 0.01$) in ISF collection. Changing the vacuum pressure in CH #1 from -20 kPa to -45 kPa yielded a more than 2-fold enlargement in the amount of collected ISF. Finally, different collection durations of 20, 30, 40, and 60 min were tested to examine the effect of sampling time on the extracted ISF volume. It was understood that there was a linear relationship between the collected ISF and sampling time, which is consistent with previous studies [48], [208]. Examination of the influence of different parameters on ISF extraction allowed us to choose the right conditions for in vivo experiments.

For ex vivo characterization of the sensing system, screen-printed electrodes were integrated into the HMN patches, followed by pressing onto the skin samples, which were soaked in artificial ISF solutions with varying values of glucose or pH level to an equilibrated state (**Figure 2.8b,d, and e**). The results of glucose sensor performance are given in **Figure 2.35a,b**. The electrochemical sensor showed a well-defined response to the glucose in ISF with a correlation coefficient of 0.99. The corresponding calibration curve was used to obtain the glucose concentration during in vivo experiments. For the pH sensing experiments, the same procedure as glucose tests was implemented. The characterization results were in good agreement with the in vitro experiments (**Figure 2.35c**). The pH sensor showed a linear response with a high correlation coefficient of 0.999. The resulting calibration curve (**Figure 2.35d**) was used to extract the pH data from the OCP response of the pH sensor during in vivo experiments.

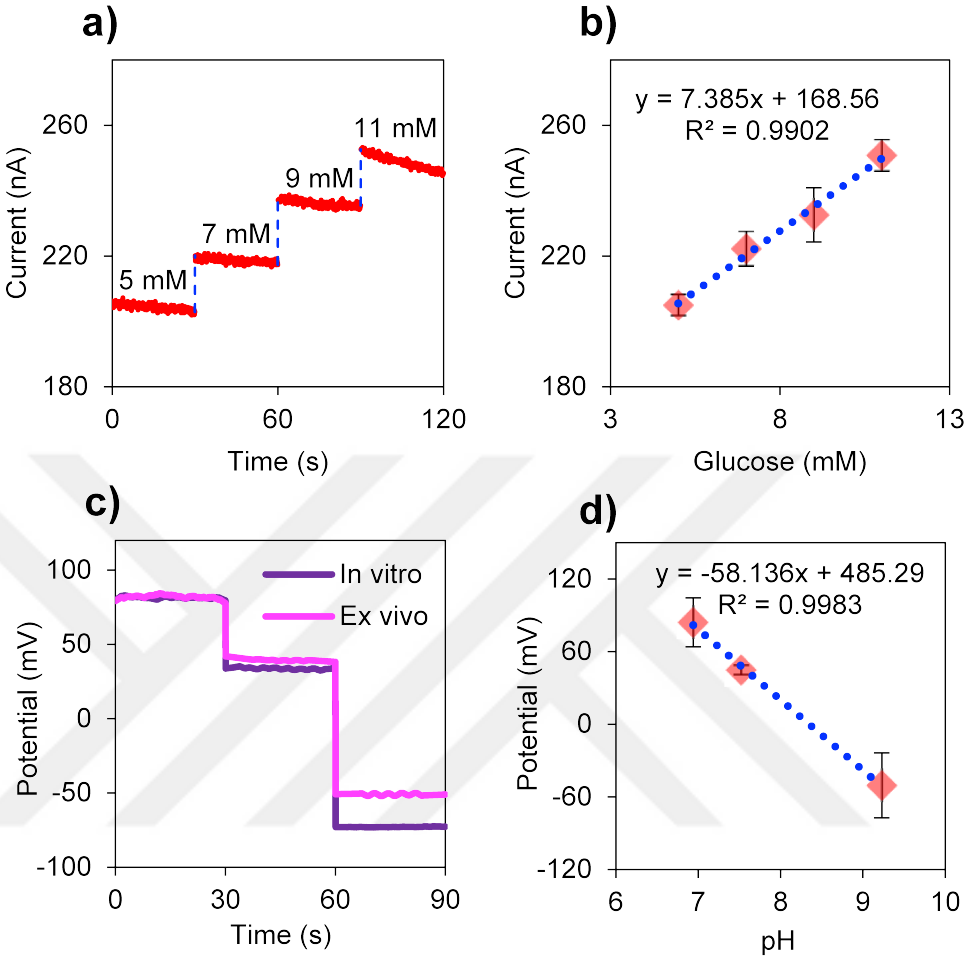


Figure 2.35. Ex vivo characterization of the electrochemical sensors. **(a)** I-t curve of the glucose sensor during ex vivo experiments. **(b)** The Corresponding calibration curve (n=3). **(c)** OCP response of the pH sensor to pH values of pH_1=6.94, pH_2=7.52, and pH_3=9.23. **(d)** The corresponding calibration curve. Data were expressed as the mean ± SD.

2.3.6 Integration of VIES and in vivo studies

Prior to conducting the in vivo extraction and sensing experiments, the effective penetration of HMNs and skin recovery post-treatment was studied. Wistar rats were used as the animal models with HMN patch administration on their dorsal side. As confirmed by the hematoxylin and eosin (H&E) staining (**Figure 2.14**), the PC-based HMNs efficiently penetrated the skin layers, with no visible inflammatory response around the micropores compared to the control sample. Also, as shown in **Figure 2.14** and **Figure 2.36**, the HMN punctures gradually disappeared over time as the skin recovered within 30 minutes. In

addition, no significant inflammation was observed 5 days after HMNs removal in the skin tissue administered with the HMN patches from the H&E staining results (**Figure 2.37**).

Next, a similar procedure with the same vacuum generation system and HMN patches of similar array sizes to the ex vivo experiments was implemented to conduct the in vivo experiments. First, the effect of number of HMNs, vacuum pressure, and extraction duration on the amount of collected ISF from rat models was examined, followed by amperometric and potentiometric sensing of glucose and pH levels in the rats using the developed VIES device. The developed flexible PCB was integrated into the device for data transmission via Bluetooth to an electronic device.

The HMN patch without screen-printed electrodes was deployed to investigate the extraction capability of the developed VIES system from the animal models (**Figure 2.38a**). As depicted in **Figure 2.38b,c**, and similar to ex vivo experiments, the rate of ISF extraction is very low in the beginning, because of the hydrophobic nature of the polymeric microchannel. After about 16 min, the vacuum pressure overcame the hydrophobic pressure barrier, and ISF started to flow into the microfluidic chamber at an increased rate. Unlike ex vivo experiments, in which the ISF filled the microfluidic chamber within a few minutes after extraction inception, it took longer to fill the chamber during in vivo experiments. This might be because of the existence of the negative pressure of ISF in live animal models, which acts as an extra resistance force against ISF extraction.

One of the challenges concerning vacuum-based ISF extraction is to prevent ISF samples from contamination with blood [32]. As can be seen in **Figure 2.38b,c**, no blood was observed in the collected ISF samples. According to previous studies, a delay in ISF extraction after vacuum administration could be beneficial to avoid blood contamination [32]. This suggests that the hydrophobic nature of the polymeric microchannels was beneficial to prevent the mixing of ISF samples with blood.

The parametric experiments showed similar results on the amount of collected ISF for different scenarios. At a vacuum pressure of -40 kPa, the amount of collected ISF per patch increased by increasing the array size (**Figure 2.39a**). The higher array size leads to extra applied pressure on the skin, which is beneficial for ISF extraction. As shown in **Figure 2.39b** Decreasing the vacuum pressure from -45 kPa to -30 kPa led to a reduction in collected ISF by almost 33%. However, at a vacuum pressure of -20 kPa, the amount of extracted ISF was

very low (1.16 ± 0.49 µL). This suggests that a minimum vacuum pressure is always needed to overcome the resistance forces against ISF extraction, which is consistent with the previous studies [32], [208]. As expected, the amount of collected ISF raised with increasing the extraction duration (**Figure 2.39c**). The collected ISF was 1.13 ± 0.26 µL after 20 min, while it increased to 5.9 ± 1.22 µL after 1 hour ($P<0.05$).

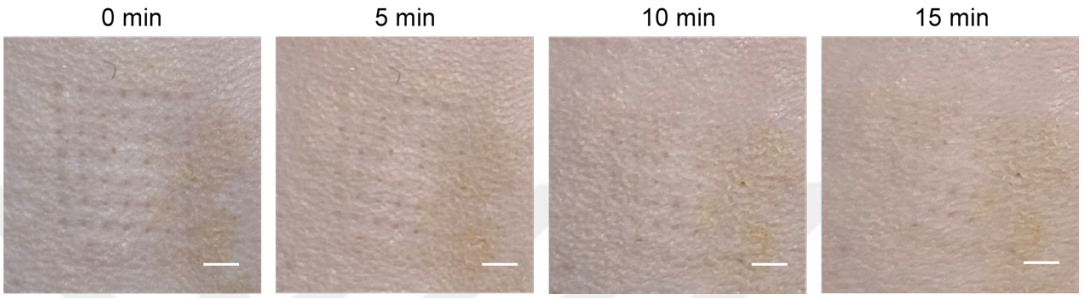


Figure 2.36. Images of skin recovery after peeling off the HMN patch. Scale bar is 2 mm.

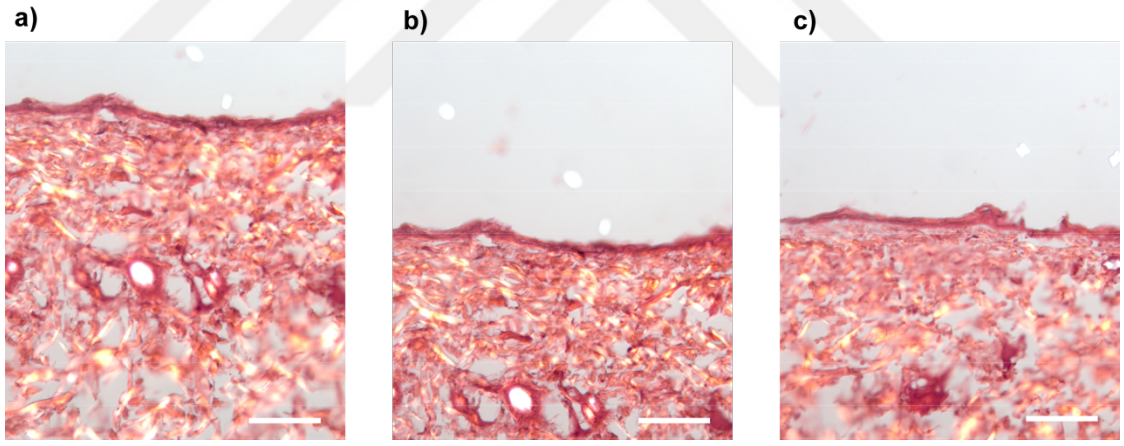


Figure 2.37. H&E-stained sections of rat skin 5 days after HMN patch removal. **(a)** Rat #1. **(b)** Rat #2. **(c)** Control (scale bar: 100 µm).

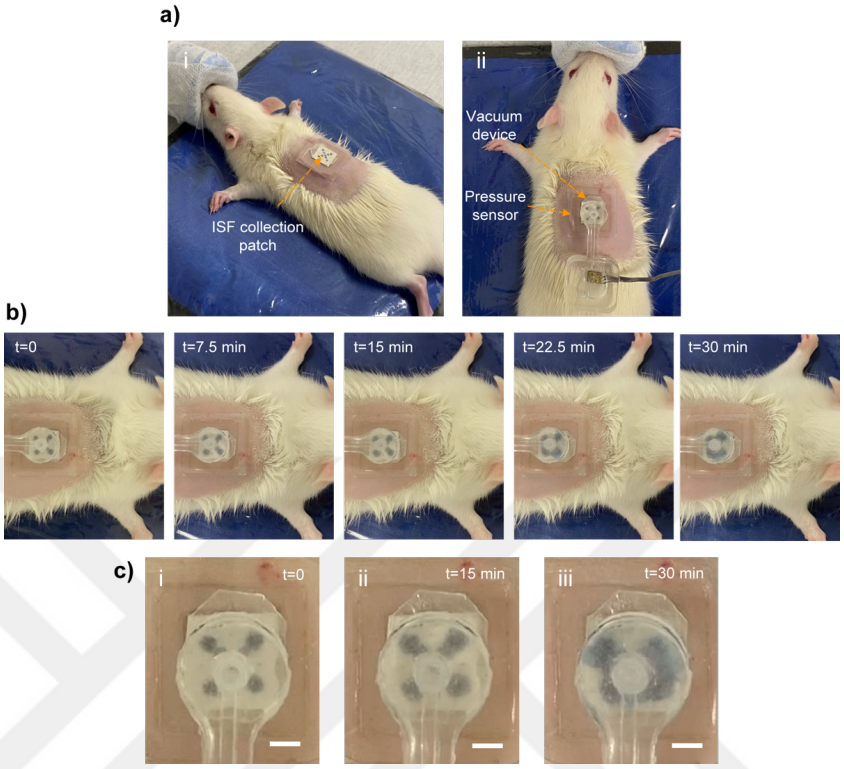


Figure 2.38. In vivo ISF collection and sensing performance of the HMN-based VIES system. **(a)** Optical images showing the administration of HMN-integrated patch on the back of rat (i) without and (ii) with the vacuum generation system. **(b)** In vivo ISF collection by the HMN-based VIES system over time. **(c)** Close-up images of extracted ISF at (i) t=0, (ii) t=15 min, and (iii) t=30 min (scale bar: 1 mm).

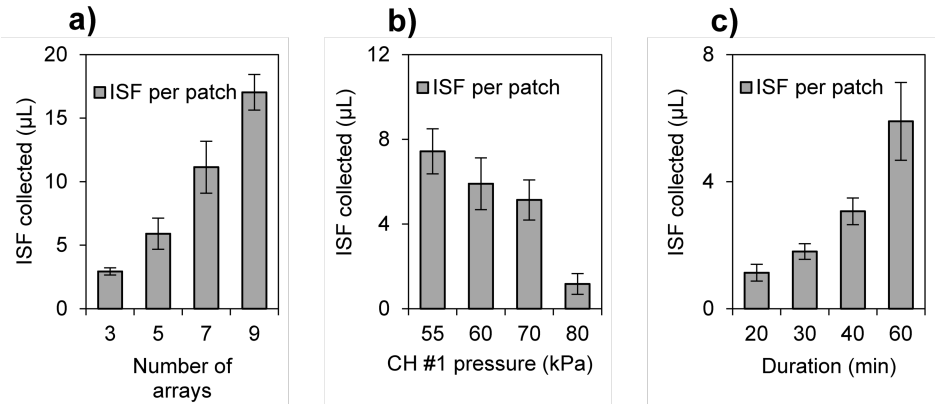


Figure 2.39. ISF extraction in vivo to investigate the effect of different parameters. Effect of **(a)** array size, **(b)** chamber pressure, and **(c)** duration on the amount of collected ISF. HMN patches of 5×5 were selected to examine the effect of vacuum pressure and extraction duration. Data were expressed as the mean ± SD.

By comparing the data presented in **Figure 2.34** and **Figure 2.39**, corresponding to ex vivo and in vivo experiments, respectively, a decrease can be seen in the rate of ISF collection for in vivo experiments. For instance, at vacuum pressure of 40 kPa (CH #1 pressure of 60 kPa) the average ISF collection rate was 7.26 ± 0.61 µL per hour for ex vivo experiments, while the corresponding collection rate was 5.9 ± 1.22 µL per hour during in vivo experiments, which shows 18.6% decrease in the collection rate. This indicates although there was a drop in the amount of collected ISF during in vivo experiments, the reduction was not significant (P=0.2). One reason for this could be recording the ISF collection rates over one hour. We were interested in ISF sampling in longer periods, because the VIES system was designed in a way to enable continuous sensing of ISF through the sampled ISF. However, the ISF turnover rate is about 60 nL min^{-1} cm^{-2} (3.5 µL h^{-1} cm^{-2}) [3], which suggests with higher ISF collection rate, as reported for hydrogel-based MNs, the ISF in the dermis might not be properly refreshed for continuous sampling of ISF.

Among the different methods of ISF collection, hydrogel-based MNs have shown excellent performance in ISF extraction within a few minutes (**Table 2.2**) [20], [76], [227]–[231]. For instance, in the study of Al Sulaiman et al., they were able to collect 6.5 µL within 2 min [20]. The problem with hydrogel-based MNs is their limited extraction capacity because of saturation. For example, although the MN patch of Al Sulaiman et al. showed high ISF collection rate (3.25 µL min^{-1}), their MN patch could not extract more than 6.5 µL. According to the data presented in **Table 2.2**, vacuum-based systems (suction blisters) have shown the best capability in extracting high volumes of ISF (≥50 µL h^{-1}) [228]–[230]. In our study, the ISF collection rate of up to 17.03 ± 1.40 µL h^{-1} was achieved. This collection rate easily overcomes the collection rates of most hydrogel-based systems over long periods (i.e., ≥30 min). Although the ISF collection rate of suction blisters are much larger compared to this work, they are not suitable for monitoring systems as the ISF turnover in skin is much slower. According to **Figure 2.39a**, there was a linear relationship between the array size and collected ISF, with a correlation coefficient of 0.99. Based on the results, by increasing the array size to 20×20, the ISF collection rate would be larger than 50 µL h^{-1}, which is comparable to the collection rates of suction blisters. However, this volume of collected ISF might only be useful for only special applications and long-term monitoring purposes, where the ISF turnover rate plays an important role.

Table 2.2. Summary table of some recent studies on ISF extraction and sensing.

Extraction Mechanism	Test Subject	ISF Collection Rate	Application	Ref.
Iontophoretic	Ex vivo: Rabbit skin In vivo: SD rat	Not reported	Continuous glucose monitoring	[34]
	Ex vivo: Pig skin	40 μL cm^{-2} h^{-1}	Analysis of molecular transport	[42]
	Ex vivo: Pig skin In vivo: Rat	Not reported	Continuous glucose monitoring	[232]
	Human Participants	Not reported	Continuous glucose monitoring	[233]
	Human Participants	Not reported	Continuous glucose monitoring	[234]
Needle and pressure	Human Participants	3.2 μL	Non-continuous glucose measuring	[235]
	Human Participants	1.1 μL within minutes	Measurement of small molecules, SARS-CoV-2 antibodies, and protein	[72]
Capillary action	Rat	1.41 mg	Detection of Cystatin-C	[236]
	Agarose gel	0.667 μL min^{-1}	-	[67]
	SD rats	0.72 ± 0.1 mg min^{-1}	Non-continuous glucose measuring	[237]
	In vitro: Agarose gel Ex vivo: Pig skin	Not reported	-	[238]
	Human participants	Not reported	Continuous glucose monitoring	[113]
	Ex vivo: Pig skin	Not reported	-	[50]
	Standard solutions	1 μL s^{-1}	Real-time glucose measurement	[55]
	Ex vivo: pig skin In vivo: Wistar rats	2 μL within 1 min	-	[134]
Swelling hydrogel	Rat	0.84 ± 0.24 mg h^{-1}	-	[239]
	Ex vivo: Pig skin In vivo: Rat and human participants	Not reported	Drug and glucose analysis	[240]
	In vitro: agarose gel In vivo: Rabbit	1.25 ± 0.37 mg within 10 min	Point-of-care testing of glucose, lactate, chlorine and BSA	[241]
	Agarose gel	3.5 ± 0.1 mg within 30 min	Non-continuous urea measuring	[222]
	In vitro: agarose gel In vivo: Wistar rat	2.5 mg within 10 min ~2.67 mg within 30 min	Non-continuous measurement of glucose and vancomycin	[220]
	In vitro: agarose gel In vivo: Rat	1.4 ± 0.3 mg within 1 min 2.3 ± 0.4 mg within 10 min	Non-continuous measurement of glucose and cholesterol	[76]
	In vitro: agarose gel In vivo: Rat	4.4 mg within 12 min	Non-continuous glucose monitoring	[231]
	Ex vivo: Pig skin In vivo: SD rat	6 μL within 10 min	Psoriasis microRNA biomarker analysis	[227]

			6.3 ± 0.6 μL within 45 min		
		Ex vivo: human abdominal skin	6.5 ± 0.2 μL within 2 min No extraction after that	Sensing of specific circulating nucleic acids	[20]
		Mouse	21.34 μL within 30 min	MicroRNA biomarker analysis	[242]
		Rat	Not reported	Non-continuous colorimetric analysis of pH, glucose, lactate, and cholesterol	[35]
		Ex vivo: Porcine skin In vivo: SD rat	Not reported	Continuous pH monitoring	[79]
Vacuum pressure	MNs	Ex vivo: Pig skin In vivo: Mouse	1.96 μL within 1 min 4.67 μL within 10 min	Non-continuous glucose monitoring	[208]
		Rat and human participants	2.3 ± 2.6 μL within 20 min	Analysis of different biomarkers	[32]
		Rat and human participants	2 μL within 15 min	Biomolecular analysis	[243]
		SD rat and human participants	1–10 μL within 2–10 min	Non-continuous glucose monitoring	[49]
	Suction blister	Human participants	Up to 2.6 ± 1.0 μL min^{-1}	Protein concentration	[244]
		Human participants	Not reported	-	[245]
		Human participants	210–700 μl within 2.5 h	Protein biomarkers	[228]
		Human participants	50-200 μL within 1.3 h	Inflammatory biomarkers	[229]
		Human participants	50 μL within 45 min	High resolution metabolics	[230]
	MNs	Ex vivo: Rat skin In vivo: Wistar rat	17.03 ± 1.40 μL h^{-1}	Continuous glucose and pH monitoring	This work

After ex vivo evaluation of the analytical performance of the VIES system, as a demonstration, we conducted in vivo experiments to assess the performance of the system on rats. **Figure 2.40a(i)** shows the developed FPCB board, which was used to record the data via Bluetooth. The VIES system was administered to shaved part of the rat with the FPCB board connected to the screen-printed electrodes (**Figure 2.40a(ii)**). In the first set of experiments, the detection of glucose in ISF using the VIES system was evaluated. The amperometric response of the glucose sensor was recorded and converted to the concentration of glucose according to the calibration curve obtained in the ex vivo experiments.

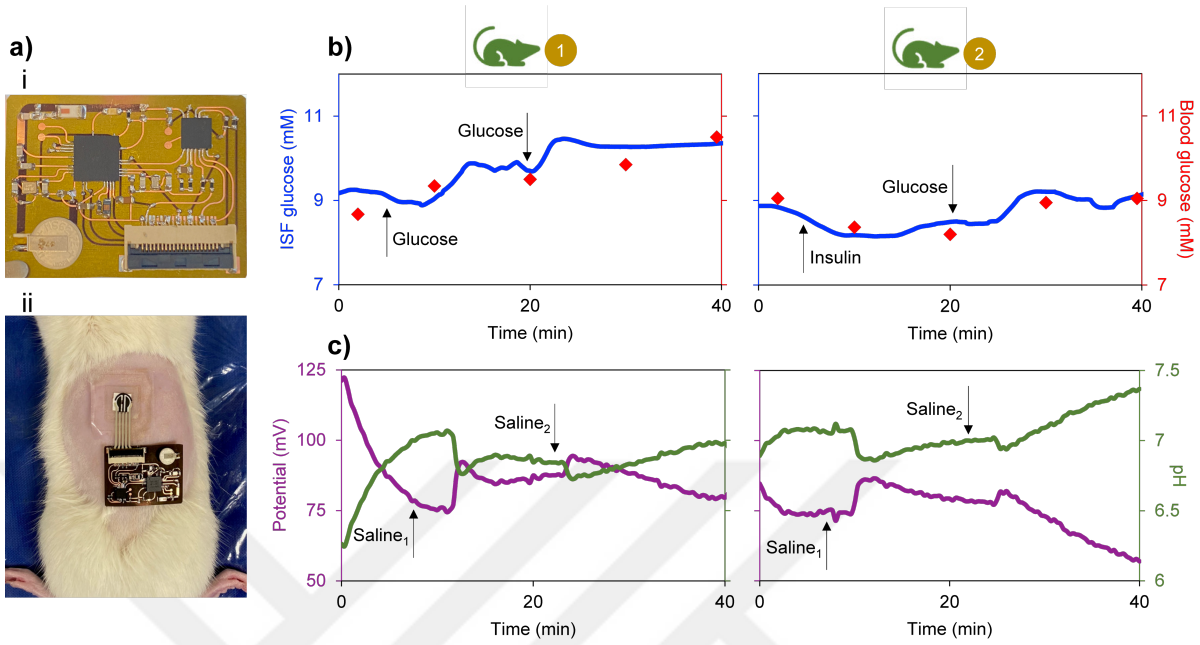


Figure 2.40. In vivo glucose and pH measurement using the VIES system. **(a)** (i) Optical image of the flexible PCB. (ii) Administration of the device on dorsal side of the rat for dynamic monitoring of glucose and pH. **(b)** Glucose sensor performance study on two Wistar rats throughout a 40-min period, during which they were injected with glucose and insulin solutions. **(c)** Dynamic potentiometric readouts of the pH sensor and the corresponding pH curves over a 40-min period on two Wistar rats. Two saline solutions with different pH values ($saline_1$: 6.5 and $saline_2$: 8.2) were injected to alter the ISF pH value.

Immediately after the extracted ISF came into contact with the whole sensor, the amperometric signal was recorded for 40 min for each rat. For the first rat, after 5 min of recording without any injection, the rat was injected intraperitoneally with 1 M glucose solution at time points t = 5 min and t = 20 min (indicated by the arrows in **Figure 2.40b**, left), to induce an increase in glucose levels of ISF. The blood glucose in the rats was also measured using a glucometer to examine the detection accuracy of the sensor. The patch was left on the rat skin for the whole 40 min. As depicted in **Figure 2.40b**, the glucose level in ISF was increased after glucose injection. Also, the dynamic response of the glucose sensor and blood glucose showed similar trends. For the second test, the rat was injected with insulin and 1 M glucose solution at time points t = 5 min and t = 20 min, respectively (**Figure 2.40b**, right). On the basis of the results, the glucose level was successfully detected using the VIES system in both rats.

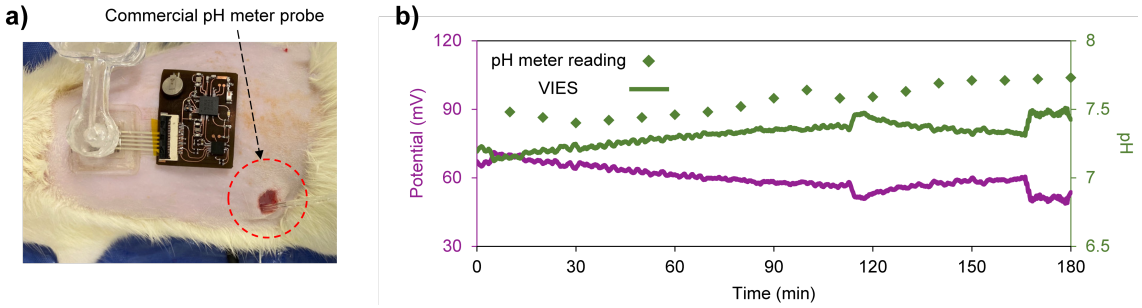


Figure 2.41. Continuous long-term in vivo investigation of the performance of pH sensor. **(a)** Optical image of administration of the flexible PCB on dorsal side of the rat and subcutaneous insertion of the commercial micro pH electrode (Orion 9826BN, micro pH electrode). **(b)** Validation of the pH measurement from the VIES device by comparing to the pH values measured by the commercial pH meter.

In the second set of experiments, the applicability of VIES system in measuring the pH level of ISF was evaluated. The pH levels in ISF were controlled by injection of saline solutions with pH values of 6.5 and 8.2 to induce the pH changes in ISF. The first 7 min of the recorded signal in **Figure 2.40c** belongs to the dermal ISF before any injection. The intraperitoneal injection of saline solutions resulted in a change in the potentiometric response of the pH sensor. The corresponding pH values were calculated using the calibration curve obtained in the ex vivo experiments. The measured pH values and behavior of the PANI-coated pH sensor were in good agreement with the previous studies.[53] Additionally, to validate the measured pH values by the VIES system, a commercial pH micro electrode was inserted subcutaneously on the dorsal side of the rat for pH reading (**Figure 2.41a**). The VIES system was able to track the pH levels in a similar profile with the commercial pH meter over a 3-hour period with a detection error of 3.18 ± 1.0% and RSD value of 4.13% (**Figure 2.41b**). This difference might be attributed to the distance between the VIES system and commercial pH probe. Overall, the in vivo results suggest that the VIES system could successfully detect the glucose and pH levels from the extracted ISF. **Table 2.2** provides a summary of some of the recent studies on continuous or non-continuous measurement of different biomarkers in ISF.

2.4 Conclusions

In this chapter, the development of a wearable vacuum-integrated ISF extraction and sensing (VIES) device for continuous collection of ISF using HMNs was demonstrated. We fabricated a laser-drilled polymeric HMN patch that could easily pierce the skin and allow ISF extraction. The HMN patch is adhered to a microfluidic module that can accommodate the collected ISF, and provides the required contact for electrochemical sensing. The VIES system produces the vacuum pressure employing self-recovery feature of PDMS, which was used to fabricate the vacuum chamber. Characterization studies of the vacuum system revealed its ability to generate and maintain the adequate vacuum pressure for ISF sampling. Implementation of passive valves enabled gradual adjustment and recovery of the vacuum pressure over long periods. In vitro and ex vivo characterization of the integrated screen-printed electrodes confirmed the sensitivity, selectivity, and stability of the sensors to measure the glucose and pH levels in the extracted ISF. Our parametric study showed that increasing the number of HMNs and enhancing the vacuum pressure can greatly affect the amount of collected ISF. Successful application of the VIES system on rat models demonstrated that the device possess the ability to extract sufficient volumes of ISF with simple one touch activation by finger operation. We further experimented in vivo application of the VIES system to demonstrate the capability of the developed device in integration into wearables. Continuous monitoring of glucose and pH levels was achieved and the measurement data were transmitted to an electronic device using the custom-designed electronics. Our proposed device holds the potential for simple and easy-to-use ISF collection, and can pave the way for integration of vacuum powering into ISF-based wearables.

3 Chapter Three: 3D-Printed Multichannel Microneedle Platform for Extraction and Colorimetric Sensing of ISF

3.1 Introduction

Recent technological advancements have significantly transformed the health sector, particularly in the development of wearable health monitoring devices [203], [246]. Despite these advancements, diagnosis and monitoring mainly rely on blood analysis for biomolecular markers, whereas transdermal biosensing offers the potential to revolutionize healthcare by enabling real-time and continuous monitoring of key biomarkers in bodily fluids [3], [247]. Dermal interstitial fluid (ISF), originating from transcapillary blood exchange and constituting approximately 75% of extracellular fluid, shares a similar composition with blood. Moreover, ISF is the most abundant accessible fluid in the body and shares a high degree of biomarkers with plasma, thus holding a great potential to replace current blood-based diagnostic techniques [18], [32].

Although ISF is readily accessible throughout the skin, sampling it remains challenging due to its low volume in the dermis. Assuming 40% of the dermis consists of ISF, only 120 $\mu L/cm^2$ is accessible in the thickest regions of the dermis. Furthermore, another significant constraint to ISF extraction is its slow natural replenishment rate within the dermis. The high hydraulic resistance of the dermis further hinders fluid flow. It takes nearly 30 hours for the dermal ISF content to fully refresh [3], [16]. Several challenges associated with conventional ISF collection techniques remain unaddressed. For instance, ISF sampling using suction blisters and biopsy punches can cause discomfort, irritation, and skin damage, and the collected fluid may be contaminated with injury-related biomarkers, leading to distorted analyte concentration [245], [248], Microdialysis requires several hours to perform, causes tissue damage, and the membrane's permeability limits the range of collected analytes [249]. Reverse iontophoresis can only collect small molecules and requires frequent calibration. ISF dilution, considerable lag time, and contamination by sweat are other drawbacks of this method [250]. Therefore, there is a demand for new, simple techniques capable of rapidly

extracting adequate amounts of ISF (≥1 μL, sufficient for many assays), while minimizing tissue damage.

MNs—micron-sized needle arrays with lengths typically ranging from 50–2000 μm—[23], have garnered significant attention in various biomedical applications, including biomarker sensing, drug delivery, and tissue sampling [251]. Due to their short length compared hypodermic needles used in commercial continuous glucose monitoring devices (CGMs) (5–13 mm) [252] MNs can pierce the stratum corneum and reach the dermis layer without stimulating dermal nerves. Despite extensive research on implementing MNs for drug and vaccine delivery and in situ biomarker monitoring [253]–[256], studies employing extracted ISF for medical applications remain scarce [3], [18]. Recently, hydrogel-forming MNs have been widely used for ISF extraction owing to their superior water absorption and swelling capabilities [45], [96], [257], [258]. Although they extract ISF more rapidly than other techniques, hydrogel MNs become saturated upon reaching their maximum absorption capacity, rendering them less suited for continuous long-term health monitoring. In addition, some metabolites become entrapped in the hydrogel matrix, necessitating cumbersome extraction processes for analysis. Hollow and porous MNs are alternative types that leverage capillary forces for ISF extraction [42], [232], [259]. Some studies have integrated vacuum systems with HMNs to enhance their ISF extraction capability [47], [120], [121]. HMNs have demonstrated the ability to extract adequate amounts of ISF to enable various biomarker sensing techniques, including electrochemical, colorimetric, and optical methods [121], [161], [260]. However, since most HMNs are fabricated from polymeric materials (e.g., via 3D printing), the hydrophobic nature of the needle bores necessitates integrating a vacuum system to initiate and maintain a continuous flow [45]. Enhancing the wettability of MN channels to promote liquid movement via improved capillary action is highly desirable.

In recent years, the accuracy and flexibility of 3D printing technology have enabled the fabrication of MNs with complex structures [57], [261], reduced tip sizes [166], [262], and higher needle densities. In particular, HMNs have benefited from 3D printing advancements due to easy fabrication, increased number of channels per needle, and customizable channel designs [23]. Extensive research has focused on integrating 3D-printed HMNs into wearable health monitoring devices. Among various 3D printing techniques, (e.g., fused deposition modelling, stereolithography, selective laser sintering, digital light processing) several studies

have used projection micro-stereolithography (PμSL) to fabricate robust and intricate MNs for wearable platforms [83], [120], [127]. However, employing these MNs for effective ISF extraction from humans without external stimuli such as vacuum remains an unmet challenge. Therefore, developing a HMN patch that can passively extract adequate amounts of ISF from live tissues could offer significant advantages.

In this study, we develop a 3D-printed HMN patch with superhydrophilic microchannels to effectively collect dermal ISF for continuous biomarker sensing. Biocompatible conical MNs with various designs and dimensions are easily fabricated using PμSL. Depositing a hydrophilic silicone oxide (SiO_2) layer on the microchannel surface significantly enhances the wettability of MNs, resulting in improved capillary forces that enables passive liquid uptake. The 3D-printed MNs exhibit excellent mechanical performance against compressive, shear, and penetration forces. The hydrophilic coating on the channel walls reduces the contact angle from 72° to 9°, creating a strong capillary action that extracts ISF from agarose gel without any external force and enhances liquid uptake from rat skin samples. We perform a parametric study to examine the effect of different MN designs on liquid uptake. Finally, we demonstrate the applicability of the developed MN patch by integrating it with a colorimetric assay for urea and pH sensing. The proposed MN device exhibits excellent mechanical and liquid uptake performance, offering a practical ISF extraction approach that eliminates the need for external forces in health monitoring devices.

3.2 Materials and Methods

3.2.1 Materials and chemicals

PDMS (Sylgard 184 Silicone Elastomer) was obtained from Dow Corning (MI, USA). Biocompatible resin (BIO) was purchased from Boston Micro Fabrication (BMF Material Technology Inc., Shenzhen, China). Urease (from Canavalia ensiformis, Jack bean, type III), agarose (for molecular biology), sodium chloride (NaCl), potassium chloride (KCl), calcium chloride ($CaCl_2$), and lithium chloride (LiCl) were bought from Sigma-Aldrich (MO, USA). D(+)-Glucose and urea crystalline pure were obtained from neoFroxx. Double-sided tape (9495 LE 300 LSE) was obtained from 3 M (MN, USA). Transparent polyethylene

terephthalate (PET) films were purchased from MG Chemicals (Burlington, Canada). Universal pH indicator was obtained from Macherey Nagel (Duren, Germany).

3.2.2 Design of MN arrays and 3D printing

The MN patches were made of a biocompatible resin (BIO, Boston Micro Fabrication) using projection micro stereolithography technology. The designs were prepared using SolidWorks 3D design software (**Figure 3.1**), and then imported into VoxelDance software to be sliced into 2D images (**Figure 3.2**), which served as the UV masks. The MNs were printed using a microArch S230 (Boston Micro Fabrication) 3D printer. The stage and needle parts of MN patches were printed in 20 μm and 5 μm thick layers, respectively. Despite the higher print time, 5 μm thick layers ensured maximum accuracy and minimum needle tip size (**Figure 3.3** and **Figure 3.4**). After importing the 2D gray images into the microArch S230, the 3D printer vat was filled with BIO resin, followed by UV exposure (405 nm light wavelength) to only the white zones of the 2D images. **Figure 3.2** shows the representative UV masks at different stages of the 3D printing process. Once the 3D printing was completed, the MN patches were scraped off the stage and washed using fresh 99% isopropyl alcohol. Then, FormCure (Formlabs) was used to post-cure the MNs with 405 nm radiation for 2 hours at 50 °C.

All MN patches were printed in 10×10 arrays except for the mechanical characterization experiments, where 5×5 arrays were used to perform the tests. Each patch contained conical MNs of 1 mm in height and center-to-center distance, base diameter of 300 μm and 500 μm, and microchannel diameter of 50 μm and 100 μm (**Table 3.1**).

Table 3.1. Design of different MN patches used in this study.

MN label	Shape	Height (mm)	Base diameter (mm)	Center to center (μm)	Number of microchannels	Microchannel diameter (μm)
MN-1	Conical	1	500	1	0	0
MN-2	Conical	1	500	1	2	100
MN-3	Conical	1	500	1	4	100
MN-4	Conical	1	300	1	2	50
MN-5	Conical	1	300	1	4	50
MN-6	Conical	1.25	500	1	2	100
MN-7	Conical	1.5	500	1	2	100

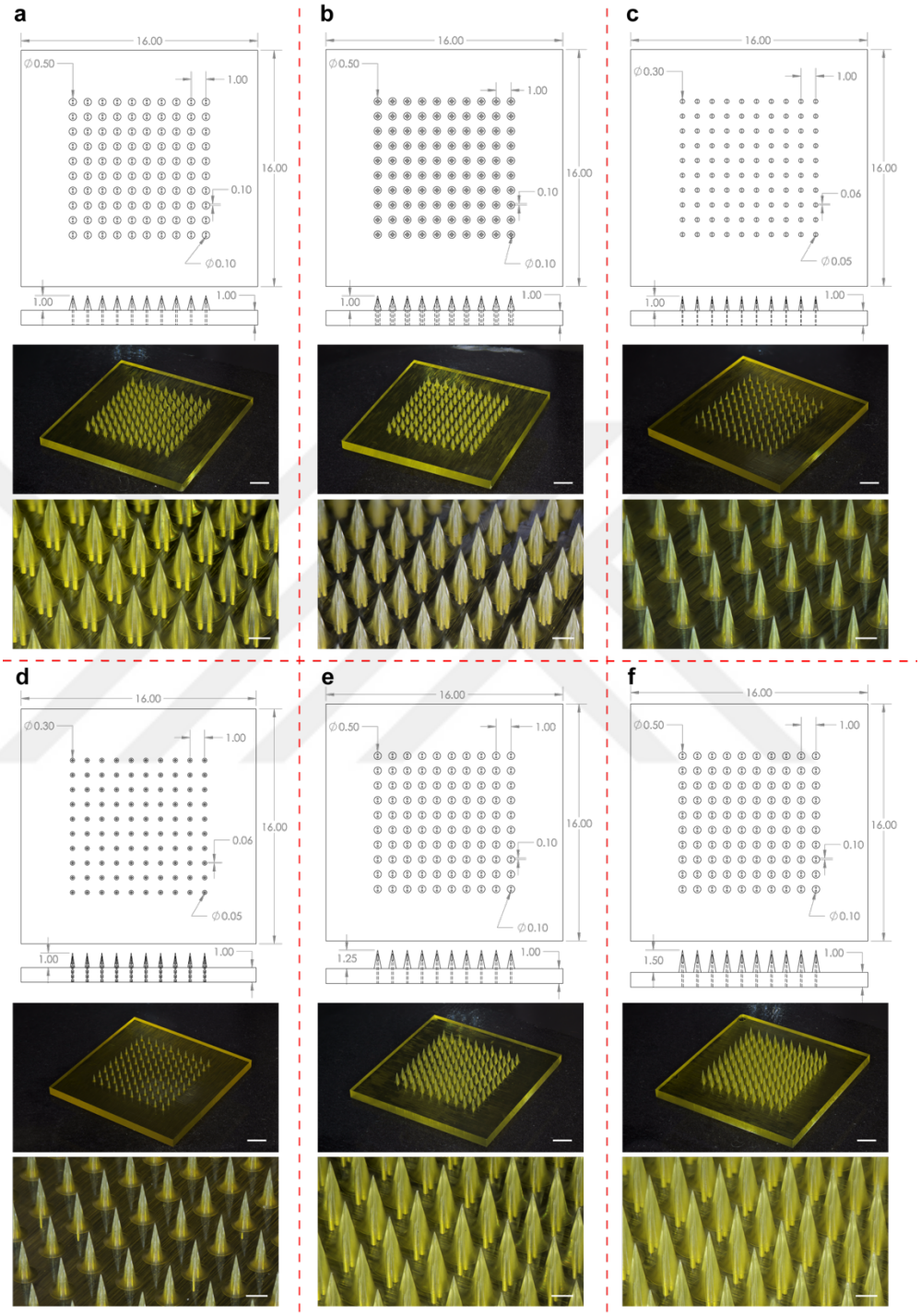


Figure 3.1. Design and dimensions of the 3D-printed HMN patches. 2D drawing (top) and optical microscopy images (bottom) of 10×10 arrays of MNs with design of **(a)** MN-2, **(b)** MN-3, **(c)** MN-4, **(d)** MN-5, **(e)** MN-6, and **(f)** MN-7. (Design details about MN-2 to MN-7 are provided in **Table 3.1**). Scale bars of microscopic images, top: 2 mm and bottom: 500 μm.

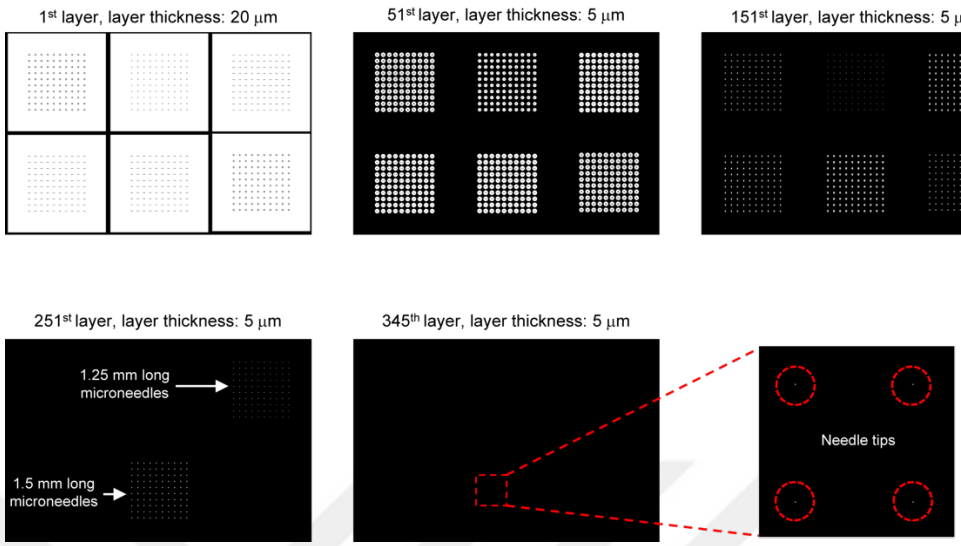


Figure 3.2. Sliced images generated by VoxelDance software, which was used as UV masks during printing process.

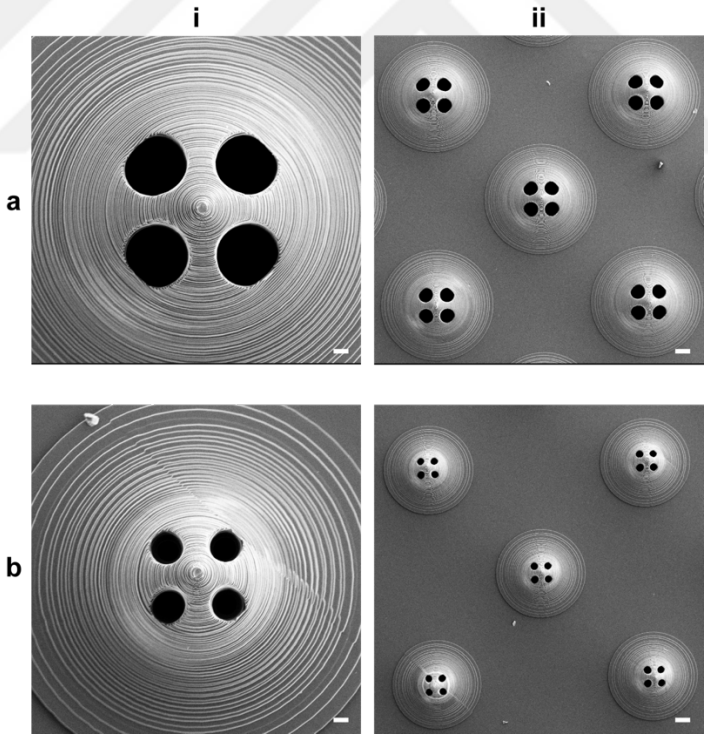


Figure 3.3. SEM top view images of 3D-printed MNs. **(a)** MN-3 (base diameter of 500 μm and channel diameter of 100 μm). **(b)** MN-5 (base diameter of 300 μm and channel diameter of 50 μm). It should be noted that fillet features were used in the MN designs to enhance their mechanical properties. Scale bars, i: 20 μm and ii: 100 μm.

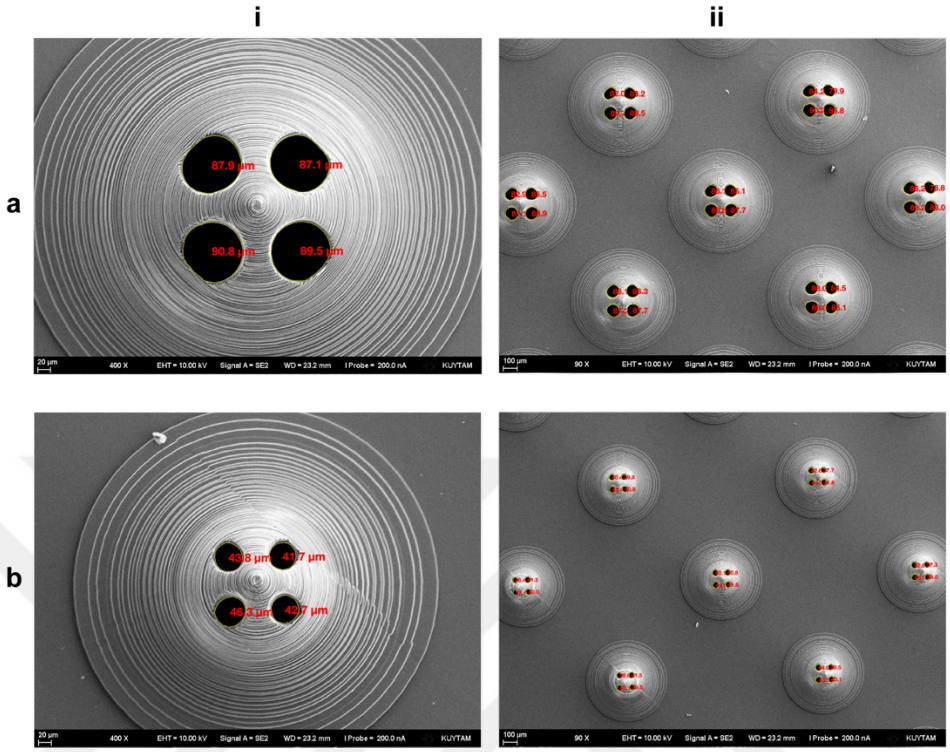


Figure 3.4. Image analysis of SEM images to determine the size of printed microchannels in the needles. **(a)** MN-3 (base diameter of 500 µm and channel diameter of 100 µm). **(b)** MN-5 (base diameter of 300 µm and channel diameter of 50 µm). SEM images were analyzed using MATLAB programming platform. Image analysis results revealed average microchannel diameter of 86.36 ± 2.89 µm (RSD: 3.35%) and 42.33 ± 2.42 µm (RSD: 5.86%) for MN-3 and MN-5, respectively. These results reveal that the 3D printer could print the MN channels with about 85% accuracy.

3.2.3 Mechanical characterization of 3D-printed MN arrays

The mechanical properties of the 3D-printed MN patches were measured using a force-displacement test setup comprising a force gauge (MARK-10) and a Z-axis stage (**Figure 3.5**, **Figure 3.6**, and **Figure 3.7**). The mechanical behavior of solid and HMNs with different diameters was examined under compression load and shear load, followed by performing the skin penetration tests. Briefly, to study the mechanical stability of MNs under compression load, the MN patch was placed on the Z-axis stage platform with needles facing toward the force sensor. The measurement started once the MN tips touched the force sensor and continued until a maximum force of 0.4 N per needle was obtained (**Figure 3.5**).

To examine the mechanical behavior of MN patches under shear load, the MN patch was attached to a rigid platform, ensuring the MNs were oriented horizontally. The sensor tip was

replaced with another tip to be able to apply the force to a single MN (**Figure 3.6**). For each MN, the measurement was continued until the fracture point was achieved. To assess the skin insertion ability, the MNs were applied to fresh rat skins while the needle tips were facing toward the skin (**Figure 3.7**). The application of vertical force on MN patches was continued until a predefined force of 0.4 N per needle was achieved. All mechanical characterization experiments were performed on MN patches with 5×5 arrays and a patch area of 7×7 mm^2.

Following each experiment, SEM and optical microscopy images of MNs were obtained to examine the robustness of the 3D-printed MNs against mechanical deformations.

3.2.4 Morphological characterization of MNs

The MN morphologies were characterized using optical and scanning electron microscopy. A 2D/3D motorized microscope (MRCL700 3D imager pro, Microqubic AG, Switzerland) was employed to take the optical images from MNs. SEM imaging was performed using ZEISS (Zeiss, Ultra Plus, Germany) scanning electron microscope. Additionally, SEM images were used to examine the robustness of HMNs after performing the mechanical characterization experiments. Furthermore, top view SEM images of the MNs were processed using MATLAB (MathWorks, MA, USA) to obtain the diameter of microchannels in the fabricated HMNs (**Figure 3.3** and **Figure 3.4**).

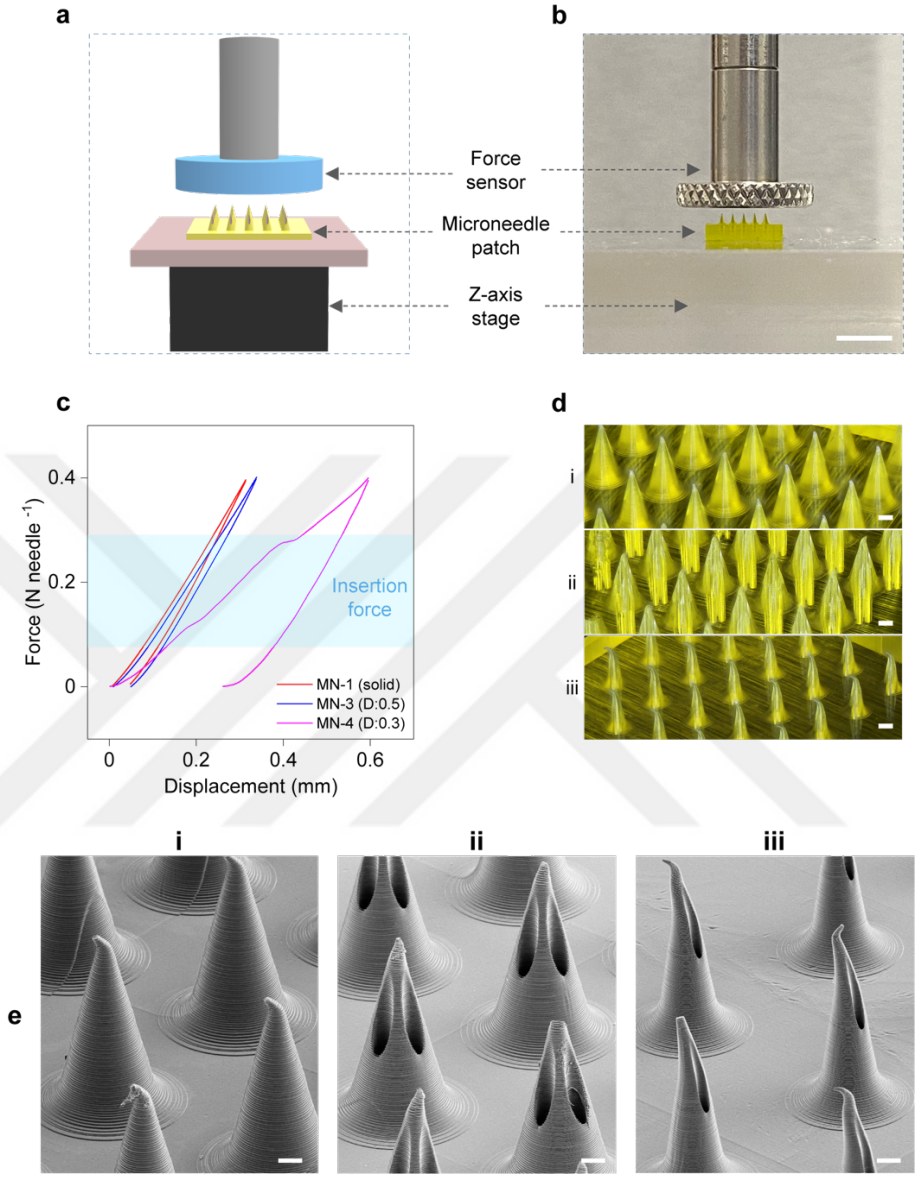


Figure 3.5. Mechanical behavior of the MN arrays under compression administered by vertical force. **(a)** Schematic and **(b)** optical image of the characterization setup used for compression experiments. **(c)** Mechanical performance of the MN arrays under compressive load. The smooth curves of MN-1 and MN-3 indicate that no observable needle fracture was formed during compression tests. By assuming a maximum needle tip radius of 40 mm, the required penetration force per needle would be in the range of 0.08–0.295 N. The administered force in compression experiments surpasses the required force to penetrate skin. **(d)** Optical microscopy images of the MN arrays after compression experiments. (i) MN-1, (ii) MN-3, and (iii) MN-4. **(e)** SEM images of (i) MN-1, (ii) MN-3, and (iii) MN-4 after compression experiments (n=5). (Design details about MN-1, MN-3, and MN-4 are provided in **Table 3.1**). Scale bars, b: 5 mm, d: 200 μm, and e: 100 μm.

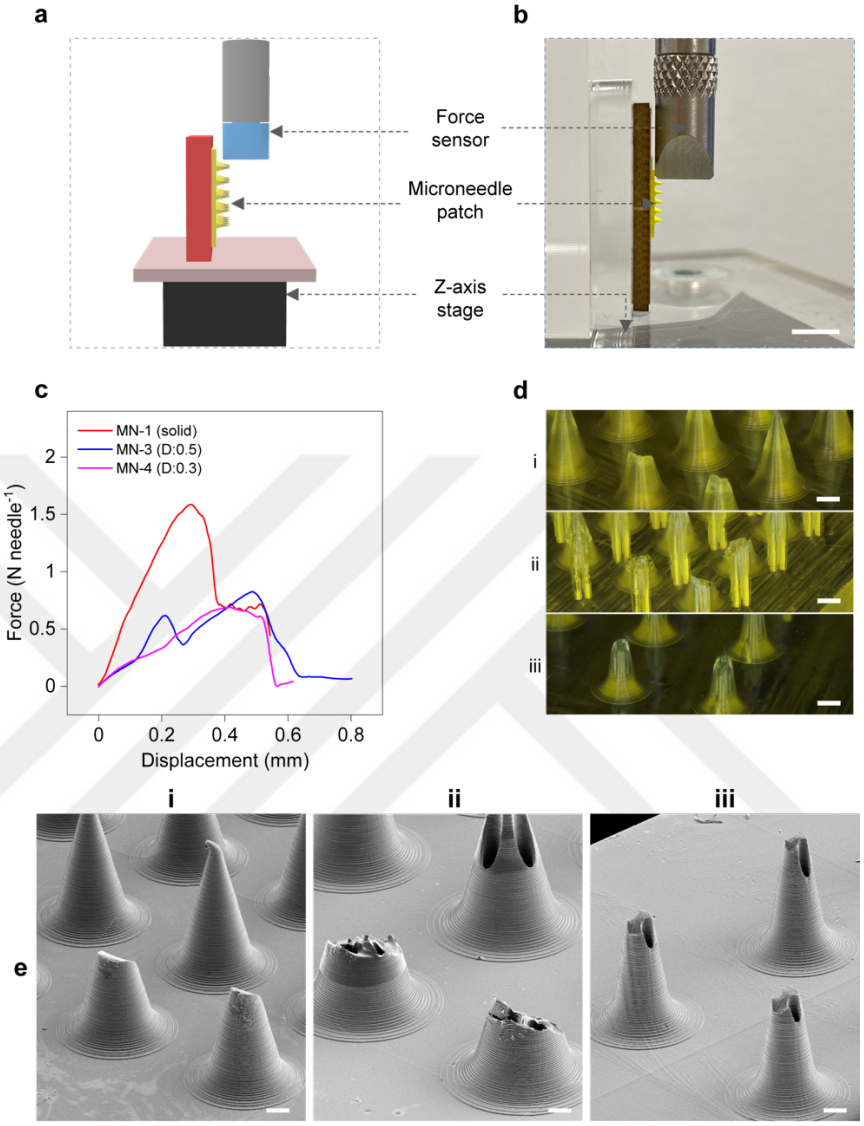


Figure 3.6. Mechanical behavior of the MN arrays under shear load. **(a)** Schematic and **(b)** optical image of the characterization setup used for shear load experiments. **(c)** Mechanical performance of the MN arrays under shear force. No needle breakage was observed for by applying shear force on solid MNs (MN-1) up to 1.5 N. The average needle deformation for applied shear forces of 0.5, 1, and 1.5 N per needle were 42.35 ± 20.95, 72.99 ± 26.75, 92.48 ± 21.48 mm, respectively. Needle fracture occurred at a shear force of 1.51 ± 0.08 N per needle for MN-1. The needle deformations for MN-3 and MN-4 under shear load of 0.5 N were 51.73 ± 22.08 and 77.69 ± 13.30 mm, respectively. The fracture forces for MN-3 and MN-4 were 0.79 ± 0.14 and 0.70 ± 0.03 N per needle, respectively. **(d)** Optical microscopy images of the MN arrays after shear experiments. (i) MN-1, (ii) MN-3, and (iii) MN-4. **(e)** SEM images of (i) MN-1, (ii) MN-3, and (iii) MN-4 after shear experiments. (Design details about MN-1, MN-3, and MN-4 are provided in **Table 3.1**). Scale bars, b: 5 mm, d: 200 μm, and e: 100 μm.

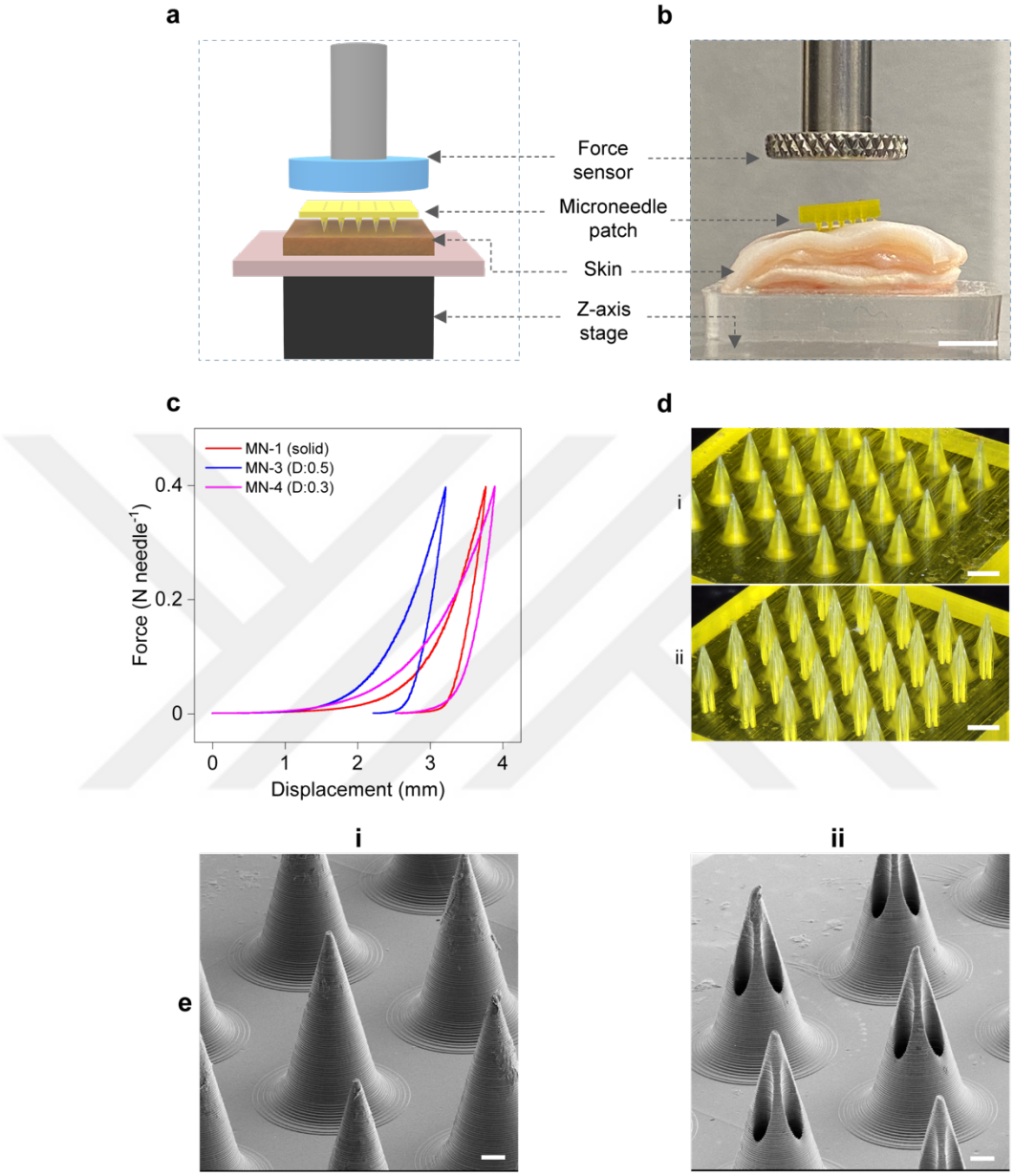


Figure 3.7. Assessment of the required force during MN administration to skin. **(a)** Schematic and **(b)** optical image of the characterization setup used skin penetration experiments. **(c)** Mechanical performance of the MN arrays when applied to the skin samples. **(d)** Optical microscopy images and **(e)** SEM images of the MN arrays after skin penetration experiments. (i) MN-1 and (ii) MN-3. (Design details about MN-1, MN-3, and MN-4 are provided in **Table 3.1**). Scale bars, b: 5 mm, d: 500 µm, and e: 100 µm.

3.2.5 Hydrophilic coating and characterization

To increase the hydrophilicity, the 3D-printed MNs were coated with a thin layer of SiO_2 using CVD. SENTECH ICP-CVD SI-500 was utilized to deposit an oxide layer of

approximately 1200 nm thickness (Figure 3c). To mitigate any adverse effect of the elevated temperature inside the CVD chamber on the 3D-printed samples, the deposition process was segmented into four stages, each with a 300 nm thickness. The thickness of the oxide layer was measured using a stylus surface profilometer (Dektak, Bruker). An optical tensiometer (ThetaLite TL 101, Biolin) was employed to measure the static water contact angle of the surfaces by placing 2 μL of DI water on the untreated and SiO_2-coated 3D-printed sample films at room temperature. The samples were printed with the surface area of 2×2 cm^2, and the water droplets were placed on different parts of the samples. Contact angles were reported as the mean value of measured water contact angles on five different locations on the surface under the same conditions.

3.2.6 Integration of microfluidic module

A microfluidic layer was integrated into the MN patch to provide a collection chamber for the extracted liquid. The chamber designs were prepared using AutoCAD (Autodesk, USA) and then transferred onto a double-sided tape (9495 LE 300 LSE) using a UV laser-cutting machine (ProtoLaser U4, LPKF, Germany). The as-prepared microfluidic layer was attached to the backside of the MN patches to serve as the ISF collection chamber, followed by enclosing the chamber using a PET layer.

3.2.7 In vitro ISF extraction experiments

The liquid collection capability of the 3D-printed MNs was evaluated by inserting the MN tips into aISF and 1.4 wt% agarose gel. The aISF solution was prepared according to the procedure previously reported in the literature [215]. The MN patch was affixed on a force sensor tip, while the chamber containing the blue-dyed agarose gel or aISF was placed on a Z-axis stage to enable vertical movement between the MN tips and the chamber. The force sensor enabled the detection of initial contact between the MN tips and the liquid or agarose gel. A microscope equipped with a camera (MRCL700 3D imager pro, Microqubic) was integrated into the experimental setup for real-time video recording of liquid extraction (**Figure 3.8**). Once the initial contact was detected using the force sensor, the MNs were inserted into the liquid medium by moving the Z-axis stage while ensuring a portion of their

length remained outside the medium (**Figure 3.9**–**Figure 3.12**). A smartphone camera (iPhone 11, Apple, USA) captured the videos of the microfluidic chamber filling (**Figure 3.12**).

The vacuum was generated using A PDMS-based finger-actuated system, which was developed in our previous study [47]. To be able to measure the vacuum level, the pressure in the system was monitored using a pressure sensor (BMP 280, Bosch). The pressure data was recorded using an Arduino board, which enabled the transfer of acquired pressure data to a personal computer. To investigate the effect of vacuum level on ISF extraction, vacuum pressures of -2 to -20 kPa was tested during in vitro experiments.

3.2.8 ISF collection from rat skin ex vivo

Rat skin samples were collected from Wistar rats immediately after euthanasia and kept at -80 °C until use. The skin samples were collected from dorsal side of the rats, which was entirely shaved before excision. Square samples (area of 2×2 cm^2) were thawed and placed in a transparent chamber with a PDMS layer underneath the skin samples (**Figure 3.13**). Before inserting the MNs, the skin samples were entirely dried using a paper towel to remove any remaining water residues on the skin surface. For better visualization of ISF extraction, blue-stained filter papers were embedded in the microfluidic chamber. After placing the skin samples in the transparent chamber, the MN patch was administered. Double-sided tapes provided secure attachment of the MNs to the skin, while ensuring reliable sealing to help minimize vacuum drop during the experiments. The experiments were performed at an average vacuum pressure of about -40 kPa. MN patches were weighted using a high precision laboratory scale before and after each experiment to determine the amount of extracted ISF.

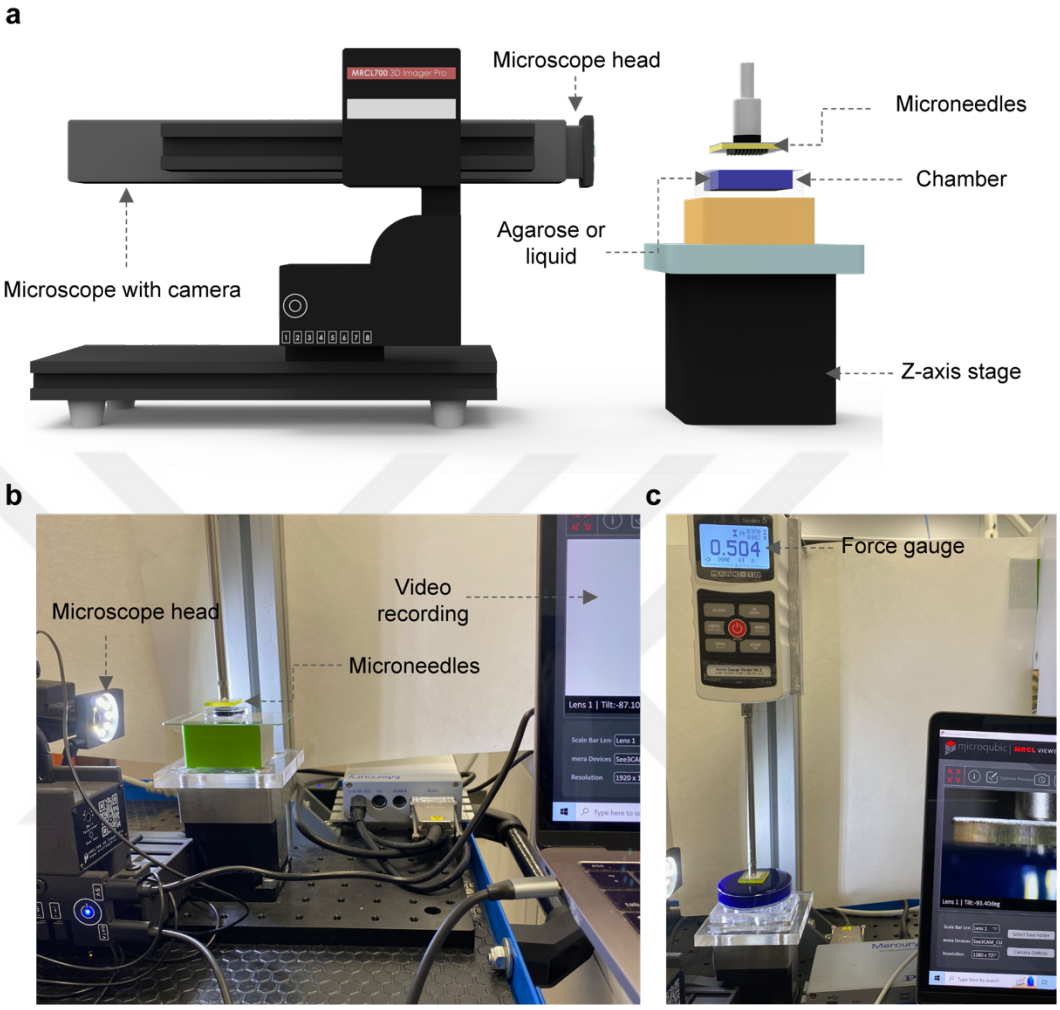


Figure 3.8. Experimental setup used for in vitro extraction experiments. Schematic illustration of different parts of the setup. **(b)** Photo of the microscope connected to a personal computer for image and video recording. **(c)** MARK-10 force gauge to monitor the interaction force between the MNs and agarose gel.

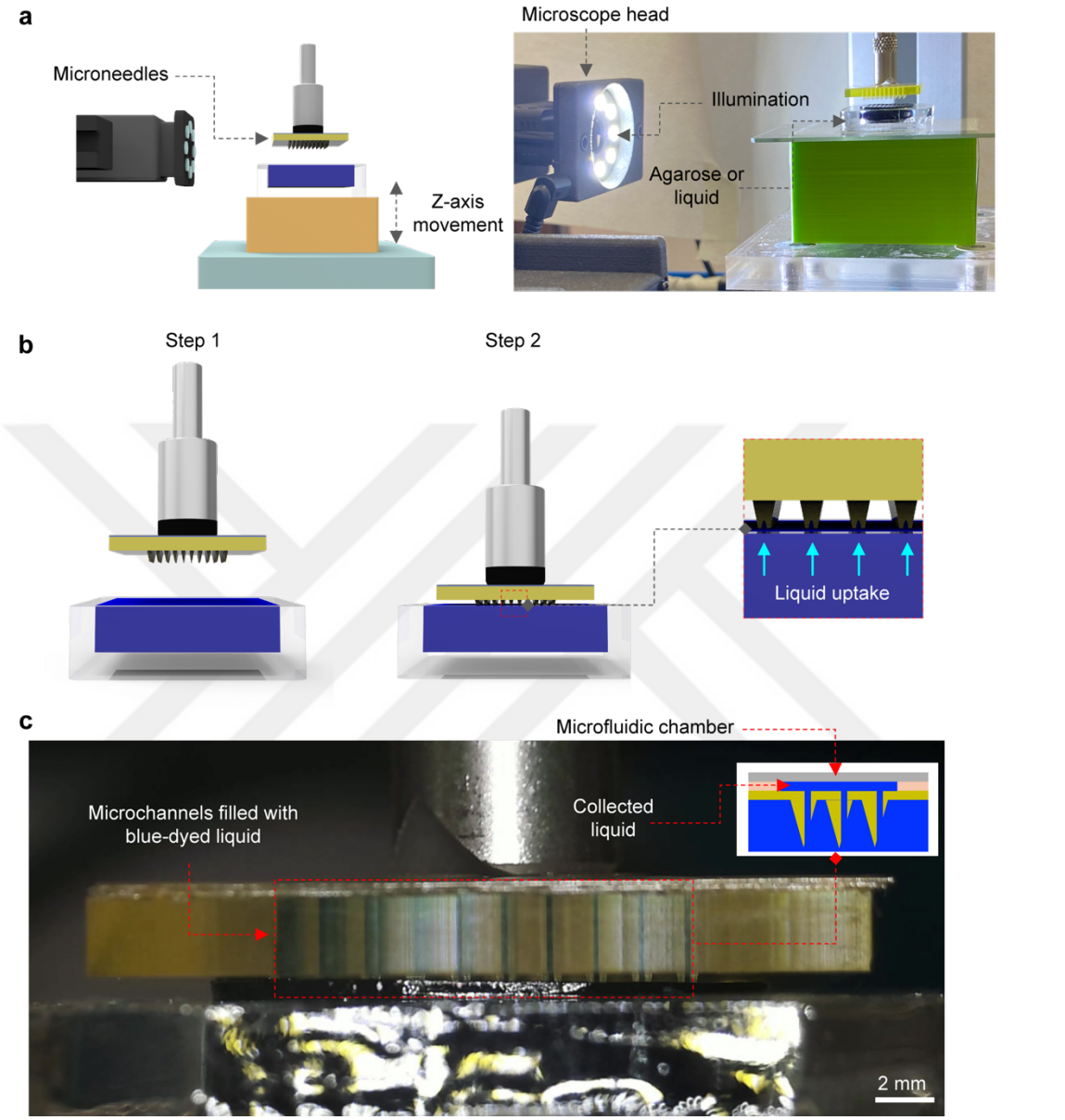


Figure 3.9. Demonstration of liquid uptake through microchannels. **(a)** Schematic illustration (left) and photographic image (right) of the liquid uptake setup. **(b)** Liquid uptake experiment. **(c)** Image recorded by the microscope that shows the liquid flow through microchannels into the microfluidic module integrated to the top of the MNs.

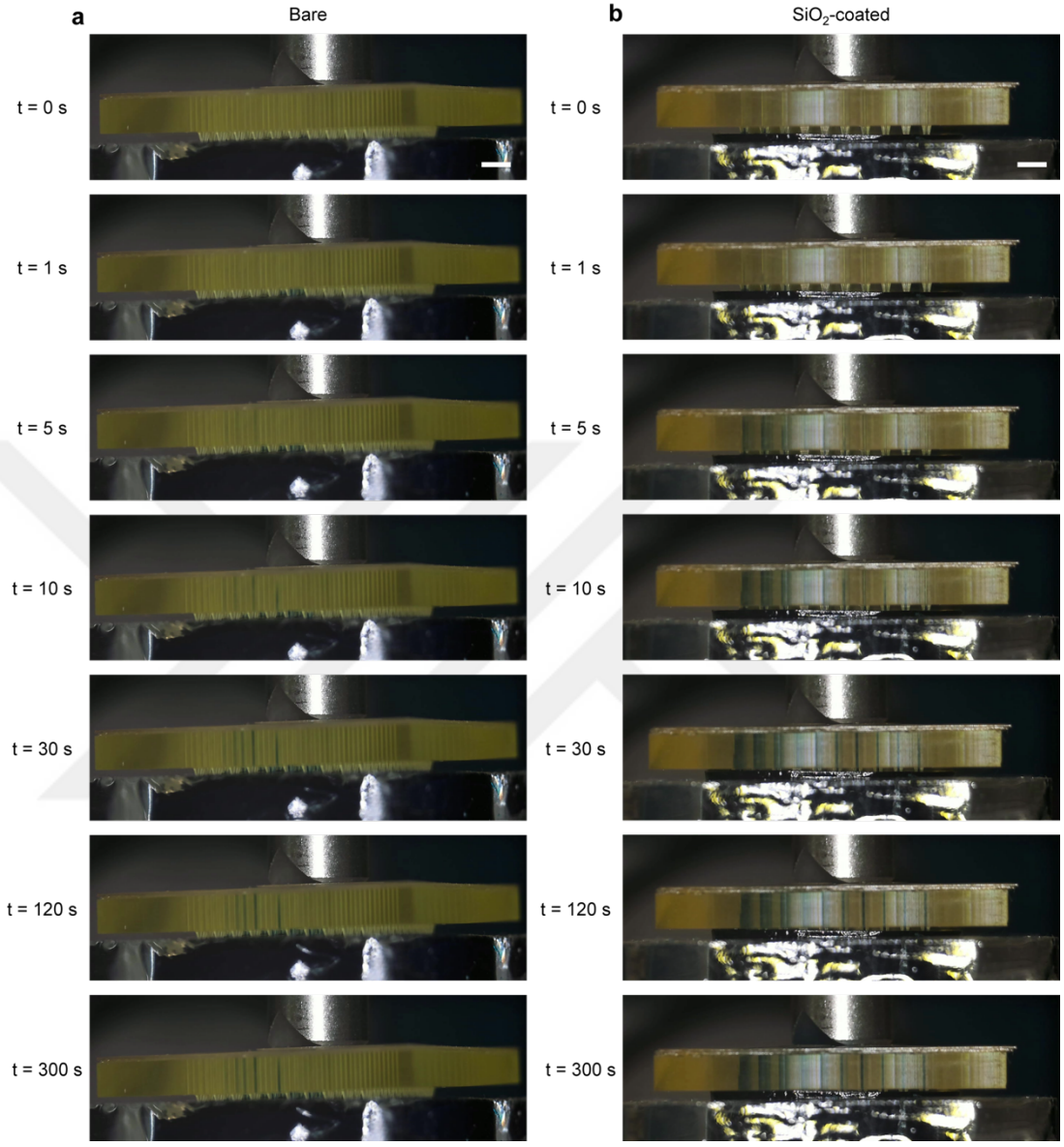


Figure 3.10. Liquid uptake by the 3D-printed MNs from blue-dyed aISF. **(a)** Bare MN patch. **(b)** SiO_2-coated MN patch. A microfluidic module was integrated into MNs to collect the extracted liquid. Scale bars are 1 mm.

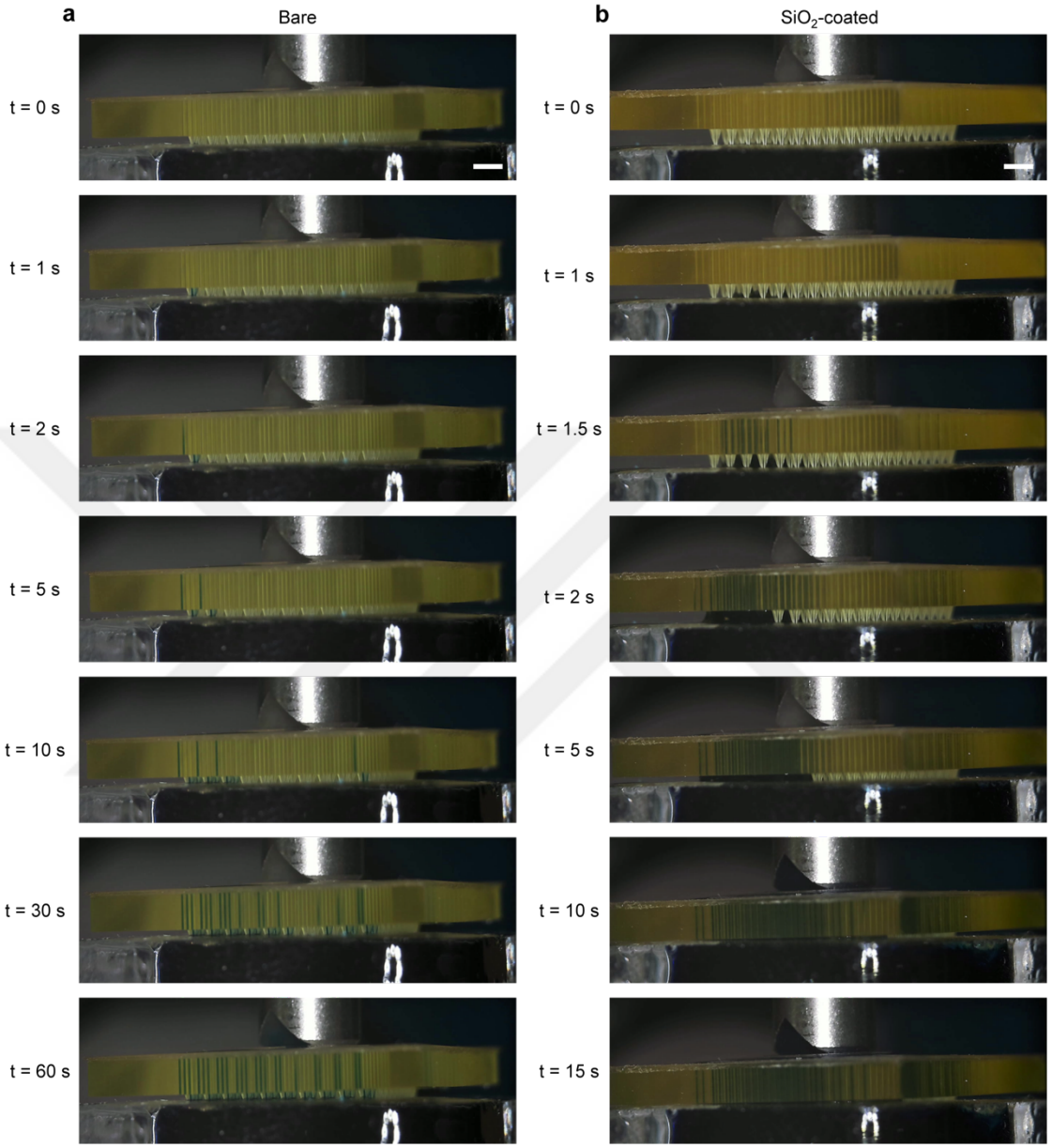


Figure 3.11. Liquid uptake by the 3D-printed MNs from agarose gel containing aISF. **(a)** Bare MN patch. **(b)** SiO_2-coated MN patch. A microfluidic module was integrated into MNs to collect the extracted liquid. Scale bars are 1 mm.

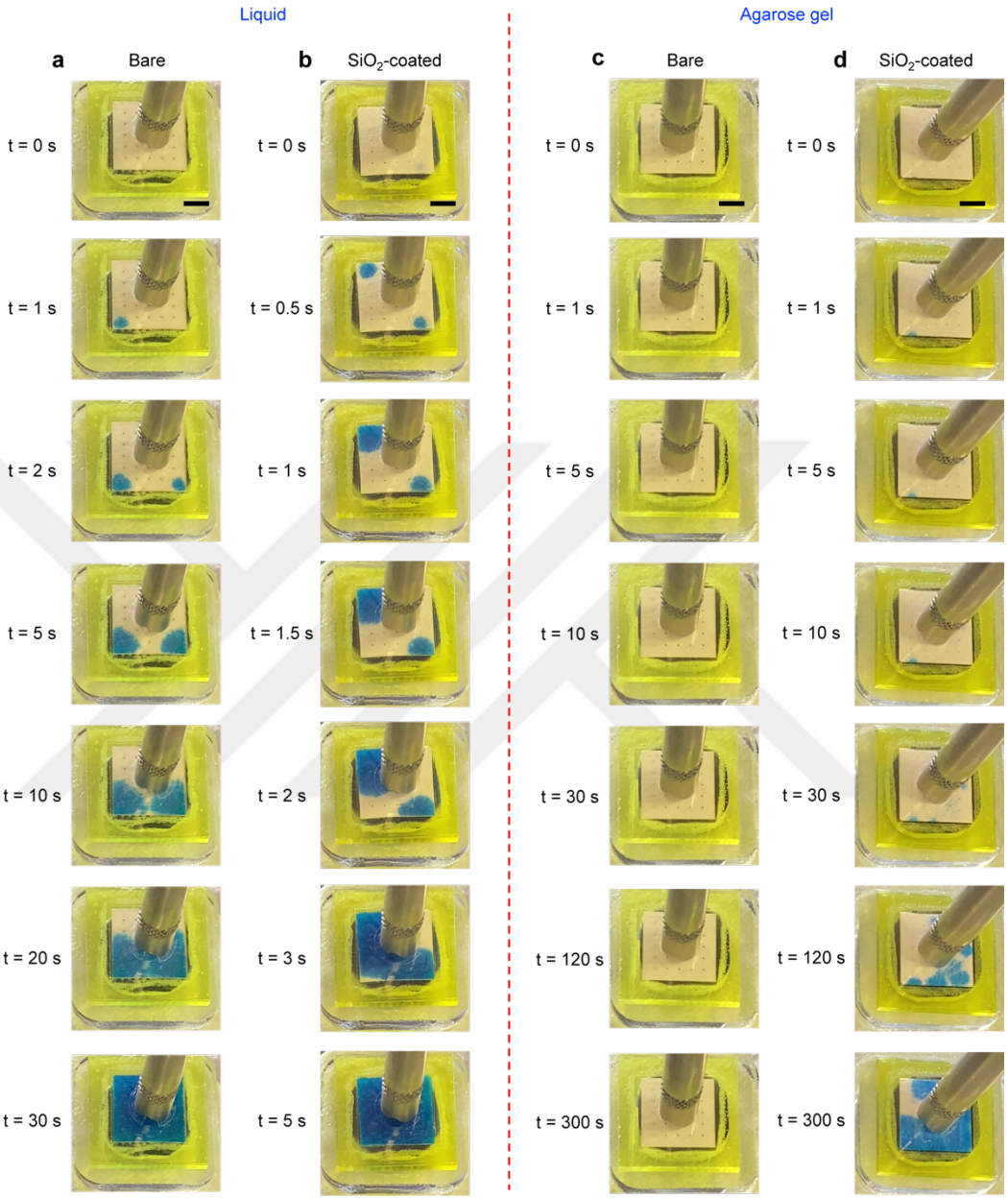


Figure 3.12. Sequential images of liquid uptake into the microfluidic chamber integrated to the MNs. Liquid uptake from a chamber containing blue-dyed aISF through **(a)** bare MNs and **(b)** SiO_2-coated MNs. Liquid uptake from agarose gel containing blue-dyed aISF through **(c)** bare MNs and **(d)** SiO_2-coated MNs . Scale bars are 5 mm.

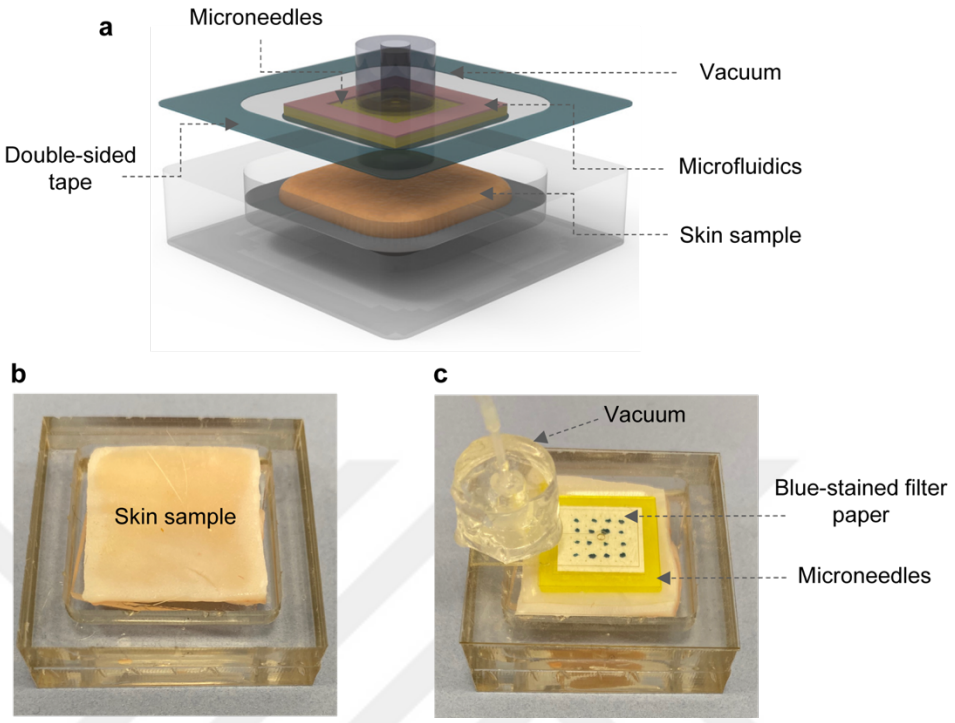


Figure 3.13. Experimental setup used for ex vivo ISF extraction experiments. **(a)** Schematic illustration of different parts of the setup. **(b)** 2×2 cm^2 rat skin sample inside the test chamber. **(c)** administration of 3D-printed MNs, assembly of the test setup, and vacuum application.

3.2.9 Forming the colorimetric assay

To prepare the sensing assay for urea, a similar approach to the previous studies was adopted here [263]. In brief, a urease solution with a concentration of 10 mg/mL was prepared in deionized water. To perform the experiments of obtaining the calibration curve, small pieces of pH paper were cut using a laser in circular shapes with a diameter of 3 mm. Additionally, rectangular shapes of pH papers (5.5×12 mm^2) were laser-cut to be integrated to the microfluidic module. To yield the urea assay, 2 and 20 µL of the urease solution were immobilized onto the circular and rectangular pH papers, respectively, followed by drying under vacuum for 15 min. For pH sensing, the circular and rectangular pH papers were utilized without any modification.

3.2.10 Color development and biomarker detection of the colorimetric assay

Standard solutions of aISF with urea concentration ranging from 1–20 mM and pH values ranging from 6.4–8.2 were prepared. The pH of standard solutions was adjusted using 0.1 M HCl and 0.1 M NaOH solutions. A commercial pH meter (Orion Dual Star, Thermo Scientific, MA, USA) was utilized to measure the pH level. To extract the reference markers for obtaining the calibration curves, 2 μL of the standard solutions were dropped onto the circular papers, followed by incubation at 37 °C for 15 min. It should be noted that for the pH assay, no incubation period was required, as the color change was visible after a few seconds. A smartphone rear camera (iPhone 11, Apple, CA, USA) was used to capture the images under controlled lighting conditions using its regular camera application. To increase the reliability of the implemented colorimetric analysis, room light was used for image acquisition, and the distance and orientation between the samples and the smartphone were kept the same to minimize the effect of external interferences. All images were captured using the same smartphone camera. Then, the images were analyzed using ImageJ software to extract the color intensity values at R, G, and B channels. A layer containing color reference markers was printed using a color laser printer with colors that matched the colors determined after performing calibration experiments. The selectivity of the urea assay was characterized by adding NaCl, $CaCl_2$, KCl, LiCl, and glucose solutions with concentrations of 5 mM to the urea assays.

For *in vitro* urea and pH sensing, 1.4 wt% agarose gels with urea concentrations of 10 and 15 mM and pH values of 6.5 and 7.0 were prepared. The as-prepared rectangular colorimetric assays were integrated into the MNs, and inserted into the agarose gel for liquid uptake. After extraction and incubation, the colorimetric responses of the assays were recorded using the smartphone camera for further analysis. For *ex vivo* experiments, skin samples were immersed in aISF solutions with urea and pH levels of 10 mM and 6.5, respectively, for 24 hours to reach an equilibrated state. Before MN application, the skin samples were carefully dried using paper towels, followed by an air gun to ensure complete removal of the remaining surface moisture. The PDMS-based vacuum source was employed as the vacuum source for ISF extraction.

3.2.11 Cell culture and cell viability assay

To investigate the biocompatibility of the employed MNs, *in vitro* cell viability experiments were performed using mouse embryonic fibroblast NIH/3T3 cell line. The complete medium was made of Dulbecco's Modified Eagle's Medium (DMEM, Biowest) supplemented with 10% Fetal Bovine Serum (FBS, Biowest) and 1% penicillin/streptomycin (PS, Gibco). The cells were cultured in a 24-well cell culture plate at a density of 1.5×10^4 cells/well with a complete medium. After allowing overnight attachment of the cells, MNs were entirely immersed into the complete medium, and cells were treated for 3 days. The seeded cells were stained with Calcein AM (Invitrogen) and propidium iodide (PI, Sigma) to assess the live/dead cells at 24 h and 72 h after treatment. Briefly, Calcein AM (1 μM) and PI (5 μg/mL) dye solutions were prepared in a complete medium, and cells were incubated for 30 min at 5% CO_2 and 37 °C. At the end of the incubation, wells were washed twice with the complete medium, and the required volume of fresh complete medium was left in the wells before imaging. Live/dead cells were monitored using a fluorescence microscope. Metabolic activity was measured with CellTiter-Glo (Promega) luminescent cell viability assay according to manufacturer's instructions at 24 h and 72 h after treatment. Luminescence signal for untreated control cells and MN treated cells were recorded with a microplate reader (BioTek, Agilent).

3.2.12 Statistical analysis

All results were presented as mean ± SD (standard deviation). P-values were calculated using an unpaired t-test with a two-tailed distribution.

3.3 Results and Discussion

3.3.1 Design and fabrication of the MN patches

The ISF sampling approach in this study relies on MN arrays with through microchannels that penetrate the dermis layer and transport dermal ISF to the integrated microfluidic module. The MN patch was fabricated employing highly reproducible PμSL technology (**Figure 3.14a,b**). This technique utilizes a three-dimensional computer-aided design for rapid photopolymerization of liquid resin using flashes of UV light. Each MN patch contains 100 (10×10 array) conical MNs within a patch area of 16×16 mm^2 (**Figure 3.14c**). Detailed

morphological characterization was performed by scanning electron microscopy (SEM) (**Figure 3.14d**). The SEM images showed that the fabricated MNs had a tip diameter of approximately 5 μm, comparable to the tip radii of MNs prepared using photolithography-based techniques [50], [53]. Image analysis of the top-view SEM images of the microchannels revealed a printing accuracy of approximately 85% (**Figure 3.4**).

3.3.2 Liquid uptake into microchannels by capillary flow

The fluid flow through microchannels in the needles by capillary action can be estimated by the Young-Laplace equation:

$$\Delta P = \gamma\left(\frac{1}{R_1}+\frac{1}{R_2}\right) \tag{3.1}$$

where R_1 and R_2 are the radii of the curvature, γ is the surface tension and ΔP is the pressure difference across the interface.

For a MN, because of the cylindrical shape of the capillary with radius of a, and considering the contact angle of θ, R_1 can be written as $\frac{a}{\cos(\theta)}$ and R_2 approaches infinity (**Figure 3.15**):

$$R_1 = \frac{a}{\cos(\theta)}$$

$$R_2 \to \infty$$

Eq. (3.1) can be written as:

$$\Delta P = \frac{2\gamma\cos(\theta)}{a} \tag{3.2}$$

The capillary rise inside the microchannels is given by:

$$h = \frac{2\gamma\cos(\theta)}{\rho g a} \tag{3.3}$$

where g is the gravitation acceleration and ρ is the fluid density.

The MNs which were used in this study had a water contact angle (WCA) of 72.27° ± 3.57° and 9.39° ± 4.11° before and after SiO_2 coating, respectively. Assuming a surface tension (γ) of 0.072 $N.m^{-1}$, g of 9.81 $m.s^{-2}$, and density (ρ) of 1000 $kg.m^{-3}$, the capillary pressure and capillary rise in a microchannel of 100 μm diameter can be calculated from Eq. (3.2) and Eq. (3.3), respectively, as:

Bare MNs:

Capillary pressure: $\Delta P_{bare} = \frac{2 \times 0.072\left(N.m^{-1}\right) \times \cos\left(72.27°\right)}{50 \times 10^{-6}(m)} \approx 877\ Pa$

Capillary rise: $h_{bare} = \frac{877(Pa)}{1000\left(kg.m^{-3}\right) \times 9.81\left(m.s^{-2}\right)} = 89.4\ mm$

SiO_2-coated MNs:

Capillary pressure: $\Delta P_{treated} = \frac{2 \times 0.072\left(N.m^{-1}\right) \times \cos\left(9.39°\right)}{50 \times 10^{-6}(m)} \approx 2843\ Pa$

Capillary rise: $h_{treated} = \frac{2843(Pa)}{1000\left(kg.m^{-3}\right) \times 9.81\left(m.s^{-2}\right)} = 289.8\ mm$

These results suggest that improving the hydrophilicity of the MNs via SiO2-coating increased the capillary pressure by approximately 224%, resulting in a greater capillary rise.

Figure 3.14e schematically illustrates the extraction process using the 3D-printed MNs. Due to the hydrophobic nature of the as-printed MNs, no liquid uptake is observed owing to the absence of capillary flow. However, enhancing the wettability of the microchannels induces capillary rise inside the channels, which assists in ISF extraction extraction. As shown in **Figure 3.14e**, while there is no capillary rise in hydrophobic microchannels, the hydrophilic microchannels exhibits liquid uptake capability due to capillary action. In this study, the MN patch was designed as a two-component system consisting of the 3D-printed HMNs (which create the micropores in the skin for ISF extraction from the dermis) and a microfluidic layer (which serves as the ISF collection chamber).

The microfluidic chambers contain paper-based colorimetric assays for detecting urea and pH in the extracted ISF. An exploded view of the different components of the multilayered colorimetric patch is illustrated in **Figure 3.14f**. Upon extraction through superhydrophilic microchannels in the MN patch, the extracted liquid is collected in the microfluidic chambers (constructed using a 170 μm-thick double-sided tape) and comes into contact with the embedded colorimetric assays for urea and pH sensing. Multiple microfluidic chambers are included for each biomarker to increase the detection accuracy. The microfluidic layer is enclosed by a thin, transparent capping layer. Finally, a layer containing color reference

markers is attached as the top layer to assist with quantitative analysis of the images. **Figure 3.14g** shows representative images of the final MN patch with integrated colorimetric assays before and after the color changes resulting from urea and pH sensing.

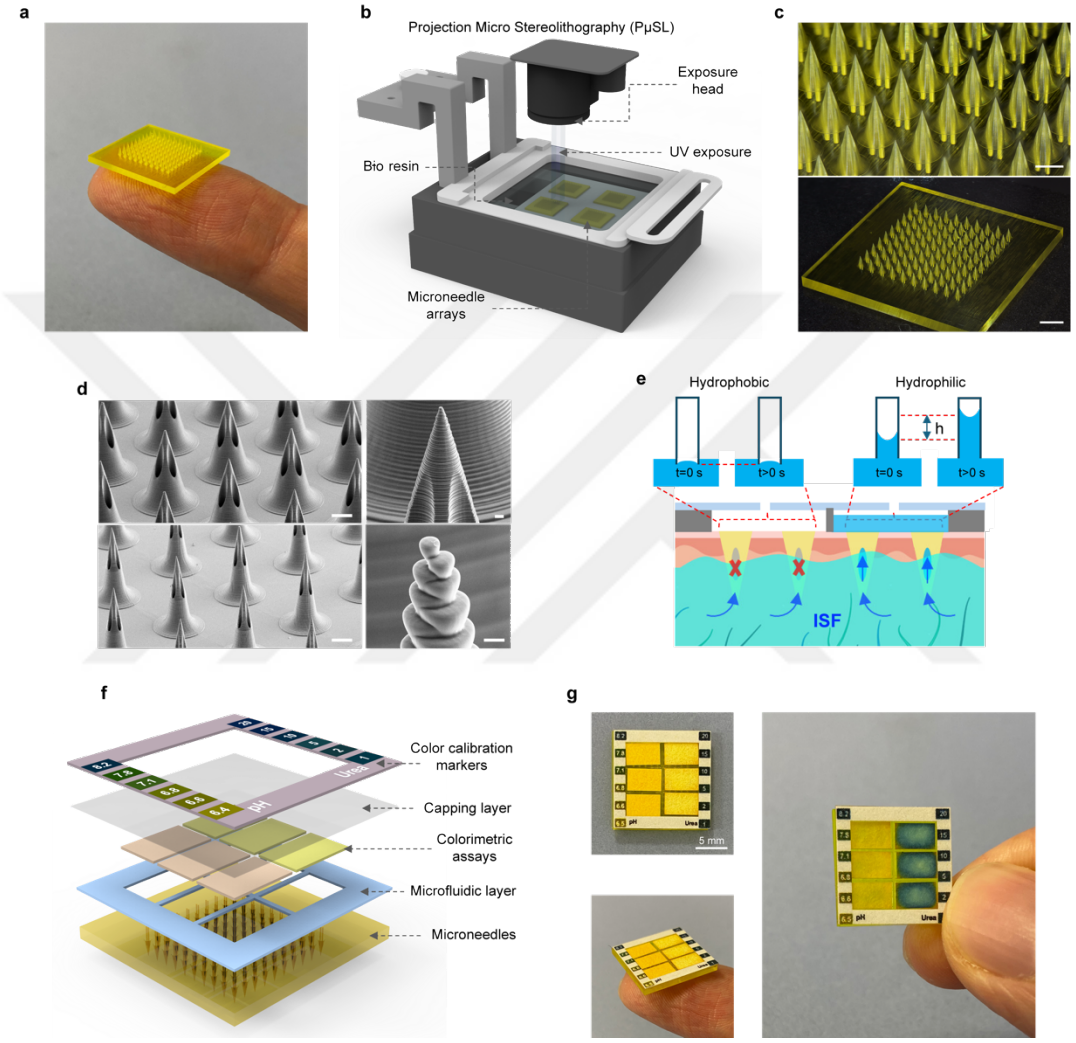


Figure 3.14. Illustration of 3D-printed MNs for extraction and colorimetric sensing of dermal ISF. **(a)** Image of the 3D-printed MNs prepared by projection micro stereolithography **(b)** Schematic representation of the fabrication process of the MNs by projection micro stereolithography. **(c)** Representative microscopy images of a MN patch with two built-in microchannels per needle (MN-2). Scale bar, top: 500 μm, bottom: 2 mm. **(d)** SEM images of 3D-printed MNs. The bottom right-hand side image displays the obtained diameter of ~5 μm for MN tips (top: MN-3 and bottom: MN-5). Scale bars, left: 200 μm, right: 5 μm. **(e)** Schematic illustration of the ISF collection using 3D-printed MNs. **(f)** Exploded view illustration of the different layers of the colorimetric patch. **(g)** Top and side view of the

assembled colorimetric patch for urea and pH detection (left side) and color change of the colorimetric assays (right side).

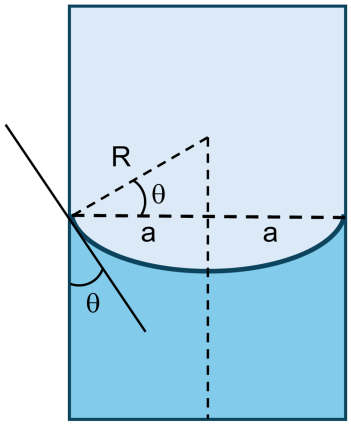


Figure 3.15. Capillary rise and the resulting meniscus inside a tube with wetting angle less than 90°.

3.3.3 Mechanical performance of the 3D-printed MNs

To determine whether the as-fabricated MNs can tolerate the required compressive and shear forces to penetrate the skin without breakage, we investigated the mechanical performance of MN patches composed of 5×5 arrays of MNs. Smooth force-displacement curves of solid and HMNs (base diameter of 500 μm) (**Figure 3.16a**) with no evidence of fracture under compression loads of up to 0.40 N per needle (**Figure 3.16b**) verify the mechanical strength of the MNs to puncture the skin without mechanical yielding [157], [264].

Over the last decades, a wide variety of needle designs have been proposed and fabricated by employing different techniques such as CNC machining, 3D printing, molding, etc. [28], [76], [125]. These MNs have been mainly utilized for therapeutic or diagnostics purposes, and various materials such as metals, glass, silicon, and polymers have been used to fabricate the MNs with feature sizes ranging from sub-micron to millimeters [47]–[50]. Despite several designs and configurations of MNs, not all of them are capable of successful penetration into skin. Therefore, it would be helpful to use theoretical models that can predict the required insertion and fracture forces for different types of MNs based on their geometry. According to the literature, the insertion force of solid MNs with tip radius of 30–80 μm can be predicted via the following equation [157], [264]:

$$F = 0.00019A - 0.66 \quad (3.4)$$

where F is the insertion force (N) and A is the cross-sectional area of the needle (μm^2). By using Eq. (3.4), and assuming the maximum needle tip radius of the utilized MNs in this study is in the range of 5–40 μm, the insertion force is in the range of 0.08–0.295 N per needle.

The resulting deformation of MN tips was measured as 35.76 ± 14.50 μm and 44.50 ± 6.63 μm for solid and HMNs, respectively, indicating similar behavior of both MN types under compressive load. MNs with a 300 μm base diameter showed weaker mechanical strength, with an average failure force of 0.12 N (**Figure 3.5**), which might be sufficient to penetrate the skin considering the small tip diameter of the MNs (5 μm). As evidenced by the shear testing data (**Figure 3.16c,d** and **Figure 3.6**), although solid MNs (MN-1) showed superior mechanical performance compared to HMNs (MN-3 and MN-5), the fracture force of the HMNs revealed their acceptable performance to withstand mild shear forces after application. The fracture forces under shear load for MN-3 and MN-5 were 0.79 ± 0.14 and 0.70 ± 0.03 N per needle, respectively. The negligible net displacement at the end of the shear cycle indicates the capability of the 3D-printed HMNs to preserve their structural integrity. The insertion study revealed that less than 0.10 N per needle was required for complete penetration of the MNs (**Figure 3.16e** and **Figure 3.7**). Moreover, the MNs demonstrated sufficient robustness against multiple skin insertions (**Figure 3.16f**). Collectively, the mechanical characterization and skin insertion studies confirmed the robustness of the 3D-printed MNs against disruptive forces relevant to various dermal applications.

3.3.4 Surface modification and biocompatibility of the MNs

Despite the widespread implementation of 3D-printed MNs for transdermal applications [18], [62], [125], the hydrophobic nature of most polymer-based MNs hinders their usage in many real-life biomedical applications, especially for ISF extraction. Improving the wettability of HMNs could expedite ISF collection and help ensure a continuous fluid flow. Several studies have employed various modification approaches to enhance the hydrophilicity of MNs and facilitate ISF extraction [48], [134], In this study, the surface of 3D-printed MN channels was coated with a silicon oxide layer using chemical vapor deposition (CVD) to increase hydrophilicity, thus enhancing ISF flow through the microchannels (**Figure 3.17a,b**). The presence of hydroxyl groups on the surface of SiO_2 coating plays the key role in its

hydrophilic properties. The wettability of the MNs was characterized by measuring the static water contact angle (WCA) before and after treatment. The WCA of MNs decreased from approximately 72° to 9° following oxide coating (P=0.00001), indicating a considerable improvement in hydrophilicity. Additionally, the treated MNs maintained their improved wettability for 4 weeks (**Figure 3.18**). **Figure 3.17c** shows the thickness of the SiO_2 coating on the 3D-printed parts, measured using a stylus profiler. The height difference between bare and coated parts was 1295.84 ± 101.66 nm.

To evaluate the cytotoxicity of the 3D-printed MNs before and after SiO_2 coating, NIH/3T3 cells (mouse embryonic fibroblast cell line) were cultured in the presence of MNs, followed by examination using viability and metabolic activity assays. As shown in **Figure 3.19a,b**, no notable differences were observed between the live/dead images of the control group and MN-immersed groups. Additionally, the cells cultured with MNs in the medium exhibited comparable cell viability to the control group after 24 h and 72 h of immersion in the complete medium, indicating nontoxic effects of the 3D-printed MNs before and after SiO_2 coating (**Figure 3.19c,d**).

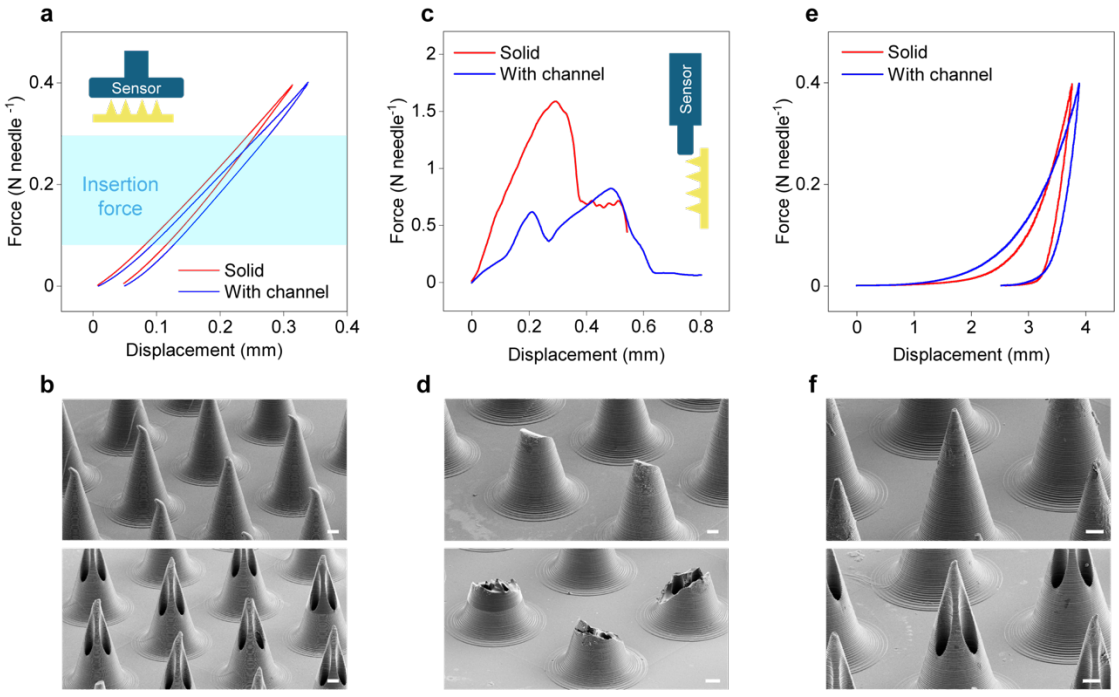


Figure 3.16. Mechanical characterization of the MN patches. (**a**) Mechanical behavior of the MN patches under compressive load with a schematic of the experimental setup (inset). (**b**) SEM images of solid and HMNs after the application of compressive force. (**c**) Mechanical

performance of the MN patches under shear load with a schematic of the test setup (inset). (**d**) SEM images of solid and HMNs after application of shear. (**e**) Mechanical performance of the MN arrays when applied to the skin samples. (**f**) SEM images of MN arrays after skin penetration experiments. (All mechanical characterization experiments and SEM imaging were performed on MNs MN-1 and MN-3, the design of which are provided in **Table 3.1**). Scale bars are 100 µm.

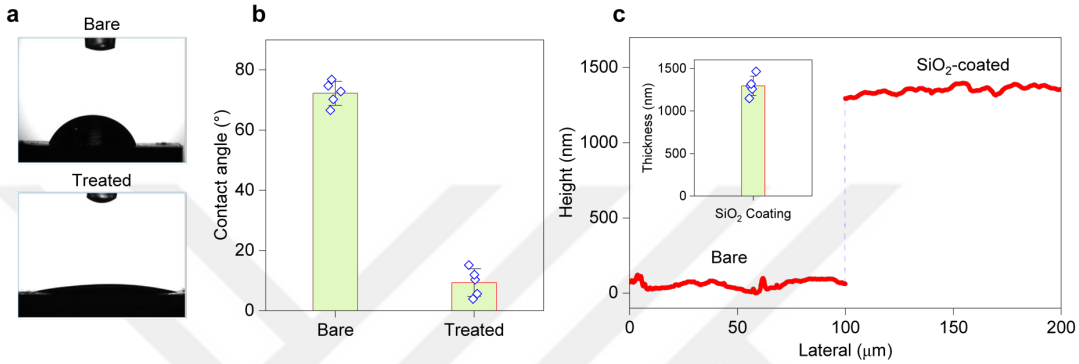


Figure 3.17. Surface modification of 3D-printed MNs to enhance the wettability. **(a)** Images of water droplets on surfaces without (top) and with (bottom) hydrophilic coating. **(b)** The measured contact angle of bare and treated samples. **(c)** Surface profile of the 3D-printed sample after SiO_2 coating. Inset: thickness results of the SiO_2-coated samples. The average thickness was 1295.84 ± 101.66 nm.

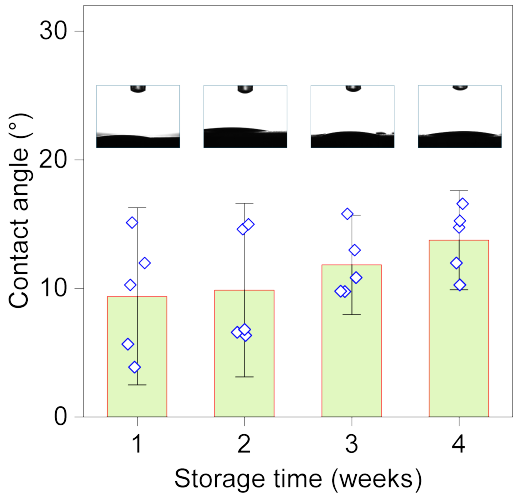


Figure 3.18. Water contact angle of the treated SiO_2-coated samples over time. There was an approximate 4° increase in WCA of the treated MNs over a period of 4 weeks (n=5). Error bars represent mean values ± s.d.

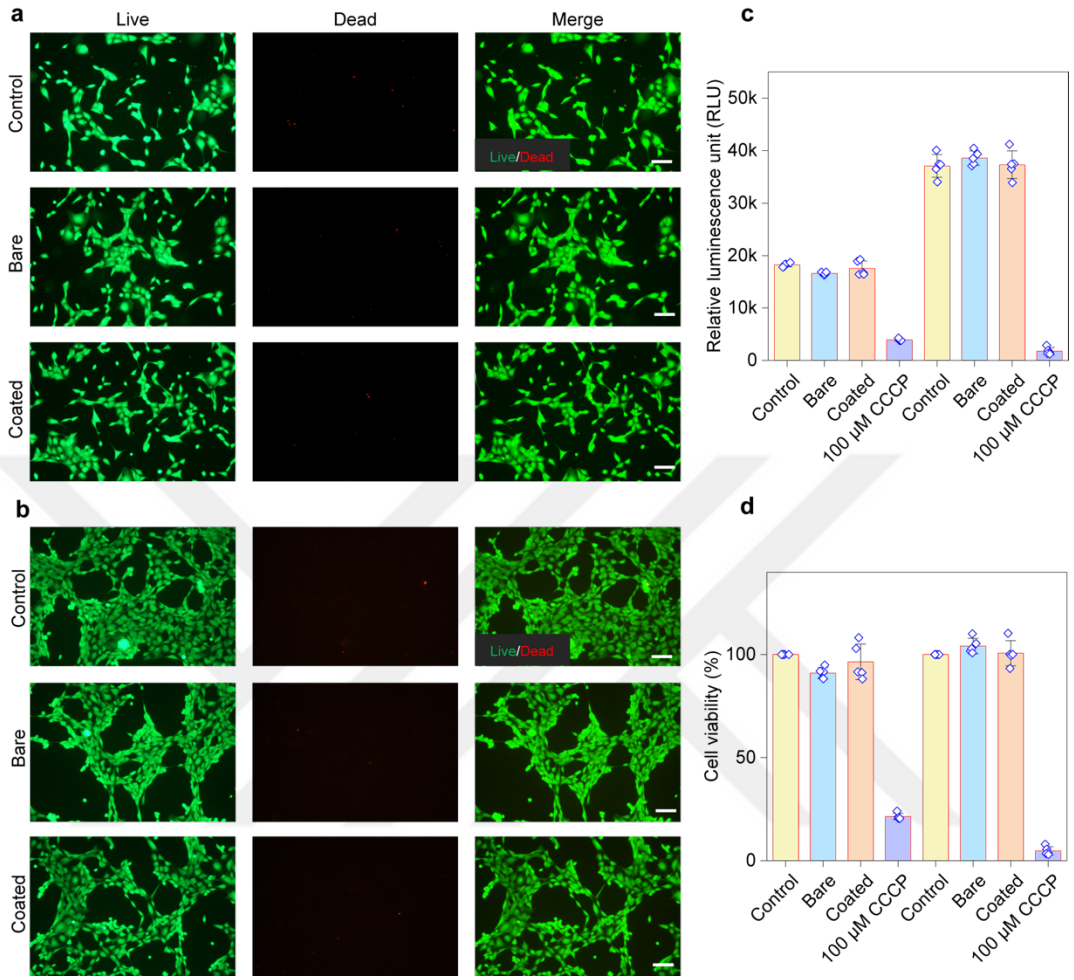


Figure 3.19. In vitro cell cytotoxicity test of the 3D-printed MNs. Representative live (green)/dead (red) images of 3T3 cells after **(a)** 24 h and **(b)** 72 h of cell culture without (control) and with 3D-printed samples (bare and coated). **(c)** Quantitative analysis of cellular metabolic activity, presented in relative luminescence units (RLU). **(d)** Quantitative analysis of cell viability images. Scale bars are 100 μm.

3.3.5 Liquid uptake capability of the MNs

The enhancement in water uptake capability of the MNs was visually observed by inserting them into liquid or agarose gel (**Figure 3.20a,b**, **Figure 3.8** and **Figure 3.9**). To better visualize the liquid flow through microchannels, a MN patch with 10×10 arrays of MNs, length of 1.5 mm, microchannel diameter of 200 μm, and backing thickness of 2 mm was 3D-printed. Briefly, the MNs were inserted into a chamber containing blue-dyed artificial ISF (aISF) or agarose gel. To ensure that liquid extraction from the medium was solely attributed to capillary action within the microchannels, the MNs were carefully positioned to avoid full

insertion into the medium. Additionally, a force sensor was integrated into the experimental setup to monitor the interaction force between the MNs and the agarose gel, thus ensuring consistent conditions across experiments (**Figure 3.20c**). The measured force was approximately 0.45 ± 0.04 N.

Upon insertion, the liquid is drawn into the MN channels due to capillary action and subsequently collected in the integrated microfluidic module. The SiO_2-coated MNs exhibited superior performance in fluid collection when inserted into liquid or agarose gel (**Figure 3.10**–**Figure 3.12**). While bare MNs failed to extract any liquid from agarose gel, the SiO_2-coated microchannels were filled with blue-dyed liquid within a few seconds. As demonstrated in **Figure 3.20c**, the untreated half of the MN patch did not exhibit any water extraction capacity upon insertion into agarose gel, whereas the SiO_2-coated MNs on the same patch initiated liquid extraction immediately upon insertion (**Figure 3.21**). The SiO_2-coated MN patch collected 20.07 ± 1.22 mg and 39.03 ± 1.54 mg of aISF within 1 and 5 min, respectively (**Figure 3.20d**). There was only a minor increase (0.82%) in the amount of collected liquid between time points of 5 and 10 min, indicating that the microfluidic chamber was filled within approximately 5 min. The reduction in the rate of liquid uptake over time could be attributed to the decreased overall capillary driving force as the collected liquid fills the microfluidic chamber. When MNs were inserted into the liquid aISF, the filling time of the integrated microfluidic module was 57.20 ± 11.40 s and 4.03 ± 1.21 s for the bare and treated MNs, respectively, showing a significant decrease (P=0.02) in the required time to collect a certain amount of liquid using the SiO_2-coated MNs (**Figure 3.20e**, left). This improvement can be attributed to the increased wettability of the microchannels. As mentioned earlier, while bare MNs could not extract any liquid from agarose gel, SiO_2-coated MNs filled the microfluidic chamber within 323.90 ± 5.40 s (**Figure 3.20e**, right). As expected, the hydrophilic nature of the agarose gel lowers the rate of liquid uptake, thereby increasing the required time to fill the microfluidic chamber.

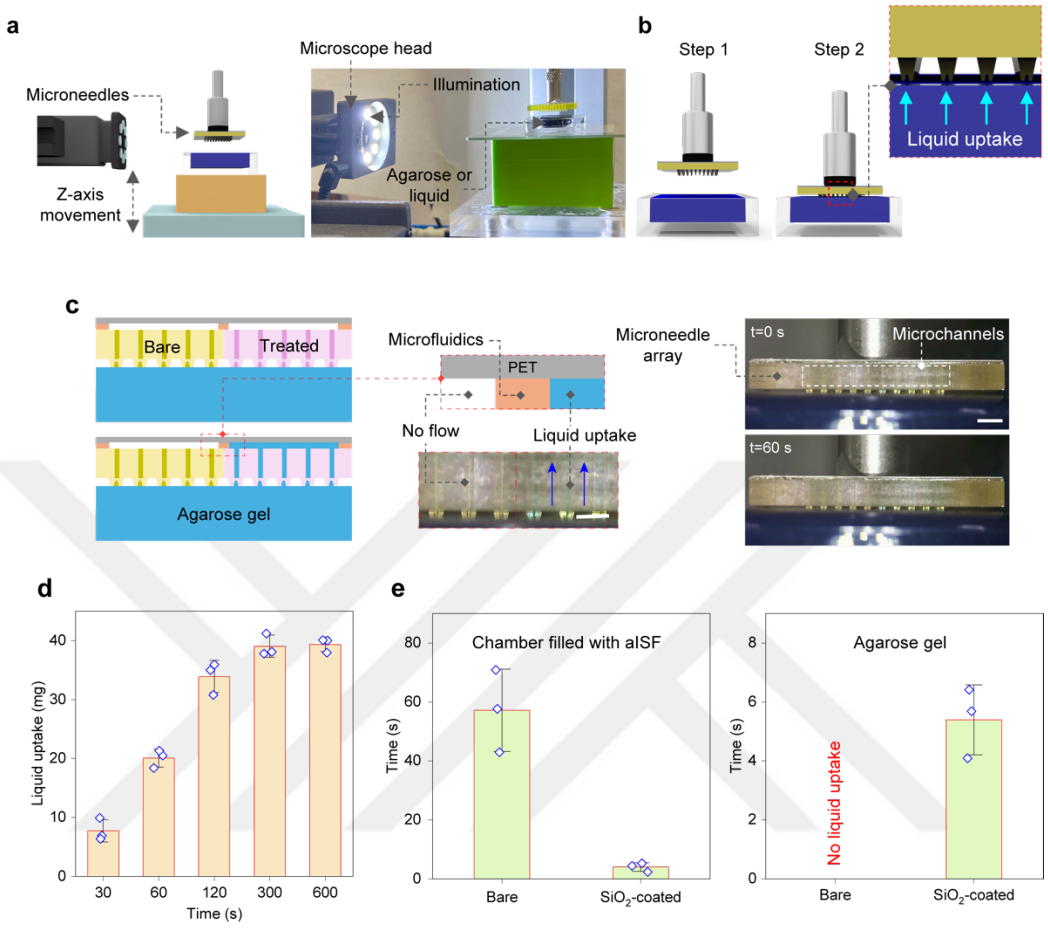


Figure 3.20. In vitro characterization of the liquid extraction capability of the MNs. **(a)** Schematic illustration (left) and photographic image (right) of the liquid uptake setup. **(b)** Liquid uptake experiment. **(c)** Schematic (left) and microscopy images (right) of liquid uptake from agarose gel. **(d)** Liquid uptake of surface modified MNs from agarose gel over different durations. **(e)** The time required for complete filling of the integrated microfluidic chamber by bare and SiO_2-coated MNs. Left: liquid collection from aISF chamber and right: liquid collection from agarose gel. All data are expressed as mean values ± s.d. (n=3). Scale bars are 1 mm.

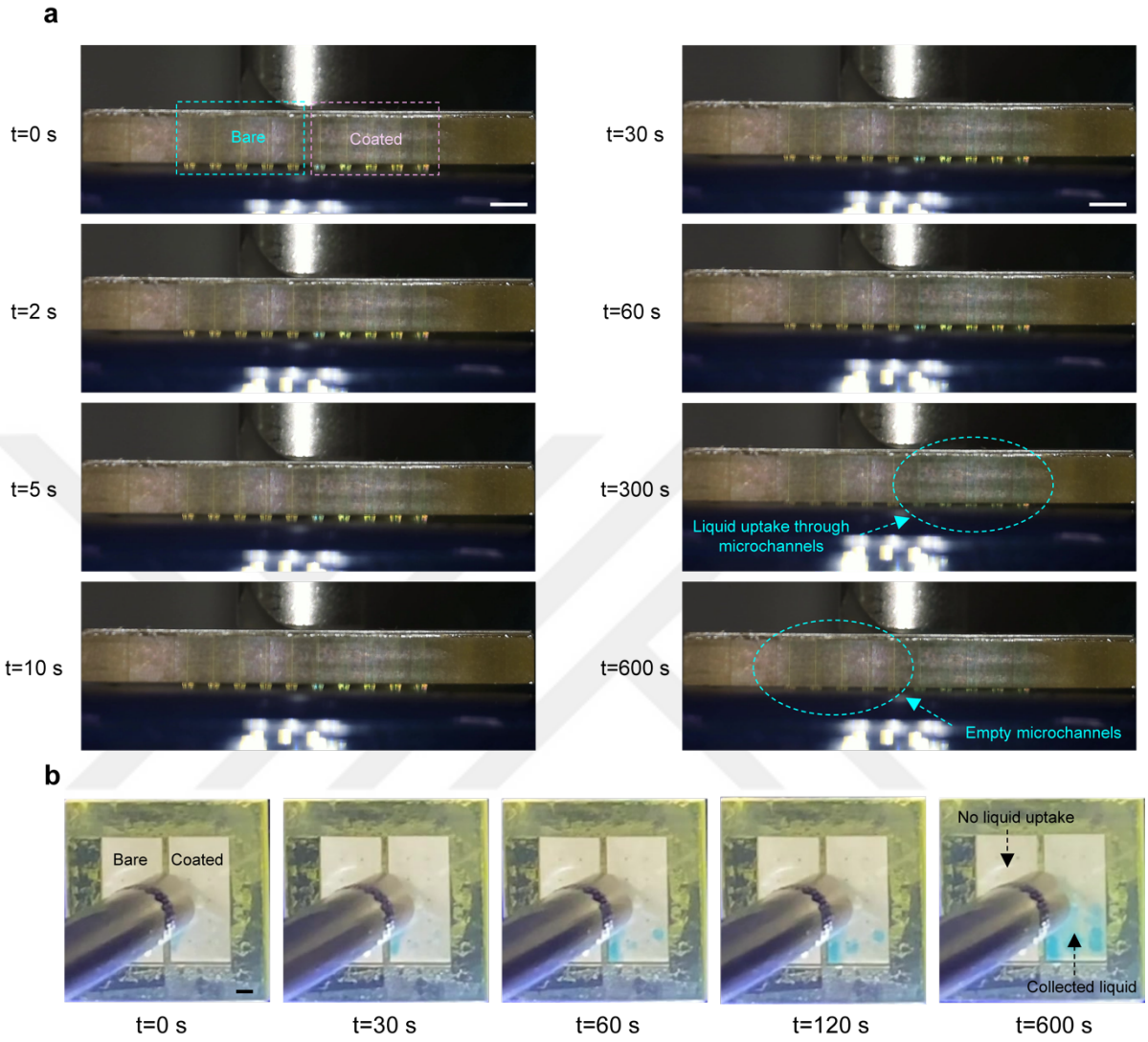


Figure 3.21. Liquid uptake by the half bare/half SiO_2-coated MN patch. **(a)** Liquid flow through microchannels. **(b)** Photos of microfluidic chamber integrated to the backside of the MNs. Scale bars are 1 mm.

3.3.6 In vitro and ex vivo parametric study on liquid uptake

First, we studied the effect of different parameters on ISF collection from agarose hydrogel. The experimental setup for *in vitro* experiments comprised a transparent chamber containing blue-stained agarose hydrogel, a MN patch, and a vacuum source (**Figure 3.22a**). To explore the effect of applied vacuum on the liquid collection, the vacuum pressure was varied between -2 and -20 kPa. As discussed earlier, bare MNs were unable to collect any liquid from agarose hydrogel by capillary force. Vacuum pressures down to -5 kPa was insufficient to initiate the

liquid flow through the microchannels. However, increasing the vacuum level to below -10 kPa enabled the MNs to extract liquid from agarose gel. For a vacuum pressure of -10 kPa, the collected liquid increased from 6.56 ± 0.89 mg to 24.85 ± 2.62 mg when the extraction time increased from 30 s to 120 s (**Figure 3.22b**). Upon application of a vacuum pressure of -20 kPa, the collected liquid almost doubled (**Figure 3.22c**). While 13.60 ± 1.71 mg of liquid was collected after 60 s for -10 kPa, the corresponding value was 24.70 ± 1.66 mg at -20 kPa, representing an 81.6% increase in liquid extraction due to the reduced vacuum pressure. Given the laminar flow inside the needle microchannels, these results are in good agreement with the classical Hagen-Poiseuille model.

To be able to specify the type of fluid flow inside the needle microchannels, the dimensionless Reynolds number was used:

$$\mathrm{Re} = \frac{\rho V D}{\mu} \tag{3.5}$$

where ρ, V, D, and μ are the fluid density, velocity, channel diameter, and dynamic viscosity, respectively.

Given the diameter of 100 μm for the needle microchannels, for fluid flow to be laminar inside the microchannels:

Laminar flow: Re < 2000

$$\frac{1000(kg.m^{-3}) \times V(m.s^{-1}) \times 10^{-4}(m)}{0.001(Pa.s)} < 2000 \quad \Rightarrow \quad V < 20\ m.s^{-1}$$

Considering the velocity of 20 $m.s^{-1}$ is beyond the real liquid velocity which was observed during in vitro extraction experiments, the fluid flow inside the microchannels was assumed to be laminar.

According to Hagen-Poiseuille's law, for a laminar flow inside channels, the relationship between pressure difference and liquid flow rate can be written as follows:

Poiseuille's law: $$\Delta P = \frac{128 Q \mu L}{\pi D^4} \tag{3.6}$$

where Δp, Q, and L are the pressure difference, liquid flow rate, and channel length. According to Eq. (3.6), the relationship between pressure difference and liquid flow rate is linear in laminar flow. ($\Delta p \propto Q$).

To investigate the effect of microchannel number on liquid extraction, MNs were fabricated with designs of 2 and 4 microchannels per needle (MN-2 and MN-3). As illustrated in **Figure 3.22d**, for a vacuum pressure of -10 kPa and an extraction time of 120 s, the liquid uptake increased from 24.85 ± 2.62 mg to 46.77 ± 1.18 mg when the number of microchannels increased from 2 to 4, indicating nearly doubled liquid collection in MNs with 4 microchannels per needle. Similar behavior was observed at a vacuum pressure of -20 kPa (**Figure 3.22e**).

When multiple pipes are connected in a parallel manner, the total liquid flow rate is calculated by summing the liquid flow rates in each pipe as follows:

$$Q_{Tot}=Q_A+Q_B+Q_C \quad (3.7)$$

where Q_{Tot} is the total flow rate and Q_A, Q_B, and Q_C are the liquid flow rates through the three parallel pipes.

In our study, the microchannels in each needle and across the 3D-printed MNs patches are connected in a parallel way. Assuming identical microchannels in all the needles on a MN patch, the liquid flow rate through each needle and the total flow rate during liquid uptake can be calculated as:

$$Q_{Needle}=n\times Q_{Microchannel} \quad (3.8)$$

$$Q_{Total}=m\times Q_{Needle}=nm\times Q_{Microchannel} \quad (3.9)$$

where Q_{Needle}, $Q_{Microchannel}$, are the liquid flow rates through each needle and each microchannel, respectively, and n and m are the number of microchannels per needle and the number of MNs per patch, respectively. Since the microchannels in each needle are connected in a parallel manner, assuming identical channels with the same frictional loss, the liquid uptake rate is linearly correlated with the number of channels.

Next, the effect of SiO_2 coating on enhancing liquid uptake from rat skin samples was examined (**Figure 3.13**). As evidenced in **Figure 3.22f**, bare MNs with a length of 1 mm could not extract any ISF after 30 min under an average vacuum pressure of approximately -40 kPa. This might stem from incomplete penetration of the MNs into the skin, leaving part of the microchannels exposed to air rather than being inside the tissue, as revealed by the formation of suction blisters on the skin samples (**Figure 3.23**). Also, the presence of ISF inside as and around the skin pores after MN removal indicates that the ISF in the dermis was unable to overcome the resistance forces against liquid flow. Increasing the needle length to 1.5 mm

resulted in an ISF extraction rate of 0.18 ± 0.03 mg min^{-1} per MN patch (**Figure 3.23f**). SiO_2-coated MNs showed superior extraction capacity from skin samples. MNs with 2 and 4 channels were able to extract 0.31 ± 0.03 and 0.32 ± 0.04 mg min^{-1} per MN patch (*P=0.007* and *P=0.008*, respectively), confirming the effectivity of the hydrophilic coating on enhancing the ISF extraction. These results suggest that increasing the number of microchannels per needle from 2 to 4 did not have any considerable effect on the amount of extracted ISF from skin samples. As shown in **Figure 3.23f**, although SiO_2 coating increased the ISF extraction rate for MNs with 1.5 mm length from 0.18 ± 0.03 to 0.32 ± 0.03 mg min^{-1} per MN patch, the extraction rate of SiO_2-coated MNs with lengths of 1 mm and 1.5 mm were almost the same.

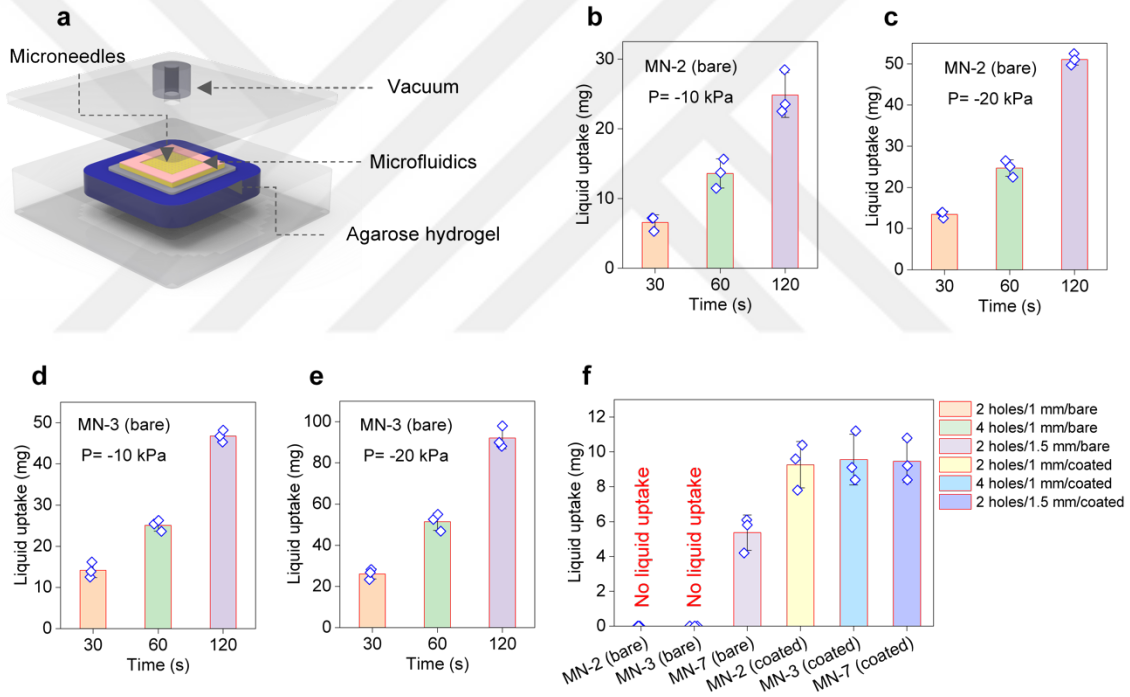


Figure 3.22. Effect of different parameters on the extraction capacity of the MNs. **(a)** Schematic illustration of the setup utilized for the liquid uptake experiments from agarose hydrogel. Liquid uptake by bare MNs with two microchannels using vacuum pressure of **(b)** -10 kPa and **(c)** -20 kPa. Liquid uptake by bare MNs with four microchannels using vacuum pressure of **(d)** -10 kPa and **(e)** -20 kPa. **(f)** Liquid uptake from rat skin samples under a vacuum pressure of -40 kPa after 30 min.

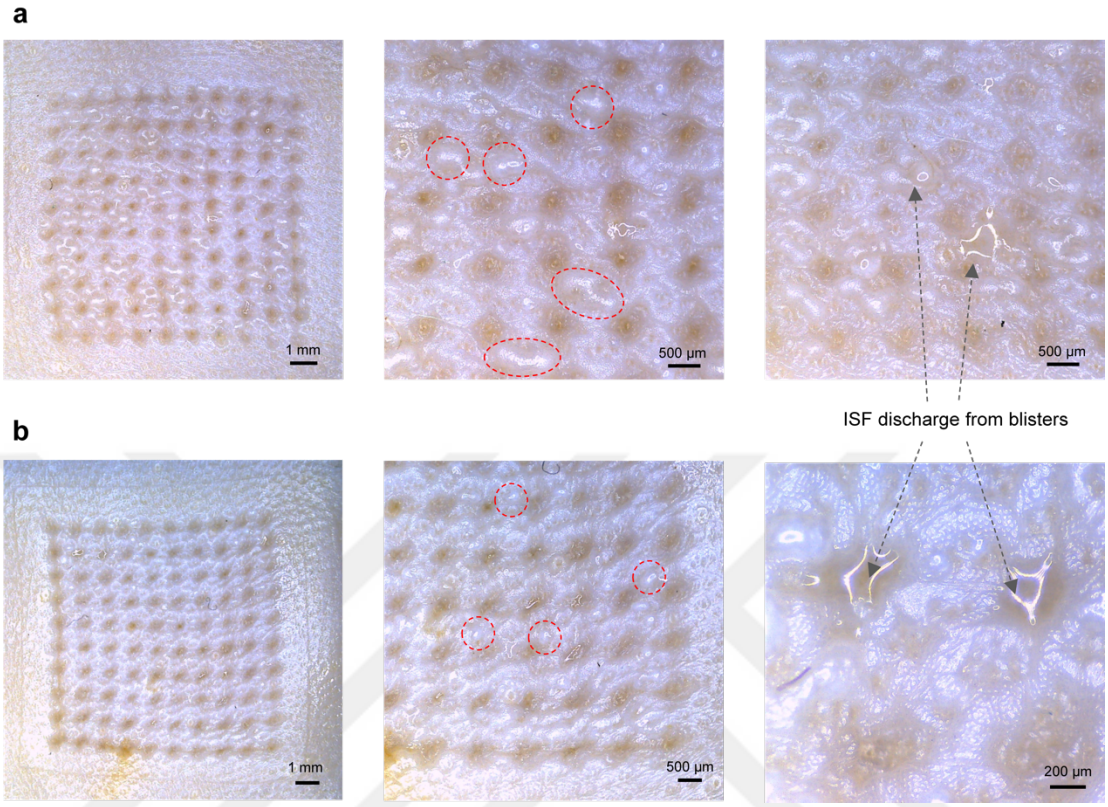


Figure 3.23. Ex vivo ISF extraction from rat skin samples. Microscopic pictures after using **(a)** MN-2 (2 microchannels) and **(b)** M-3 (4 microchannels). The experiments were performed for 1 hour under an average vacuum pressure of -40 kPa. Red circles in the images show the created blisters caused by the applied vacuum. Later, the blisters were pierced using an insulin needle, an as can be observed in the images, the ISF inside the blisters is discharged.

3.3.7 Quantitative colorimetric analysis and detection of biomarkers

As previously illustrated, the developed MN patches offer great promise for minimally invasive and effective ISF extraction, enabling colorimetric analysis of various biomarkers in ISF. For proof-of-concept demonstration, urea and pH were selected as the target biomarkers. Both of these biomarkers could provide crucial information associated with health problems such as kidney and renal malfunctions. For healthy individuals, the normal urea level ranges from 3 to 7.5 mM, whereas for patients with chronic kidney dysfunctions, the urea level might elevate up to 8–15.1 mM [265], [266]. While the normal blood pH level is maintained between 7.35 and 7.45 by pH buffering substances like proteins and phosphates [224], due to the lack of buffering capacity in ISF, the pH of ISF can deviate from the normal range (6.6–7.6) [224],

[267]. For instance, the pH level ranges from 5.45 to 8.65 in chronic wounds, and it may decrease to 5.4 in inflamed tissues [268], [269].

Most of the previously reported methods for measuring urea rely on electrochemical sensors [168], [270], NMR [271] or HPLC [272]. The colorimetric method implemented here for the detection of urea is based on the pH rise resulting from urease-catalyzed hydrolysis of urea, thereby releasing ammonium and hydroxide ions into the solution [273]:

$$NH_2(CO)NH_2 + 3H_2O \xrightarrow{\text{Urease}} 2NH_4^+ + HCO_3^- + OH^-$$

By immobilizing urease onto colorimetric pH papers, the hydrolysis reaction of urea is effectively catalyzed, thus altering the pH level and color of the pH paper. The resulting changes in the color intensity of the pH papers are well-correlated to the urea concentration. The detection range for urea was selected between 1 and 20 mM, relevant to physiological urea concentrations in ISF under normal or disease states. As shown in **Figure 3.24a**, the color of sensing regions changed from dark green to dark blue when the urea concentration increased from 1 to 20 mM. Quantitative analysis of RGB values in the captured images showed a decrease in intensities at the R and G channels and an increase in B channel with increasing urea concentrations. Since the B channel intensity values exhibited the most significant changes with urea concentration, the B channel was selected for quantification. During the detection of pH, the color changed from browny green to dark blue, as the pH increased from 6.45 to 8.20, relevant to the physiological pH level in ISF (**Figure 3.24b**).

The corresponding calibration curve for urea detection showed a linear behavior with the correlation coefficient of R^2 = 0.98 and limit of detection (LOD=3.3σ/S, where σ is the standard deviation and S is the slope of calibration curve) of 0.83 mM (**Figure 3.24c**). Quantitative analysis of the captured images showed a linear decrease (correlation coefficient of 0.98) in R channel intensity values with increasing pH (**Figure 3.24d**). Although the rate of urea hydrolysis into ammonium and hydroxide can be affected by the solution pH [274], thus influencing the required incubation period, the final RGB intensities across different urea concentrations were not affected considerably by the solution pH (**Figure 3.24e**). We further characterized the performance of the colorimetric urea assay against the presence of possible interferents in ISF. As evidenced by the results presented in **Figure 3.24f**, the color of urea assay was negligibly influenced upon addition of target interferents.

Next, the colorimetric assays were integrated with the 3D-printed MNs to validate the performance of the developed technique for biomarker detection in the extracted ISF. Agarose hydrogel was selected as the skin model to mimic the penetration of MNs into the skin. Due to the improved water extraction capacity of the SiO_2-coated MNs owing to their enhanced hydrophilicity, they were inserted into the agarose hydrogel without using vacuum pressure. As shown in **Figure 3.24g,h**, there was a good agreement between the detected urea and pH levels and the actual values. Finally, the MN patch with the colorimetric assays was inserted into equilibrated skin samples to detect the urea and pH level. Once the extracted ISF came into contact with the colorimetric assays, the color change showed the urea and pH levels (**Figure 3.24i**). Overall, the colorimetric results revealed the great potential of integrating colorimetric assays into superhydrophilic MNs with passive ISF extraction capability for urea and pH sensing.

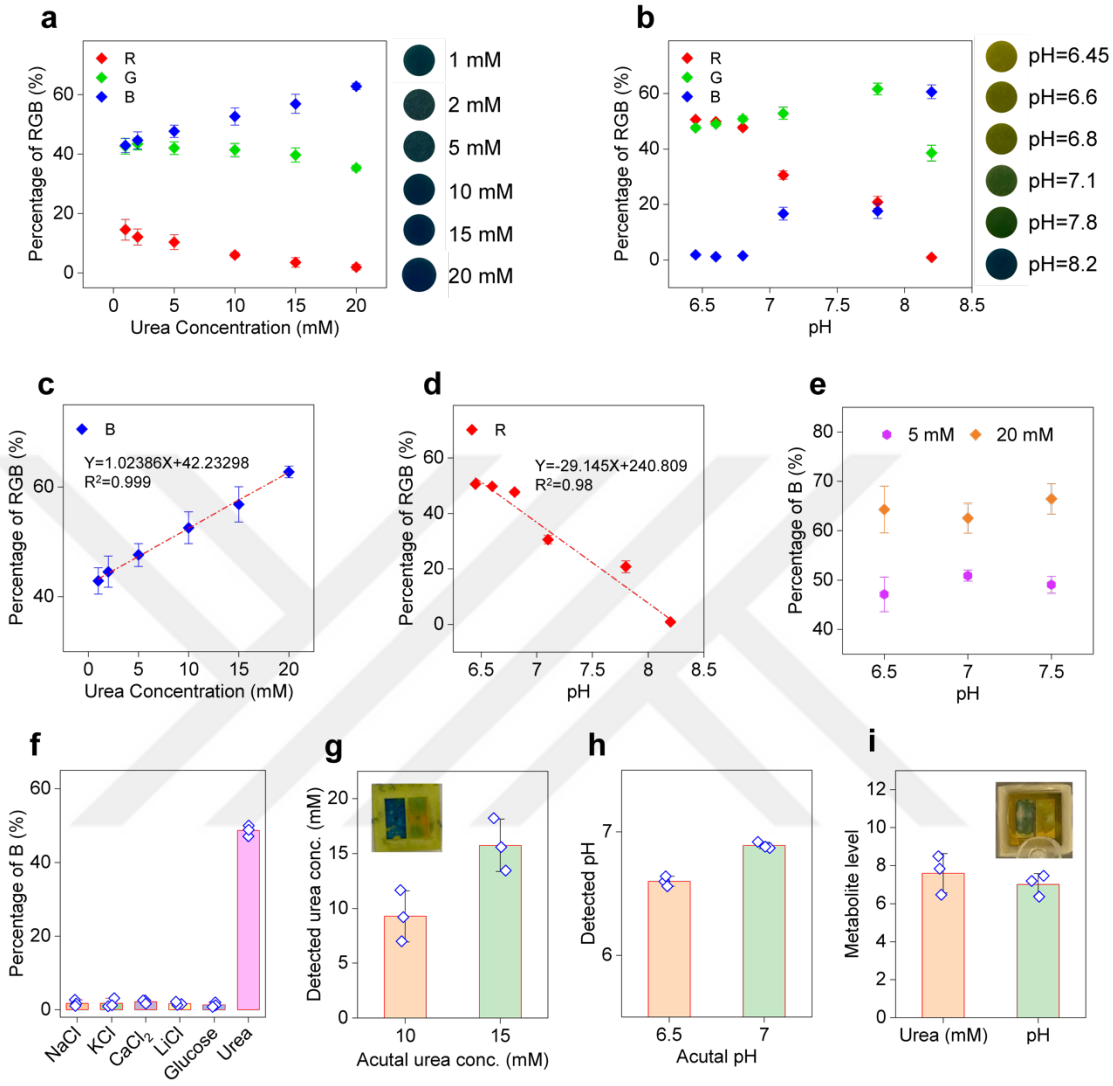


Figure 3.24. Colorimetric detection of urea and pH. Colors and RGB intensities during the detection of **(a)** urea and **(b)** pH. **(c)** The linear correlation between the intensity of B and urea concentration. **(d)** The linear correlation between the intensity of R and pH level. **(e)** Effect of pH on the urea detection. **(f)** Response of the urea assay against various interferents. **(g)** In vitro urea detection on agarose gel with pH of 7. **(h)** In vitro pH detection on agarose gel with urea concentration of 10 mM. **(i)** Ex vivo response of the urea and pH assays and urea on rat skin. All data are expressed as mean values ± s.d. (n=3).

3.4 Conclusions

In this chapter, we developed a 3D-printed MN patch with superhydrophilic microchannels to effectively and continuously extract dermal ISF for health monitoring applications. Conical HMNs with different lengths, base diameters, and microchannel counts were printed via high-precision PμSL technology using a biocompatible resin. Mechanical testing experiments

revealed the excellent mechanical resistance of the MNs against disruptive forces. Cytotoxicity experiments validated the biocompatibility of the 3D-printed MN patches before and after oxide layer deposition. To enhance hydrophilicity, we deposited a thin SiO_2 layer on the MN patch and decreased its static water contact angle from approximately 72° to 9°. The hydrophilic coating endowed the MNs with liquid uptake capability from agarose hydrogel. Although increasing the number of microchannels per needle from 2 to 4 greatly enhanced the extraction capability of the MNs *in vitro*, there was negligible effect on the extraction rate from the rat skin samples. Hydrophilic MNs with a height of 1 mm showed superior ISF extraction capability from rat skin samples compared to the bare MNs. However, increasing the height of SiO_2-coated MNs from 1 to 1.5 mm did not result in an increase in ISF extraction from the skin samples. The SiO_2-coated MNs extracted approximately 0.3 mg min^{-1} per patch, confirming its effectiveness for ISF sampling-based health monitoring devices. We successfully demonstrated the applicability of the platform for detecting ISF biomarkers by integrating a microfluidic module and colorimetric assays for urea and pH. Upon ISF extraction from rat skin samples, the urea and pH levels in the ISF were measured by recording the RGB values of the colorimetric assays. This hydrophilic MN patch could be integrated into various ISF-based devices to expand its application for detecting a wide spectrum of biomarkers in ISF and holds a significant promise to benefit health monitoring and disease management.

4 Chapter Four: Conclusion and Future Outlook

4.1 Summary and Conclusions

The growing demand for personalized health monitoring devices has brought about rapid development of numerous wearable devices for real-time detection of different health-related biomarkers. Dermal ISF, which is a rich source of different biomarkers with similar concentrations to that of blood, has emerged as the target biofluid for many health monitoring devices. While many efforts have focused on the development of MN-based in-skin electrochemical sensing, there are still several unmet issues associated with these systems, such as unreliable penetration of all the MNs, biofouling, and sensor instability. Alternatively, HMNs can be used to collect biofluid samples within a microfluidic chamber, where the target biomarkers come in contact with electrochemical or optical sensors. This thesis has summarized our endeavors to develop wearable devices integrated with HMNs ISF extraction and sensing.

We have leveraged the self-recovery feature of PDMS to develop a wearable finger-activated vacuum generation device capable of reaching the minimum negative pressure for ISF extraction. Unlike other finger-actuated vacuum pumps in the literature, the special design of the vacuum generation system with the addition of two check valves enabled a stepwise reduction in the vacuum pressure and fine adjustment of the pressure inside the system. Moreover, this resulted in a controlled collection of the extracted ISF in the microfluidic chamber. Integration of hot embossing and laser-drilling for fabricating polycarbonate HMNs enabled fast fabrication of the desired MNs at low cost. The employed UV-based laser was able to precisely open through MNs in the polymeric MNs, forming the final HMNs. We demonstrated the applicability of the developed platform for continuous monitoring by real-time in vivo measuring of the glucose and pH in animal models. Our parametric study showed that, depending on the number of needles on the MN patch and the applied pressure, the platform is capable of collecting ISF in the range of 17 $\mu L\ h^{-1}$. The integrated microfluidic

module provided the necessary contact between the sampled ISF and electrochemical glucose and pH sensors.

Next, in Chapter three, we developed a multichannel 3D-printed hydrophilic HMN platform for ISF sampling. The fabricated MNs featured highly sharp tips (tip diameter of less than 5 μm), comparable to that of silicon and 2PP-fabricated MNs. Moreover, PμSL technology enabled the fabrication of carefully-tailored multichannel MNs. Hydrophilic microchannels were realized by PECDV-coating of a thin SiO_2 layer on the surface of the 3D-printed parts. Consequently, the contact angle was decreased from 72° to 9°, showing the enhanced wettability of the MNs caused by the oxide layer. The hydrophilic multichannel MNs exhibited enhanced performance in liquid uptake from the agarose gel and skin models. We further demonstrated the applicability of the HMN-based system by integrating colorimetric assays for the detection of pH and urea.

In summary, both laser-drilled and 3D-printed HMNs showed great promise in integration into health monitoring devices. While the finger-actuated vacuum system can be worn by the user, enabling the development of a fully wearable ISF extraction device, hydrophilic HMNs obviate the need for an external force to draw ISF out of the dermis. We showed that by integrating microfluidic modules into HMNs, both electrochemical and optical sensors can be used for the detection of the target biomarkers.

4.2 Future Directions

While the aforementioned innovations assisted in the development of HMN-based sampling and sensing devices, there are still lingering unmet challenges associated with these devices that need to be addressed before integrating ISF extraction devices with sensing platforms for clinical applications. Further research could be conducted to enhance the ISF extraction rate from the dermis, as most of the developed HMN-based devices have shown low extraction capacities (<20 μm). Increasing the ISF collection rate allows for high-precision ex situ measurement of the target biomarkers. Additionally, further studies should be carried out to establish the correlation between the concentration of different analytes in ISF and blood. Moreover, by performing ISF extraction experiments using different designs of MNs, the effect of MN structure, such as length, channel diameter, and number of microchannels, on the amount of collected ISF can be investigated. Although the application

of vacuum pressure provides the necessary driving force for drawing dermal ISF, the decreased pressure leads to an increased evaporation rate. Therefore, for future experiments, it is necessary to evaluate the effect of vacuum on ISF evaporation in the system and the resulting change in the concentration of biomarkers.

The development of closed-loop systems is another area that requires investigation, as no such system has yet been established using HMN-based ISF sampling devices. Closed-loop systems could provide strong control over the disease by automatic monitoring of the biomarkers and rapid response of the drug delivery system. For this purpose, artificial intelligence can significantly contribute to the optimal performance of the device.

Although there has been a growing interest in the implementation of MNs for health monitoring devices, to the best of our knowledge, currently, there is no FDA-approved commercially available MN-based biomarker monitoring device. This may be attributed to the unresolved challenges associated with solid MN-based in situ devices. However, these issues can be partially mitigated by employing HMNs. For instance, as the electrochemical sensors are integrated into microfluidic modules rather than positioned on the surface of MNs, concerns regarding the inconsistent penetration of MNs into the device are minimal. Ultimately, further in vivo and clinical experiments should be performed to investigate the shortcomings of MN-based sensing devices, thus paving the way for the incorporation of these platforms in our daily healthcare system.

BIBLIOGRAPHY

[1] W. Montagna, *The structure and function of skin*. Elsevier, 2012.

[2] H. A. E. Benson and A. C. Watkinson, *Topical and transdermal drug delivery: principles and practice*. John Wiley & Sons, 2012.

[3] M. Friedel *et al.*, "Opportunities and challenges in the diagnostic utility of dermal interstitial fluid," *Nat. Biomed. Eng.*, pp. 1–15, 2023.

[4] W. Groenendaal *et al.*, "Quantifying the composition of human skin for glucose sensor development." Sage Publications Sage CA: Los Angeles, CA, 2010.

[5] P. M. Elias, "Epidermal lipids, membranes, and keratinization.," *Int. J. Dermatol.*, vol. 20, no. 1, 1981.

[6] A. S. Michaels *et al.*, "Drug permeation through human skin: theory and in vitro experimental measurement," *AIChE J.*, vol. 21, no. 5, pp. 985–996, 1975.

[7] B. Amirlak *et al.*, "Skin anatomy," *Medscape Ref*, vol. 1, p. 7, 2013.

[8] P. Humbert *et al.*, *Agache's measuring the skin*. Springer International Publishing New York, 2019.

[9] K. Aukland and G. Nicolaysen, "Interstitial fluid volume: local regulatory mechanisms.," *Physiol. Rev.*, vol. 61, no. 3, pp. 556–643, 1981.

[10] J. Scallan and V. Huxley, "Capillary fluid exchange: regulation, functions, and pathology," 2009.

[11] A. C. Shore, "Capillaroscopy and the measurement of capillary pressure," *Br. J. Clin. Pharmacol.*, vol. 50, no. 6, pp. 501–513, 2000.

[12] R. H. Stewart, "A modern view of the interstitial space in health and disease," *Front. Vet. Sci.*, vol. 7, p. 609583, 2020.

[13] H. Wiig *et al.*, "Interstitial fluid pressure, composition of interstitium, and interstitial exclusion of albumin in hypothyroid rats," *Am. J. Physiol. Circ. Physiol.*, vol. 278, no. 5, pp. H1627–H1639, 2000.

[14] N. Fogh-Andersen *et al.*, "Composition of interstitial fluid," *Clin. Chem.*, vol. 41, no. 10, pp. 1522–1525, 1995.

[15] J. H. Bauer and C. S. Brooks, "Body-fluid composition in normal and hypertensive man.," *Clin. Sci. (London, Engl. 1979)*, vol. 62, no. 1, pp. 43–49, 1982.

[16] R. Ibrahim *et al.*, "Dermal clearance model for epidermal bioavailability calculations," *J. Pharm. Sci.*, vol. 101, no. 6, pp. 2094–2108, 2012.

[17] J. Heikenfeld *et al.*, "Accessing analytes in biofluids for peripheral biochemical monitoring," *Nat. Biotechnol.*, vol. 37, no. 4, pp. 407–419, 2019.

[18] H. Teymourian *et al.*, "Lab under the skin: microneedle based wearable devices," *Adv. Healthc. Mater.*, vol. 10, no. 17, p. 2002255, 2021.

[19] A. C. Müller *et al.*, "A comparative proteomic study of human skin suction blister fluid from healthy individuals using immunodepletion and iTRAQ labeling," *J. Proteome Res.*, vol. 11, no. 7, pp. 3715–3727, 2012.

[20] D. Al Sulaiman *et al.*, "Hydrogel-Coated Microneedle Arrays for Minimally Invasive Sampling and Sensing of Specific Circulating Nucleic Acids from Skin Interstitial Fluid," *ACS Nano*, vol. 13, no. 8, pp. 9620–9628, Aug. 2019.

[21] H. Sun *et al.*, "Wearable Clinic: From Microneedle-Based Sensors to Next-Generation Healthcare Platforms," *Small*, p. 2207539, 2023.

[22] D. D. Zhu *et al.*, "Microneedle-Coupled Epidermal Sensors for In-Situ-Multiplexed Ion Detection in Interstitial Fluids," *ACS Appl. Mater. Interfaces*, 2023.

[23] Á. Cárcamo-Martínez *et al.*, "Hollow microneedles: A perspective in biomedical applications," *Int. J. Pharm.*, vol. 599, p. 120455, Apr. 2021.

[24] K. M. Saifullah and Z. Faraji Rad, "Sampling Dermal Interstitial Fluid Using Microneedles: A Review of Recent Developments in Sampling Methods and Microneedle-Based Biosensors," *Adv. Mater. Interfaces*, p. 2201763, 2023.

[25] G. S. Liu *et al.*, "Microneedles for transdermal diagnostics: Recent advances and new horizons," *Biomaterials*, vol. 232. Elsevier Ltd, p. 119740, Feb. 01, 2020.

[26] W. H. Smart and K. Subramanian, "The use of silicon microfabrication technology in painless blood glucose monitoring," *Diabetes Technol. Ther.*, vol. 2, no. 4, pp. 549–559, 2000.

[27] E. V Mukerjee *et al.*, "Microneedle array for transdermal biological fluid extraction and in situ analysis," *Sensors Actuators A Phys.*, vol. 114, no. 2–3, pp. 267–275, 2004.

[28] F. Tehrani *et al.*, "An integrated wearable microneedle array for the continuous monitoring of multiple biomarkers in interstitial fluid," *Nat. Biomed. Eng.*, pp. 1–11, 2022.

[29] J. J. García-Guzmán *et al.*, "Toward in Vivo Transdermal pH Sensing with a Validated Microneedle Membrane Electrode," *ACS Sensors*, vol. 6, no. 3, pp. 1129–1137, 2021.

[30] M. Parrilla *et al.*, "Wearable all-solid-state potentiometric microneedle patch for intradermal potassium detection," *Anal. Chem.*, vol. 91, no. 2, pp. 1578–1586, 2018.

[31] Y. Yang and W. Gao, "Wearable and flexible electronics for continuous molecular monitoring," *Chem. Soc. Rev.*, vol. 48, no. 6, pp. 1465–1491, Mar. 2019.

[32] P. P. Samant *et al.*, "Sampling interstitial fluid from human skin using a microneedle patch," *Sci. Transl. Med.*, vol. 12, no. 571, p. eaaw0285, 2020.

[33] S. Lin *et al.*, "Wearable microneedle-based electrochemical aptamer biosensing for precision dosing of drugs with narrow therapeutic windows," *Sci. Adv.*, vol. 8, no. 38, p. eabq4539, 2022.

[34] Y. Cheng *et al.*, "A touch-actuated glucose sensor fully integrated with microneedle array and reverse iontophoresis for diabetes monitoring," *Biosens. Bioelectron.*, p. 114026, Jan. 2022.

[35] D. D. Zhu *et al.*, "Colorimetric microneedle patches for multiplexed transdermal detection of metabolites," *Biosens. Bioelectron.*, vol. 212, p. 114412, Sep. 2022.

[36] M. Zheng *et al.*, "Osmosis-Powered Hydrogel Microneedles for Microliters of Skin Interstitial Fluid Extraction within Minutes," *Adv. Healthc. Mater.*, vol. 9, no. 10, p. 1901683, May 2020.

[37] H. Huang *et al.*, "A microneedle patch for breast cancer screening via minimally invasive interstitial fluid sampling," *Chem. Eng. J.*, vol. 472, no. July, p. 145036, 2023.

[38] Y.-C. Hsieh *et al.*, "Controllable-Swelling Microneedle–Assisted Ultrasensitive Paper Sensing Platforms for Personal Health Monitoring," *Adv. Healthc. Mater.*, p. 2300321, Apr. 2023.

[39] Q. Wang *et al.*, "A hydrogel-based biosensor for stable detection of glucose," *Biosens. Bioelectron.*, vol. 221, p. 114908, 2023.

[40] J. Yang *et al.*, "Masticatory system–inspired microneedle theranostic platform for intelligent and precise diabetic management," *Sci. Adv.*, vol. 8, no. 50, p. eabo6900, 2022.

[41] X. Li *et al.*, "A Fully Integrated Closed-Loop System Based on Mesoporous Microneedles-Iontophoresis for Diabetes Treatment," *Adv. Sci.*, vol. 8, no. 16, p. 2100827, Aug. 2021.

[42] S. Kusama *et al.*, "Transdermal electroosmotic flow generated by a porous microneedle

array patch," *Nat. Commun.*, vol. 12, no. 1, p. 658, 2021.

[43] E. Larrañeta *et al.*, "Microneedle arrays as transdermal and intradermal drug delivery systems: Materials science, manufacture and commercial development," *Mater. Sci. Eng. R Reports*, vol. 104, pp. 1–32, 2016.

[44] Y.-C. Kim *et al.*, "Microneedles for drug and vaccine delivery," *Adv. Drug Deliv. Rev.*, vol. 64, no. 14, pp. 1547–1568, 2012.

[45] L. K. Vora *et al.*, "Microneedle-based biosensing," *Nat. Rev. Bioeng.*, vol. 2, no. 1, pp. 64–81, 2023.

[46] W. Xue *et al.*, "Developing porous microneedles patch for the detection of wound infections," *Adv. Mater. Technol.*, vol. 9, no. 4, p. 2301572, 2024.

[47] T. Abbasiasl *et al.*, "A Wearable Touch-Activated Device Integrated with Hollow Microneedles for Continuous Sampling and Sensing of Dermal Interstitial Fluid," *Adv. Mater.*, vol. 36, no. 2, p. 2304704, Jan. 2024.

[48] P. P. Samant and M. R. Prausnitz, "Mechanisms of sampling interstitial fluid from skin using a microneedle patch," *Proc. Natl. Acad. Sci.*, vol. 115, no. 18, pp. 4583–4588, 2018.

[49] P. M. Wang *et al.*, "Minimally invasive extraction of dermal interstitial fluid for glucose monitoring using microneedles," *Diabetes Technol. Ther.*, vol. 7, no. 1, pp. 131–141, 2005.

[50] Y. Li *et al.*, "Fabrication of sharp silicon hollow microneedles by deep-reactive ion etching towards minimally invasive diagnostics," *Microsystems Nanoeng.*, vol. 5, no. 1, p. 41, 2019.

[51] K. Ita, "Ceramic microneedles and hollow microneedles for transdermal drug delivery: Two decades of research," *J. Drug Deliv. Sci. Technol.*, vol. 44, pp. 314–322, 2018.

[52] M. Dervisevic *et al.*, "Transdermal electrochemical monitoring of glucose via high-density silicon microneedle array patch," *Adv. Funct. Mater.*, vol. 32, no. 3, p. 2009850, 2022.

[53] M. Dervisevic *et al.*, "Wearable microneedle array-based sensor for transdermal monitoring of pH levels in interstitial fluid," *Biosens. Bioelectron.*, vol. 222, p. 114955, 2023.

[54] B. Chua *et al.*, "Effect of microneedles shape on skin penetration and minimally

invasive continuous glucose monitoring in vivo," *Sensors Actuators A Phys.*, vol. 203, pp. 373–381, Dec. 2013.

[55] L. M. Strambini *et al.*, "Self-powered microneedle-based biosensors for pain-free high-accuracy measurement of glycaemia in interstitial fluid," *Biosens. Bioelectron.*, vol. 66, pp. 162–168, Apr. 2015.

[56] A. Jina *et al.*, "Design, development, and evaluation of a novel microneedle array-based continuous glucose monitor," *J. Diabetes Sci. Technol.*, vol. 8, no. 3, pp. 483–487, 2014.

[57] D. Han *et al.*, "4D printing of a bioinspired microneedle array with backward-facing barbs for enhanced tissue adhesion," *Adv. Funct. Mater.*, vol. 30, no. 11, p. 1909197, 2020.

[58] K. Lee *et al.*, "Drawing lithography: three-dimensional fabrication of an ultrahigh-aspect-ratio microneedle," *Adv. Mater.*, vol. 22, no. 4, pp. 483–486, 2010.

[59] W. Li *et al.*, "Rapidly separable microneedle patch for the sustained release of a contraceptive," *Nat. Biomed. Eng.*, vol. 3, no. 3, pp. 220–229, 2019.

[60] K. T. M. Tran *et al.*, "Transdermal microneedles for the programmable burst release of multiple vaccine payloads," *Nat. Biomed. Eng.*, vol. 5, no. 9, pp. 998–1007, 2021.

[61] K. Lee and H. Jung, "Drawing lithography for microneedles: a review of fundamentals and biomedical applications," *Biomaterials*, vol. 33, no. 30, pp. 7309–7326, 2012.

[62] U. Detamornrat *et al.*, "The Role of 3D Printing Technology in Microengineering of Microneedles," *Small*, p. 2106392, Mar. 2022.

[63] M. Starlin Chellathurai *et al.*, "Biodegradable polymeric insulin microneedles–a design and materials perspective review," *Drug Deliv.*, vol. 31, no. 1, p. 2296350, 2024.

[64] Z. Le *et al.*, "Design principles of microneedles for drug delivery and sampling applications," *Mater. Today*, vol. 63, pp. 137–169, 2023.

[65] Z. Karim *et al.*, "Polymeric microneedles for transdermal drug delivery-a review of recent studies," *J. Drug Deliv. Sci. Technol.*, vol. 77, p. 103760, 2022.

[66] Q. Yang *et al.*, "Recent progress of 3D-printed microneedles for transdermal drug delivery," *Int. J. Pharm.*, vol. 593, p. 120106, 2021.

[67] K. Takeuchi *et al.*, "Microfluidic chip to interface porous microneedles for ISF collection," *Biomed. Microdevices*, vol. 21, pp. 1–10, 2019.

[68] X. Jiang and P. B. Lillehoj, "Microneedle-based skin patch for blood-free rapid diagnostic testing," *Microsystems Nanoeng. 2020 61*, vol. 6, no. 1, pp. 1–11, Nov. 2020.

[69] J. G. Turner *et al.*, "Hydrogel-Forming Microneedles: Current Advancements and Future Trends," *Macromol. Biosci.*, vol. 21, no. 2, p. 2000307, Feb. 2021.

[70] J. W. Lee *et al.*, "Dissolving microneedles for transdermal drug delivery," *Biomaterials*, vol. 29, no. 13, pp. 2113–2124, 2008.

[71] T. M. Blicharz *et al.*, "Microneedle-based device for the one-step painless collection of capillary blood samples," *Nat. Biomed. Eng.*, vol. 2, no. 3, pp. 151–157, Feb. 2018.

[72] F. Ribet *et al.*, "Microneedle Patch for Painless Intradermal Collection of Interstitial Fluid Enabling Multianalyte Measurement of Small Molecules, SARS-CoV-2 Antibodies, and Protein Profiling," *Adv. Healthc. Mater.*, p. 2202564, Feb. 2023.

[73] B. Q. Tran *et al.*, "Proteomic Characterization of Dermal Interstitial Fluid Extracted Using a Novel Microneedle-Assisted Technique," *J. Proteome Res.*, vol. 17, no. 1, pp. 479–485, Jan. 2018.

[74] X. Huang *et al.*, "3D-assembled microneedle ion sensor-based wearable system for the transdermal monitoring of physiological ion fluctuations," *Microsystems Nanoeng.*, vol. 9, no. 1, p. 25, 2023.

[75] X. Huang *et al.*, "Microarrow sensor array with enhanced skin adhesion for transdermal continuous monitoring of glucose and reactive oxygen species," *Bio-Design Manuf.*, vol. 7, no. 1, pp. 14–30, Jan. 2024.

[76] H. Chang *et al.*, "A swellable microneedle patch to rapidly extract skin interstitial fluid for timely metabolic analysis," *Adv. Mater.*, vol. 29, no. 37, p. 1702243, 2017.

[77] S. A. N. Gowers *et al.*, "Development of a Minimally Invasive Microneedle-Based Sensor for Continuous Monitoring of β-Lactam Antibiotic Concentrations in Vivo," *ACS Sensors*, vol. 4, no. 4, pp. 1072–1080, Apr. 2019.

[78] T. M. Rawson *et al.*, "Microneedle biosensors for real-time, minimally invasive drug monitoring of phenoxymethylpenicillin: a first-in-human evaluation in healthy volunteers," *Lancet Digit. Heal.*, vol. 1, no. 7, pp. e335–e343, Nov. 2019.

[79] S. Odinotski *et al.*, "A Conductive Hydrogel-Based Microneedle Platform for Real-Time pH Measurement in Live Animals," *Small*, vol. 18, no. 45, p. 2200201, 2022.

[80] J. E. Park *et al.*, "Plasmonic Microneedle Arrays for in Situ Sensing with Surface-

Enhanced Raman Spectroscopy (SERS)," *Nano Lett.*, vol. 19, no. 10, pp. 6862–6868, Oct. 2019.

[81] H. X. Nguyen *et al.*, "Poly (vinyl alcohol) microneedles: Fabrication, characterization, and application for transdermal drug delivery of doxorubicin," *Eur. J. Pharm. Biopharm.*, vol. 129, pp. 88–103, 2018.

[82] L. Zheng *et al.*, "A silk-microneedle patch to detect glucose in the interstitial fluid of skin or plant tissue," *Sensors Actuators B Chem.*, vol. 372, p. 132626, Dec. 2022.

[83] Y. Liu *et al.*, "Continuous monitoring of diabetes with an integrated microneedle biosensing device through 3D printing," *Microsystems Nanoeng. 2021 71*, vol. 7, no. 1, pp. 1–12, Sep. 2021.

[84] Y. Yao *et al.*, "Integration of interstitial fluid extraction and glucose detection in one device for wearable non-invasive blood glucose sensors," *Biosens. Bioelectron.*, vol. 179, p. 113078, May 2021.

[85] X. Jiang *et al.*, "Microneedle-based sampling of dermal interstitial fluid using a vacuum-assisted skin patch," *Cell Reports Phys. Sci.*, vol. 0, no. 0, p. 101975, May 2024.

[86] X. Huang *et al.*, "Technological Advances of Wearable Device for Continuous Monitoring of In Vivo Glucose," *ACS sensors*, vol. 9, no. 3, pp. 1065–1088, 2024.

[87] M. Zheng *et al.*, "A skin patch integrating swellable microneedles and electrochemical test strips for glucose and alcohol measurement in skin interstitial fluid," *Bioeng. Transl. Med.*, Oct. 2022.

[88] J. Kim *et al.*, "Development of an electrochemical biosensor for non-invasive cholesterol monitoring via microneedle-based interstitial fluid extraction," *Talanta*, vol. 280, p. 126771, Dec. 2024.

[89] D. M. E. Freeman *et al.*, "Continuous Measurement of Lactate Concentration in Human Subjects through Direct Electron Transfer from Enzymes to Microneedle Electrodes," *ACS Sensors*, vol. 8, pp. 1639–1647, 2022.

[90] P. Bollella *et al.*, "Microneedle-based biosensor for minimally-invasive lactate detection," *Biosens. Bioelectron.*, vol. 123, pp. 152–159, Jan. 2019.

[91] A. M. Downs *et al.*, "Microneedle electrochemical aptamer-based sensing: Real-time small molecule measurements using sensor-embedded, commercially-available

stainless steel microneedles," *Biosens. Bioelectron.*, vol. 236, p. 115408, 2023.

[92] Y. Zheng *et al.*, "A Wearable Microneedle-Based Extended Gate Transistor for Real-Time Detection of Sodium in Interstitial Fluids," *Adv. Mater.*, vol. 34, no. 10, p. 2108607, 2022.

[93] Á. Molinero-Fernández *et al.*, "In Vivo Transdermal Multi-Ion Monitoring with a Potentiometric Microneedle-Based Sensor Patch," *ACS sensors*, 2022.

[94] C. Moonla *et al.*, "Continuous Ketone Monitoring via Wearable Microneedle Patch Platform," *ACS sensors*, vol. 9, no. 2, pp. 1004–1013, 2024.

[95] G. Zhong *et al.*, "Fully integrated microneedle biosensor array for wearable multiplexed fitness biomarkers monitoring," *Biosens. Bioelectron.*, vol. 265, p. 116697, Dec. 2024.

[96] Y. Li *et al.*, "Hydrogel-Coated SERS Microneedles for Drug Monitoring in Dermal Interstitial Fluid," *ACS Sensors*, vol. 9, no. 5, pp. 2567–2574, May 2024.

[97] D. G. Koutsonanos *et al.*, "Transdermal influenza immunization with vaccine-coated microneedle arrays," *PLoS One*, vol. 4, no. 3, p. e4773, 2009.

[98] E. M. Cahill *et al.*, "Metallic microneedles with interconnected porosity: A scalable platform for biosensing and drug delivery," *Acta Biomater.*, vol. 80, pp. 401–411, 2018.

[99] S. R. Corrie *et al.*, "Surface-modified microprojection arrays for intradermal biomarker capture, with low non-specific protein binding," *Lab Chip*, vol. 10, no. 20, pp. 2655–2658, 2010.

[100] Z. Wang *et al.*, "Microneedle patch for the ultrasensitive quantification of protein biomarkers in interstitial fluid," *Nat. Biomed. Eng.*, vol. 5, no. 1, pp. 64–76, Jan. 2021.

[101] Z. Chen *et al.*, "Rapid fabrication of microneedles using magnetorheological drawing lithography," *Acta Biomater.*, vol. 65, pp. 283–291, 2018.

[102] X. Li *et al.*, "Limpet tooth-inspired painless microneedles fabricated by magnetic field-assisted 3D printing," *Adv. Funct. Mater.*, vol. 31, no. 5, p. 2003725, 2021.

[103] J.-H. Park *et al.*, "Polymer particle-based micromolding to fabricate novel microstructures," *Biomed. Microdevices*, vol. 9, pp. 223–234, 2007.

[104] P. Liu *et al.*, "Polymer microneedles with interconnected porous structures via a phase inversion route for transdermal medical applications," *J. Mater. Chem. B*, vol. 8, no. 10, pp. 2032–2039, 2020.

[105] K. Nagamine *et al.*, "An array of porous microneedles for transdermal monitoring of intercellular swelling," *Biomed. Microdevices*, vol. 19, pp. 1–6, 2017.

[106] H. Lee *et al.*, "Porous microneedles on a paper for screening test of prediabetes," *Med. Devices Sensors*, vol. 3, no. 4, p. e10109, 2020.

[107] Y.-E. Kang *et al.*, "Nanochannel-driven rapid capture of sub-nanogram level biomarkers for painless preeclampsia diagnosis," *Biosens. Bioelectron.*, vol. 163, p. 112281, 2020.

[108] K. Yi *et al.*, "Aptamer-decorated porous microneedles arrays for extraction and detection of skin interstitial fluid biomarkers," *Biosens. Bioelectron.*, vol. 190, p. 113404, 2021.

[109] Y. Li *et al.*, "Iontophoresis-driven porous microneedle array patch for active transdermal drug delivery," *Acta Biomater.*, vol. 121, pp. 349–358, Feb. 2021.

[110] Q. yao He *et al.*, "Reverse iontophoresis generated by porous microneedles produces an electroosmotic flow for glucose determination," *Talanta*, vol. 267, p. 125156, Jan. 2024.

[111] K. Takeuchi *et al.*, "Microfluidic chip connected to porous microneedle array for continuous ISF sampling," *Drug Deliv. Transl. Res.*, vol. 12, no. 2, pp. 435–443, Feb. 2022.

[112] A. M. V. Mohan *et al.*, "Continuous minimally-invasive alcohol monitoring using microneedle sensor arrays," *Biosens. Bioelectron.*, vol. 91, pp. 574–579, May 2017.

[113] F. Ribet *et al.*, "Real-time intradermal continuous glucose monitoring using a minimally invasive microneedle-based system," *Biomed. Microdevices*, vol. 20, no. 4, pp. 1–10, Dec. 2018.

[114] H. Li *et al.*, "Microneedle-Based Potentiometric Sensing System for Continuous Monitoring of Multiple Electrolytes in Skin Interstitial Fluids," *ACS Sensors*, vol. 6, no. 6, pp. 2181–2190, Jun. 2021.

[115] J. Yang *et al.*, "Development of Smartphone-Controlled and Microneedle-Based Wearable Continuous Glucose Monitoring System for Home-Care Diabetes Management," *ACS Sensors*, vol. 8, no. 3, pp. 1241–1251, Mar. 2023.

[116] H. Teymourian *et al.*, "Microneedle-Based Detection of Ketone Bodies along with Glucose and Lactate: Toward Real-Time Continuous Interstitial Fluid Monitoring of

Diabetic Ketosis and Ketoacidosis," *Anal. Chem.*, vol. 92, no. 2, pp. 2291–2300, Jan. 2020.

[117] R. K. Mishra *et al.*, "Continuous Opioid Monitoring along with Nerve Agents on a Wearable Microneedle Sensor Array," *J. Am. Chem. Soc.*, vol. 142, no. 13, pp. 5991–5995, Apr. 2020.

[118] B. Yang *et al.*, "Engineered Microneedles for Interstitial Fluid Cell-Free DNA Capture and Sensing Using Iontophoretic Dual-Extraction Wearable Patch," *Adv. Funct. Mater.*, vol. 30, no. 24, p. 2000591, Jun. 2020.

[119] P. R. Miller *et al.*, "Microneedle-Based Transdermal Sensor for On-Chip Potentiometric Determination of K +," *Adv. Healthc. Mater.*, 2013.

[120] Y. Xie *et al.*, "Enhanced Interstitial Fluid Extraction and Rapid Analysis via Vacuum Tube-Integrated Microneedle Array Device," *Adv. Sci.*, p. 2308716, Mar. 2024.

[121] J. Cheng *et al.*, "Hollow microneedle microfluidic paper-based chip for biomolecules rapid sampling and detection in interstitial fluid," *Anal. Chim. Acta*, vol. 1255, no. March, p. 341101, 2023.

[122] T. Q. Ma *et al.*, "Wearable microneedle sensor with replaceable sensor base for multi-purpose detecting in skin interstitial fluid," *Microchem. J.*, vol. 203, p. 110933, Aug. 2024.

[123] C. Kolluru *et al.*, "Plasmonic Paper Microneedle Patch for On-Patch Detection of Molecules in Dermal Interstitial Fluid," *ACS Sensors*, vol. 4, no. 6, pp. 1569–1576, Jun. 2019.

[124] J. Xiao *et al.*, "Microfluidic-based plasmonic microneedle biosensor for uric acid ultrasensitive monitoring," *Sensors Actuators B Chem.*, vol. 398, p. 134685, Jan. 2024.

[125] L. Lin *et al.*, "Multimicrochannel microneedle microporation platform for enhanced intracellular drug delivery," *Adv. Funct. Mater.*, vol. 32, no. 21, p. 2109187, 2022.

[126] S. A. Ranamukhaarachchi *et al.*, "Integrated hollow microneedle-optofluidic biosensor for therapeutic drug monitoring in sub-nanoliter volumes," *Sci. Rep.*, vol. 6, no. 1, p. 29075, 2016.

[127] Z. Chen *et al.*, "3D-printed integrated ultrasonic microneedle array for rapid transdermal drug delivery," *Mol. Pharm.*, vol. 19, no. 9, pp. 3314–3322, 2022.

[128] J. Yang *et al.*, "Recent advances of microneedles used towards stimuli-responsive drug

delivery, disease theranostics, and bioinspired applications," *Chem. Eng. J.*, vol. 426, p. 130561, 2021.

[129] J. Yang *et al.*, "Recent advances of microneedles for biomedical applications: drug delivery and beyond," *Acta Pharm. Sin. B*, vol. 9, no. 3, pp. 469–483, 2019.

[130] X. Huang *et al.*, "In Situ Tyrosinase Monitoring by Wearable Microneedle Patch toward Clinical Melanoma Screening," *ACS Nano*, vol. 17, no. 20, pp. 20073–20086, Oct. 2023.

[131] Y. Xie *et al.*, "Controlled transdermal delivery of model drug compounds by MEMS microneedle array," *Nanomedicine Nanotechnology, Biol. Med.*, vol. 1, no. 2, pp. 184–190, 2005.

[132] M. Reynoso *et al.*, "3D-printed, aptamer-based microneedle sensor arrays using magnetic placement on live rats for pharmacokinetic measurements in interstitial fluid," *Biosens. Bioelectron.*, vol. 244, p. 115802, Jan. 2024.

[133] C. Yang *et al.*, "Glucose-responsive microneedle patch for closed-loop dual-hormone delivery in mice and pigs," *Sci. Adv.*, vol. 8, no. 48, p. 3197, Dec. 2022.

[134] C. Kolluru *et al.*, "Recruitment and collection of dermal interstitial fluid using a microneedle patch," *Adv. Healthc. Mater.*, vol. 8, no. 3, p. 1801262, 2019.

[135] Y. Hu *et al.*, "Microneedle Sensors for Point-of-Care Diagnostics," *Adv. Sci.*, p. 2306560, Jan. 2024.

[136] G. Kim *et al.*, "Microneedle sensors for dermal interstitial fluid analysis," *Med-X 2024 21*, vol. 2, no. 1, pp. 1–23, Oct. 2024.

[137] H. J. G. E. Gardeniers *et al.*, "Silicon micromachined hollow microneedles for transdermal liquid transport," *J. Microelectromechanical Syst.*, vol. 12, no. 6, pp. 855–862, 2003.

[138] C. J. W. Bolton *et al.*, "Hollow silicon microneedle fabrication using advanced plasma etch technologies for applications in transdermal drug delivery," *Lab Chip*, vol. 20, no. 15, pp. 2788–2795, 2020.

[139] P. Khanna *et al.*, "Sharpening of hollow silicon microneedles to reduce skin penetration force," *J. Micromechanics Microengineering*, vol. 20, no. 4, p. 45011, 2010.

[140] P. Griss and G. Stemme, "Side-opened out-of-plane microneedles for microfluidic transdermal liquid transfer," *J. Microelectromechanical Syst.*, vol. 12, no. 3, pp. 296–

301, 2003.

[141] B. Stoeber and D. Liepmann, "Arrays of hollow out-of-plane microneedles for drug delivery," *J. Microelectromechanical Syst.*, vol. 14, no. 3, pp. 472–479, Jun. 2005.

[142] M. W. Ashraf *et al.*, "Design, fabrication and analysis of silicon hollow microneedles for transdermal drug delivery system for treatment of hemodynamic dysfunctions," *Cardiovasc. Eng.*, vol. 10, pp. 91–108, 2010.

[143] P. Jurčíček *et al.*, "Design and fabrication of hollow out-of-plane silicon microneedles," *Micro Nano Lett.*, vol. 8, no. 2, pp. 78–81, 2013.

[144] K. B. Vinayakumar *et al.*, "Fabrication and characterization of gold coated hollow silicon microneedle array for drug delivery," *Microelectron. Eng.*, vol. 128, pp. 12–18, 2014.

[145] Y. Xuan *et al.*, "Fabrication and use of silicon hollow-needle arrays to achieve tissue nanotransfection in mouse tissue in vivo," *Nat. Protoc.*, vol. 16, no. 12, pp. 5707–5738, 2021.

[146] J. Wang *et al.*, "Preparation of microneedle array mold based on MEMS lithography technology," *Micromachines*, vol. 12, no. 1, p. 23, 2020.

[147] W. Hu *et al.*, "High aspect ratio silicon ring-shape micropillars fabricated by deep reactive ion etching with sacrificial structures," *Micro Nano Eng.*, vol. 22, p. 100234, 2024.

[148] J. Ji *et al.*, "Microfabricated hollow microneedle array using ICP etcher," in *Journal of Physics: Conference Series*, 2006, vol. 34, no. 1, p. 1132.

[149] C. O'Mahony *et al.*, "Hollow silicon microneedles, fabricated using combined wet and dry etching techniques, for transdermal delivery and diagnostics," *Int. J. Pharm.*, vol. 637, p. 122888, Apr. 2023.

[150] D. V McAllister *et al.*, "Microfabricated needles for transdermal delivery of macromolecules and nanoparticles: fabrication methods and transport studies," *Proc. Natl. Acad. Sci.*, vol. 100, no. 24, pp. 13755–13760, 2003.

[151] S. P. Davis *et al.*, "Fabrication and characterization of laser micromachined hollow microneedles," in *TRANSDUCERS'03. 12th International Conference on Solid-State Sensors, Actuators and Microsystems. Digest of Technical Papers (Cat. No. 03TH8664)*, 2003, vol. 2, pp. 1435–1438.

[152] S. P. Davis *et al.*, “Insertion of microneedles into skin: measurement and prediction of insertion force and needle fracture force,” *J. Biomech.*, vol. 37, no. 8, pp. 1155–1163, Aug. 2004.

[153] J. Son *et al.*, “Cactus-Spine-Inspired Sweat-Collecting Patch for Fast and Continuous Monitoring of Sweat,” *Adv. Mater.*, vol. 2102740, pp. 1–9, 2021.

[154] X. Wang *et al.*, “Surface Wettability for Skin-Interfaced Sensors and Devices,” *Adv. Funct. Mater.*, vol. 32, no. 27, p. 2200260, 2022.

[155] K. Kim and J. B. Lee, “High aspect ratio tapered hollow metallic microneedle arrays with microfluidic interconnector,” *Microsyst. Technol.*, vol. 13, no. 3–4, pp. 231–235, Feb. 2007.

[156] K. Kim *et al.*, “A tapered hollow metallic microneedle array using backside exposure of SU-8,” *J. Micromechanics Microengineering*, vol. 14, no. 4, p. 597, 2004.

[157] S. P. Davis *et al.*, “Insertion of microneedles into skin: measurement and prediction of insertion force and needle fracture force,” *J. Biomech.*, vol. 37, no. 8, pp. 1155–1163, 2004.

[158] G. Anbazhagan *et al.*, “Design, analysis and fabrication of solid polymer microneedle patch using CO2 laser and polymer molding,” *Drug Deliv. Transl. Res.*, vol. 13, no. 6, pp. 1813–1827, 2023.

[159] Y.-W. Chen *et al.*, “A facile approach for rapid prototyping of microneedle molds, microwells and micro-through-holes in various substrate materials using CO2 laser drilling,” *Biomedicines*, vol. 8, no. 10, p. 427, 2020.

[160] M. Parrilla *et al.*, “Wearable microneedle-based array patches for continuous electrochemical monitoring and drug delivery: toward a closed-loop system for methotrexate treatment,” *ACS sensors*, vol. 8, no. 11, pp. 4161–4170, 2023.

[161] M. Parrilla *et al.*, “Wearable hollow microneedle sensing patches for the transdermal electrochemical monitoring of glucose,” *Talanta*, vol. 249, p. 123695, 2022.

[162] K. B. Vinayakumar *et al.*, “A hollow stainless steel microneedle array to deliver insulin to a diabetic rat,” *J. Micromechanics Microengineering*, vol. 26, no. 6, p. 65013, 2016.

[163] T. D. Ngo *et al.*, “Additive manufacturing (3D printing): A review of materials, methods, applications and challenges,” *Compos. Part B Eng.*, vol. 143, pp. 172–196, 2018.

[164] Z. F. Rad *et al.*, "Parametric optimization of two-photon direct laser writing process for manufacturing polymeric microneedles," *Addit. Manuf.*, vol. 56, p. 102953, 2022.

[165] Z. F. Rad *et al.*, "Rapid prototyping and customizable microneedle design: Ultra-sharp microneedle fabrication using two-photon polymerization and low-cost micromolding techniques," *Manuf. Lett.*, vol. 30, pp. 39–43, 2021.

[166] Z. Faraji Rad *et al.*, "High-resolution two-photon polymerization: The most versatile technique for the fabrication of microneedle arrays," *Microsystems Nanoeng.*, vol. 7, no. 1, p. 71, 2021.

[167] Z. F. Rad *et al.*, "High-fidelity replication of thermoplastic microneedles with open microfluidic channels," *Microsystems Nanoeng. 2017 31*, vol. 3, no. 1, pp. 1–11, Oct. 2017.

[168] M. Dervisevic *et al.*, "Wearable Microneedle Patch for Transdermal Electrochemical Monitoring of Urea in Interstitial Fluid," *ACS sensors*, vol. 9, no. 2, pp. 932–941, 2024.

[169] M. Dervisevic *et al.*, "3D Polymeric Lattice Microstructure-Based Microneedle Array for Transdermal Electrochemical Biosensing," *Adv. Mater.*, p. 2412999, 2024.

[170] S. Shukla *et al.*, "Microneedle-Integrated Device for Transdermal Sampling and Analyses of Targeted Biomarkers," *Small Sci.*, p. 2200087, Apr. 2023.

[171] J. Bai *et al.*, "Coin-sized, fully integrated, and minimally invasive continuous glucose monitoring system based on organic electrochemical transistors," *Sci. Adv.*, vol. 10, no. 16, p. 1856, Apr. 2024.

[172] Q. Wang *et al.*, "Wearable Vertical Graphene-Based Microneedle Biosensor for Real-Time Ketogenic Diet Management," *Anal. Chem.*, 2024.

[173] A. Trautmann *et al.*, "Towards a versatile point-of-care system combining femtosecond laser generated microfluidic channels and direct laser written microneedle arrays," *Microsystems Nanoeng. 2019 51*, vol. 5, no. 1, pp. 1–9, Feb. 2019.

[174] A. Doraiswamy *et al.*, "Two photon induced polymerization of organic–inorganic hybrid biomaterials for microstructured medical devices," *Acta Biomater.*, vol. 2, no. 3, pp. 267–275, 2006.

[175] C. Liao *et al.*, "Two-photon nanolithography of tailored hollow three-dimensional microdevices for biosystems," *ACS omega*, vol. 4, no. 1, pp. 1401–1409, 2019.

[176] C. Plamadeala *et al.*, "Bio-inspired microneedle design for efficient drug/vaccine

coating," *Biomed. Microdevices*, vol. 22, pp. 1–9, 2020.

[177] A. S. Cordeiro *et al.*, "Two-photon polymerisation 3D printing of microneedle array templates with versatile designs: application in the development of polymeric drug delivery systems," *Pharm. Res.*, vol. 37, pp. 1–15, 2020.

[178] A. Aksit *et al.*, "In-vitro perforation of the round window membrane via direct 3-D printed microneedles," *Biomed. Microdevices*, vol. 20, pp. 1–12, 2018.

[179] M. Suzuki *et al.*, "3D laser lithographic fabrication of hollow microneedle mimicking mosquitos and its characterisation," *Int. J. Nanotechnol.*, vol. 15, no. 1–3, pp. 157–173, 2018.

[180] P. Miller *et al.*, "Towards an integrated microneedle total analysis chip for protein detection," *Electroanalysis*, vol. 28, no. 6, pp. 1305–1310, 2016.

[181] Q. Ge *et al.*, "Projection micro stereolithography based 3D printing and its applications," *Int. J. Extrem. Manuf.*, vol. 2, no. 2, p. 22004, 2020.

[182] Y. Ren *et al.*, "Customized flexible hollow microneedles for psoriasis treatment with reduced-dose drug," *Bioeng. Transl. Med.*, vol. 8, no. 4, p. e10530, 2023.

[183] "https://www.ascilion.com/."

[184] S. J. Moon *et al.*, "Fabrication of microneedle array using LIGA and hot embossing process," *Microsyst. Technol.*, vol. 11, pp. 311–318, 2005.

[185] M. Parrilla *et al.*, "3D-printed microneedle-based potentiometric sensor for pH monitoring in skin interstitial fluid," *Sensors Actuators B Chem.*, vol. 378, p. 133159, Mar. 2023.

[186] M. Parrilla *et al.*, "A 3D-printed hollow microneedle-based electrochemical sensing device for in situ plant health monitoring," *Biosens. Bioelectron.*, vol. 251, p. 116131, May 2024.

[187] C. G. Li *et al.*, "An optimized hollow microneedle for minimally invasive blood extraction," *Biomed. Microdevices*, vol. 15, pp. 17–25, 2013.

[188] M. Bariya *et al.*, "Wearable sweat sensors," *Nat. Electron.*, vol. 1, no. 3, pp. 160–171, 2018.

[189] W. Gao *et al.*, "Fully integrated wearable sensor arrays for multiplexed in situ perspiration analysis," *Nature*, vol. 529, 2016.

[190] M. Vinayagam *et al.*, "Soft microfiber-based hollow microneedle array for stretchable

microfluidic biosensing patch with negative pressure-driven sampling," *Biosens. Bioelectron.*, vol. 237, no. May, p. 115468, 2023.

[191] H. C. Ates *et al.*, "End-to-end design of wearable sensors," *Nat. Rev. Mater.*, vol. 7, no. 11, pp. 887–907, 2022.

[192] Y. Wang *et al.*, "Electrochemical sensors for clinic analysis," *Sensors*, vol. 8, no. 4, pp. 2043–2081, 2008.

[193] Changyuan Zhan *et al.*, "A 3D-printed microneedle extraction system integrated with patterned electrodes for minimally invasive transdermal detection," *Biomater. Sci.*, 2023.

[194] Z. Li *et al.*, "Development of an osmosis-assisted hollow microneedle array integrated with dual-functional electrochemical sensor for urea and pH monitoring in interstitial fluid," *Sensors Actuators B Chem.*, vol. 422, p. 136606, Jan. 2025.

[195] J. Leanpolchareanchai and N. Nuchtavorn, "Wearable microneedle-based colorimetric and fluorescence sensing for transdermal diagnostics," *Talanta Open*, vol. 8, no. April, p. 100247, 2023.

[196] T. Kant *et al.*, "Progress in the design of portable colorimetric chemical sensing devices," *Nanoscale*, vol. 15, no. 47, pp. 19016–19038, 2023.

[197] H. Yang *et al.*, "A swellable bilateral microneedle patch with core-shell structure for rapid lactate analysis and early melanoma diagnosis," *Chem. Eng. J.*, vol. 455, p. 140730, Jan. 2023.

[198] Z. Wang *et al.*, "Transdermal colorimetric patch for hyperglycemia sensing in diabetic mice," *Biomaterials*, vol. 237, p. 119782, 2020.

[199] X. Li *et al.*, "Swellable colorimetric microneedles for glucose detection based on glucose oxidase-like gold nanoparticles," *Anal. Chim. Acta*, vol. 1288, p. 342152, Feb. 2024.

[200] X. Q. You *et al.*, "Multi-groove microneedles based wearable colorimetric sensor for simple and facile glucose detection," *Microchem. J.*, vol. 190, no. February, p. 108570, 2023.

[201] Z. Bao *et al.*, "Wearable Microneedle Patch for Colorimetric Detection of Multiple Signature Biomarkers in vivo Toward Diabetic Diagnosis," *Adv. Healthc. Mater.*, p. 2303511, 2024.

[202] C. G. Li *et al.*, "One-touch-activated blood multidiagnostic system using a minimally invasive hollow microneedle integrated with a paper-based sensor," *Lab Chip*, vol. 15, no. 16, pp. 3286–3292, 2015.

[203] Y. Yang and W. Gao, "Wearable and flexible electronics for continuous molecular monitoring," *Chem. Soc. Rev.*, vol. 48, no. 6, pp. 1465–1491, 2019.

[204] T. Saha *et al.*, "Access and Management of Sweat for Non-Invasive Biomarker Monitoring: A Comprehensive Review," *Small*, p. 2206064, 2022.

[205] H. Song *et al.*, "Wireless Non-Invasive Monitoring of Cholesterol Using a Smart Contact Lens," *Adv. Sci.*, vol. 9, no. 28, p. 2203597, 2022.

[206] L. Lipani *et al.*, "Non-invasive, transdermal, path-selective and specific glucose monitoring via a graphene-based platform," *Nat. Nanotechnol.*, vol. 13, no. 6, pp. 504–511, 2018.

[207] J. R. Sempionatto *et al.*, "An epidermal patch for the simultaneous monitoring of haemodynamic and metabolic biomarkers," *Nat. Biomed. Eng.*, vol. 5, no. 7, pp. 737–748, 2021.

[208] M. Zheng *et al.*, "Osmosis-powered hydrogel microneedles for microliters of skin interstitial fluid extraction within minutes," *Adv. Healthc. Mater.*, vol. 9, no. 10, p. 1901683, 2020.

[209] J. Zhu *et al.*, "Gelatin Methacryloyl Microneedle Patches for Minimally Invasive Extraction of Skin Interstitial Fluid," *Small*, vol. 16, no. 16, p. 1905910, Apr. 2020.

[210] Q. Yang *et al.*, "Microneedle Array Encapsulated with Programmed DNA Hydrogels for Rapidly Sampling and Sensitively Sensing of Specific MicroRNA in Dermal Interstitial Fluid," *ACS Nano*, vol. 16, no. 11, pp. 18366–18375, 2022.

[211] R. K. Sivamani *et al.*, "Microneedles and transdermal applications," *Expert Opin. Drug Deliv.*, vol. 4, no. 1, pp. 19–25, 2007.

[212] C. Y. Jin *et al.*, "Mass producible and biocompatible microneedle patch and functional verification of its usefulness for transdermal drug delivery," *Biomed. Microdevices*, vol. 11, no. 6, pp. 1195–1203, 2009.

[213] M. A. Eddings *et al.*, "Determining the optimal PDMS–PDMS bonding technique for microfluidic devices," *J. Micromech. Microeng.*, vol. 18, no. 6, p. 67001, 2008.

[214] W. Gao *et al.*, "Fully integrated wearable sensor arrays for multiplexed in situ

perspiration analysis," *Nature*, vol. 529, no. 7587, pp. 509–514, 2016.

[215] A. H. Bretag, "Synthetic interstial fluid for isolated mammalian tissue," *Life Sci.*, vol. 8, no. 5, pp. 319–329, 1969.

[216] C.-H. Heldin *et al.*, "High interstitial fluid pressure—an obstacle in cancer therapy," *Nat. Rev. Cancer*, vol. 4, no. 10, pp. 806–813, 2004.

[217] N. Roxhed *et al.*, "Penetration-enhanced ultrasharp microneedles and prediction on skin interaction for efficient transdermal drug delivery," *J. Microelectromechanical Syst.*, vol. 16, no. 6, pp. 1429–1440, 2007.

[218] S. D. Gittard *et al.*, "The effects of geometry on skin penetration and failure of polymer microneedles," *J. Adhes. Sci. Technol.*, vol. 27, no. 3, pp. 227–243, 2013.

[219] O. Olatunji *et al.*, "Influence of array interspacing on the force required for successful microneedle skin penetration: theoretical and practical approaches," *J. Pharm. Sci.*, vol. 102, no. 4, pp. 1209–1221, 2013.

[220] J. Zhu *et al.*, "Gelatin methacryloyl microneedle patches for minimally invasive extraction of skin interstitial fluid," *Small*, vol. 16, no. 16, p. 1905910, 2020.

[221] S. Park *et al.*, "Rapid extraction and detection of biomolecules via a microneedle array of wet-crosslinked methacrylated hyaluronic acid," *Adv. Mater. Technol.*, vol. 7, no. 3, p. 2100874, 2022.

[222] D. F. S. Fonseca *et al.*, "Swellable gelatin methacryloyl microneedles for extraction of interstitial skin fluid toward minimally invasive monitoring of urea," *Macromol. Biosci.*, vol. 20, no. 10, p. 2000195, 2020.

[223] J. Wang, "Electrochemical glucose biosensors," *Chem. Rev.*, vol. 108, no. 2, pp. 814–825, 2008.

[224] Y. Marunaka, "Roles of interstitial fluid pH in diabetes mellitus: Glycolysis and mitochondrial function," *World J. Diabetes*, vol. 6, no. 1, p. 125, 2015.

[225] N. Xu *et al.*, "Microneedle-Based Technology: Toward Minimally Invasive Disease Diagnostics," *Adv. Mater. Technol.*, vol. 7, no. 9, p. 2101595, 2022.

[226] S. Alamri *et al.*, "Controlling the wettability of polycarbonate substrates by producing hierarchical structures using Direct Laser Interference Patterning," *Eur. Polym. J.*, vol. 99, pp. 27–37, 2018.

[227] E. Laszlo *et al.*, "Superswelling microneedle arrays for dermal interstitial fluid (prote)

omics," *Adv. Funct. Mater.*, vol. 31, no. 46, p. 2106061, 2021.

[228] J. Kool *et al.*, "Suction blister fluid as potential body fluid for biomarker proteins," *Proteomics*, vol. 7, no. 20, pp. 3638–3650, 2007.

[229] U. Sjöbom *et al.*, "Inflammatory markers in suction blister fluid: a comparative study between interstitial fluid and plasma," *Front. Immunol.*, vol. 11, p. 597632, 2020.

[230] M. M. Niedzwiecki *et al.*, "Human suction blister fluid composition determined using high-resolution metabolomics," *Anal. Chem.*, vol. 90, no. 6, pp. 3786–3792, 2018.

[231] N. Xu *et al.*, "Swellable PVA/PVP hydrogel microneedle patches for the extraction of interstitial skin fluid toward minimally invasive monitoring of blood glucose level," *Analyst*, vol. 147, no. 7, pp. 1478–1491, Mar. 2022.

[232] X. Li *et al.*, "A fully integrated closed-loop system based on mesoporous microneedles-iontophoresis for diabetes treatment," *Adv. Sci.*, vol. 8, no. 16, p. 2100827, 2021.

[233] A. Sieg *et al.*, "Noninvasive glucose monitoring by reverse iontophoresis in vivo: application of the internal standard concept," *Clin. Chem.*, vol. 50, no. 8, pp. 1383–1390, 2004.

[234] R. O. Potts *et al.*, "Glucose monitoring by reverse iontophoresis," *Diabetes. Metab. Res. Rev.*, vol. 18, no. S1, pp. S49–S53, 2002.

[235] M. E. Collison *et al.*, "Analytical characterization of electrochemical biosensor test strips for measurement of glucose in low-volume interstitial fluid samples." Oxford University Press, 1999.

[236] S. V. Puttaswamy *et al.*, "Nanophotonic-carbohydrate lab-on-a-microneedle for rapid detection of human cystatin C in finger-prick blood," *ACS Nano*, vol. 14, no. 9, pp. 11939–11949, 2020.

[237] J. Chen *et al.*, "Fabrication of sponge-forming microneedle patch for rapidly sampling interstitial fluid for analysis," *Biomed. Microdevices*, vol. 21, pp. 1–10, 2019.

[238] L. Liu *et al.*, "Porous polymer microneedles with interconnecting microchannels for rapid fluid transport," *RSC Adv.*, vol. 6, no. 54, pp. 48630–48635, May 2016.

[239] A. V. Romanyuk *et al.*, "Collection of analytes from microneedle patches," *Anal. Chem.*, vol. 86, no. 21, pp. 10520–10523, Oct. 2014.

[240] E. Caffarel-Salvador *et al.*, "Hydrogel-forming microneedle arrays allow detection of drugs and glucose in vivo: potential for use in diagnosis and therapeutic drug

monitoring," *PLoS One*, vol. 10, no. 12, p. e0145644, 2015.

[241] R. He *et al.*, "A Hydrogel Microneedle Patch for Point-of-Care Testing Based on Skin Interstitial Fluid," *Adv. Healthc. Mater.*, vol. 9, no. 4, p. 1901201, Feb. 2020.

[242] Y. Qiao *et al.*, "A sample and detection microneedle patch for psoriasis MicroRNA biomarker analysis in interstitial fluid," *Anal. Chem.*, vol. 94, no. 14, pp. 5538–5545, 2022.

[243] P. R. Miller *et al.*, "Extraction and biomolecular analysis of dermal interstitial fluid collected with hollow microneedles," *Commun. Biol.*, vol. 1, no. 1, pp. 1–11, Dec. 2018.

[244] C. Svedman *et al.*, "Plasma proteins in a standardised skin mini-erosion (II): effects of extraction pressure," *BMC Dermatol.*, vol. 2, pp. 1–3, 2002.

[245] U. Kiistala, "Suction Blister Device for Separation of Viable Epidermis from Dermis*," *J. Invest. Dermatol.*, vol. 50, no. 2, pp. 129–137, 1968.

[246] J. Min *et al.*, "Skin-Interfaced Wearable Sweat Sensors for Precision Medicine," *Chem. Rev.*, Mar. 2023.

[247] M. Bariya *et al.*, "Wearable sweat sensors," *Nature Electronics*, vol. 1, no. 3. Nature Publishing Group, pp. 160–171, Mar. 01, 2018.

[248] H. Haslene-Hox *et al.*, "A new method for isolation of interstitial fluid from human solid tumors applied to proteomic analysis of ovarian carcinoma tissue," *PLoS One*, vol. 6, no. 4, p. e19217, 2011.

[249] S. Schmidt *et al.*, "Clinical microdialysis in skin and soft tissues: an update," *J. Clin. Pharmacol.*, vol. 48, no. 3, pp. 351–364, 2008.

[250] H. Teymourian *et al.*, "Lab under the Skin: Microneedle Based Wearable Devices," *Advanced Healthcare Materials*. Wiley-VCH Verlag, p. 2002255, 2021.

[251] M. Zheng *et al.*, "Microneedle biomedical devices," *Nat. Rev. Bioeng.*, vol. 2, no. 4, pp. 324–342, 2023.

[252] M.-N. Chien *et al.*, "Continuous glucose monitoring system based on percutaneous microneedle array," *Micromachines*, vol. 13, no. 3, p. 478, 2022.

[253] Y. Dong *et al.*, "Opportunities and challenges of microneedle electrochemical sensors for interstitial fluid detection," *TrAC Trends Anal. Chem.*, vol. 180, p. 117891, Nov. 2024.

[254] J. Li *et al.*, "A review of recent advances in microneedle-based sensing within the dermal ISF that could transform medical testing," *ACS sensors*, vol. 9, no. 3, pp. 1149–1161, 2024.

[255] C. Wu *et al.*, "Microneedles as Transdermal Drug Delivery System for Enhancing Skin Disease Treatment," *Acta Pharm. Sin. B*, 2024.

[256] X. He *et al.*, "Microneedle system for transdermal drug and vaccine delivery: devices, safety, and prospects," *Dose-response*, vol. 17, no. 4, p. 1559325819878585, 2019.

[257] I. Rahmi Ausri *et al.*, "Multifunctional Dopamine-Based Hydrogel Microneedle Electrode for Continuous Ketone Sensing," *Adv. Mater.*, p. 2402009, Jun. 2024.

[258] Y. Dai *et al.*, "Wearable Sensor Patch with Hydrogel Microneedles for In Situ Analysis of Interstitial Fluid," *ACS Appl. Mater. Interfaces*, Dec. 2023.

[259] Y. Pang *et al.*, "Porous Microneedles Through Direct Ink Drawing with Nanocomposite Inks for Transdermal Collection of Interstitial Fluid," *Small*, p. 2305838, 2024.

[260] S. A. Ranamukhaarachchi *et al.*, "Design considerations of a hollow microneedle-optofluidic biosensing platform incorporating enzyme-linked assays," *J. Micromechanics Microengineering*, vol. 28, no. 2, p. 024002, Dec. 2017.

[261] L. Barnum *et al.*, "3D-Printed Hydrogel-Filled Microneedle Arrays," *Adv. Healthc. Mater.*, vol. 10, no. 13, p. 2001922, Jul. 2021.

[262] Z. Faraji Rad *et al.*, "High-fidelity replication of thermoplastic microneedles with open microfluidic channels," *Microsystems Nanoeng.*, vol. 3, no. 1, pp. 1–11, 2017.

[263] Y. Zhang *et al.*, "Passive sweat collection and colorimetric analysis of biomarkers relevant to kidney disorders using a soft microfluidic system," *Lab Chip*, vol. 19, no. 9, pp. 1545–1555, May 2019.

[264] M. R. Prausnitz, "Microneedles for transdermal drug delivery," *Adv. Drug Deliv. Rev.*, vol. 56, no. 5, pp. 581–587, 2004.

[265] M. Dervisevic *et al.*, "Skin in the diagnostics game: Wearable biosensor nano-and microsystems for medical diagnostics," *Nano Today*, vol. 30, p. 100828, 2020.

[266] S. M. Laville *et al.*, "Urea levels and cardiovascular disease in patients with chronic kidney disease," *Nephrol. Dial. Transplant.*, vol. 38, no. 1, pp. 184–192, 2023.

[267] W. Aoi and Y. Marunaka, "Importance of pH homeostasis in metabolic health and diseases: crucial role of membrane proton transport," *Biomed Res. Int.*, vol. 2014, no.

1, p. 598986, 2014.

[268] K. H. Steen *et al.*, "A dominant role of acid pH in inflammatory excitation and sensitization of nociceptors in rat skin, in vitro," *J. Neurosci.*, vol. 15, no. 5, pp. 3982–3989, 1995.

[269] J. Dissemond *et al.*, "pH values in chronic wounds. Evaluation during modern wound therapy," *Hautarzt.*, vol. 54, no. 10, pp. 959–965, 2003.

[270] W. O. Ho *et al.*, "Electrochemical sensor for measurement of urea and creatinine in serum based on ac impedance measurement of enzyme-catalyzed polymer transformation," *Anal. Chem.*, vol. 71, no. 10, pp. 1940–1946, 1999.

[271] L. Liu *et al.*, "Quantitative analysis of urea in human urine and serum by 1 H nuclear magnetic resonance," *Analyst*, vol. 137, no. 3, pp. 595–600, 2012.

[272] M. Czauderna and J. Kowalczyk, "Simple, selective, and sensitive measurement of urea in body fluids of mammals by reversed-phase ultra-fast liquid chromatography," *Czech J Anim Sci*, vol. 57, pp. 19–27, 2012.

[273] H. Ray *et al.*, "Characterization of urea hydrolysis in fresh human urine and inhibition by chemical addition," *Environ. Sci. Water Res. Technol.*, vol. 4, no. 1, pp. 87–98, 2018.

[274] M. Fidaleo and R. Lavecchia, "Kinetic study of enzymatic urea hydrolysis in the pH range 4-9," *Chem. Biochem. Eng. Q.*, vol. 17, no. 4, pp. 311–318, 2003.

List of Publications

1. **Abbasiasl, T**.; Mirlou, F.; Mirzajani, H.; Bathaei, M.J.; Istif, E.; Shomalizadeh, N.; Cebecioğlu, R.E.; Özkahraman, E. E.; Yener, U. C.; Beker, L. "A wearable Touch-activated Device Integrated with Hollow Microneedles for Continuous Sampling and Sensing of Dermal Interstitial Fluid". Advanced Materials, **2024**. https://doi.org/10.1002/adma.202304704
2. Mirlou, F.; **Abbasiasl, T**.; Mirzajani, H.; Istif, E.; Akhtar, M. J.; Cakir, C.; Beker, L. "Continuous Glycemic Monitoring Enabled by a Wi-Fi Energy-Harvesting Wearable Sweat-Sensing Patch". Advanced Materials Technologies, **2024**. https://doi.org/10.1002/admt.202301583
3. Isgor, P.K.; **Abbasiasl, T.**; Das, R.; Istif, E.; Yener, U. C.; Beker, L. "Paper Integrated Microfluidic Contact Lens for Colorimetric Glucose Detection". Sensors & Diagnostics. **2024**. https://doi.org/10.1039/D4SD00135D
4. Bathaei, M.J.; Singh, R.; Mirzajani, H.; Istif, E.; Akhtar, M. J.; **Abbasiasl, T**.; Beker, L. "Photolithography-Based Microfabrication of Biodegradable Flexible and Stretchable Sensors". Advanced Materials, **2023**. https://doi.org/10.1002/adma.202207081
5. **Abbasiasl, T.**; Mirlou, F.; Istif, E.; Koydemir, H. C.; Beker, L. "A Wearable Paper-integrated Microfluidic Device for Sequential Analysis of Sweat Based on Capillary Action**"**. Sensors & Diagnostics. **2022**. https://doi.org/10.1039/D2SD00032F
6. Mirzajani, H.; Istif, E.; **Abbasiasl, T.**; Mirlou, F.; Özkahraman, E. E.; Hasanreisoglu, M.; Beker, L. "Femtosecond Laser Ablation Assisted NFC Antenna Fabrication for Smart Contact Lenses". Advanced Materials Technologies, **2022**. https://doi.org/10.1002/admt.202101629

7. Mirzajani, H.; **Abbasiasl, T.**, Mirlou, F.; Istif, E.; Bathaei, M. J.; Çağdas D.; Deyneli, O.; Yazıcı, D.; Beker, L. “An Ultra-Compact and Wireless Tag for Battery-Free Sweat Glucose Monitoring”. Biosensors & Bioelectronics **2022**. https://doi.org/10.1016/j.bios.2022.114450